



EDINBURGH
UNIVERSITY
LIBRARY

Author's Surname
Catalogue Number

FAHMI

Ph.D., 1980.

of Mark

JCM Library



30150

000669785

SIMULATION OF LARGE EARTHQUAKE MOTIONS
FROM SMALLER EARTHQUAKE RECORDS

by

KHALID J. FAHMI

(BSc. Baghdad University, 1974)

Thesis submitted for the degree of
Doctor of Philosophy
at the University of Edinburgh

February 1980



In The Name of Allah, The Compassionate, The Merciful

And that man hath that for which
he maketh effort. And that his
efforts shall be scrutenized.
Then he shall be justly requited
for them.

The Glorious Koran

The Star : Meccan 39-4

To My Parents:

Whose love, understanding and support
brought me success and fortune beyond
expectation.

ABSTRACT

In this research a contribution is made towards the assessment of seismic hazards by simulating the source mechanism of a large earthquake. The adopted working hypothesis is that the motion of a large earthquake seismogram could be represented by a summed succession of smaller earthquakes appropriately triggered in a temporal and spatial sequence by a wave front spreading from an initial point source throughout the focal region of the large shock.

As summation progresses, the size of the simulated source increases as evidenced by the definite shift of the spectral content towards the longer periods. This is because the lower frequency components add up according to the first power of the number of input records while the short period elements accumulate at random and construct according to the square root of the input records.

The hypothesis is applied to two data sets : the far-field Chile source where the receiver is an array of stations and to the near-field Rabaul source where the receiver is a single station within a network.

In processing the data a new analogue instrument is used to recover the long period contents inherent in short period recordings. These modified records are then used in the summation procedure.

In the analysis stage a numerically stable smoothing technique is used to assess the seismic spectra of the input records and results.

It is shown in this thesis that the hypothesis is effective in the far-field observations where the seismic spectrum is approximated by a point double couple source. In the near-field source, however, the

results generally show that the approach is applicable but that effects due to the proximity of a fault have a greater influence on the construction of longer periods in addition to record quantity.

ACKNOWLEDGMENTS

My sincere thanks and appreciation are due to Dr. P.L. Willmore, Head of the Global Seismology Unit, IGS for his continuous encouragement, support and guidance throughout this research and for making available full use of the facilities and equipment of his unit.

This project was made possible through the co-operation of GSU-IGS and the Geophysics Department, Edinburgh University, from which I wish to thank Professor K.M. Creer, Head of Geophysics, for his joint supervision and support and the Postgraduate Studies Committee at Edinburgh for granting me a studentship which supported me financially for 3 years.

From the Global Seismology staff I would like to thank Drs. S. Crampin and C.W.A. Browitt for their constant assistance and fruitful discussions. Special thanks and gratitude are due to Dr. P.W. Burton for his guidance and for allowing me to use his analysis program. The help and assistance of D.C. Booth was invaluable in the initial stages of this project. My sincere thanks and appreciation to him.

I am deeply indebted to the electronics engineers: D.J. Houlston, J. Laughlin, and G. Waugh for their relentless help and patience in explaining the intricacies of system hardware and for making it possible for me to use with success their new developments and instrumentation.

I am grateful to G. Neilson for his continuous provision of information and expertise. To him I owe a great deal for patiently teaching me the ABC of seismology and in guiding me through reading the seismogram.

In computing I greatly benefited from the assistance of C.J. Fyfe. His wide computing experience and his vast multitude of programs were

indispensable to my research. My thanks and appreciation to him.

I thank R.B. Jones for his assistance with the Rabaul data set and for permitting me to use some of his unpublished information. I am grateful to Mrs. G. Hall, the Unit secretary, for being above all a great friend and for miscellaneous typing.

During the nearly four years I spent at Global Seismology, I benefited much from the discussions and help of Drs. Assumpcao and Makropoulos who were research students at the time. To them and to my dear friend Miss K. Damer, I express my thanks and appreciation. I thank J. Singh for his help in travel-time calculations and for general discussions.

Miss E. Scott took up the task of typing this thesis. Her patience, style, speed and perfection made scribbles of manuscript turn into a typed masterpiece. My special thanks and appreciation to her for her valuable time and great effort. I thank Miss M. Kennedy for drawing most of the diagrams to textbook standard.

Finally I would like to thank the Iraqi Government for courteously allowing me to pursue my postgraduate research in the UK.

CONTENTS

	<u>PAGE NO.</u>
CHAPTER 1 <u>INTRODUCTION:</u>	
1.0.0 SEISMIC ZONING	1
2.0.0 CURRENT ZONING PROCEDURES	2
2.1.0 Macrozoning	2
2.2.0 Microzoning	5
2.3.0 Disadvantage of Conventional Zoning	6
2.4.0 The IGS Contribution to Seismic Hazard Assessment	7
3.0.0 THE SIMULATION CONTRIBUTION TO HAZARD ASSESSMENT	8
3.1.0 Objectives and Advantages	8
3.2.0 Difficulties Foreseen	9
3.3.0 Possibilities for Further Work	12
4.0.0 BRIEF BACKGROUND	13
5.0.0 AN OUTLINE OF THE WORK IN THIS THESIS	15

1.0.0	INTRODUCTION	19
2.0.0	THE ANALOGUE PROCESSING SYSTEM	19
2.1.0	The EMI SELAB 5000B Replay Unit	20
2.2.0	Programming Board	21
2.3.0	Analogue Filters	21
2.4.0	Ink-Jet Recorder	22
2.5.0	The Audio Monitor	23
2.6.0	The Bass-Lift Unit	23
2.6.1	Amplitude and Phase Response	24
2.6.2	Transient Response	27
3.0.0	THE DIGITAL PROCESSING SYSTEM	28
3.1.0	The PDP 11/50 Computer	28
3.1.1	Central Processor Unit (CPU)	29
3.1.2	Memory	29
3.2.0	Interfacing	30
3.2.1	General Device Interface (DR11-C)	30
3.2.2	Analogue-to-Digital Subsystem (AD01-D)	31
3.2.3	Digital-to-Analogue Subsystem (DA11-D)	31
3.3.0	Peripherals	31
3.3.1	Storage Media	31
3.3.2	Input/Output and Display Media	32
3.4.0	RT-11 System	33
4.0.0	DATA PROCESSING PROCEDURE	34
4.1.0	General Considerations	35
4.2.0	Event Selection	36
4.3.0	Filtering and Bass-Lifting	36
4.4.0	Digitization	37
4.5.0	Examples of Processed Seismograms	38

1.0.0	INTRODUCTION	41
2.0.0	FUNDAMENTAL CONCEPTS	41
2.1.0	The Earthquake Process	41
2.2.0	Point Source Theory	43
2.3.0	Dislocation Theory and Source Parameters	43
2.4.0	Seismic Spectrum and Corner Frequency	46
2.5.0	Earthquake Size	47
2.6.0	Far- and Near-Field Observations	48
3.0.0	METHODOLOGY	48
3.1.0	The Approach	49
3.2.0	The Summation Method	50
3.3.0	Assessing the Simulation Process	51
4.0.0	EXPERIMENTAL PROCEDURE	53
4.1.0	Preliminary Steps	53
4.2.0	Beamforming	55
4.3.0	"BEAM" and Input Parameters	57
4.4.0	Testing "BEAM"	57
4.5.0	Application to Real Data and Discussion	58
4.5.1	Single-Event-Multistation Case	58
4.5.2	Single-Station-Multievent Case	60
5.0.0	INCOMPLETENESS OF EARTHQUAKE SAMPLES	62

CHAPTER 4

ANALYSIS TECHNIQUES:

1.0.0	INTRODUCTION	63
2.0.0	SPECTRAL ANALYSIS	63
2.1.0	The Seismic Signal	63
2.2.0	The Spectrum	64
2.3.0	Fourier Analysis	65
2.4.0	Limits of Spectra and Contamination	67
2.5.0	Discretization and the Fast Fourier Transform	67
3.0.0	PRACTICAL CONSIDERATIONS	69
3.1.0	Differences Between Theoretical and Observed Spectra	69
3.2.0	Choice of Spectral Scales	70
3.3.0	P- vs S- Corner Frequency	71
3.4.0	Source, Earth, and Receiver Functions	73
4.0.0	ANALYSIS SOFTWARE	74
4.1.0	Transient Signal Analysis Program (TSAP)	74
4.1.1	Program Procedure	75
4.1.2	Examples Illustrating Spectral Analysis using TSAP	77
4.2.0	Spectral Smoothing and "CUFIT"	79
4.3.0	Aliasing	81
4.4.0	Influence of Frequencies Below Bass-Lift Cutoff	82
4.5.0	Pre-Signal Noise and the Final Picture	84
4.6.0	Discussion	84

CHAPTER 5

CHILE DATA: DESCRIPTION AND OBSERVATION:

1.0.0	INTRODUCTION	86
2.0.0	THE ARRAY	87
2.1.0	SAAS Location and Layout	87
2.2.0	Topography and Surface Geology Occupied by SAAS	87
2.3.0	SAAS Instrumentation	89
2.3.1	Detection Equipment	89
2.3.2	Recording Equipment	89
2.3.3	Instrumental Response	89
2.4.0	SAAS Capability	90
2.4.1	Effect of Structure Under SAAS	91
2.4.2	Seismic Path Properties	92
3.0.0	GENERAL SEISMOTECTONICS OF SOUTH AMERICA	93
3.1.0	Geological Setting of Northern Chile	93
3.2.0	Seismicity and Spatial Distribution of Earthquakes Around the Source	95
3.3.0	Mechanism of Earthquakes Near the Source	96
4.0.0	THE DATA	97
4.1.0	The Main Shock	99
4.2.0	The Aftershock Sequence	99
4.3.0	Three Additional Events	99
4.4.0	Discussion	102

SEISMOGRAM ANALYSIS:

1.0.0	INTRODUCTION	105
2.0.0	SOURCE PARAMETERS	105
2.1.0	Event Relocation	105
2.1.1	"SPEEDY"	105
2.1.2	Results	108
2.2.0	Observation of P-Wave Residuals	110
2.3.0	Estimation of Body-Wave Magnitude " m_b "	113
2.4.0	Surface-Wave Magnitude-Energy Estimation	116
2.5.0	Source Dimensions of the Large Shock	117
2.6.0	Focal Mechanisms	118
2.7.0	Discussion	120
3.0.0	SEISMOGRAM ANALYSIS	122
3.1.0	The 20° -Discontinuity and Phase Identification	122
3.1.1	Observation of P-Phases	123
3.1.2	Observation of S- and Surface Phases	124
3.2.0	Estimation of Apparent Velocity and Azimuth	125
3.3.0	The Summation Scheme	128
3.3.1	Rupture Velocity at the Far-Field	129
3.3.2	Transposition of Array to Source	132
3.3.3	Direction and Sequence of Trigger	134
4.0.0	RESULTS AND DISCUSSION	136
4.1.0	Comparison of ALL, EW, and NS Individual Event Sums	136
4.2.0	Attempting to Construct a Larger Source	139

CHAPTER 6

CHILE DATA: SOURCE PARAMETERS AND

SEISMOGRAM ANALYSIS:

(continued)

5.0.0	GENERAL CONCLUSIONS	142
6.0.0	DISCUSSION	144

OBSERVATIONS

1.0.0	INTRODUCTION	146
2.0.0	GENERAL SEISMOTECTONICS	147
2.1.0	Geology and Surface Structure of New Britain and New Ireland	147
2.1.1	New Britain Arc	148
2.1.2	Admiralty Arc	148
2.2.0	Seismicity and Focal Mechanism of the Source Region	149
3.0.0	THE NETWORK AND DATA	151
3.1.0	The Rabaul Seismic Network	151
3.2.0	The Data	152
4.0.0	SOURCE PARAMETERS	154
4.1.0	Event Location	154
4.2.0	Magnitude Estimation	155
5.0.0	SEISMOGRAM ANALYSIS	161
5.1.0	Phase Identification	161
5.2.0	Estimation of Apparent Velocity and Azimuth	162
5.3.0	The Summation Scheme	164
5.3.1	Event Grouping and Triggering Sequence	164
5.3.2	Rupture Velocity at the Near-Field	167
6.0.0	RESULTS AND DISCUSSION	169
6.1.0	Individual Group Sums	169
6.2.0	Comparison of the Summed Spectra	172
6.3.0	Comparison of the Spectra with RDD72 and RDM73	172

CHAPTER 7

RABUL DATA: AN EXAMPLE ON NEAR-FIELD

OBSERVATIONS:

(continued)

7.0.0	GENERAL CONCLUSIONS	175
8.0.0	DISCUSSION	176

CHAPTER 8

CONCLUSIONS

1.0.0	GENERAL	178
2.0.0	SPECIFIC CONCLUSIONS	178
3.0.0	THE CONTRIBUTION OF THIS RESEARCH IN RELATION TO THE ORIGINAL PROPOSAL	181

LIST OF ILLUSTRATIONS

FOLLOWING PAGE OR
FIGURE NO.

CHAPTER 2

2.1	Typical SELAB 5000B Replay Unit	20
2.2	Preamplification and Demodulation Stages	2.1
2.3	Programming Board Functions	21
2.4	Filter Response Characteristics	2.3
2.5	Amplitude Response of Bass-Lift	25
2.5a	Overall Amplitude Response (10s Filter)	2.5
2.6	Phase Response of Bass-Lift	26
2.6a	Overall Phase Response (10s Filter)	2.6
2.7	Transient Response to 10s Filter	27
2.8	Transient Response to 5 and 20s Filters	2.7
2.9	PDP 11/50 Computer System	29
2.10	Rabaul Data: Major and Minor events at ETV	38
2.11	Chile Data: Event CB001 at SAAS: S4 and S5	39
2.12	Chile Data: Event CB022 at SAAS: S2 and S5	2.11
2.13	Chile Data: Event CB014 at SAAS: S4 and S5	2.12
2.14	Chile Data: Event CB014 at SAAS: S5	2.13

CHAPTER 3

3.1	Schematic Representation of Seismic Spectra	46
3.2	Examples of Collated Files	54
3.3	Sine Wave Output from "BEAM"	58
3.4	Single Event at 10 Array Stations ready for "BEAM"	59
3.5	Single Event Sum at Different Azimuths showing P-phases	3.4
3.6	Single Event Sum at Different Velocities showing P, S, and LQ	3.5
3.7	Single Event Sum showing S- and LQ-phases	3.6
3.8	Single Event Sum showing Amplitude Build-up	3.7
3.9	Multiple Event Sum at Different Velocities showing P, S, and LQ	61
3.10	Multiple Event Sum showing S- and LQ-phases	3.9
3.11	Multiple Event Sum showing Amplitude Build-up	3.10

CHAPTER 4

4.1	Schematic Representation of the Spectrum	65
4.2	Rabaul Data Illustrating Linear Spectra	78
4.3	Chile Data Illustrating Linear Spectra	4.2
4.4	Rabaul Data Illustrating Log Spectra	4.3
4.5	Chile Data Illustrating Log Spectra	4.4
4.6	Rabaul Data: RDD72 Illustrating Spectral Difference between Z/SP and Z/BL	4.5
4.7	Rabaul Data: R0068 Illustrating Spectral Difference between Z/SP and Z/BL	4.6
4.8	Chile Data: CB001 Illustrating Spectral Difference between Z/SP and Z/BL	4.7
4.9	Chile Data: CB011 Illustrating Spectral Difference between Z/SP and Z/BL	4.8
4.10	Chile Data: CB001 Comparison between Original and Smoothed Spectra	81
4.11	Rabaul Data: RDD72 Comparison between Original and Smoothed Spectra	4.10
4.12	Chile Data: CB011 Showing the Effect of Spectral Contamination	82
4.13	Chile Data: CB022 Illustrating Z/SP and Influence of Frequencies below Z/BL on the Spectrum	4.12
4.14	Chile Data: CB022 Difference between Smoothed Spectra	83
4.15	Chile Data: CB022 Difference between Smoothed Z/SP and Z/BL Spectra	4.14

CHAPTER 4 (continued)

4.16	Chile Data: CB014 Spectral Difference between Signal and Pre-signal Noise at 6 Array Stations	4.15
4.17	Chile Data: CB022 Smoothed Spectra at 10 Array Stations	4.16
4.18	Chile Data: All Event Spectra at a Single Station	4.17

CHAPTER 5

5.1	Area of Study	86
5.2	The South American Array System	87
5.3	Willmore MKII Seismometer	90
5.4	Tectonic Model of Central South America	92
5.5	Late Distribution of Cenozoic Volcanism in Northern Chile	95
5.6	Inferred Geometry of Descending Nazca Plate under Northern Chile	95
5.7	Seismicity of the Source Region	98
5.8	ISC Locations of Earthquakes Studied	99

CHAPTER 6

6.1	Relocation of the Chile Earthquakes	109
6.1a	P-Wave Residuals	112
6.2	Focal Mechanisms of the Chile Earthquakes	118
6.3a	CB018	123
6.3b	CB013	6.3a
6.3c	CB011	6.3b
6.3d	CB014	6.3c
6.3e	P, PP, PPP Phases	6.3d
6.3f and g	P_1 - P_2 Phases	6.3e
6.4a	CB001	124
6.4b	CB022	6.4a
6.4c	CB00A	6.4b
6.4d	CB00B	6.4c
6.4e	CB00C	6.4d
6.5	CB014	126
6.6	Sum of CB014	6.5
6.7	CB022	6.6
6.8	Sum of CB022	6.7
6.9	Principle of Transposition of Array to Source	133
6.10	Cross Section Along Fault Strike Showing Position of Hypocenters and Direction of Trigger	6.9
6.11	Transposition of SAAS to Source Region	134
6.12	CB014: Sum of Short and Long Period Ranges	135
6.13	CB022: Sum at Short and Long Period Ranges	6.12
6.14	All Events at SAAS: E4	136

CHAPTER 6 (continued)

6.15	Spectra of All Events at SAAS: E4	6.14
6.16a	AF/N-S : 4km/s	6.15
6.16b	AF/N-S : 10km/s	6.16a
6.17b	OF/NW-SE : 4km/s	6.16b
6.17b	OF/NW-SE : 10km/s	6.17a
6.18a	OF/NE-SW : 4km/s	6.17b
6.18b	OF/NE-SW : 10km/s	6.18a
6.19	Spectra of Sums at 4km/s	137
6.20	Spectra of Sums at 10km/s	6.19
6.21a	Spectral Comparison of Approximate Fits	6.20
6.21b	Seismograms of Approximate Fits	6.21a
6.22	Example of Ringing Effect in Final Sum	139
6.23	Eliminating Ringing Effect	140
6.24	Case (1)	6.23
6.25	Case (2)	6.24
6.26	Spectra of Cases (1) and (2)	6.25
6.27	Case (7)	6.26
6.28	Case (8)	6.27
6.29	Spectra of Cases (7) and (8)	6.28
6.30	Case (3)	6.29
6.31	Case (6)	6.30
6.32	Spectra of Cases (3) and (6)	6.31
6.33	Case (4)	6.32
6.34	Case (5)	6.33
6.35	Spectra of Cases (4) and (5)	6.34

CHAPTER 7

7.1	Area of Study	146
7.2	Geology of New Britain and New Ireland	147
7.3	Surface Faulting and Bathymetry of New Britain and New Ireland	148
7.4	Inferred Plate Motions Near the Source Region	149
7.5	Location of Rabaul Network 1970-1973	152
7.6	Location Map of the Rabaul Data Showing Grouping	157
7.6a	Rabaul Data: M_L from ETV	159
7.6b	Rabaul Data: M_L from ESM and EVZ	161
7.7	Rabaul Data: Record Sections	162
7.7a	Record Section of Group (1)	163
7.7b	Record Section of Group (2)	7.7a
7.7c	Record Section of Group (3)	7.7b
7.7d	Record Section of Group (4)	7.7c
7.8	Grouping of Events	165
7.9a	Group (1)	169
7.9b	Group (1) : S-Wave	7.9a
7.9c	Sum of Group (1)	7.9b
7.9d	Sum of Group (1) : S-Waves with $M = 0.37$	7.9c
7.10a	Group (2)	7.9d
7.10b	Group (2) : S-Waves	7.10a
7.10c	Sum of Group (2)	7.10b
7.10d	Sum of Group (2) : S-Wave with $M = 0.49$	7.10c
7.11a	Group (3)	7.10d
7.11b	Group (3) : S-Waves	7.11a
7.11c	Sum of Group (3)	7.11b

CHAPTER 7 (continued)

7.11d	Sum of Group (3) : S-Waves with $M = 0.72$	7.11c
7.12a	Group (4)	7.11d
7.12b	Group (4) : S-Waves	7.12a
7.12c	Sum of Group (4)	7.12b
7.12d	Sum of Group (4) : S-Waves with $M = 0.80$	7.12c
7.13	Spectra of Each Group with their Sums	170
7.14	Spectra of Each Group in Each Direction	7.13
7.15a	Group Sums : NW-SE	174
7.15b	Group Sums : S-Waves with $M = 0.7$	7.15a
7.16a	Group Sums : SE-NW	7.15b
7.16b	Group Sums : S-Waves with $M = 0.7$	7.16a
7.17a	Group Sums : DOWNWARD	7.16b
7.17b	Group Sums : S-Waves with $M = 0.7$	7.17a
7.18a	Group Sums : UPWARD	7.17b
7.18b	Group Sums : S-Waves with $M = 0.7$	7.18a
7.19a	Final Sums : Four Directions	7.18b
7.19b	Final Sums : S-Waves with $M = 0.7$	7.19a
7.20	Spectra of Final Sums	7.19b

LIST OF TABLES

	<u>PAGE NO</u>
CHAPTER 5	
5.1 SAAS Station Coordinates and Altitudes	88
5.2 Kinematic Parameters of Earthquakes Studies	100
5.3 The Selected Earthquakes	104
CHAPTER 6	
6.1 Re-evaluation of Kinematic Parameters	109
6.2 P-Residuals at SAAS: E4 and S5	111
6.3 Body Wave Magnitudes and Residuals at SAAS	115
6.4 Surface Wave Magnitudes and Energies	115
6.5 Focal Mechanism Parameters	119
CHAPTER 7	
7.1 Rabaul Station Coordinates and Altitudes	153
7.2 Kinematic Parameters and Local Magnitudes	156/157
7.3 Rupture Velocities	169
REFERENCES	185
ADDITIONAL REFERENCES	203
APPENDICES (A) : LISTING OF "BEAM"	
(B) : LISTING OF "CUFIT"	
(C) : FOCAL MECHANISMS OF THE CHILE EARTHQUAKES	

CHAPTER 1
INTRODUCTION

1.0.0 SEISMIC ZONING:

One approach in evaluating the damage to life and property in the aftermath of a catastrophic earthquake would be to establish technically consistent and economically viable criteria for earthquake-resistant design. For this purpose and for regional and local urban planning in developing as well as industrialized countries, seismic zoning and micro-zoning are essential tools towards the formulation of uniform criteria. While seismic zoning takes into account the distribution of earthquake hazard over the entire country or region, seismic microzoning defines the detailed distribution of earthquake risk within each seismic zone.

In principle, therefore, the main product of seismic zoning is to compile a zoning map displaying a parameter or group of parameters related to the expected frequency or intensity of shaking (in the case of macrozoning) or to the influence of local soil conditions on structural foundations (in the case of microzoning) that may be caused by future large earthquakes.

According to Karnik and Algermissen (1978) the meaning of seismic zoning has undergone some changes. While some zoning maps summarize the observations on past earthquake effects making the assumption that the same pattern of seismic activity will be valid for the future; other maps extrapolate from regions of past earthquakes to potential source regions. Both of these categories of maps are compiled based on the needs and according to the geological and geophysical information available for each region.

Most of the currently used zoning maps subdivide a particular territory into a number of zones classified either in terms of intensity degrees or simply as zones which are related to seismic parameters tabulated in official building codes. Such compilations grossly oversimplify the earth conditions surrounding the region under question. A further disadvantage of these maps is that no consideration is given to quantities directly related to earthquake-resistant design such as: peak acceleration or velocity, period of shaking, spectral density, and their probability of occurrence. As a direct consequence zoning errors can occur, and indeed have occurred.

An ideal zoning study would, therefore, be to provide for each site, the "design spectra" which would be generated by expected earthquakes of a given magnitude and to determine the probability of their occurrence.

2.0.0 CURRENT ZONING PROCEDURES:

2.1.0 Macrozoning:

The present state of the art in zoning procedures may be classified into 4 categories:

- (a) Maximum intensity.
- (b) Engineering zoning.
- (c) Maximum ground motion for different return periods.
- (d) Seismic risk.

The first type of procedure leads to constructing zoning maps

of either maximum observed intensity or maximum expected intensity. Zoning maps based on expected intensities require information about the source region, statistics on past seismicity and empirical attenuation functions of hypocentral depth and distance. The resulting map displays either isolines of different intensities for a given return period or isolines of return periods for a given intensity.

In some engineering zoning maps, seismic zones are classified according to a single or group of seismic parameters related to a building code. This code then specifies the variation of a particular parameter according to the ground conditions and type of structure. Other maps simply separate zones of destructive, moderate, weak effects without any quantitative indication.

A more frequently used zoning map in engineering design is one based on maximum acceleration or particle velocity. As with the intensity zoning maps, these are constructed using either deterministic or probabilistic assumptions. The principal disadvantage of deterministic acceleration or velocity maps is that no information is given regarding the frequency of occurrence of severe ground motion. This has been shown to be a serious set back (Algermissen, et al, 1972).

Cornell (1968) gives a detailed method for the evaluation of ground motion parameters. His technique incorporates geological information when modelling the earthquake source. This is approximated by simple geometrical shapes like circles, annuli and sectors thereof. The basic assumptions behind Cornell's method are:

- (a) earthquakes originating from a source area or line are equally likely anywhere in the area or along the line.
- (b) the average rate of occurrence of earthquakes in a source area is constant in time.
- (c) A Poisson distribution of recurrences is assumed.
- (d) An unlimited exponential distribution of earthquake magnitudes is assumed.

Kallberg (1969) applied Cornell's method in Southern California and Merz and Cornell (1974) have considered the contribution of aftershocks to the ground motion.

A slightly different approach was used by Milne and Davenport (1965, 1969) through the use of historical records of earthquakes as "sources", applied an attenuation law and obtained cumulative frequency distributions at a series of points on an arbitrary grid. No geological information was used in defining the "sources" of earthquakes.

Algermissen and Perkins (1972) apply a similar technique to Cornell's except that certain integrations have been replaced by discrete summations for flexibility in representing attenuation functions and source areas.

Bayesian statistics has been recently used in the estimation of ground motion parameters and the approach appears to show some promise (Esteva and Villaverde, 1974).

The concept of earthquake risk according to Vere-Jones (1973) involves seismic, engineering as well as insurance risk. Risk

maps contain information on the extent and probability of life or material losses. A considerable amount of work has been done on seismic risk analysis so far. The method and its use in different parts of the world is discussed by Burton (1979).

2.2.0 Microzoning:

Seismic microzoning, as defined by USSR investigators, consists of evaluating the increment of the design seismic intensity due to site conditions, considering the type of soils in the surface layers and investigating the depth of the water table. The design seismic intensity - with a correction for the appropriate structure - is obtained by adding an increment to the basic level of seismicity. Design seismic coefficients are then selected for the corresponding design intensity according to building code requirements.

Past earthquake damage and its relation to soil conditions led Japanese investigators to developing a method for seismic microzoning. A classification of soil conditions into 4 categories (zones) was therefore proposed and the required design seismic coefficients for different types of buildings and corresponding soil categories was incorporated into building codes. As a result the first microzoning map of Yokohama city was compiled by Ohsaki (1972). This was followed by microzoning maps of other major cities such as Wellington in New Zealand (Grant-Taylor, et al, 1974). All these maps subdivide a city into seismic microzones based on soil conditions.

According to Petrovski (1978) the ground motion characteristics at any site could be determined if use could be made of small earthquakes and microtremors to provide a basis for evaluating site effects. One major conclusion Petrovski arrives at is that the study of an assembly of small earthquake records at a particular site complemented by a probabilistic evaluation of expected ground motions in the known and potential seismic zones appears to be most promising and is probably a valid topic for scientific research.

2.3.0 Disadvantages of Conventional Zoning:

The major areas of weakness in conventional zoning are the following:

(i) Intensity is not a function of distance alone.

Distorting factors include the nature of the radiation pattern of seismic waves, variations in attenuation along propagation paths, and local differences between structures and foundation conditions for a given site.

(ii) Microzoning maps which attempt to describe departures from simple zoning are not independent of magnitude, i.e: local corrections derived from observations of small earthquakes do not generate microzoning surveys of large ones.

(iii) Serious seismic hazards (as with nuclear power plants) have to be assessed at very low probability levels, i.e: over considerably long recurrence intervals over

a limited time span can give warning of short-term danger quite effectively, but fail to give much assurance of safety in the long term.

2.4.0 The IGS Contribution to Seismic Hazard Assessment:

From the general outline given in Section 2.0.0 and in view of the particular problems mentioned in Section 2.3.0, the Institute of Geological Sciences - Global Seismology Unit's contribution to hazard assessment is being developed along three parallel lines:

- (a) Statistically: To recognize the combinations of earthquake magnitude and distance which generate the most severe hazards in any given region (Willmore and Burton, 1975) or through seismic risk evaluation using the Statistics of Extremes (Makropoulos, 1979).
- (b) Deterministically: To assess the conditions which can generate a maximum magnitude earthquake in a given region, thereby localizing as much as possible of the observed total seismicity in relation to permanent tectonic features (Lilwall, 1976; Burton, 1978).
- (c) By Simulation (the contribution in this thesis): Through the use of suites of small earthquake records representing the actual earth

motions to be expected in any given region.

3.0.0 THE SIMULATION CONTRIBUTION TO HAZARD ASSESSMENT:

The approach to seismic hazard assessment adopted in this research is directed towards attempting to simulate a large earthquake motion from the simple time domain summation - after introducing the necessary time delays - of a population of smaller earthquakes known to have occurred in the vicinity of the focal region of the large source.

The underlying hypothesis is that the mechanism of the large shock can be simulated by a selected succession of smaller ones, triggered in an appropriate temporal and spatial sequence by a wave front spreading from an initial point focus throughout the earthquake region of the large event.

As the size of the simulated earthquake increases, the spectral content shifts towards longer periods because the lower frequency components of the input records interfere constructively while the short period elements accumulate at random. The resulting simulated seismogram would then contain an enhanced long period content proportional to the first power of the number of input records which represent an approximation to the mechanism and propagation effects produced by a large source.

3.1.0 Objectives and Advantages:

From the preceding discussions two major objectives become

apparent in this research:

- (a) To improve the general understanding of the earthquake process.
- (b) Thereby to improve the basis of seismic zoning.

The advantages of the simulation method over purely theoretical methods of seismogram synthesis are that the stress-drop and fault orientation characteristics of the source region, as well as the transfer function of the ray path (in so far as it is linear with respect to amplitude) are contained in the small earthquake seismograms and are preserved in the summation process. Therefore, they do not have to be introduced as new parameters in the simulation procedure. As a result, one can concentrate on the phasing of the small earthquake records at the receiving station, in the hope and expectation that the phasing pattern which gives the best eventual fit with the large earthquake seismogram will reveal useful information regarding the faulting mechanism of the large source. If such simulations could be repeated at a number of different sites, then variations in the simulated particle motion should reflect the spatial variation in the effects of the large shock in locations for which no seismic record is available.

3.2.0 Difficulties Foreseen:

While we begin to move in the direction of record simulation it would be relevant to consider the following:

(a) Non-linearity at the point of observation:

The effects of large earthquake motion on buildings and foundation materials are often highly non-linear, and this is, undoubtedly, one of the reasons why microzoning maps showing the effects of small earthquakes are poorly correlated with those of large earthquakes.

Non-linearity is, however, largely due to the weakness of surface materials and structures in comparison with bedrock. Our predictions must therefore be limited to effects within the linear range of bedrock materials, leaving it to the earthquake engineer or soil mechanist to advise on structural and near-surface responses.

(b) Non-linearity in the focal region:

It is not clear whether this is a serious problem. Evidently, every element of material which is in the process of failing is in the non-linear range, as in the case of an isolated small earthquake. The material outside the wavefront has the pre-existing ambient stress, again as for the small earthquake. The material inside the wavefront, on the other hand, has been, at least partially, de-stressed and most of it is probably more linear than before. Only in the actual surface of fracture, where brecciation and possible melting may have occurred, do we have strong prima facie reason to expect highly anomalous behaviour. Thus, whilst bearing these possibilities in mind, we may expect to have to look rather hard for the evidence of non-linearity in the focal

region with a view of making some specific deductions from it.

- (c) Difference in mechanism between small and large earthquakes:

This could indeed occur, and could be informative if brought up by the study. A priori, we might expect some differences in character between foreshock and aftershock sequences, in that foreshocks might be viewed as localized failure in the weakest parts of the focal region, occurring in response to a stress pattern which is building up to the critical level of extensive propagation.

Aftershocks, however, could be more complex, in that material near the previously fractured zone has been unloaded and might therefore show reverse motion at the sites of previous foreshocks, whereas material beyond the stopping-point of the main fracture would show stress increase in the direction of build-up for the next large earthquake.

- (d) Incompleteness of small earthquake sample:

Real samples of the small earthquake population will probably be far from complete, and we will be requiring methods of "filling-in" the focal region. A useful exercise, therefore would be to take 2 small events and to use the records of these to produce an interpolation, which would simulate a recording of an event on the line joining the 2 primary foci. Given 3 such sources, we could fill the whole triangular area between the 3 primary

foci and could then, by further repetitions of the process, fill the tetrahedral volume bounded by 4 foci.

3.3.0 Possibilities for Further Work:

The simulation of large earthquake motions at one station opens several possibilities for related studies. Some examples are given below:

(a) Relevance to microzoning:

If one were to set up a network of stations, covering a region in which the microzoning study of a large earthquake had been carried out, each station should yield a suite of records of succeeding small shocks from which the record of the large expected earthquake, at that station, could be simulated. Such an experiment should indicate the extent to which the differences between the station records were consistent with the differences to be expected from the results of the microzoning study.

(b) Substitution of earthquakes by explosions:

Ideally, the use of small earthquakes as the input elements in the simulation procedure introduces some similarity in focal mechanism, as well as utilizing the same propagation paths as the main shock. The use of explosions instead of small earthquakes would sacrifice a good deal of this similarity, but enough might be preserved for the experiment to be worthwhile. The most relevant examples would be those in which one had a substantial collection of explosions along a profile, or

covering an area. This might, for example be obtained by "listening in" on a major crustal structure experiment.

(c) Possibilities of path-reversals:

It could happen that potential interest might be attached to a focal region which is not sufficiently seismic to yield an adequate set of small natural earthquakes. A particularly relevant example is that of a naturally quiet area in which a potential inducing source (such as a large dam-site) was to be expected. A path-reversal study would involve covering the possible focal region with a seismometer network, recording a number of small earthquakes from points outside the region, and then using the summation process on records from the network to simulate the appearance of a large earthquake in the network area, as recorded at the site of each of the small earthquakes.

4.0.0 BRIEF BACKGROUND:

The concept that a large earthquake motion may be regarded as being made up of many smaller ones is not new. This idea which later came to be known amongst workers as the "Multiple Shock" hypothesis was originally introduced to explain the complex portion of large earthquake seismograms such as those of the Mongolian earthquake of 1931 (Stonely, 1937); the Boso-oki earthquake of 1953 (Usami, 1956); the Alaskan earthquake of 1964 (Wyss and Brune, 1967); the Imperial Valley earthquake of 1940 (Trifunac and Brune, 1970); and the San Fernando earthquake of 1971 (Kamb, et al, 1971; Jungels and Frazier, 1973).

Haskell (1964) suggested that in order to match observations, earthquakes should be modelled as the sum of several smaller sources, some of which would have to be tensional in order to explain the observed amplitude ratios of short period P- and S- waves. This work as well as most of the above investigations involved theoretical calculations of the radiation pattern of seismic waves generated by kinematic sources in a homogeneous layered half- or full-space. These radiation functions were then used to calculate synthetic seismograms.

The major goal in this thesis is similar to these works but our approach is fundamentally different. The difference lies in the fact that we will be taking actual small earthquake records, sum them in the appropriate sequence and therefrom predict the waveform of the most likely fit to the large earthquake seismogram.

Hartzell's (1978) recent investigation into earthquake after-shocks is the only work known to us in which the author uses actual displacement records (of the 1940 Imperial Valley earthquake) to model the displacement seismogram of the main shock as Green's functions. Hartzell attributes his success to the superior data set, to the previous source studies made by Trifunac and Brune (1970), and to the use of displacement records which accent the long period content and have an averaging effect (Hartzell, personal communication).

The work of Hartzell differs from the work in this thesis by the following respects:

- (1) There is no evidence in the investigation that the author

considers near- and far-field observations and hence the differences in radiation pattern and propagation effects.

- (2) The limitation of Hartzell's work to the time domain, i.e: there is no consideration of seismic spectra, their assessment or spectral comparisons between large and small earthquakes.
- (3) As a consequence there is no mention of source parameters or dimensions and how these could be related to earthquake size.
- (4) The author had not speculated about differences in the fracturing mechanism of the main shock and aftershock sequence which might have been useful in understanding the rupture process of the large earthquake.

We therefore believe, that these points plus other aspects reported in this thesis make our approach in handling this particular problem more comprehensive.

5.0.0 AN OUTLINE OF THE WORK IN THIS THESIS:

This thesis is conveniently divided into 2 parts. The first consists of chapters 2, 3 and 4 which outline, describe and discuss the topics of data processing, experimental procedure and analysis techniques. The second part includes chapters 5, 6 and 7 where we discuss the data sources and present the results obtained through the use of the methods and techniques developed in the first part.

In the system hardware and data processing chapter we discuss

the analogue and digital equipments used in this research followed by a description of how these systems were utilized in processing the earthquake data. The subject is highlighted by giving examples.

In Chapter 3 we present the methodology and discuss experimental procedure. We begin the chapter with a discussion of fundamental concepts relevant to our approach such as source theories and parameters. Next we introduce the approach to earthquake simulation employed in this research, pointing out the assumptions and the source model adopted. This is followed by experimental procedure in which we describe the software in the time domain summation with examples on artificial and real data. The chapter is concluded with a discussion of the problem of incompleteness of the earthquake samples.

Chapter 4 is devoted to analysis techniques. These include the Fourier Transform method and a description of the software used in obtaining the spectra. The concept of corner frequencies is dealt with and the differences between theoretical and real spectra investigated. Next we introduce the cubic spline approximation to smooth the seismic spectra, how it was applied and how it compares with the original spectrum. The chapter is concluded with examples of some important features encountered on the spectra of the analysed earthquakes.

Chapter 5 heralds the beginning of the second part of this thesis in which we describe the far-field Chile data set observed from SAAS. Divided into 3 sections the first

discusses the array, the second gives a general description of South American seismotectonics with emphasis on the source region, while the third is an outline of the earthquakes studied and presented in Chapter 6.

Chapter 6 reports the results obtained for the Chile source. The chapter begins with a re-evaluation of the kinematic and some dynamic source parameters of the earthquakes studied. This is followed by a discussion of phase identification and how the apparent velocities and azimuths used in the simulation process were estimated. The summation scheme, the principle of array transposition to the source and the direction and sequence of trigger is next discussed. In the final section we present and discuss the results arrived at in both time and frequency domains.

In a generally similar manner we present in Chapter 7 our findings regarding the Rabaul data set which represents an example on near-field observations. Disimilar, however, from the far-field source by the fact that no consideration is given to dynamic source parameters due to unavailability of data. The chapter begins with a description of the seismotectonics and geology of the source region. Next we briefly outline the receiving network and the data. The following 2 sections include event relocation local magnitude estimation, phase identification and estimation of velocities and azimuths. Next we discuss the summation scheme and how the local shocks were segregated into groups. The final section consists of the results with discussion.

In the concluding chapter - Chapter 4 - we draw upon general

as well as specific conclusions arrived at during our research. Possibilities for future research based on the work in this thesis is finally discussed.

CHAPTER 2

SYSTEM HARDWARE AND DATA PROCESSING

1.0.0 INTRODUCTION:

Seismic data are recorded either in analogue form or more recently through on-line digital recording systems. The IGS magnetic tape library consists of recordings of the former where seismic data is recorded on multichannel, frequency modulated carrier waveforms on 1- or $\frac{1}{2}$ -inch magnetic tapes.

This chapter is intended to discuss existing IGS processing methods and instrumentation, most of which were utilized in processing the earthquake data used in this research. For a comprehensive account of data processing facilities available at the Global Seismology Unit, IGS, the reader is referred to Houlston (1975) and Houlston et al (1976).

The chapter first describes one of the analogue processing systems, its instrumentation and functions. This is followed by a section discussing the main digital processing system comprising the PDP 11/50 computer, its interfacing modules, peripheries and some of its data handling software. In both of these sections we have included some rigorous technical detail which is useful information and which we believe is relevant and complementary to the third section. The third and final section discusses how these systems were used in processing the earthquake data in preparation for experimentation and subsequent analysis. This is highlighted by giving specific examples.

2.0.0 THE ANALOGUE PROCESSING SYSTEM:

This is the main on-line analogue processing system, situated in the IGS Computer Suite on level 5. In addition to

providing analogue replay facilities, the system is interfaced with the PDP 11/50 computer to provide for analogue-to-digital (digitization) or digital-to-analogue conversion.

In processing our data, the above system was used with the following incorporated units:

- (a) Replay Unit.
- (b) Programming Board.
- (c) Analogue Pass-Band filters.
- (d) Ink-jet Recorder.
- (e) Audio Monitor.
- (f) Bass-lift Unit.

2.1.0 The EMI SELAB 5000B Replay Unit:

The SELAB 5000B unit is fitted with frequency modulation (FM) playback modules providing a 24-track data-replay facility. The TD10MK-3 tape-transport incorporated in the unit is equipped with 2 x 12-track interlaced replay heads. Provision is made for the transport to handle 1-inch (24.5mm) wide magnetic tapes at 8 standard speeds: 120, 60, 30, 15, $7\frac{1}{2}$, $3\frac{3}{4}$, $1\frac{7}{8}$, and $\frac{15}{16}$ in/s. (Fig. 2.1). The FM playback modules are set to low-band operational mode, such that tape speeds of 15, 30, and 60 in/s will select filters with bandwidths of 2.5, 5 and 10 KHz respectively.

The pre-amplification and demodulation stages incorporated in the unit are schematically illustrated in Figure 2.2. The demodulation output sensitivity is set to ± 5 volts for a maximum carrier frequency deviation of 40%. Flutter compensation is achieved by applying the output of the flutter

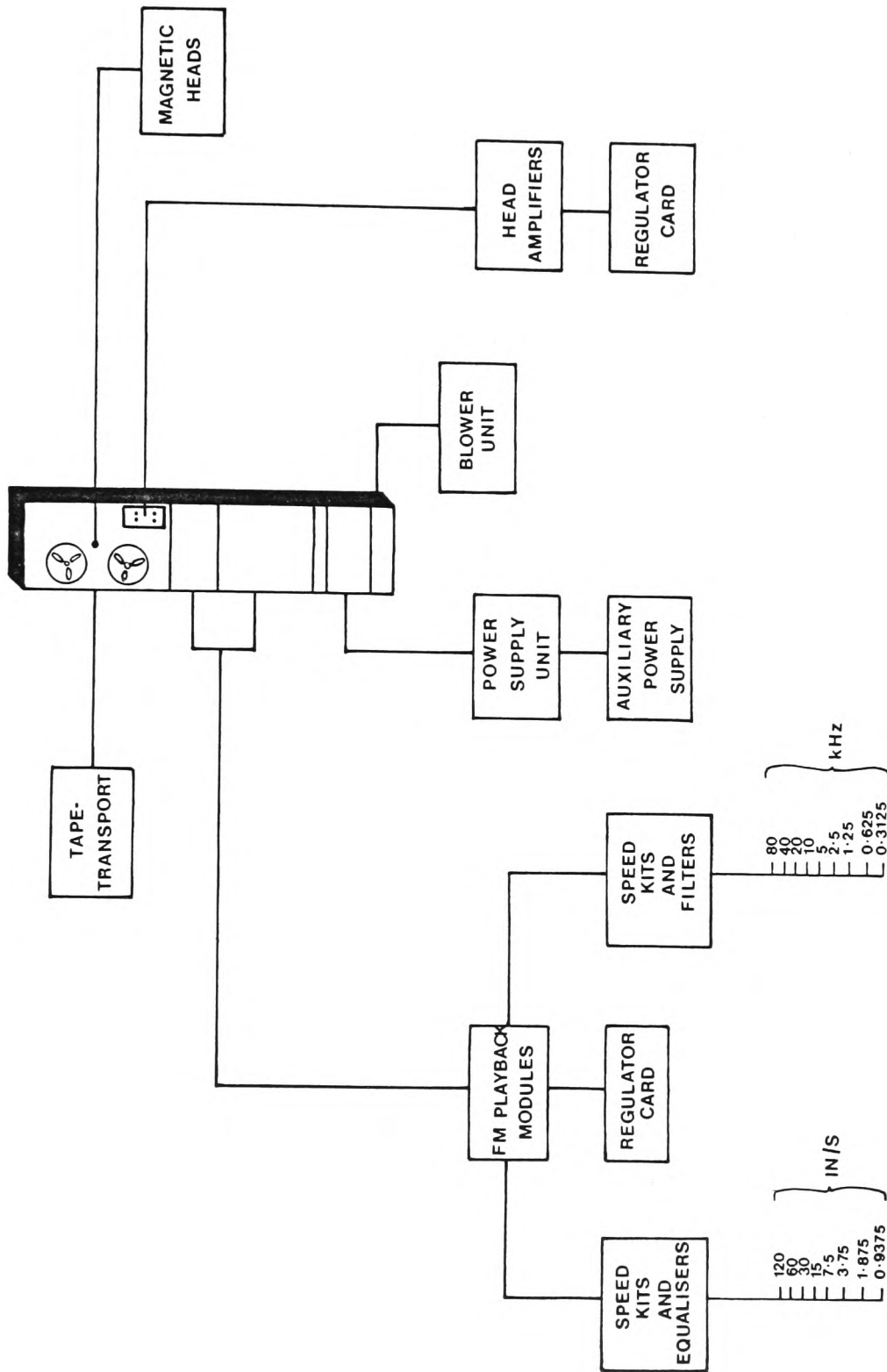
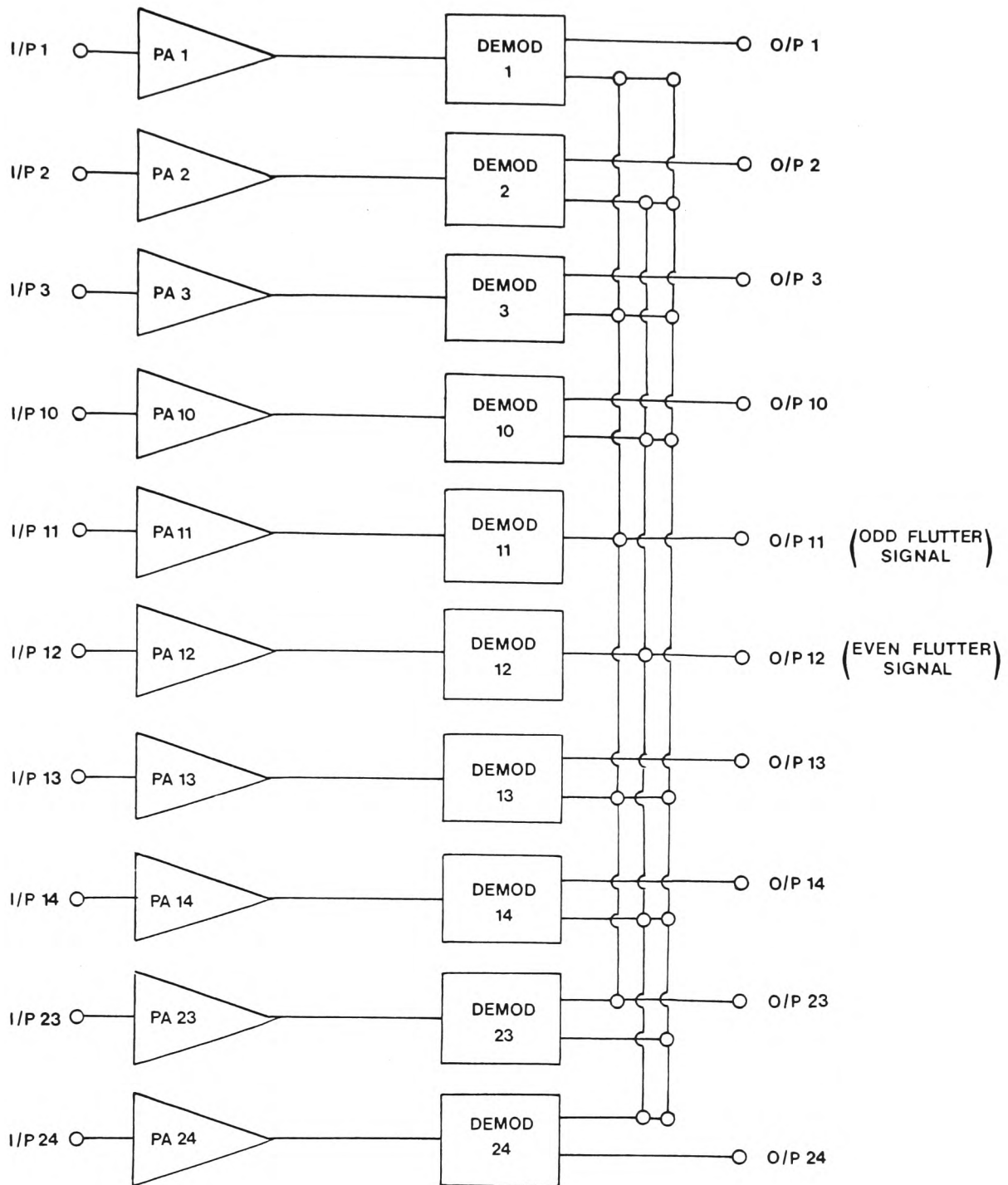


FIG 2-1 TYPICAL SELAB 5000B REPLAY UNIT



I/P = INPUT CHANNEL
 O/P = OUTPUT CHANNEL
 PA = PREAMPLIFICATION
 DEMOM = DEMODULATION

FIG 2-2
PREAMPLIFICATION AND DEMODULATION STAGES

compensation reference track (11 - odd and 12 - even) in anti-phase fashion to the output of all other FM channels. This is equivalent to subtracting the flutter signal from all other channels. By this means, as much as 97% of the flutter can be eliminated from a seismic trace (Houliston, 1975).

The tape speed and tension on the unit are separately servo-controlled, to ensure that tape "flutter", "skew", and "time-displacement" errors are kept to a minimum. Replay could be performed in both forward and reverse directions.

The playback speed, when the data was digitized was set to $7\frac{1}{2}$ in/s (x64 of actual recording speed). This gives an r.m.s. S/N ratio of 48 dB with the -3 dB point at a bandwidth of 1.25 KHz.

2.2.0 Programming Board:

The SELAB unit, as well as all other analogue units, is connected to a programming board. This acts as a "connecting centre" to facilitate the interconnections between various instruments. By suitably inserting "shorting pins", it is possible to connect channel outputs to jet-pen inputs, include or exclude filters, incorporate bass-lift circuitry or not. Some of the various functions of the programming board are shown in Figure 2.3.

2.3.0 Analogue Filters:

The filters incorporated in processing are a set of 16-KEMO type VBF/8, solid state, dual variable, analogue filters with digitally tuned cut-off frequencies. Each dual filter

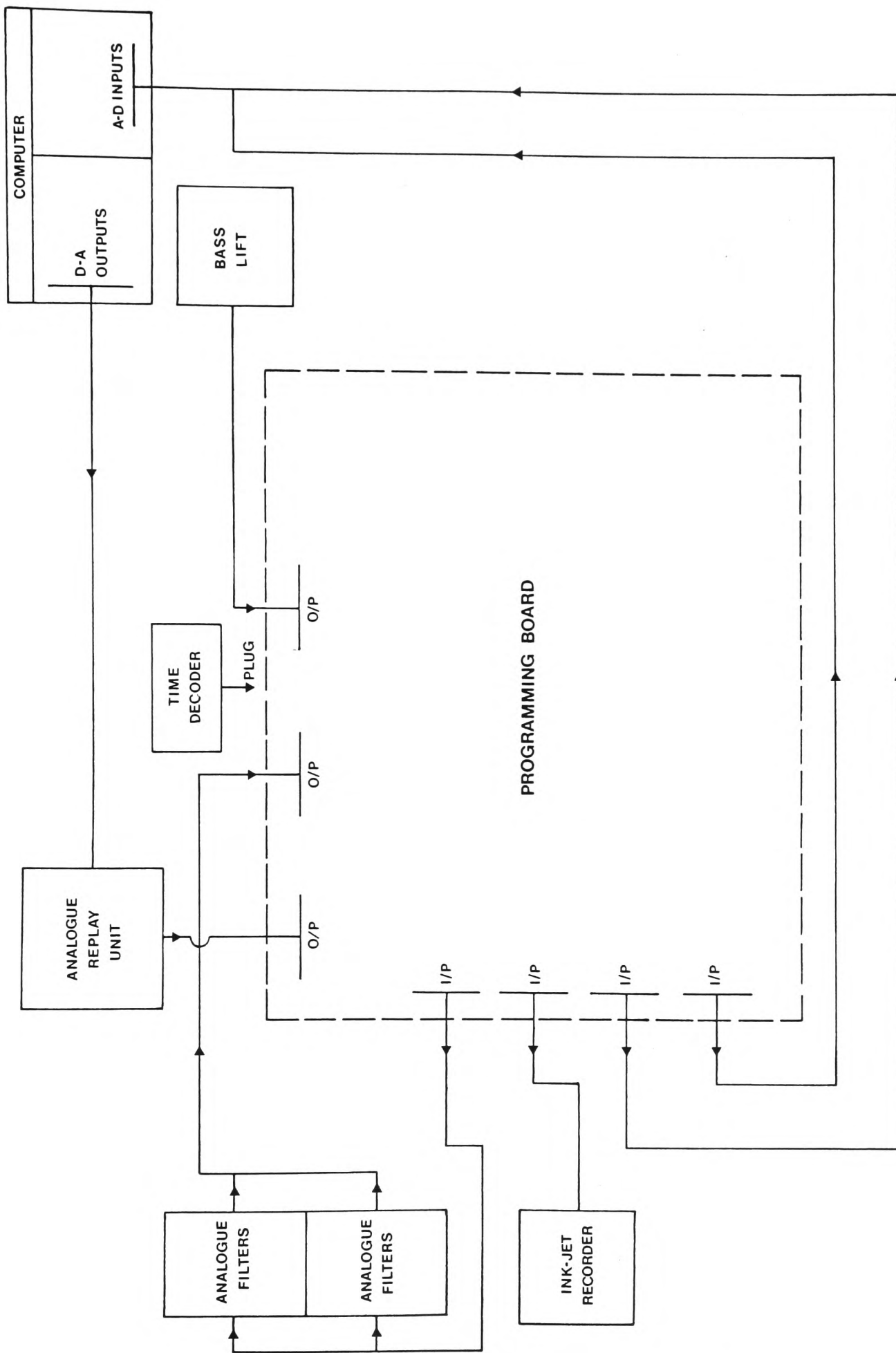


FIG 2-3 PROGRAMMING BOARD FUNCTIONS

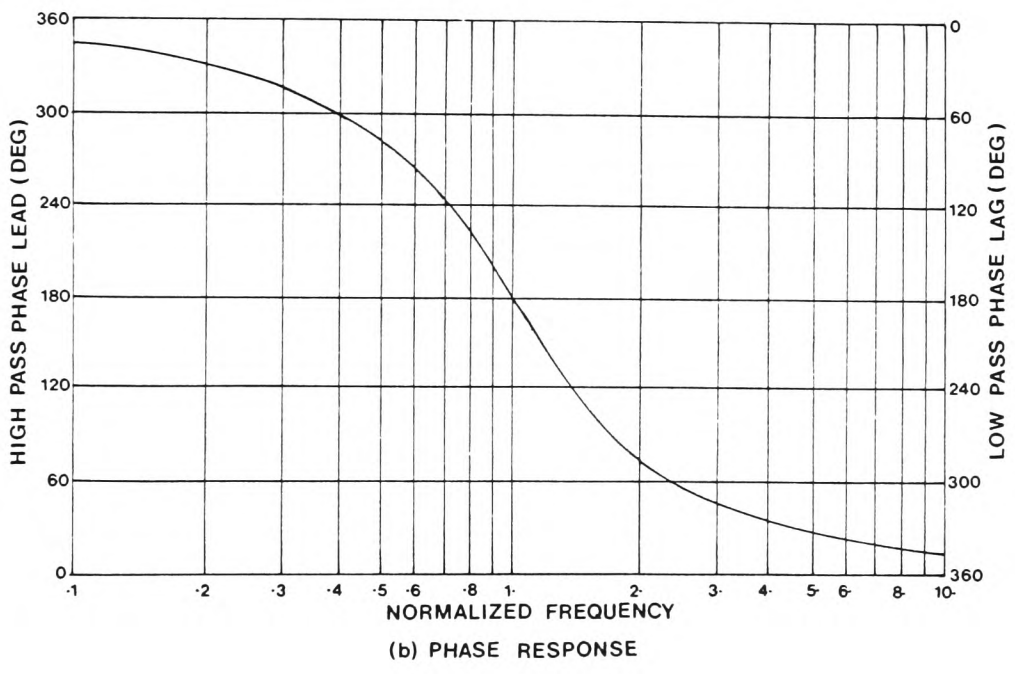
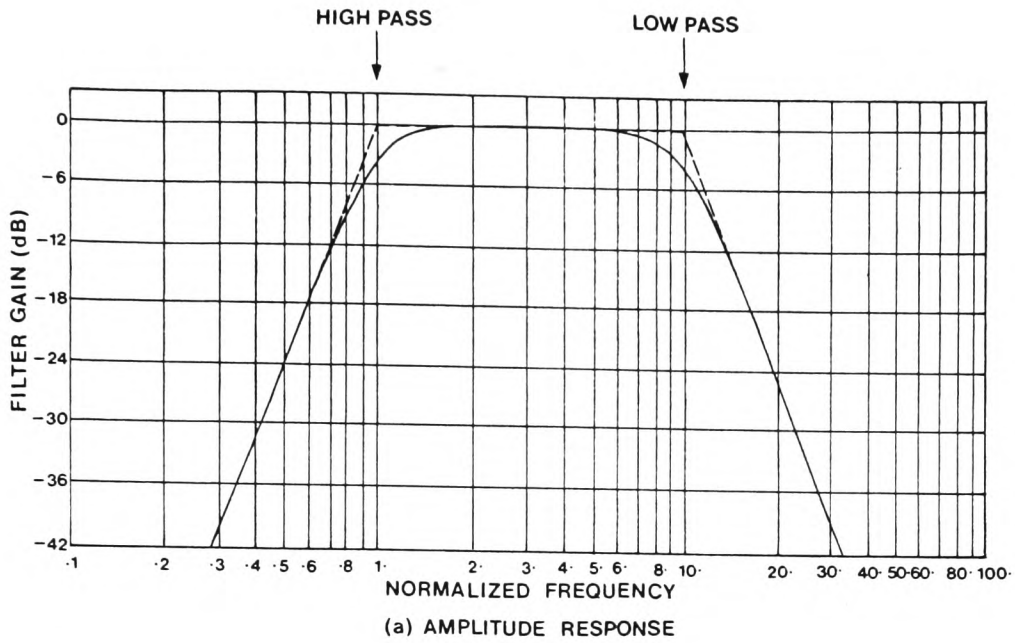


FIG 2-4 FILTER RESPONSE CHARACTERISTICS

consists of 2 separate channels, when connected in "DISCRETE" mode function as a high-pass or a low-pass with an attenuation rate of 48 dB/octave. In "SERIES" mode the filter channels function as a bandpass with cut-off limits from 0.001 Hz - 100 KHz attenuating at 24 dB/octave.

The bandpass is selected through 3 rotary decade switches (tens, units and tenths) plus a 5-decade multiplier (0.1 Hz - 1 KHz) located on the front panel.

The transient frequency response of these filters is a fourth-order Butterworth with maximal flatness for optimum performance in the frequency domain. The normalized amplitude and phase characteristics are shown in Figure 2.4a and b.

2.4.0 Ink-Jet Recorder:

The ink-jet recorder (ELMA-SCHÖNANDER) used to obtain paper records is one of several owned by IGS. The most important components are the following:

(i) Attenuator Unit: This is equipped with 16 input channels and a panel provided with the equivalent number of rotary switches each of which has 8 positions giving output sensitivity of 0.025, 0.1, 0.25, 1.0, 2.5, 10, 25 and 100 v/cm. An extra "time channel" is provided to give 1 Hz spikes for real time markings.

(ii) Ink unit and galvanometers: The high pressure ink fed by the ink passes through a filter in each of the 16 galvos, then through a glass capillary and finally leaves a nozzle as a narrow and steady jet. When the galvo electromagnets are energized, the permanent magnet,

attached to each capillary, rotates, thus rotating the nozzle and the ink-jet is deflected. The maximum deflection is $\pm 40^\circ$ and the frequency response of the galvos is flat out to 1.2 KHz.

(iii) Paper feed unit: This unit consists of an electronic servo-amplifier with a D.C. motor, a tachometer generator and a mechanical gear. Three speeds are provided by the gear: 25, 50 and 100 mm/s with a speed-up of x10 and a speed-reduction of x0.1.

2.5.0 The Audio Monitor:

This is a small unit consisting of a stereo amplifier and headphones. The principle of operation is simple, fast, efficient and effective. By plugging the headphones into the desired input channel on the jet-pen panel, and replaying the tape at selected speeds (usually $3\frac{3}{4}$ of $7\frac{1}{2}$ in/s), it is possible to bring typical short period seismic frequencies (0.3 - 20 Hz) into the human audibility range (30 Hz - 20 KHz). The ear then becomes sensitive to any sudden change in amplitude or frequency, thus indicating a disturbance. With experience, these disturbances could be deciphered as seismic or non-seismic events.

2.6.0 The Bass-Lift Unit:

One of the most effective and essential components employed in the processing of the earthquakes used in this research was the bass-lift instrument. The design and development of this analogue equipment was motivated by the need to recover

long periods (>1.0s) seismic waves from magnetic tapes recorded by short period seismometers such as the Willmore MKII. Achieving this aim had a direct bearing on the research project. Since by recovering long periods it was possible to:

- (a) reveal to the naked eye the longer period contents inherent in the records which would otherwise have passed unrecognized.
- (b) use these bass-lifted traces in experimentation with the objective of constructing a larger earthquake motion from smaller earthquake records.

Furthermore, and a point well worth emphasizing, is the fact that the signal-to-noise ratio at long periods, as recovered by the bass-lift, is better than that obtained if the 60 dB (± 12 bit) digitizer is operated on the original short period recording. This effectively means that we can process signals in the composite system which could not have been handled entirely digitally (see Section 4.5.0).

2.6.1 Amplitude and Phase Response:

The design and circuit diagram of the bass-lift is described by Laughlin and Waugh (1979). This section is therefore intended as a brief outline of the basic function of the instrument.

The bass-lift circuit is designed to extend the velocity response of a Willmore MKII seismometer (or similar short period instruments) down to selected longer periods. This is achieved by employing a high-pass filter placed in series in

than that at which the MKII starts to roll-off, thus causing "over-compensation". As the 12 dB/octave slope is fully attained this diminishes to "perfect-compensation" represented by the flat from 0.3 - 0.1 Hz. The figure also depicts that the overall asymptotes intersect slightly beyond 12.5s. Giving a 3 dB point at about 15s period. This suggests that the 10s bass-lift compensation is probably good out to about 15s.

It is worth noting that if an under-damped response were to be used the "hump" would almost certainly be sharper and more pronounced due to the coupled effect of the short period response at the beginning of the roll-off and the mis-match in frequencies mentioned above.

The phase response of the circuit for 10, 20 and 40s periods is shown in Figure 2.6. It is interesting to point out that these responses do not peak at the 3 dB point neither do their peaks attain 180° . This we believe, is due partly to the extra compensation provided by the active filter as compared with the simple R.C. approximation, and partly to the fact that the bandwidth is too narrow to allow the full asymptotic condition to be attained.

Figure 2.6a is a schematic plot illustrating the overall phase response at the 10s filter with the equivalent bass-lift response and a calculated short period response for a pendulum at 0.6 critical damping (see for example: Richter, 1958; Willmore, 1960; Luh, 1977). The figure indicates that the overall phase delay around 10s is a lag of about $\pi/2$, while at 1.0s it becomes a lead of about $\pi/4$. This disagrees with

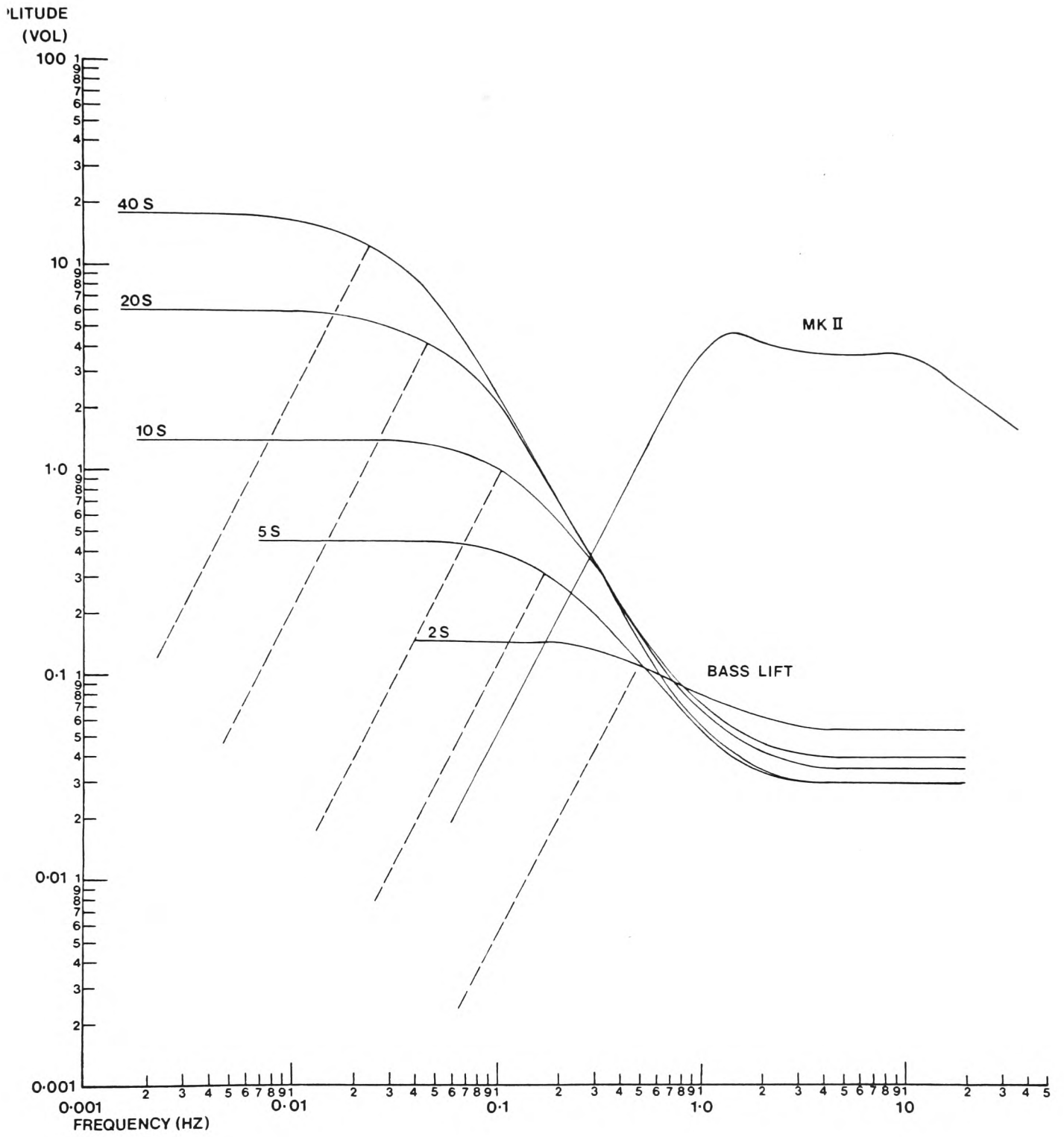


FIG 2.5 AMPLITUDE RESPONSE OF BASS-LIFT

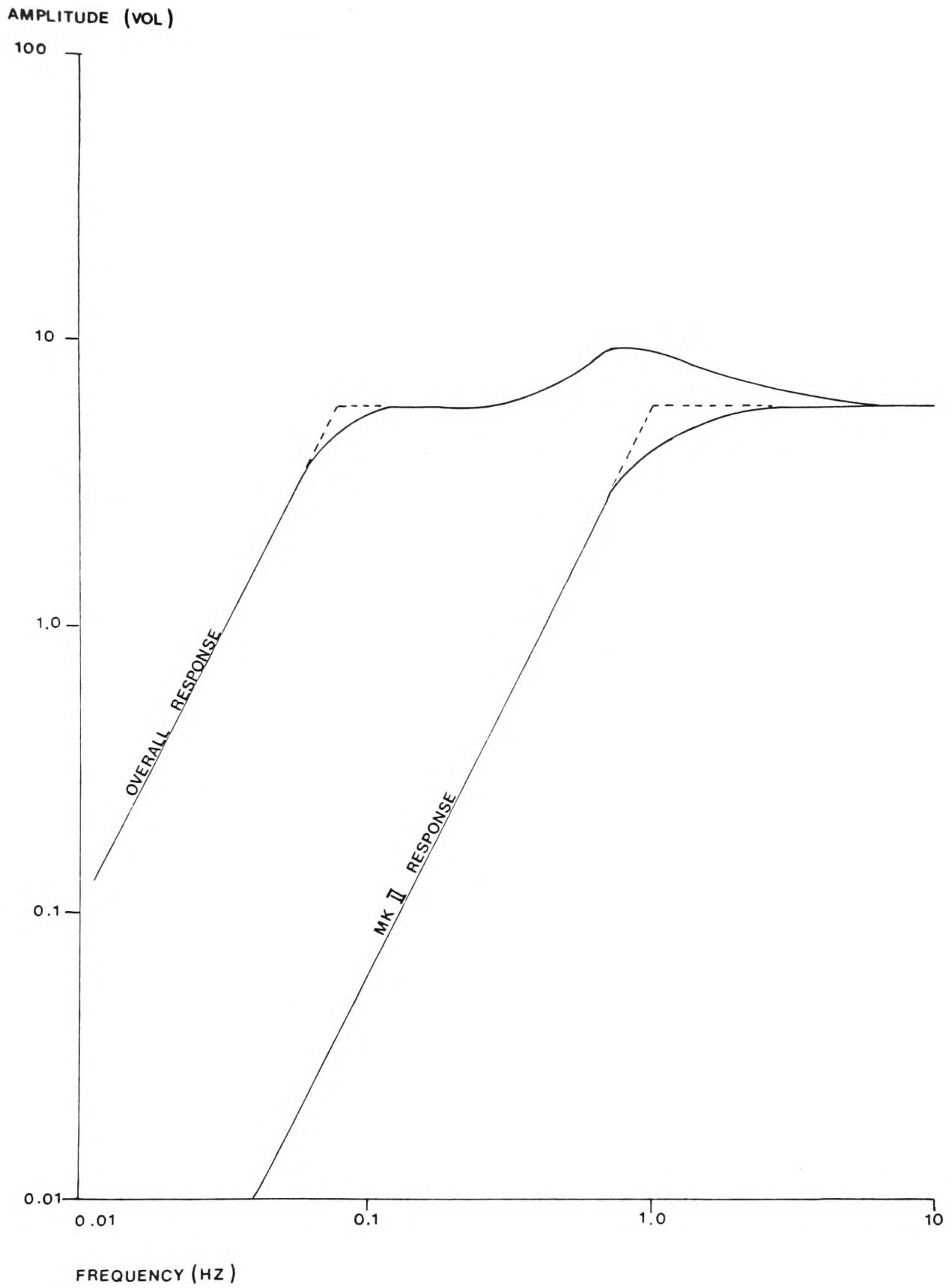


FIG (2.5a) OVERALL AMPLITUDE RESPONSE (10.S FILTER)

the feedback loop of an operational amplifier.

The network consists of two such modules connected in series. Each filter module has an attenuation of 6 dB/octave. The gain of the amplifier thus increases, in this ratio, as the frequency of the input signal decreases. The upper limit of gain in each module is governed by a feedback resistor in parallel with the high-pass filter. This inturn dictates the input period beyond which the circuit ceases to compensate for the seismometer response.

The resistor is switchable to give overall responses of 2, 5, 10, 20 and 40s periods. Beyond the 3 dB of the 40s filter, instrumental noise prevails and becomes troublesome. Provision is made for 3 speed-up factors of x40, x64 and x80 in addition to 4 input/output channels.

The amplitude response of the bass-lift at the different filters is shown in Figure 2.5. For comparison, the figure also depicts an under-damped MKII velocity response at an arbitrary gain. The broken line, parallel to the MKII roll-off, intersects the response curves of the respective filter settings at their 3 dB value. This schematically illustrates how the bass-lift effectively extends the velocity flat to selected longer periods.

Figure 2.5a shows the overall amplitude response at 10s period obtained from the sum of a 10s filter response and that of an MKII at 0.6 critical damping. The "hump" over the frequency range of 5 - 0.3 Hz is believed to be due to the fact that the bass-lift begins to provide compensation at a frequency higher

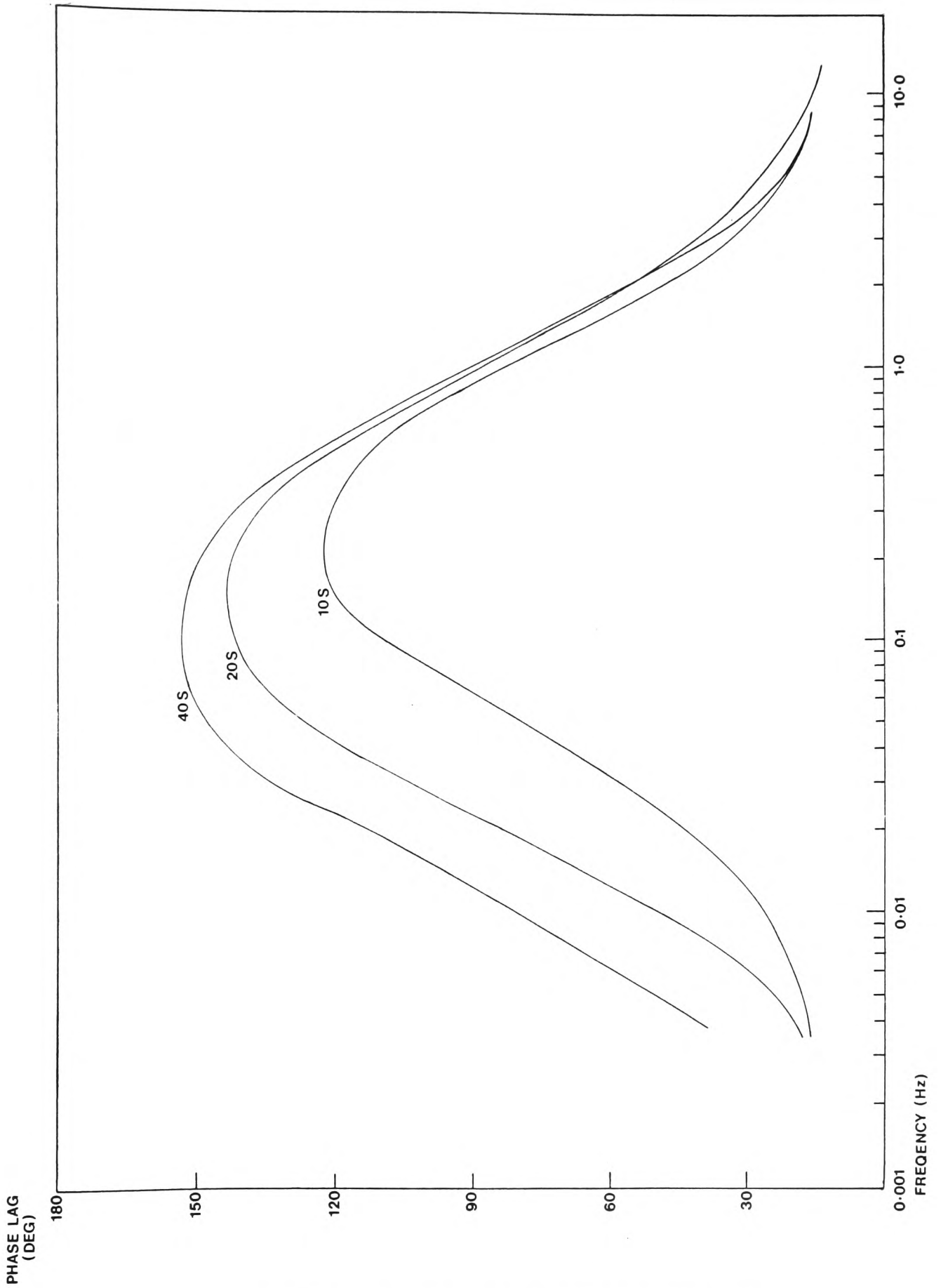
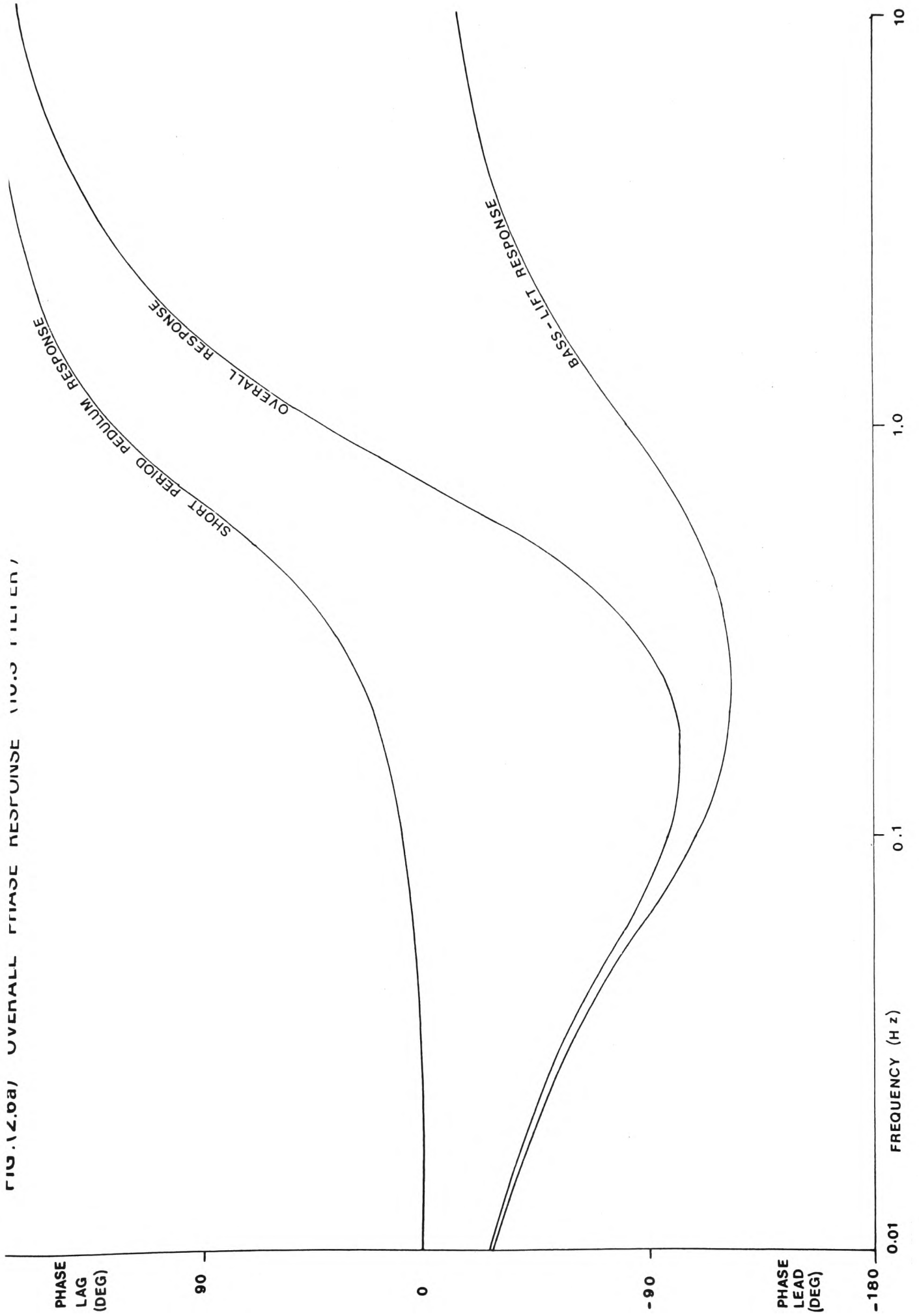


FIG 2-6 PHASE RESPONSE OF BASS-LIFT
(AFTER LAUHLIN AND WAUGH)

FIG. 14.8a) OVERALL GEAR RESPONSE (10.3 HILLEN)



our observations where the maximum detectable delay between the short period and bass-lifted channels for 1.0s period seismic waves is a lag of about 0.1s (see Section 4.5.0). At 10s periods, of course, it was extremely difficult to measure phase delays since on the short period seismograms these periods are drowned in background noise.

It is important to note also that Figure 2.6a is purely schematic, and is only intended to give an idea of phase responses. For actual measurements of phase delays the figure should contain the phase response of an experimentally derived short period electromagnetic transducer and not that of a pendulum undergoing simple harmonic motion.

The observed minor departures of the actual phase response from the ideal target are not critical if all channels are well matched to each other. This is because our prime interest will be focused on the bass-lifted traces of different events at a single station or the same event at different stations. In either case, as will be shown in Chapter 3, we collate the bass-lifted records according to a reference trace or according to the time channel.

2.6.2 Transient Response:

To test how the bass-lift responds to transients we implemented the following experiment. A decaying, 1 Hz sine wave was generated by an oscillator and input to the circuit. The amplitude and duration of the transient was controlled by a waveform function regulator. The input (S/N) and output (S/BL) at 3 filters viz: 5, 10 and 20s, are shown in Figures 2.7 and

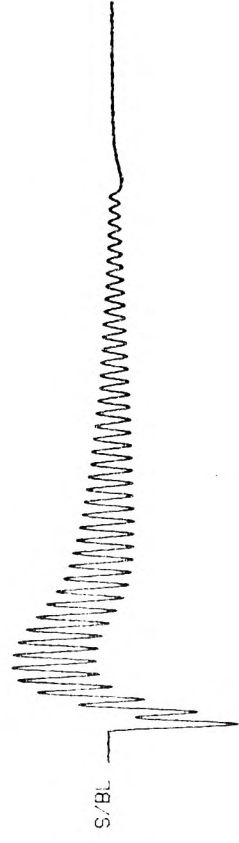
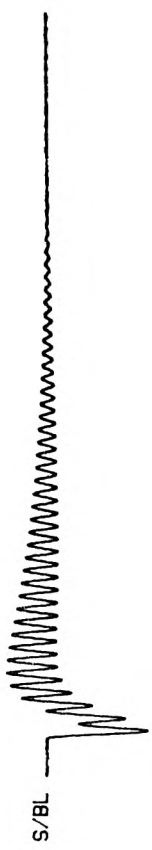
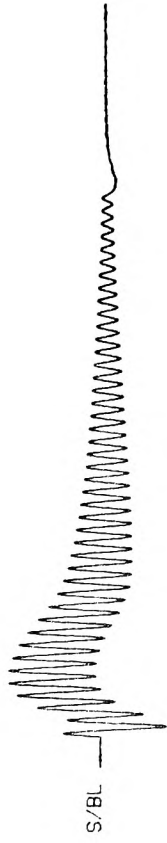


Fig. 2.7 TRANSIENT RESPONSE TO 10s FILTER

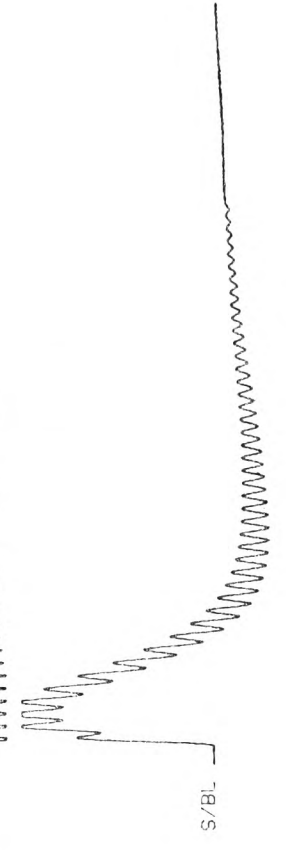
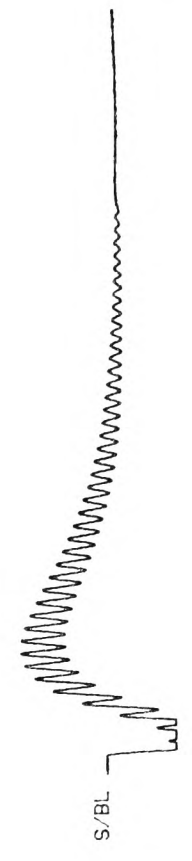
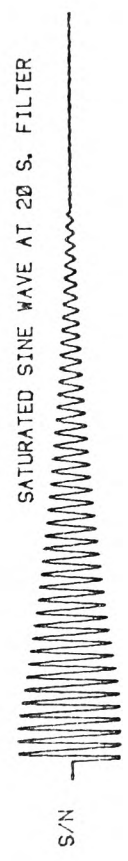


Fig. 2.8 TRANSIENT RESPONSE TO 5 AND 20s FILTERS

2.8. It is evident from these figures that the response of the bass-lift is ultimately dependent on the amplitude, duration and polarity of the input transient. Note particularly how the circuit responds to a partly saturated input signal (Fig. 2.7).

In examples later in this chapter, we show how this "ringing" feature is encountered in actual earthquake records where a substantial part of the P-coda is overloaded.

Having given an outline of analogue instrumentation and functions we turn to discussing the digital processing system used to digitize and handle our earthquake data.

3.0.0 THE DIGITAL PROCESSING SYSTEM:

This section deals with a description of the digital processing facilities available at IGS. The systems flexibility, interfacing, wide variety of peripherals and software make it a unique and powerful ensemble of digital equipment capable of processing seismic data from all on-line analogue replay systems.

3.1.0 The PDP 11/50 Computer:

The DEC PDP 11/50 is a medium range computer designed as a powerful computational tool for high speed real-time seismic applications. The machine has 32K-word (1K = 1024 words) of addressable memory space.

3.1.1 Central Processor Unit (CPU):

The CPU has a cycle time of 300 ns and performs all arithmetic and logical operations required in by the system. The central processor consists of two modules mounted integrally: A floating point processor (FPP) providing real and integer arithmetic operations; a memory management unit (MMU) which functions as a complex memory management through relocation and protection. The PDP 11/50 hardware is optimized towards a multiprogramming environment and the processor therefore operates in 3 modes: Kernal, Supervisor and User. When in Kernal the program has complete control of the machine. In the other two modes the CPU is inhibited from executing certain instructions and can be denied direct access to the system peripherals.

The central processor contains 16 general registers which can be used as accumulators, index registers or stack points. The processor status word (PSW) contains information on the current status of the machine.

Communication of the CPU with the memories, registers, and peripherals is performed through a bidirectional asynchronous bus known as the UNIBUS. Figure 2.9 is a block diagram illustrating the CPU data paths.

3.1.2 Memory:

Memory is the primary storage medium for instructions and data manipulation. Three types are available on the 11/50:

(a) Solid State (MOS) Memory: The MOS has a cycle time of

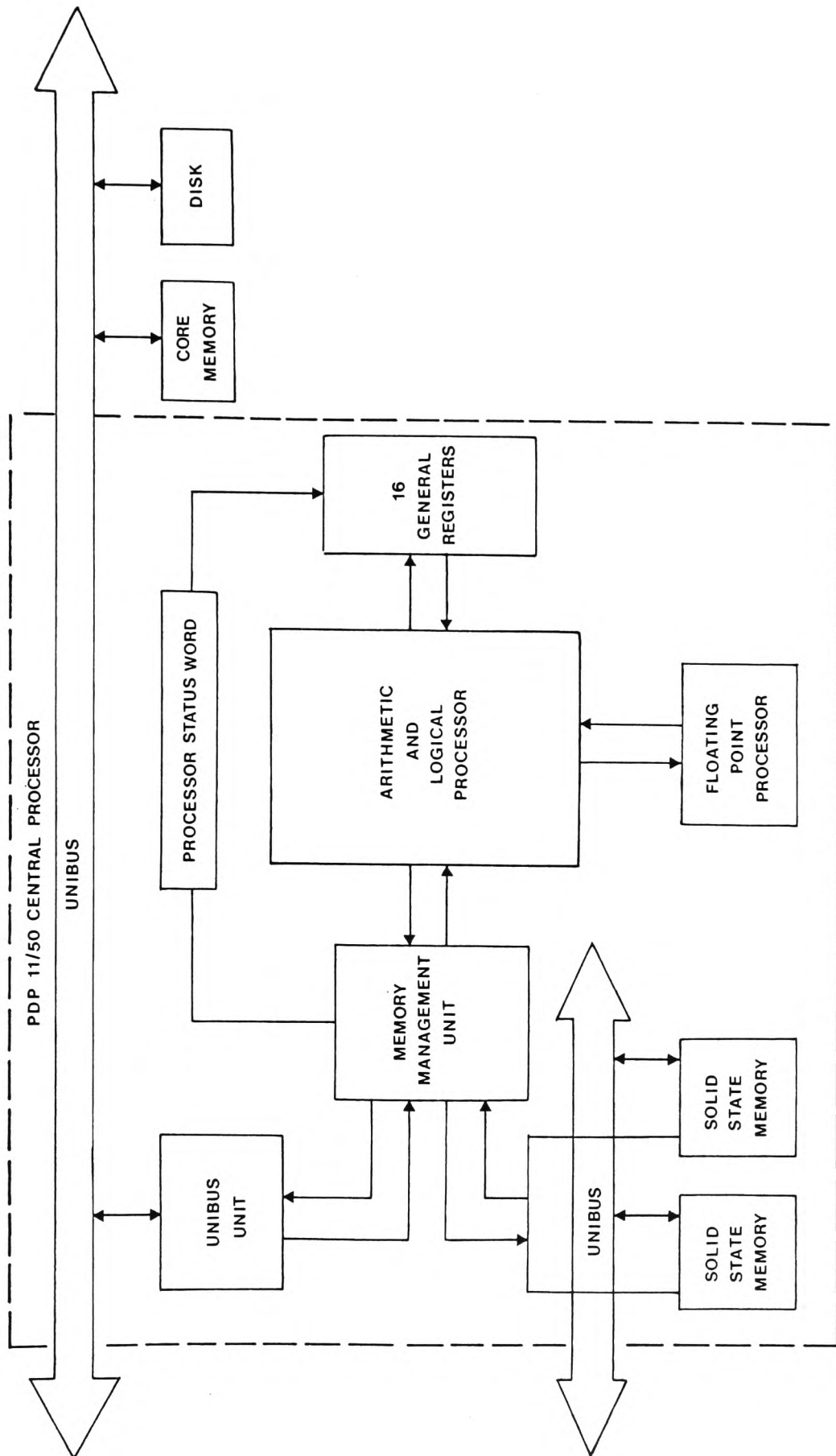


FIG 2-9 PDP 11/50 COMPUTER SYSTEM

450 ns and communicates directly with the CPU through an internal UNIBUS. The CPU controls the MOS memory by means of a solid state memory controller containing 4 x 4K-word of MOS thus allowing the user to access a total of 16K-word of MOS.

(b) Core Memory: The core is a read/write, random access, coincident current memory with a cycle time of 850 ns. It is organized in a 3-D planar configuration using 18 mil. magnetic cores and giving 16K-word of store.

(c) Cache Buffer Memory: This module has a cycle time of 300 ns and resides in the CPU. The cache buffer provides the necessary control logic to map overlay the entire main memory, thus achieving an average increase of 35% in the speed of the MOS memory.

3.2.0 Interfacing:

The logic equipment through which the machine communicates with the outside world is called an interface. Three such modules exist on the 11/50:

3.2.1 General Device Interface (DR11-C):

This is a general purpose interface between the PDP 11/50 UNIBUS and the user's peripherals. It provides the logic and buffer register necessary for program-controlled parallel transfers of 16-bit (2-word) data between the system and an external device. The DR11-C also includes status and control bits that may be controlled by either the program or the external device for command, monitoring, and interrupt functions.

3.2.2 Analogue-to-Digital Subsystem (A001-D):

This module is a flexible, multi-channel digitizer which interfaces directly with the computer. It consists of a 32-channel solid state input multiplexer, programmable input range selector, A/D converter, control and bus interface. The A001-D is connected to 2 Schmitt triggers and provides 10-bit digitization accuracy of unipolar high-level analogue signals having a nominal full-scale range of 0.0 to 0.25, 2.5, 5.0, or 10.0 volts. An optional sign-bit allows 11-bit bipolar operation up to a maximum sampling rate of 12,000 SPS. Sampling may be controlled from the flutter carried signal of an analogue tape via one of the Schmitt triggers or by means of an internal computer clock. The other trigger may be used for end-of-tape (EOT) detection by prompting the machine to cease processing.

3.2.3 Digital-to-Analogue Subsystem (DA11-D):

This module provides 12-bit bipolar digital-to-analogue conversion. The DA11-D is equipped with 16 replay channels compatible with the jet-pen recorder and has a full scale output voltage from 0 to ± 10 volts.

3.3.0 Peripherals:

3.3.1 Storage Media: Three types are available:

- (a) Two RK05 Cartridge Disks, one fixed (system disk), the other removable. This device provides a mass storage medium for large volume, random-access data. Permanently

mounted in a protective case, each disk cartridge has the capacity to hold 1.2 million words and has an average access time of 70ms.

- (b) Two RX01 Floppy Disks: These are thin, flexible, oxide coated diskettes similar to the 45-rpm phonographic record. This random-access device provides a low cost storage, interchange and software distribution medium for critical I/O applications. Each diskette is capable of storing up to 256,256 8-bit bytes (1 byte = $\frac{1}{2}$ word).
- (c) Two DIGI-DATA Magnetic Tape Transports: These 9-track drives provide a high performance, virtually unlimited capacity medium for reading, writing and storing large volumes of data and programs in a serial manner. The subsystem uses $\frac{1}{2}$ -inch magnetic tapes loaded on 7-, 8 $\frac{1}{2}$ - and 10 $\frac{1}{2}$ -inch diameter reels giving 600-, 1200- and 2400-feet of tape respectively. With two tape densities of 800 and 1600 BPI a 2400 ft tape has the capacity to store 18 or 36 million bits of data.

3.3.2 Input/Output and Display Media:

- (a) PC11 Reader/Punch is a high-speed paper tape reader and punch reading at 50 characters/s.
- (b) LA180 Line Printer operates on-line with the computer and its associated peripherals and is capable of printing 132 characters per line.
- (c) DACOL VDU Terminal is an alphanumeric display device consisting of a CRT (Cathode ray tube) screen and a self-

contained keyboard. The VDU is used to compose, edit and forward information to the computer; retrieve and update alphanumeric data contained in the computer files; receive instructions from the CPU; and perform on-line debugging. The device is provided with data transfer rates of 100, 300, 600, 1200, 2400, 4800 and 9600 Baud and a full duplex and $\frac{1}{2}$ duplex option.

(d) Tektronix 4014 Terminal is a versatile display device which operates in both alphanumeric and graphic mode. In addition to the VDU functions, the terminal is connected to a VERSATEC hard copy unit to produce fast copies of what is displayed on the screen.

(e) HP7221A Graphics Plotter is directly interfaced with the 11/50 and offers a hard copy, A3 size, multicolour, plotting facility. This plotter is useful for obtaining high quality plots.

Almost all the above mentioned devices, modules and interfaces plus the main computer memory were heavily used in our data processing and experimentation. Some of the more important software utilized in conjunction with the digital equipment discussed so far, is next outlined.

3.4.0 RT-11 System:

The PDP 11/50 computer is operated through the RT-11 programming and operating system. This permits the use of all peripherals as well as 28K-word of either MOS or core memory. The RT-11 is set to a single-job operating environment although this could be changed to a foreground/background monitor

capability. In addition to the monitor facilities, the system offers a complement of handling software using high level languages such as FORTRAN IV or assembly languages like MARCO.

The Text Editor (EDIT) is used to create or modify source files for use as input to language processing programs such as the assembler or FORTRAN.

The Peripheral Interchange Program (PIP) is the RT-11 file maintenance and utility software used to transfer, rename, list files ... etc. The Linker Program (LINK) fixes the values of relocatable symbols and converts the object files into load module to be run in the foreground. The FORTRAN Compiler and System Library (SYSLIB) are both used to write some source programs which when compiled and linked can be executed by the computer.

The above handling software plus specialized programs to digitize (MTDIG), replay (MTREAD and REPLAY), select (FINDEV and HDP), collate (BEIN) digitized files or channels were again indispensable to our needs in processing.

4.0.0 DATA PROCESSING PROCEDURE:

So far we have described, in some detail and length, the analogue and digital processing systems available at Global Seismology, IGS. The aim of such an account is to give an idea of the variety and diversity of hardware utilized in processing the earthquake data used in this research.

To go into the details of processing in a step-by-step

fashion is not an easy task and could well prove to be of little significance. There are, however, a number of fundamentally important criteria that must be taken into consideration before embarking upon a successful processing scheme. It is appropriate, therefore, to discuss these criteria, which it is hoped, when put together form an outline of what is actually involved in data processing.

4.1.0 General Considerations:

Before converting an analogue trace into digital form, many aspects have to be considered. First and foremost is record content and hence the aim of the seismological investigation undertaken.

In this research we are interested in record simulation with the object of constructing a large earthquake source from the sum of individual smaller shocks. We, therefore, need to show in both time and frequency domains how the constructed record progresses towards a large source motion. This means that we are dealing with time series as well as spectral analysis. For this reason and because we need eventually to evaluate and assess the spectrum with some dynamic source parameters, the complete seismogram with its different waves and periods is paramount and should be included in processing (see Section 3.0.0 of Chapter 4 for other reasons).

Subsidiary to the above but equally important are considerations like the bandwidth of the seismometers, dynamic range of the recording ... etc. These have to be clearly known in order to ensure optimum transfer of information from analogue

to digital records.

4.2.0 Event Selection:

In selecting our data sets we made a great deal of use of both visual and audio techniques, i.e: by replaying records on paper and by "listening in" to events.

The audio method was particularly useful in searching through the Rabaul tapes where numerous, small magnitude, local shocks were picked-up, replayed, processed and analysed (see Chapter 7).

The Chile data set, on the other hand, were initially selected from seismological bulletins like NEIS-PDE monthly listings and ISC bulletins. The SAAS tapes for these shocks were then replayed, visually identified, processed and analysed (see Chapters 5 and 6).

At this stage of processing we used the replay unit, programming board, ink-jet and audio monitor described in Section 2.0.0.

4.3.0 Filtering and Bass-Lifting:

Having selected the data from both sources we proceed to filter and bass-lift. Here it is important to consider the energy and frequency content of the signals coming from the two different source regions.

For the Rabaul events where the source-receiver distance ranges from 40-160km, it was observed that almost all shocks have a

substantial amount of energy at frequencies between 8-12 Hz. Therefore a filter bandwidth of DC-15 Hz was sufficient. For such relatively high frequency local earthquakes, and from our experience with the bass-lift unit, it was appropriate to set the circuit period to 5.0s. This would effectively limit the high-pass to 0.2 Hz. Beyond this period system noise prevails. This is because the small amplitudes of these events do not rise above system and/or earth noise at the longer periods.

The situation was different for the Chile earthquakes where seismic frequencies fall in the teleseismic range (0.2 - 300s). The shortest periods observed on these seismograms were between 0.2 - 0.4s. Hence a 5 Hz low-pass was selected and the low frequency end was limited by the 10s bass-lift filter. Here again we found that beyond this period system noise prevails.

4.4.0 Digitization:

Digitization is actually performed by the A/D subsystem described in Section 3.2.0 through the use of the relevant software (Section 3.4.0).

The frequency content of the earthquake records replayed at a certain speed in relation to the cycle-time and core size of the computer determine the optimum sampling frequency. This frequency must be, at least, an octave (ratio of 1:2) higher than the low pass or high cut-off. The sampling rate for the Rabaul events was therefore set to 30 SPS, while that for the Chile earthquakes was selected as 10 SPS. It immediately follows from these values that the maximum

retrievable or Nyquist frequencies will be 15 and 5 Hz respectively. This and the general topic of spectral analysis is the subject matter of Chapter 4.

As far as the gain of digitization was concerned, this was set to 1.25 volts throughout the digitization of the Rabaul data except R0072 and RDM73 where 10 volts was chosen. On the other hand, and for the larger shocks amongst the Chile source viz: CB001, CB022, CB00A, CB00B, and CB00C, the gain was set to 10 volts, while for the other lower magnitude aftershocks a 2.5 volts gain was appropriate.

4.5.0 Examples of Processed Seismograms:

Here we present specific examples of processed seismograms from both data sources which are now ready for experimentation and analysis. The intention is to illustrate to some extent what we have been discussing pointing out salient features most important of which is bass-lifting. Note that all seismograms shown have 3 channels: Time; a normal vertical component (Z/N); and a Bass-lifted version (Z/BL).

In Figure 2.10 examples are shown of a major and minor event from Rabaul as seen by ETV. The upper RDM73 seismogram illustrates the unavoidable problem of saturation. Taking the Z/BL trace it is possible to observe the difference between original overloading (first 30s) and that produced by the digitizer overflow (the following 2 minutes). This is despite selecting the maximum dynamic range of the digitizer i.e: 10 volts.

The Z/BL trace of the lower RD043 seismogram illustrates to

RABAUL DATA MAJOR EVENT: R073 AT ETV (900/1410/12000/0.00002/0.0005)

1 MIN.

TIME



RABAUL DATA MINOR EVENT: R0043 AT ETV (300/1590/3600/0.00002/0.0005/0.0014)

10 S.

TIME

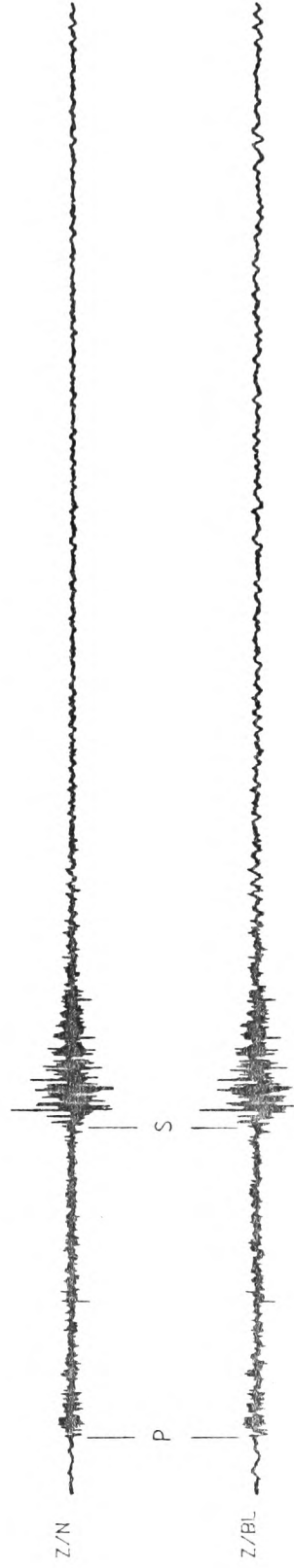


Fig. 2.10 RABAUL DATA : MAJOR AND MINOR EVENTS AT ETV

some extent the 5.0s filter. Comparing that with its Z/N trace, it is possible to notice some longer periods rising above noise.

Figures 2.11 through to 2.14 illustrate examples of seismograms from the Chile source at some southern array stations. Figure 2.11 again shows the overloading problem we were faced with the Z/BL at both stations showing original saturation as well as digitizer overflow. Original saturation of large events like CB001 at SAAS stations is unavoidable because of the array's common gain (see Chapter 5).

We are well aware that this problem causes waveform distortion and generates spurious high frequencies. Nevertheless, this set back did not hinder our efforts to proceed with experimentation and analysis because it will be seen in Chapter 4 how this particular problem is insignificant, as reflected on the spectrum, compared with clipping on the Z/N channels.

Perhaps Figure 2.12 is a good example of the basic function of the bass-lift instrument. It is clear here that the surface waves revealed on the Z/BL of both stations are quite conspicuous and show high resolution while they could pass unnoticed on the Z/N traces. This is the outstanding advantage of the bass-lift mentioned earlier (Section 2.6.0).

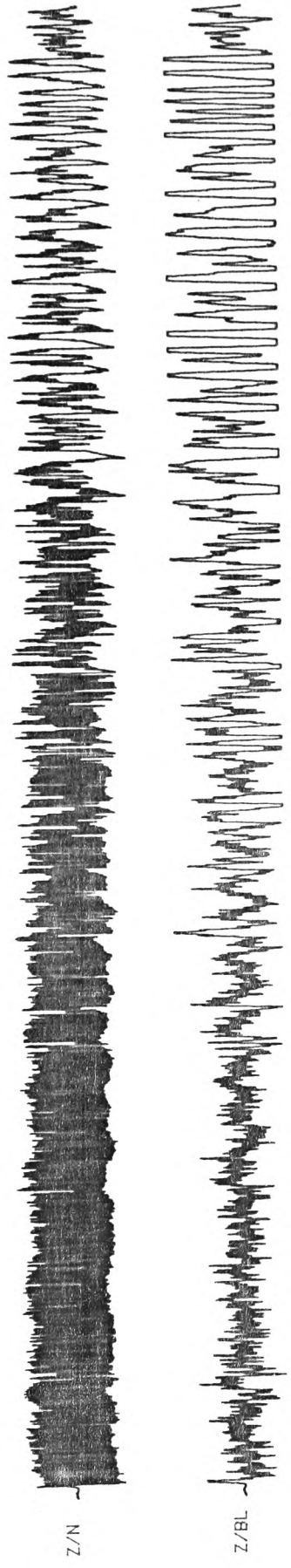
The figure also depicts what we have previously identified as "ringing" due to the input of a partly saturated signal (Section 2.6.2). The transient due to overloading of the P-arrivals seems quite similar to those illustrated in Figure 2.7.

The ringing problem, will obviously distort the seismic spectrum

CHILE DATA EVENT: CB001 AT SAAS: S4 (600/700/8000/0.0001/0.0005)

1 MIN

TIME



CHILE DATA EVENT: CB001 AT SAAS: S5 (600/730/8000/0.0001/0.0005)

1 MIN

TIME

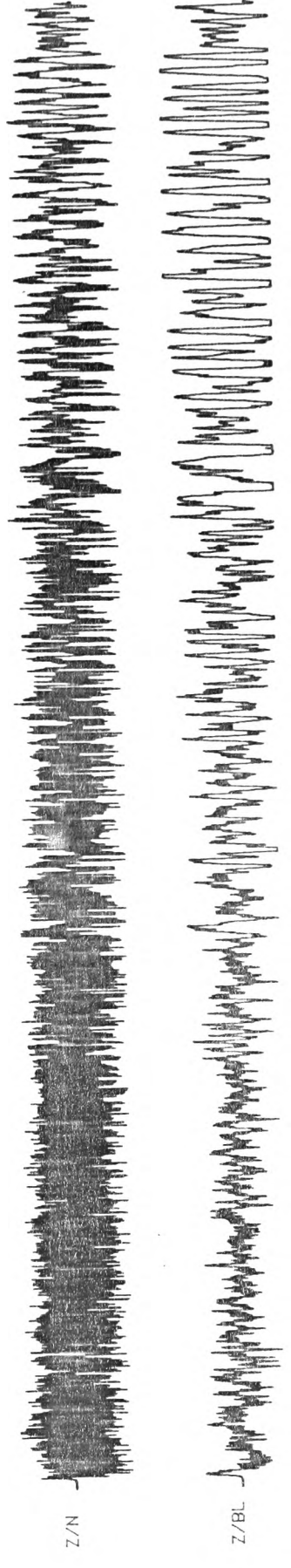
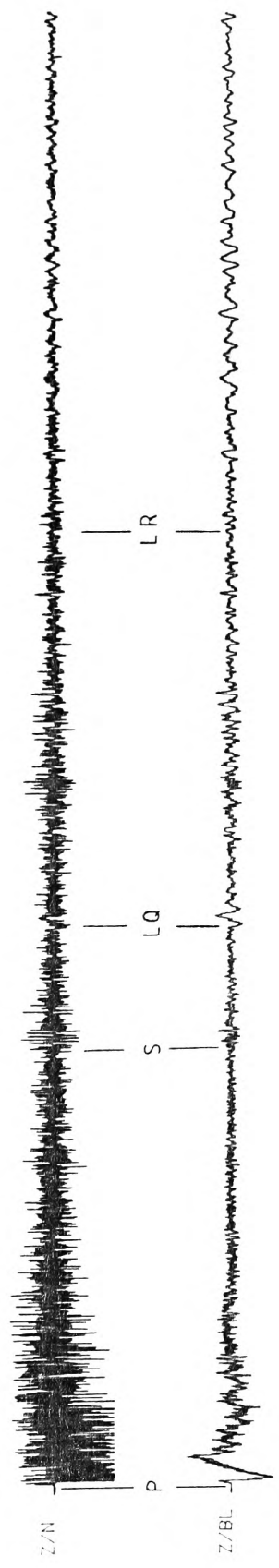


Fig. 2.11 CHILE DATA : EVENT CB001 AT SAAS : S4 AND S5

CHILE DATA EVENT: CB022 AT SAAS: S2 (600/500/8000/0.0001/0.0005)

1 MIN.

TIME



CHILE DATA EVENT: CB022 AT SAAS: S5 (600/500/8000/0.0001/0.0005)

1 MIN.

TIME

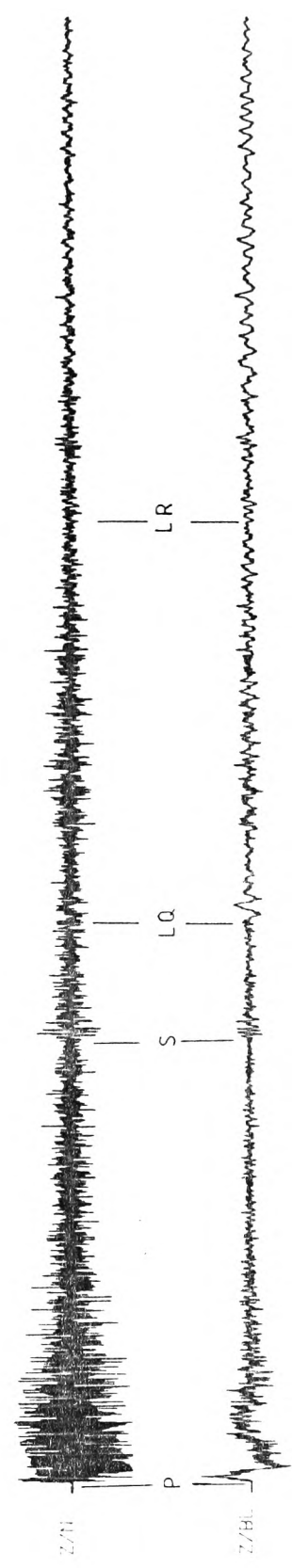


Fig. 2.12 CHILE DATA : EVENT CB022 AT SAAS : S2 AND S5

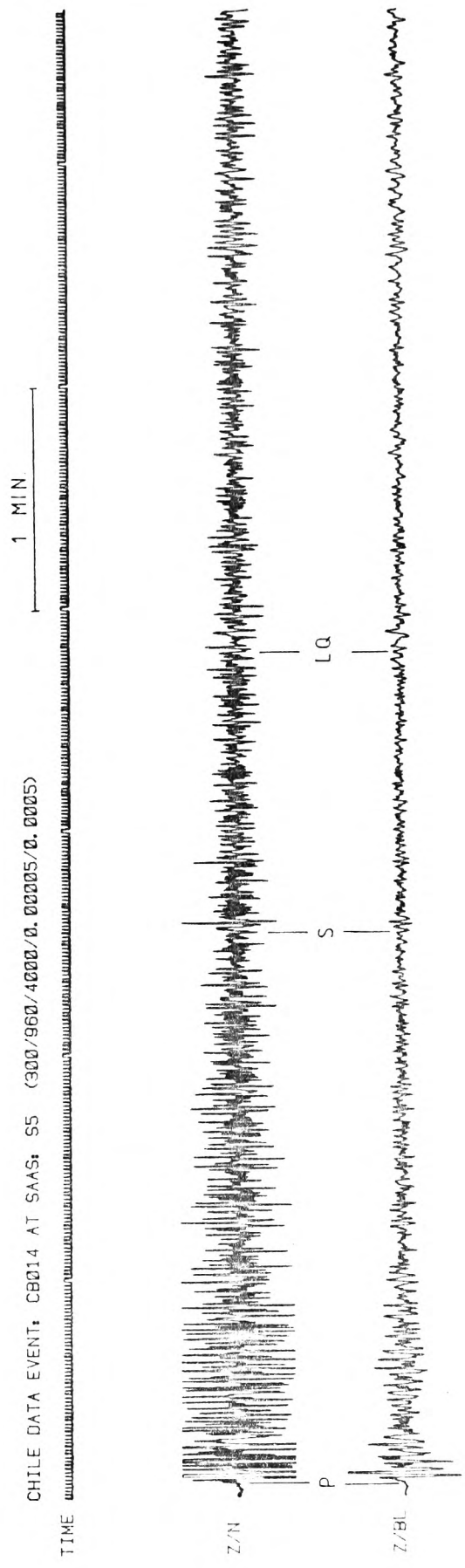
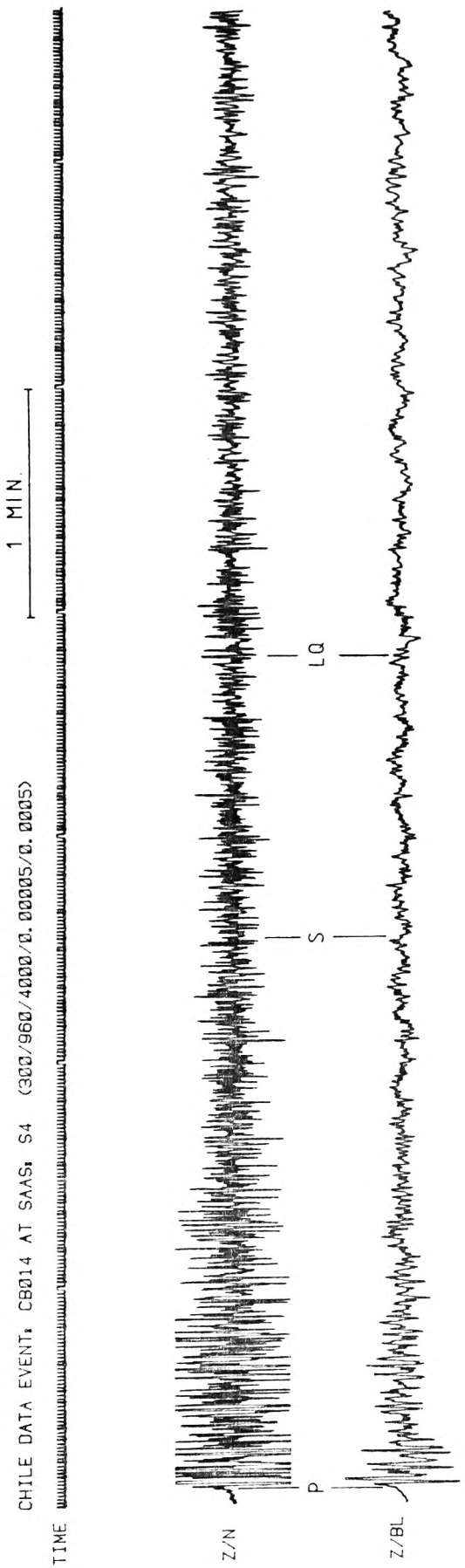


Fig. 2.13 CHILE DATA : EVENT CB014 AT SAAS : S4 AND S5

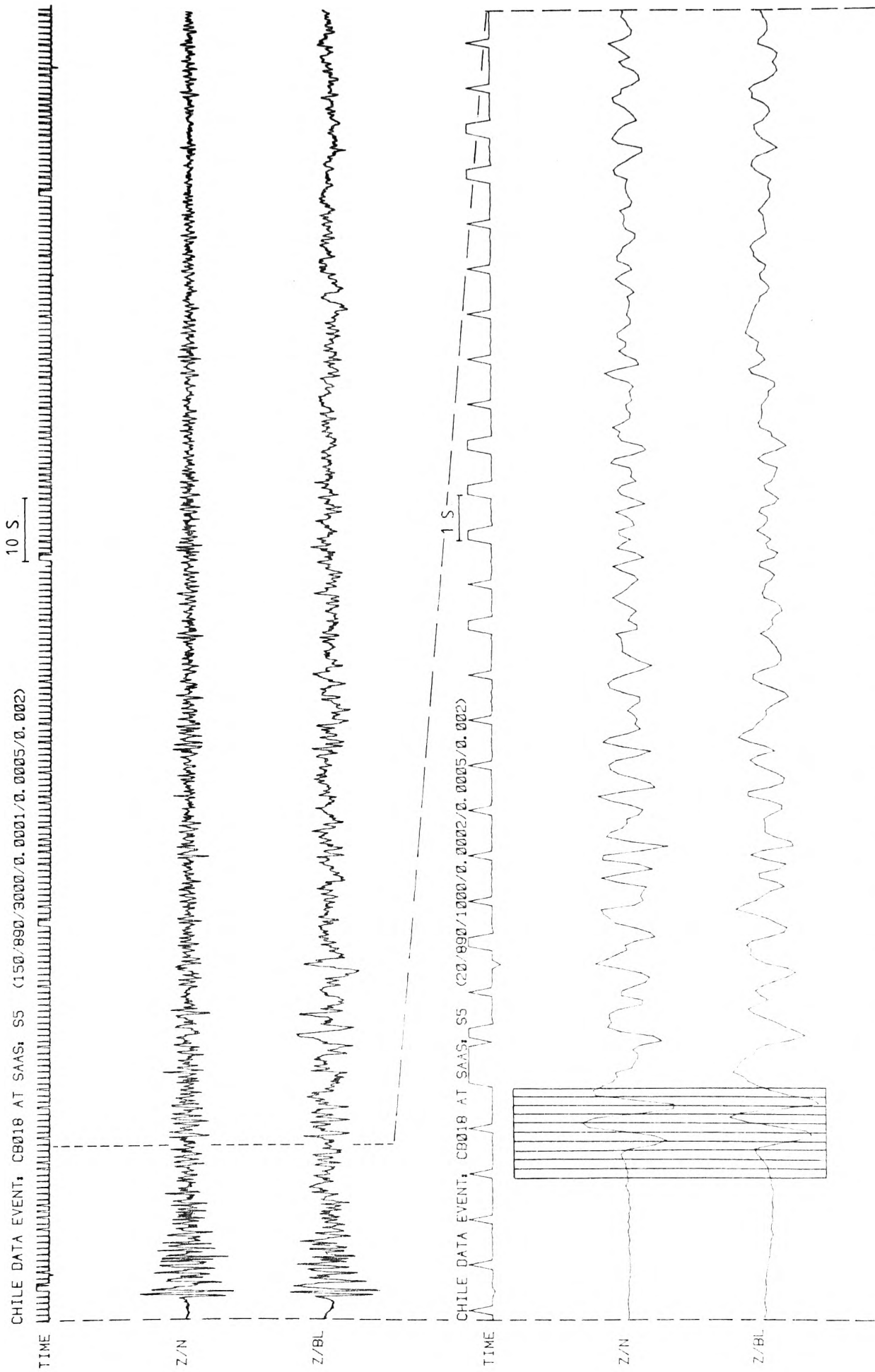


Fig. 2.14 CHILE DATA : EVENT CB018 AT SAAS : S5

and is therefore treated in Chapter 4.

Another Chile event showing a noisy and quiet station is pictured in Figure 2.13. As outlined in Chapter 5, there are some array stations noisier than others, but such local noise is randomised as much as possible in summation (Chapter 3) and hence does not pose a major problem in analysis.

Finally Figure 2.14 depicts the phase lag of the bass-lift 10s filter. For the first few p-phases, it is evident that the Z/BL lags by no more than 0.1s.

CHAPTER 3

METHODOLOGY AND EXPERIMENTAL PROCEDURE

1.0.0 INTRODUCTIDN:

This chapter is intended to explain the method and experimental procedure adopted in our attempts to model large earthquake motions from smaller earthquake records.

The chapter begins with a discussion of fundamental concepts relevant to our approach. These include the physics of an earthquake process, point source and dislocation theory, source parameters, size of shocks and near- and far-field concepts.

Next we introduce the approach to earthquake simulation employed in this research, pointing out the assumptions involved and the working source model adopted. Under this section we also discuss the method used to assessing the simulated source.

Experimental procedure is next discussed with an outline of the beamforming technique, and the program used, how it is tested and applied to some earthquake ensembles. This is highlighted by examples on real data with discussion.

The chapter is concluded by discussing the topic of incompleteness of earthquake samples.

2.0.0 FUNDAMENTAL CONCEPTS:

2.1.0 The Earthquake Process:

An earthquake is a physical process whereby large volumes of rock, previously in a state of high stress, undergo sudden rupture. This phenomenon usually occurs along pre-existing fault surfaces representing zones of weakness in the earth's

lithosphere or upper mantle. The actual process may be summarized as follows:

- (a) Due to long-term relative tectonic motions between lithospheric plates a dynamic stress field is generated (in the vicinity of a fault).
- (b) As this stress gradually increases it eventually exceeds the strength of the rock material in the focal region. At that instant faulting occurs and the stored elastic energy is converted to kinetic energy radiated as seismic waves, transformed into heat, or is stored as potential energy elsewhere in the region.
- (c) After an earthquake, the stressed medium is gradually restored to an equilibrium state, through the release of residual strains in the form of aftershocks and fault creep.

Stressdrop occurring along and over a limited part of the fault surface is therefore an important source factor in defining an earthquake process. This parameter amongst others, collectively known as dynamic source parameters have been extensively used especially in recent investigations of the earthquake source.

Studies aimed at understanding the physics of an earthquake process began with the work of Reid (1910) in his study of the San Francisco earthquake of 1906. Reid's elastic rebound theory set the physical foundation of what we now understand as the theory of the source.

2.2.0 Point Source Theory:

The theory of point sources stemmed from the early work of Love (1927) and is well described by Brune (1976). The radiation pattern of long-period waves from earthquakes at teleseismic distances can be approximated by this approach. The model consists of a system of 4 forces in equilibrium symmetrically arranged into 2 couples, acting at a point along the fault. This double couple source and its P- and S-wave radiation pattern has been used to obtain fault orientations (P-waves) and slip directions (S-waves) by fault plane solutions (Hodgson, 1957; Honda, 1957; Keilis-Borok, 1957; Balakina, et al, 1961; Stauder, 1962, Ritsema, 1964, and many others).

2.3.0 Dislocation Theory and Source Parameters:

It was not until the late 1950's that much theoretical consideration was given to the source through the work of Vvedenskaya (1956), Steketee (1958) and Knopoff and Gilbert (1959). The mathematical framework upon which source studies are based is called elastic dislocation, shear dislocation or simply dislocation theory.

In this theory an earthquake fault is mathematically modelled by a slip-displacement discontinuity $U(\vec{r}, t)$ along a fault surface Σ in an elastic medium. The slip function is usually a step or ramp in time with (\vec{r}) describing the position along the fault relative to the focus. Since most observations agree with a double couple force system to represent an earthquake source, the perpendicular slip component to the fault is neglected and the slip then becomes

a shear dislocation.

The dislocation is assumed to propagate along the fault at constant rupture velocity v_R , usually about $0.72 - 0.9\beta$, the shear wave velocity.

In approximating the shape and size of sources the geometry of a fault has been modelled as rectangles, circles, or ellipsoids with the rupture propagating in a unidirectional or bidirectional manner. Within dislocation theory, a number of so-called kinematic models have been proposed to explain the earthquake source (Ben-Menahem, 1961; Haskell, 1964, 1966; Savage, 1966; Aki, 1967; Wyss and Brune, 1967; Trifunac and Brune, 1970).

In all of these fault models, the slip function $U(\vec{r}, t)$ arbitrarily describes the rupture growth on a fault surface. To eliminate this arbitrariness, the problem of the rupture process has to be solved. Some progress has been made in this direction by the introduction of dynamic models such as those proposed by Kostrov (1966), Archambeau (1968), Burridge (1969), Brune (1970), Hanson, et al (1971), and Madariaga (1976, 1978).

A useful review of theoretical relationships describing different source models is given by Kanamori and Anderson (1975) and Geller (1976). We, therefore, mention here some important, partly empirical, parameters common to all source models:

(a) Seismic Moment: The total moment of the double couple force system on the fault surface equivalent to the dislocation is given by:

$$M_0 = \mu \bar{U} S$$

where: S is the fault area

\bar{U} is the final dislocation $U(\vec{r}, \infty)$ averaged over S.

μ is the rigidity usually taken as 3×10^{11} dyne/cm²

(b) Apparent Stress : This is defined by:

$$\eta \bar{\sigma} = \mu E / M_0'$$

where: E is the radiated seismic energy

η is the efficiency of radiation

σ is the average of the initial stress σ_0 and final stress σ_1 along the fault.

(c) Stress Drop : This is the difference between σ_0 and σ_1 defined as:

$$\Delta \sigma = c M_0' / S^{3/2}$$

The constant c depends on the fault shape and slip direction:

For circular faults: $c = \frac{7}{16} \pi^{3/2}$ (Eshelby, 1967; Keilis-Borok, 1959).

For rectangular faults with length L and width W where $L > W$:

$$c = 4/\pi (L/W)^{1/2} \text{ - buried strike-slip (Knopoff, 1958)}$$

and

$$c = 16/3\pi (L/W)^{1/2} \text{ - buried dip-slip (Starr, 1928)}$$

A medium to large size earthquake seismogram usually carries information relevant to the above parameters. This coupled with prior knowledge of the geology and tectonic setting of the focal region is frequently used to assess the hazard of

an earthquake-prone area.

Some of the theoretical relationships published by Kanamori and Anderson (1975) are used in Chapter 6 to estimate certain source parameters of the far-field Chile data set.

2.4.0 Seismic Spectrum and Corner Frequency:

We mention this topic in passing since it is discussed in more detail in Chapter 4.

The seismic energy radiated from an earthquake is the basis of our knowledge regarding the details of the source. The amplitude spectrum of the displacement function used in dislocation theory has become a valuable tool for investigating some dynamic source parameters. As a result, the various models proposed for the earthquake source have approximated the source spectrum with two asymptotes: one of constant amplitude characterizing the low frequency portion of the spectrum; the other inversely proportional to some power of frequency, characterizing the high-frequency portion. With these approximations seismic spectra have been represented on log-log plots by three source parameters, (Fig. 3.1):

- (a) Low-frequency level Ω_0 proportional to M_0 .
- (b) Corner frequency ω_c related to S .
- (c) High - frequency asymptotes ω^{-1} , ω^{-2} , and ω^{-3} related to the degree of dislocation discontinuity and to the details of the fracturing mechanism.

According to Randall (1973), all source models agree on the

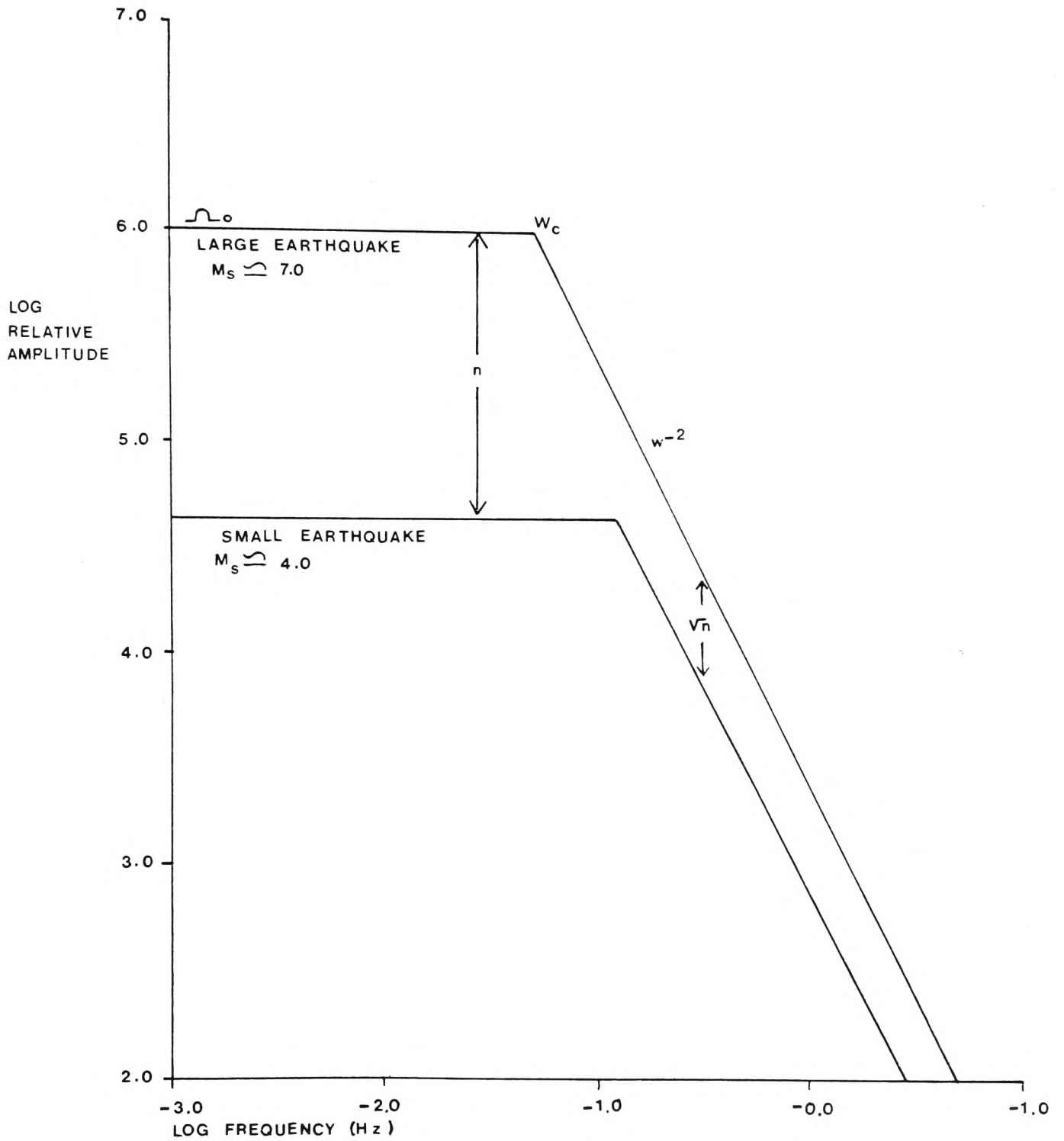


FIG.(3.1) SCHEMATIC REPRESENTATION OF SEISMIC SPECTRA.
(AFTER AKI, 1967;1972)

gross spectral shape of Figure 3.1, but there is still controversy regarding the high-frequency asymptotes (Aki, 1972) and the P- and S- corner frequencies (see Chapter 4).

2.5.0 Earthquake Size:

The magnitude scale was the first and most widely used quantitative estimate of the size and strength of an earthquake. Richter's (1935) local magnitude M_L uses short period (0.1 - 2.0s) crustal waves from earthquakes at short distances. This is equivalent to wavelengths of 300m to 6km.

Gutenberg (1945a,b,c) extended the M_L measure to earthquakes from distant sources, by introducing the m_b and M_s scales. M_s measures the energy contained in 20s surface waves while m_b corresponds to body waves having periods of about 1.0 - 5.0s. These magnitude scales and their inter-relationships (Gutenberg and Richter, 1956a,b) cover fault lengths of the order of 3 - 60km.

For greater fault lengths, these scales "saturate" because they represent estimates of seismic energy at specified wave periods. This inherent weakness in magnitude determination seems to have been overcome by the introduction of a new scale, M_w (Kanamori, 1977a, 1978). In this scheme the overall size of an earthquake is calculated from M_0 which involves integration of the seismic energy release over the whole spectrum. Such a spectral description of the source gives a more realistic representation of the time-space history of the faulting mechanism.

This new convention will be the basis of our assessment of the seismic spectrum as will be seen later.

2.6.0 Far- and Near-Field Observations:

Earthquakes originating at epicentral distances greater than 20° are known to most investigators as far-field observations. At these distances and for periods greater than the source size, a fault can be approximated as a point double couple. Consequently, the spectral shape of the radiation assumes the form represented in Figure 3.1, with its absolute value increasing in proportion to the product of dislocation and total fault area.

At short distances, i.e. in the near-field, the spectrum becomes nearly independent of the total area of the fault and depends only on the amount of dislocation (Aki, 1968a). The difference, therefore, between short and long distances makes the use of far- and near-field seismic spectra a powerful method for the study of earthquake source mechanisms (Aki, 1969). For this reason and others we have selected earthquakes from both types of sources in the hope that their study will disclose information relevant to the mechanics of earthquake rupture in general.

Having outlined these topics of relevance, we now set out to explain the method and procedure adopted in our simulation technique.

3.0.0 METHODOLOGY:

One of the established approaches to earthquake prediction

research is to find the state of stress inside the earth from seismograms of numerous small earthquakes occurring in the general area where a large earthquake is expected (Aki, 1968b). As outlined in Chapter 1, the hypothesis underlying this research is that large and small earthquakes probably share the same tectonic causes.

3.1.0 The Approach:

A large earthquake mechanism is viewed in the light of Huygen's Principle in which a propagating wavefront is postulated to consist of point sources emitting spherical waves travelling at a certain velocity. The total field at some later time is then the sum of the fields of each of these point sources. Taking this physical principle as a basis we equate remote effects to the summation in appropriate time sequence, of the effects generated by the stress release in each element of the wavefront. We make the additional hypothesis that a small earthquake record is a reasonable approximation to the contribution produced by an element in the wavefront of a large earthquake, when the front passes through the small focus. Therefore, and according to the above, a large earthquake process could be approximated by a summed succession of smaller ones, triggered by a propagating dislocation originating from a point source and spreading in the most likely direction of stress relief along the fault. This displacement must be a linear function of stress within the focal region.

Numerous papers have been published in recent years on the synthesis of complete seismograms or specific waves radiating

from known or postulated sources and structures (see for example: Wiggins and Helmberger, 1974; Vered and Ben-Menahem, 1974; Fuchs, 1975; Kennett, 1975; Kelly et al, 1976; Khattri and Gir, 1976; Sprenke and Kanasevich, 1977; Keith and Crampin, 1977). Comparison of such theoretical seismograms with actual records can yield valuable information on the agreement between hypotheses and reality. Our target is similar but the approach is different. It will be to take actual records of small events in an unknown structure, and therefrom to predict the waveform of a large earthquake.

3.2.0 The Summation Method:

To implement the approach suggested above we ideally require a suite of small earthquake records of sufficient quantity to sample the focal region of a large source. This population, should in addition, share similar faulting mechanisms with the large shock. The collection of small records will then be the input to a simple time domain summation process, the output or resultant sum of which will be compared with a large earthquake record known to have occurred in the same region. The ultimate goal would therefore be to obtain a simulated earthquake motion that carries the best approximation to the actual large earthquake motion.

The summation of component seismograms is performed by introducing appropriate time delays to account for rupture propagation velocity and travel times of the different seismic phases. Long period components characteristic of large motions will emerge because low frequency components of the

input records interfere constructively while the short period elements accumulate at random. The resulting simulated record would then contain an enhanced long period content representing an approximation to the mechanism and rupture propagation process produced by a large source which was built into the summation procedure.

On the seismic spectrum, this constructed motion will have essentially a scaling effect. As magnitude increases or more precisely, as M_0 increases, and at periods longer than the total duration of faulting, the simulated earthquake spectrum will be proportional to "n" (no. of component records), while the high frequency portion will interfere according to " \sqrt{n} ". Thus the spectral ratio between large and small earthquakes at low frequency will be the square of the ratio at high frequency. This is schematically illustrated in Figure 3.1.

The advantages of this method over purely theoretical methods of seismogram synthesis are that the stress-drop and faulting mechanism characteristics of the source region as well as the transfer function of the ray path and receiver are all contained in the individual component records and are preserved in summation. Therefore, they do not have to be introduced as new parameters in the process. Instead, we focus our attention on the phasing of the small earthquakes at the receiver, with the aim of producing the phasing pattern which gives the best eventual fit to the large earthquake motion.

3.3.0 Assessing the Simulation Process:

In order to relate the seismic spectrum to earthquake size and



hence to measure the progress and degree of success in simulation, we require a source model that satisfies two criteria:

(a) it is based on dislocation theory.

(b) it is geometrically simple.

A rectangular dislocation, known as the Haskell model meets the above criteria (Haskell, 1964, 1966, 1969; Aki, 1967; Savage, 1972). The basic assumption behind this model is that large and small earthquakes are essentially similar phenomena, an idea originally advocated by Tsuboi (1956). According to Aki (1972), this implies the same fault geometry, constant stress-drop, constant rupture and slip velocities independent of earthquake magnitude. This concept was supported by the observations of Bath and Duda (1964) and used by Aki (1967, 1972) in his ω -square model.

From our point of view and in order to base our hypothesis on a mathematical framework, we make use of the Haskell model in conjunction with the similarity condition and assume that they are adequate as a first approximation to our observations. If this were the case, then the problem of assessing the size of the simulated source would be reduced to observing two parameters on the seismic spectrum: ω_c which would be inversely proportional to fault length (Bracewell, 1965; Aki, 1967) and Ω_0 which is proportional to M_0 . Therefore a definite shift of the corner to lower frequencies with a simultaneous build-up of the Ω_0 level according to "n" in the simulated spectrum will point in the direction of construction of a greater fault

dimension and hence a larger earthquake.

In order for such a spectrum to exist, the equivalent time series signature, i.e: the simulated seismogram should contain, at least in part, a constructed low frequency content characteristic of a large earthquake motion. In other words our strategy in experimentation and in subsequent analysis will be in the following fashion:

- (a) Selecting small earthquake records known to have occurred in a common source region.
- (b) Grouping, phasing and summing, in the time domain, these small sources with the objective of constructing a large earthquake motion.
- (c) Transforming the individual records and final sum into the frequency domain.
- (d) Assessing the spectral properties of the results in the long and short period ranges (see Chapter 4).

Having established a physical basis for measuring the simulated source, we go on to explain the procedure involved in summation.

4.0.0 EXPERIMENTAL PROCEDURE:

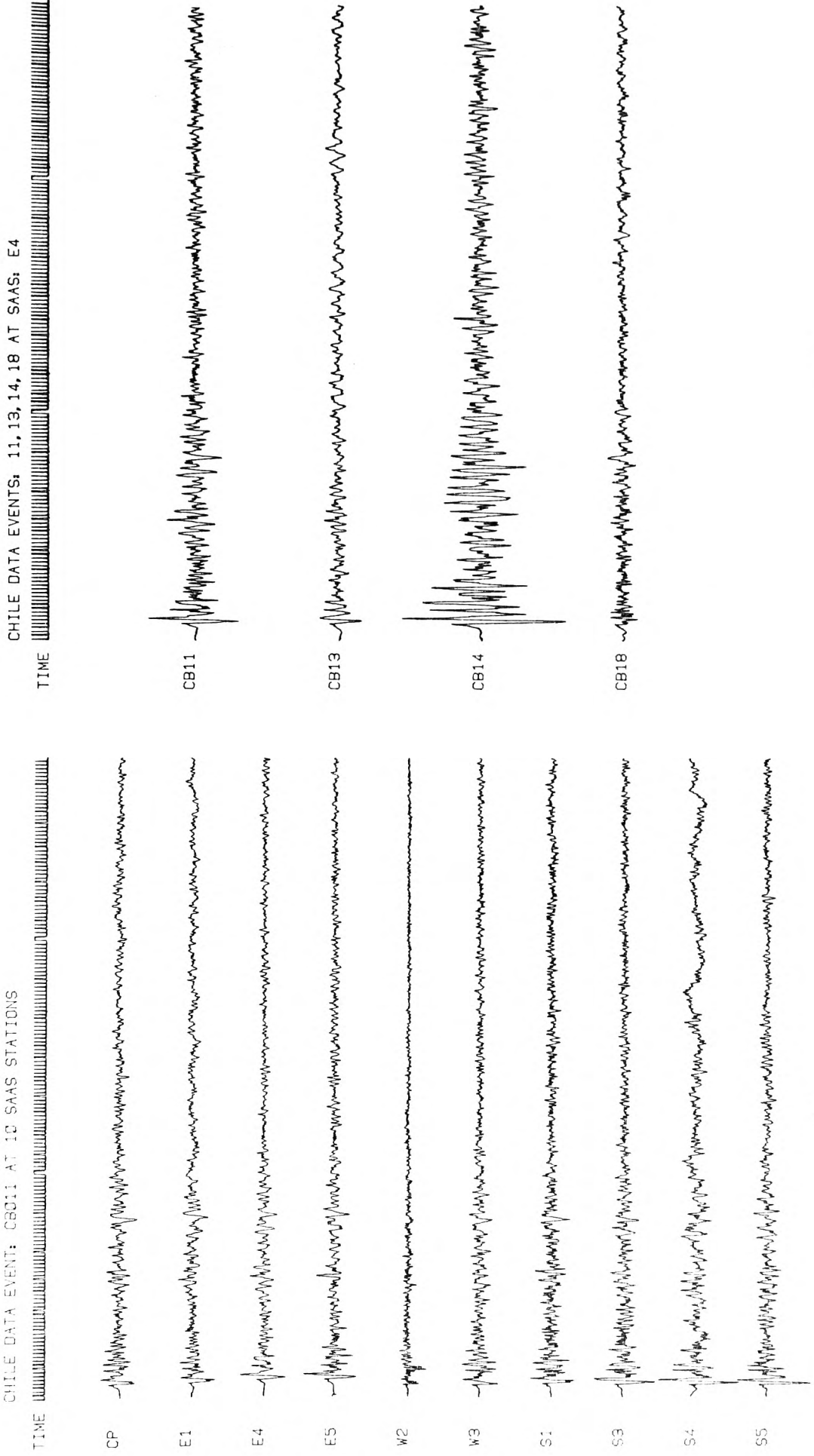
4.1.0 Preliminary Steps:

Before discussing the summation procedure involved and the program employed we need to identify certain aspects of direct relevance.

The first is the type of observation and hence the frequency content, sampling rate, and size of the earthquake files. This point was discussed and established for both data sets in Chapter 2.

Next is the number of station-event combination. In the near-field case, a single network station was used to monitor a population of local earthquakes. Therefore it falls in the category of a single station-multievent case (Section 4.5.2). For the Chile source, on the other hand, the receiver end was an array of stations recording teleseismic activity. Hence both single station-multievent case and multistation-single event case exist. In all cases and in order to create a file containing the Z/BL channels of the group of events or stations of interest we must select from each individual file the Z/BL trace and collate them with respect to a reference trace. A simple program was therefore written to perform this, which writes the output into a group file ready for summation. Figure 3.2 shows examples of such files.

Of course, the triggering mechanism represented by the sequence of sum, and hence the order in which channels are collated and aligned, will eventually depend on what we consider to be the most likely direction in which the assumed initial dislocation sweeps across the fault area. This matter is of cardinal importance in our thesis since it will ultimately determine whether we are on the right path to constructing a large source mechanism or not. To this end, we have devoted appropriate sections in Chapters 6 and 7 where we explain the reasoning behind selecting the triggering sequence in both



(A)

(B)

Fig. 3.2 EXAMPLES OF COLLATED FILES

source regions.

4.2.0 Beamforming:

The software used in phasing and summing the collated seismograms such as those shown in Figure 3.2 is an existing IGS program known as "BEAM". The logic is based on the principle of beamforming - a method well known to seismologists as an array processing technique. A useful review of this method with extensive references is given by Dahlman and Israelson (1977). Another authoritative reference on array processing is the AWRE Report on the Detection and Recognition of Underground Explosions published in 1965. The description below is mainly taken from the above two references.

Beamforming is an elementary method in which the records of an array are combined to give a seismogram with improved signal-to-noise ratio. If there are "n" seismometers, the signal "S" at each seismometer (assuming equal performance) is summed, after inserting appropriate time delays, to form an output of nS. At the same time, the noise "N" will be randomly phased and when added will produce an amplitude of $\sqrt{n}N$. Theoretically, therefore, there will be an enhancement of \sqrt{n} in the S/N ratio.

In practice, however, this theoretical gain is difficult to achieve, and the observed gain is usually several dB's below the value of \sqrt{n} (Green et al, 1965). The sum is referred to as the "beam" since the time delays are introduced in such a way that the output is focused or "beamed" in almost any direction with respect to a point on the earth's surface.

If a seismic wave is travelling along the array it will reach each seismometer with a time delay governed by the ground velocity, the velocity in the horizontal plane of the earth's surface, and by the seismometer spacing. A line of seismometers parallel to the wavefront of the required signal has the best azimuthal resolution, and has the advantage that the outputs can be added directly without introducing time delays. On the other hand, it has no power to discriminate between signals of the correct azimuth but different velocity. Conversely, a line array which is parallel to the direction of propagation has maximum velocity discrimination but poor azimuthal resolution. To get good azimuth and velocity discrimination for any azimuth, cross array configurations are used. The total summed response for a cross array has a relatively poor azimuthal response, whilst the velocity response is poor for azimuths which are close to the normal to either line array.

It is common practice to describe a beamed seismic wave by its horizontal wave-number vector \vec{k} . This characterizes the direction of approach (azimuth) and the wavelength of the seismic wave of interest (Kelly, 1964). For a given array configuration the separation capability or total summed response can be mapped as a function of \vec{k} , resulting in a representation called the "beam-pattern" (see for example Capon, 1971). The array has its maximum gain at the origin of this pattern which corresponds to the \vec{k} value at which the signal is phased. This central maximum is called the "main-lobe". Effective signal enhancement and separation is achieved in the \vec{k} -plane when the central lobe is sharp and

well separated from the secondary maxima or "side-lobes".

4.3.0 "BEAM" and Input Parameters:

The summing and delay aspects of BEAM as well as the program's simplicity, flexibility and speed were the outstanding features of interest. This in addition to the program's capacity to run on the PDP 11/50 made it ideal for our use in experimentation.

BEAM (listed in Appendix A) reads-in the records as a sequence of frames, forms a delay table from a pre-determined range of azimuth (Az) and apparent velocity (AV), sums, averages (optional) and writes the result into a file which can be plotted. Provision is made for 16 different combinations of Az and AV. Therefore, BEAM can be re-run with a narrower range of parameters around the values of the previous run, until resolution is optimized and the S/N ratio is no longer improved.

In addition to Az and AV, the program requires station coordinates in the case of the same event at different stations or event locations when summing various events at one station. The program then calculates the distances and azimuths of the input with respect to the reference trace.

It transpires therefore that the most important input parameters are Az and AV and prior knowledge of their approximate values is required. In Chapters 6 and 7 we explain how these were obtained for both data sets.

4.4.0 Testing "BEAM":

To investigate how BEAM works we input a 1 Hz sine wave and

assume it arrives at a line array with normal incidence. Because of this and because the waveform is a constant amplitude frequency sinusoid, there will be no path differences and hence the AV parameter will be the same. However variation of Az will affect the total sum. Figure 3.3a illustrates the output when the waves arrive from North to South at azimuthal increments of 45° . As expected, maximum construction occurs when the waves arrive normal to the array. Figure 3.3b shows a narrower range of azimuths at steps of 15° through to 90° . Here the lags formed by the program are evident as a D.C. line preceding the onsets, and increasing as Az approaches 90° . It is interesting to note that despite the lag, almost complete destructive interference occurs at 60° . This is because 2/3 of the traces are out-of-phase while at 30° , 2/3 are in-phase. This exercise, although on artificial data, nevertheless demonstrates that "BEAM" does delay and sum.

4.5.0 Application to Real Data and Discussion:

Perhaps, BEAM can best be illustrated by giving examples of runs on actual earthquake records. For this purpose we chose groups of station-event combinations from Chile because they not only offer a wider range of combinations, but also their seismograms show body as well as surface wave phases.

Note that since the S and LQ phases are less obvious than P, their expected arrivals are marked on the seismogram. The broad pips on the time channel refer to minute marks.

4.5.1 Single-Event-Multistation Case:

SINE WAVE (AZ=0-180 AT 45)

TIME _____



(A)

SINE WAVE (AZ=0-90 AT 15)

TIME _____



(B)

Fig. 3.3 SINE WAVE OUTPUT FROM "BEAM"

This is illustrated by experimenting on CB014 at 10 SAAS stations shown in Figure 3.4. In the first instance we fix $AV = 10\text{km/s}$ and change Az . Figure 3.5a shows a run for 8 major directions at steps of 45° . Here we notice that at 270° the main P-phases are rather impressive and are well above noise. A smaller range is therefore selected around this value to observe further. Figure 3.5b shows this. Here it is difficult to decipher significant changes in amplitude or coherency of the P-arrivals. Therefore a range of Az between 250-290 seems adequate. In fact the calculated azimuth is around 253 and hence is considered appropriate.

Fixing this azimuth value, we next take a range of AV between 6-12km/s. This is illustrated in Figure 3.6a where, for that part of the seismogram a good fit seems to be around $AV = 10-12\text{km/s}$. This agreed well with published P-phase velocities around the 20° -discontinuity (see Chapter 6).

For the same azimuth the program is re-run between $Az = 2-7$ km/s to investigate the shear and surface waves (Fig. 3.6b). A more closer range of 5-7km/s at 0.5 increments is shown in Figure 3.7a. Here the S onset looks like beginning to emerge at about 5.5km/s. A similar situation is evident for the surface waves at around 4km/s (Fig. 3.7b).

An essential requirement in our experimental procedure is to observe a build-up in amplitude as summation progresses. This aspect is demonstrated to a certain extent by Figure 3.8. Here we see the sums of 2, 4, 6, 8, and 10 stations plotted to the same scale. The top trace is CB014 at CP. In this case the averaging option of BEAM is disactivated and an $AV = 10\text{km/s}$ is

CHILE DATA EVENT: CB014 AT 10 SAAS STATIONS

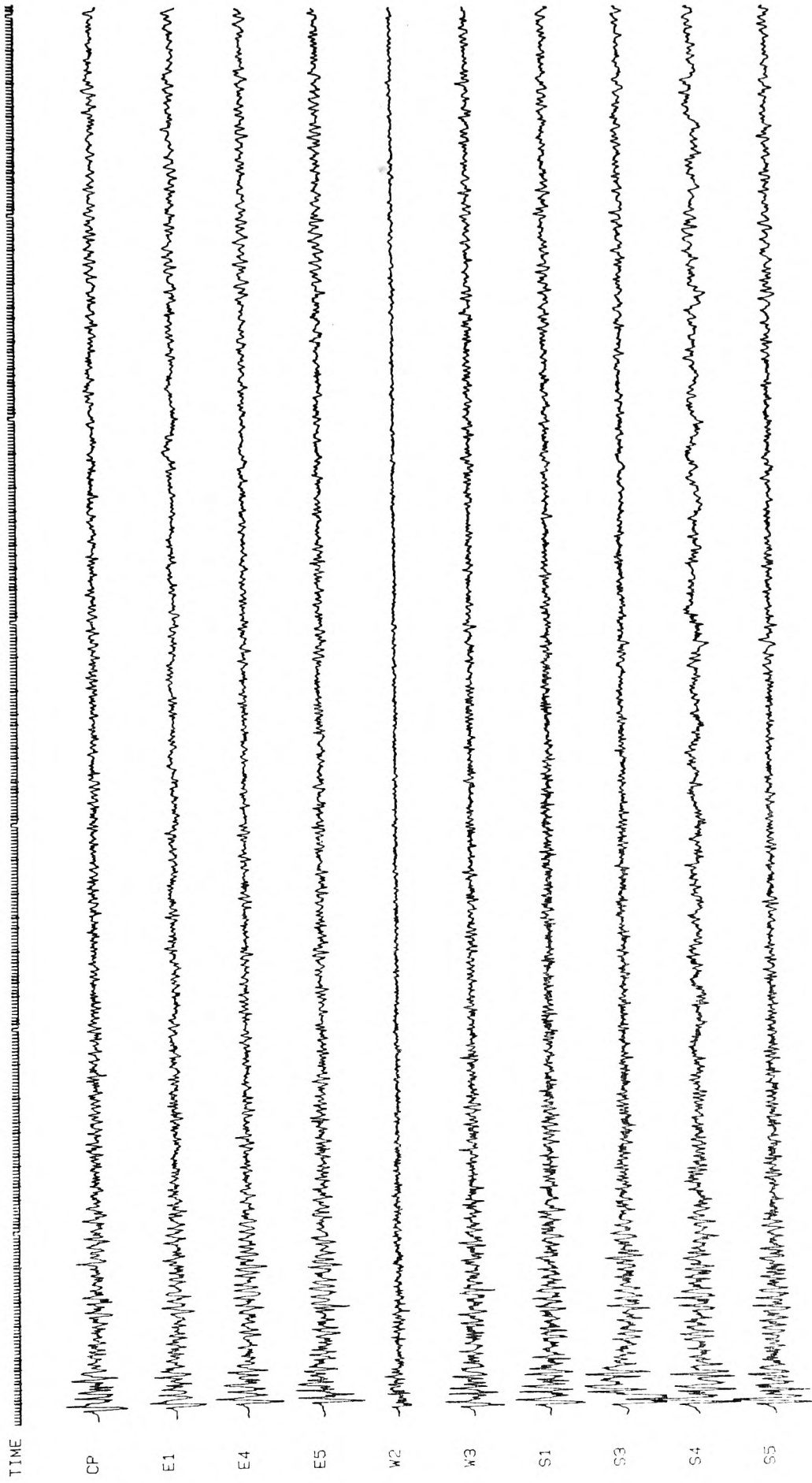
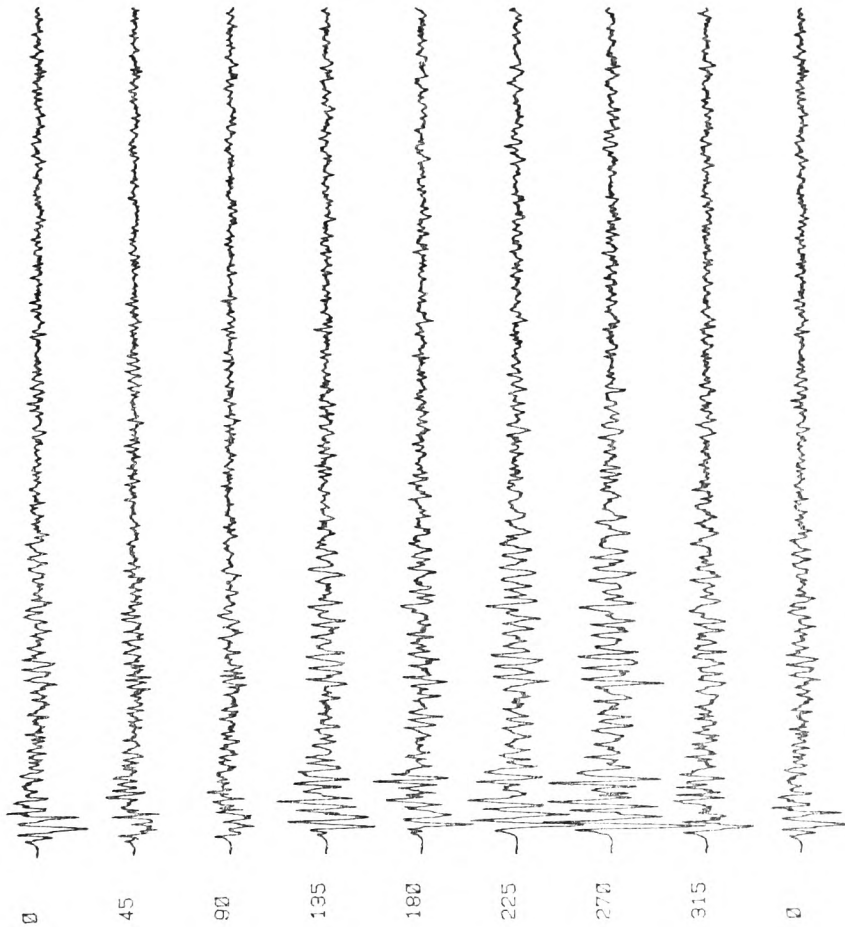


Fig. 3.4 SINGLE EVENT AT 10 ARRAY STATIONS READY FOR "BEAM"

CB014 - SUM OF 10 STATIONS AT 8 AZIMUTHS (A. V=10 KM/S)

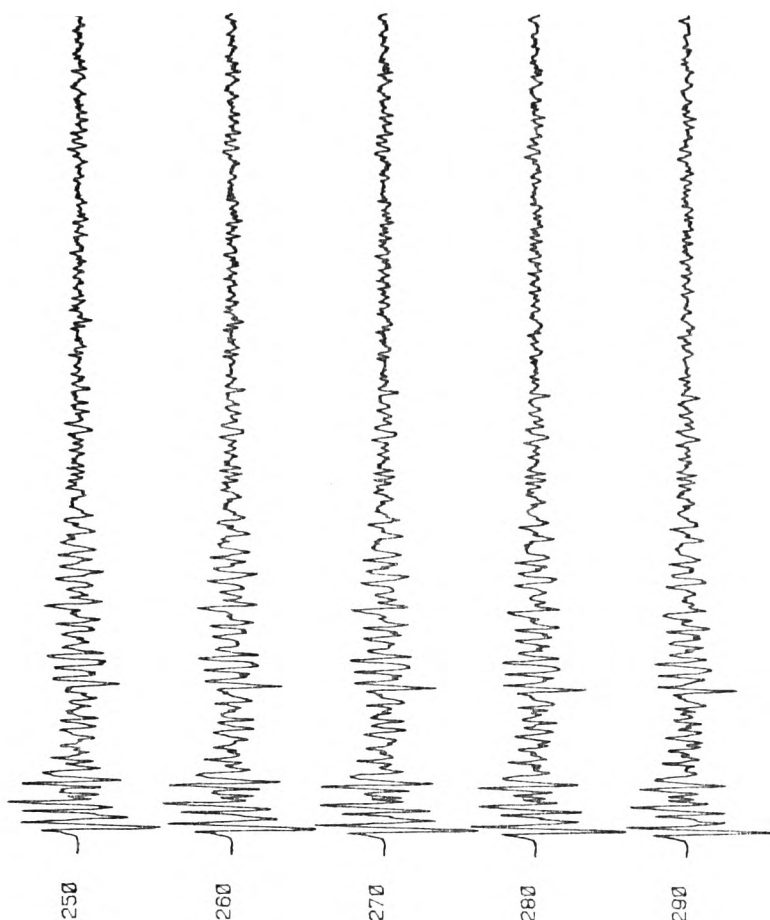
TIME



(A)

CB014 - SUM OF 10 STATIONS AT 5 AZIMUTHS (A. V=10 KM/S)

TIME

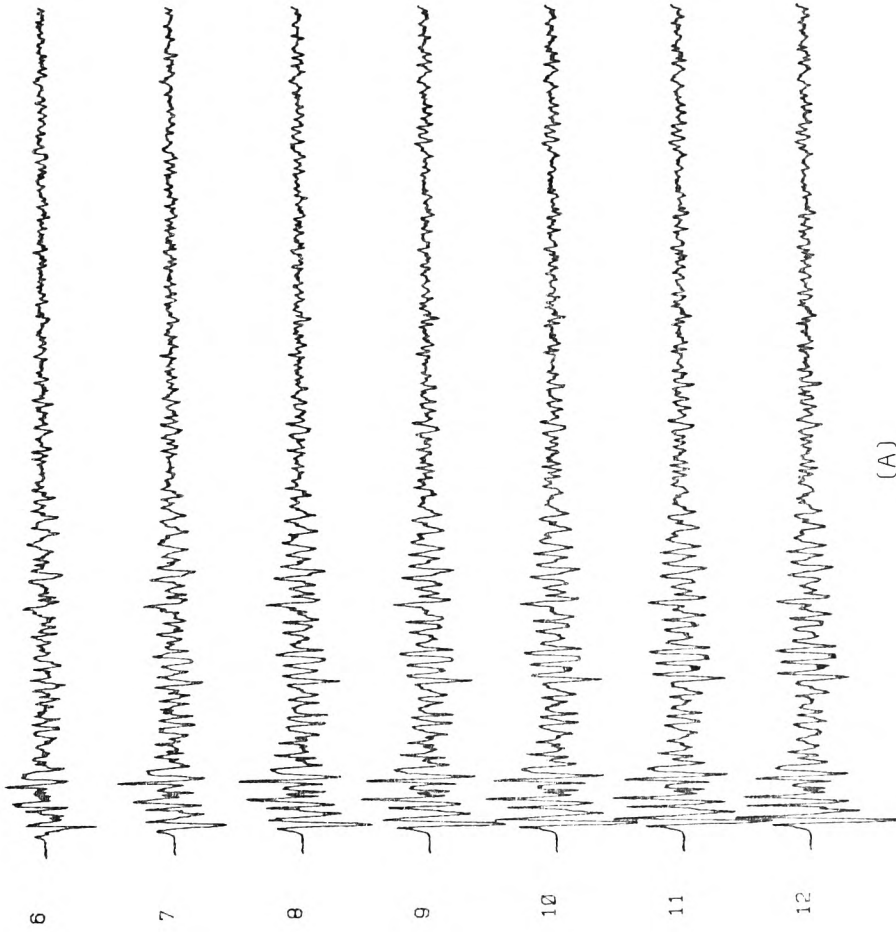


(B)

Fig. 3.5 SINGLE EVENT SUM AT DIFFERENT AZIMUTHS SHOWING P-PHASES

CB014 - SUM OF 10 STATIONS AT A. V=6-12 KM/S (AZ=253)

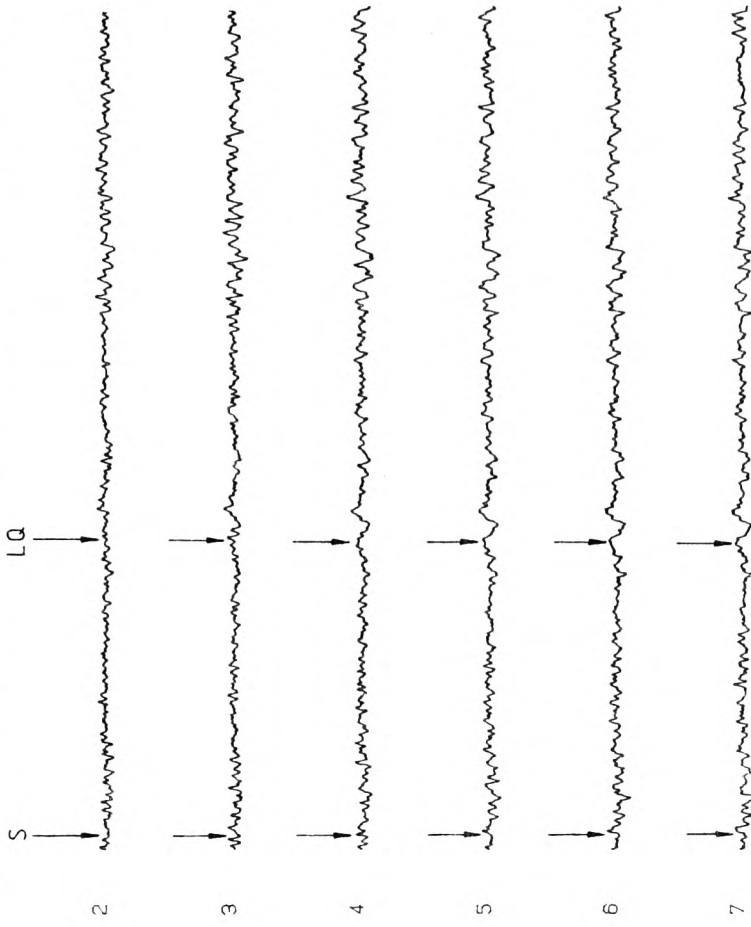
TIME



(A)

CB014 - SUM OF 10 STATIONS AT A. V=2-7 KM/S (AZ=253)

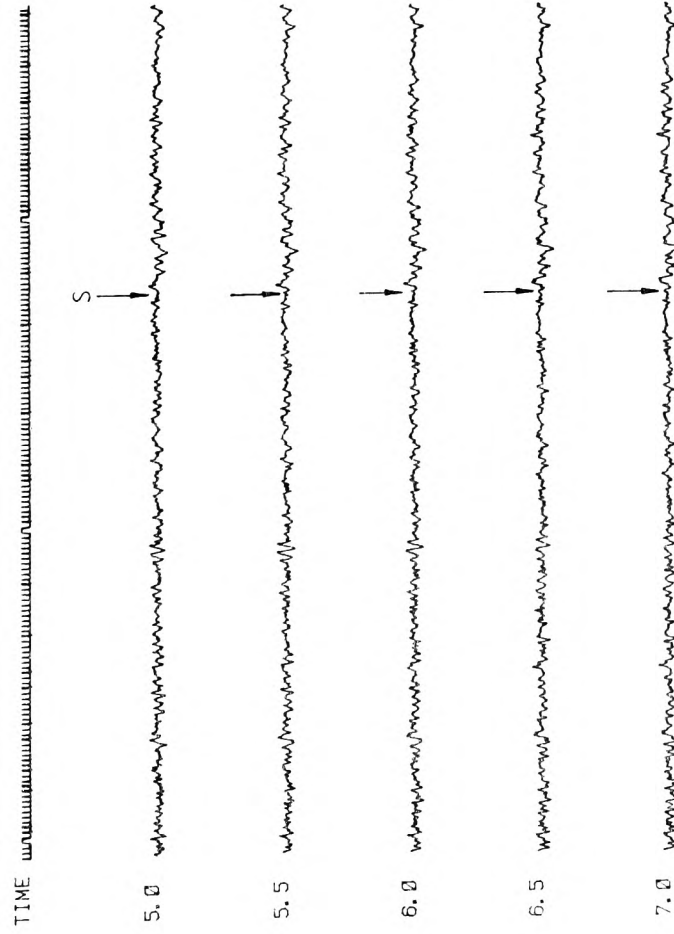
TIME



(B)

Fig. 3.6 SINGLE EVENT SUM AT DIFFERENT VELOCITIES SHOWING P, S, AND LQ

CB014 - SUM OF 10 STATIONS AT A. V=5-7 KM/S (AZ=253)



CB014 - SUM OF 10 STATIONS AT A. V=2.5-4.5 KM/S (AZ=253)

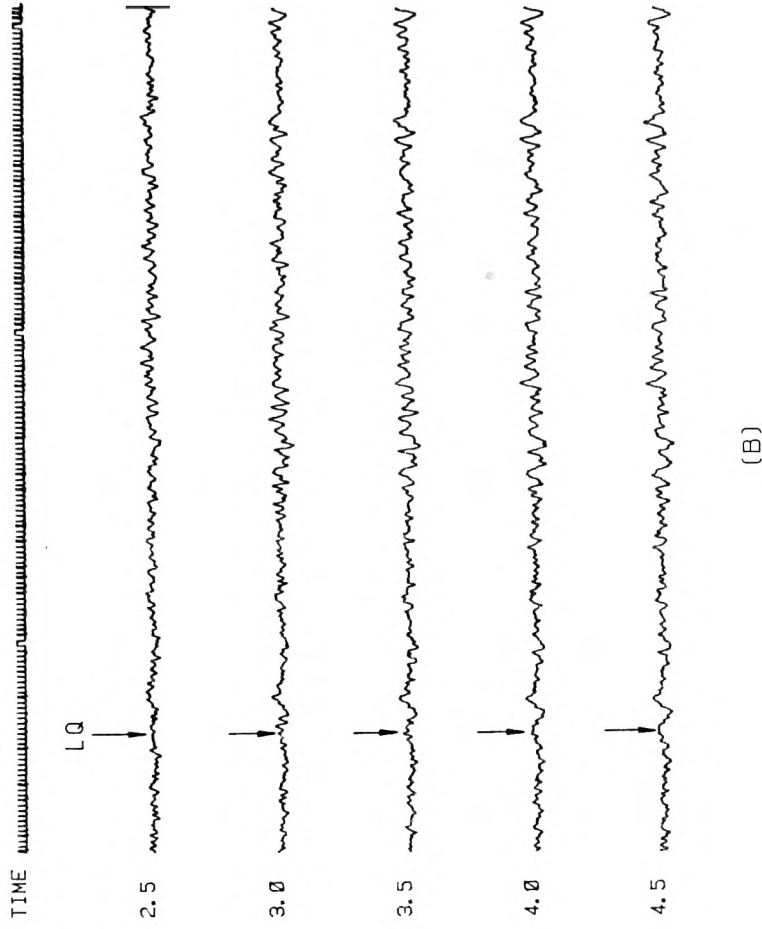


Fig. 3.7 SINGLE EVENT SUM SHOWING S AND LQ PHASES

CB014 - SUM OF 2, 4, 6, 8, 10 STATIONS SUCCESSIVELY (AZ=253/A. V=10 KM/S)

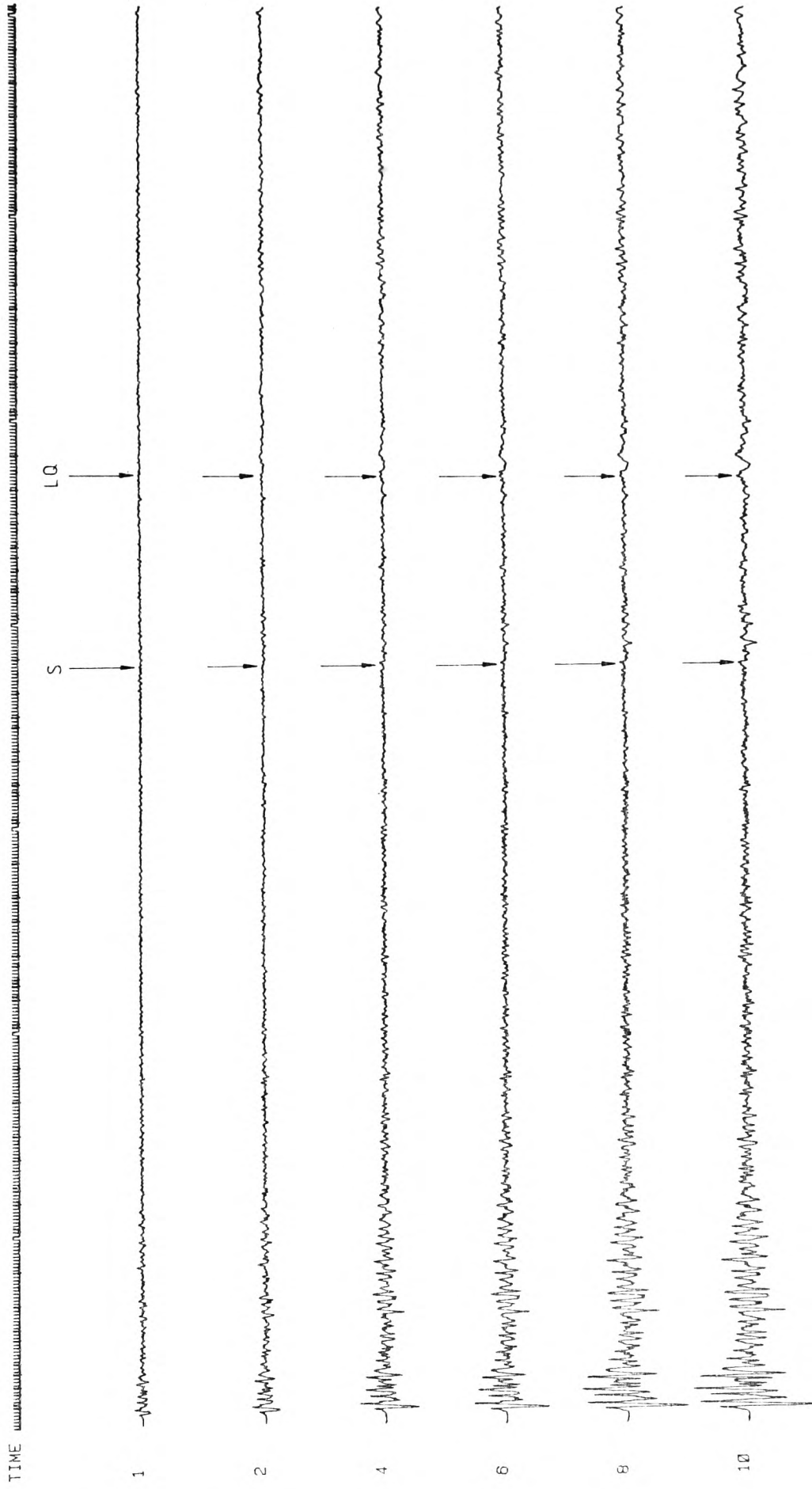


Fig. 3.8 SINGLE EVENT SUM SHOWING AMPLITUDE BUILD-UP

selected. It is quite obvious that there is considerable difference in size between the top and bottom traces with the P-phases 6 times as large in the final sum. This is expected since we phased on AV around the P-phases. More remarkable, however, seems to be the longer periods where from the sum of 4 to 10 traces, the S- and LQ-phases enhance about 4-5 times while the P amplitude is only doubled. This is in general support of the concept that long periods approximately construct according to "n" whereas shorter periods enhance in proportion to " \sqrt{n} ". Of course a similar sum at AV around S and LQ should reveal this fact more clearly especially for larger magnitude earthquakes (see Chapter 6).

4.5.2 Single-Station-Multievent Case:

To demonstrate the situation where a number of events are to be summed at the same station, we collate 4 of the Chile events viz: CB011, CB013, CB014 and CB018 at S5 according to their time of occurrence as shown in Figure 3.2. Here, the reference seismogram is that of CB011 and the input station file is that of the locations of the above events in the same order. This is, in a sense, the reverse procedure since the station will now resemble a virtual source observed from the earthquake epicenters for which the sum is to be performed. It immediately follows from this that the azimuth of the reference trace will be in the first quadrant rather than in the third. Az for CB011 at S5 is about 73° . As in the previous case, we fix this value of Az and change AV. Figure 3.9a shows the sum of these events at a range of 6-12km/s. The result, as expected is more or less similar to the previous case at the same range of

velocities (Fig. 3.6a). This is because the earthquakes originate from a similar source and hence share a similar travel path.

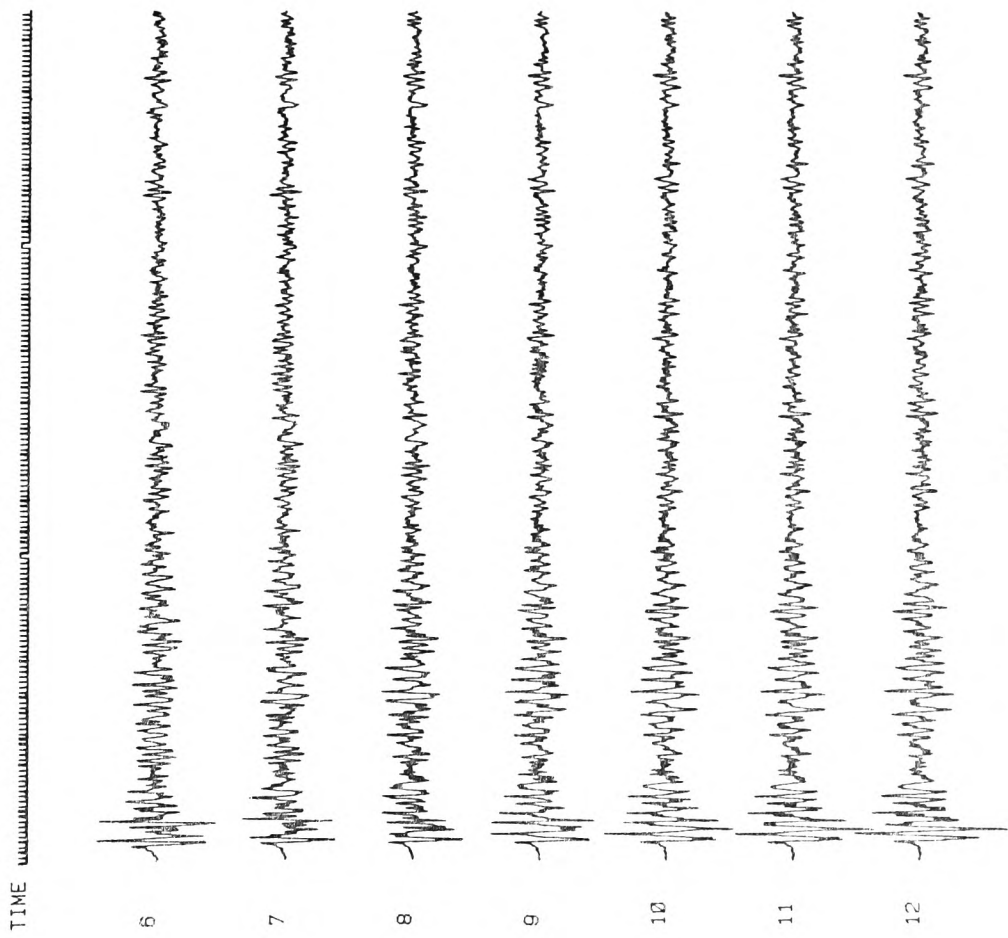
Figures 3.9a, 3.10a and b have the same input AV's to those in Figures 3.6b, 3.7a and b. In all of these figures it is difficult to recognize significant enhancement of the S- and LQ-phases. Perhaps around 6.5km/s (Fig. 3.10a) S is more coherent, although this is doubtful. Similarly the LQ-phase in Figure 3.10b seems to be drowned in noise.

Figure 3.11 is a plot, on the same scale, of the 4 events with their sum at 10km/s. Here, the picture is perhaps slightly more encouraging with the S and LQ barely above noise. The sum in fact resembles CB014.

In the context of our methodology, there is a simple and straightforward answer to this unimpressive result. Firstly there is a deficient number of earthquake records. Secondly these events vary in size as evidenced by the dynamic range of their maximum amplitude P-arrival. Consequently the contribution of each seismogram to the total sum will depend on its weight. Therefore the largest will carry the biggest weight. Thirdly, and a point well worth mentioning here is the fact that this sequence of sum does not give the best fit. Furthermore, there is the possibility of slight differences in focal mechanism between the shocks although this is unlikely from Figure 3.11 and from the solutions given in Chapter 6.

It transpires, therefore, that the main contributing factors to an effective and significant overall result is earthquake quantity, size and more importantly triggering sequence. All

EVENTS: 11, 13, 14, 18 AT SAAS, S5 A. V=6-12 KM/S (AZ=73.0)



EVENTS: 11, 13, 14, 18 AT SAAS, S5 A. V=2-7 KM/S (AZ=73)

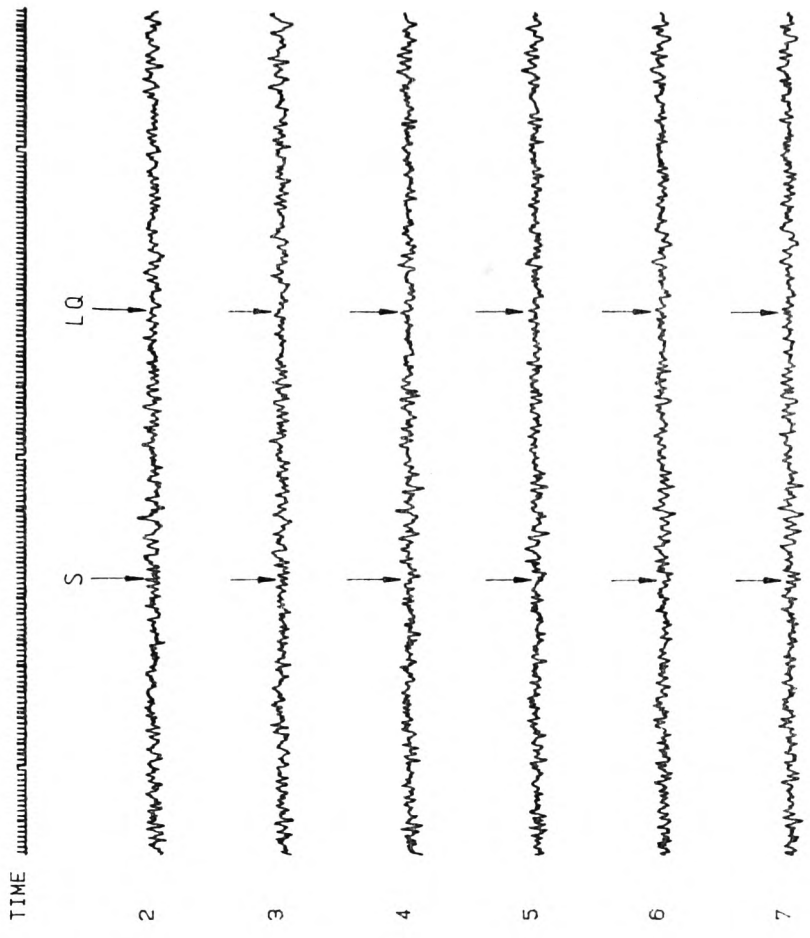


Fig. 3.9 MULTIPLE EVENT SUM AT DIFFERENT VELOCITIES SHOWING P, S, AND LQ PHASES

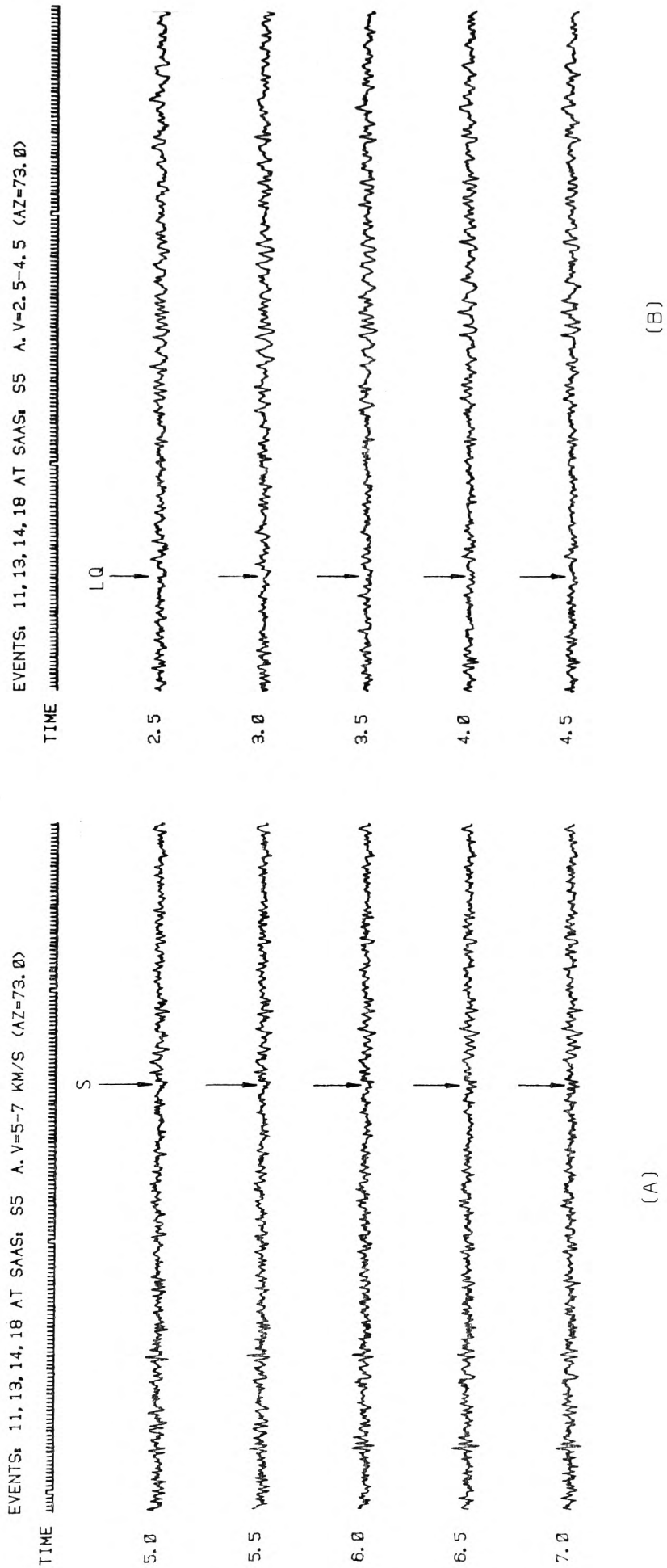


Fig. 3.10 MULTIPLE EVENT SUM SHOWING S AND LQ PHASES

EVENTS: 11, 13, 14, 18 AND THEIR SUM AT SAAS: S5 (AZ=73/A. V=10 KM/S)

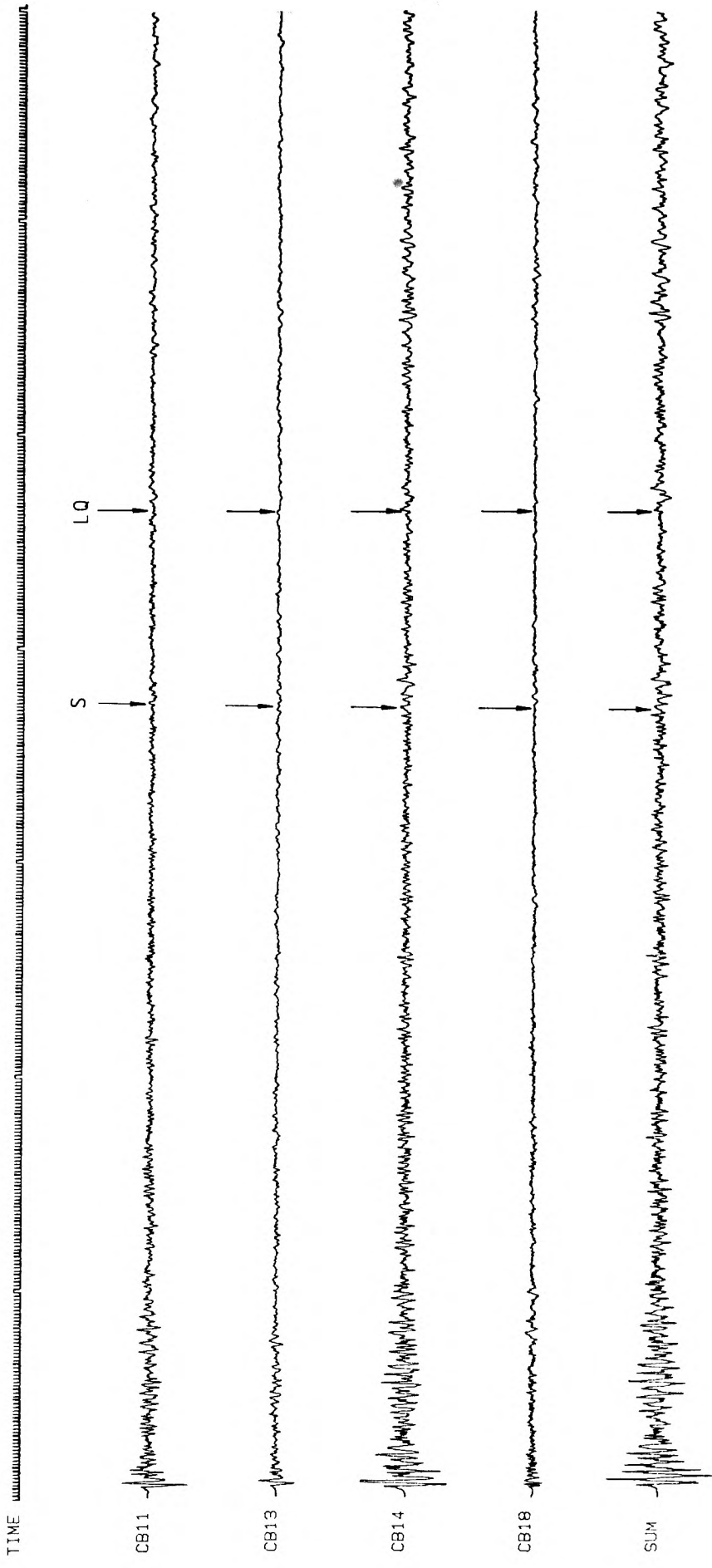


Fig. 3.11 MULTIPLE EVENT SUM SHOWING AMPLITUDE BUILD-UP

three factors are dealt with in more detail in Chapters 6 and 7.

5.0.0 INCOMPLETENESS OF EARTHQUAKE SAMPLES:

The subject of incompleteness of earthquake sample, as will be seen in later chapters is a major set back that influenced our results. In the original statement of the project it was suggested that in order to fill the focal region of a large earthquake source with enough small earthquake samples, it would be useful to design and implement a method whereby the records of 2 small events could be conveniently "stretched" or "compressed" to produce a synthetic interpolation which would simulate the record of an event occurring on the line joining the 2 primary foci. In such a way it would be possible to generate populations of small earthquakes to fill the triangular plane defined by 3 primary foci, or the tetrahedral volume bounded by 4 foci.

During our research, however, it was not possible to pursue this suggestion mainly because of our involvement in the search for real data sets. We, therefore, believe that this particular topic merits a separate research effort directed entirely towards generating hybrid records from actual earthquake seismograms.

CHAPTER 4
ANALYSIS TECHNIQUES

1.0.0 INTRODUCTION:

In the previous two chapters and under the general topic of data handling and treatment we covered the areas of data processing and experimental procedure. What remains to discuss is how these data were analysed and presented. This is the subject matter of the present chapter.

In Section 3.3.0 of Chapter 3 we explained that in order to assess a simulated large earthquake record we need to transform from time to frequency with the object of examining the properties of the constructed seismic spectrum. To achieve this we use the well know Fourier method. This topic amongst others is discussed in the first section of the chapter under the general title of Spectral Analysis.

Next we investigate the seismic spectrum and explain the concept of corner frequency in more detail pointing out the differences between theoretical and real spectra.

A description of the software used to analyse the data is next discussed with examples. This is followed by a discussion of the cubic spline approximation to smooth the seismic spectra, how it was applied and how it compares with the original spectrum. The chapter is concluded with examples of some important features encountered on the seismogram as they were reflected in the frequency domain.

2.0.0 SPECTRAL ANALYSIS:

2.1.0 The Seismic Signal:

A seismic signal generated by an energy source (earthquake or

explosion) has been classified as a transient signal due to the limited action of the source in space and time. The seismogram is one such representation in which the space parameter is kept constant and the wave field is fully defined by its time variable. Such a function has the form: $f(t)$; where f is amplitude, power, ..etc. and t is time. Thus all the information describing the seismic disturbance is contained in a seismic record.

Since the seismic signal is a physical phenomenon which fluctuates in time and/or space, the rate of fluctuation or the frequency becomes an important parameter in defining the function and a more significant independent variable to use than time. Spectral analysis is therefore the process of transforming the seismogram content into the frequency domain resulting in a representation called the spectrum. One major advantage of spectra over pure time measurements is that the whole waveform (which in discrete form should contain a range of frequencies up to the Nyquist) is utilized in the analysis whereas in the time domain, the readings are point measurements.

2.2.0 The Spectrum:

A spectrum is a (statistical quantity with a definite) mathematical expression, derived from time or space functions by certain transformations. In general it is a complex function which may be represented by the following two forms:

(a) Sum of real and imaginary parts:

$$F(\omega) = a(\omega) - ib(\omega)$$

(b) Product of real and complex parts:

$$F(\omega) = |F(\omega)|e^{i\phi(\omega)}$$

$$\text{where } |F(\omega)| = [a^2(\omega) + b^2(\omega)]^{\frac{1}{2}}$$

$$\phi(\omega) = \tan^{-1} [-b(\omega)/a(\omega)] + 2\pi n$$

$$n = 0, \pm 1, \pm 2, \dots$$

$$\omega = \text{angular frequency} = 2\pi\nu \text{ (radians/s)}$$

$$\nu = \text{cyclic frequency (Hz)}$$

In the above expressions, $F(\omega)$ is the spectrum. If $a(\omega)$ and $b(\omega)$ are amplitudes, then $|F(\omega)|$ is the amplitude spectrum and $\phi(\omega)$ is the corresponding phase spectrum. This representation is termed one-dimensional spectral or Fourier analysis since there is only one independent variable ω (Fig. 4.1). Throughout the analysis, we will concentrate on this one-dimensional representation.

2.3.0 Fourier Analysis:

Most investigators will no doubt be acquainted with Fourier Analysis methods and their application to geophysical research. Some excellent and most authoritative textbooks have been published on this subject and the reader is referred to those by Robinson (1967), Beauchamp (1973), Bath (1974), Childers and Durling (1975), and Kanasewich (1975). We therefore confine ourselves to outlining some essential relationships expressing the basics of Fourier theory.

The Fourier spectrum, mentioned in the previous section, is obtained by transforming real time $f(t)$ to a complex function

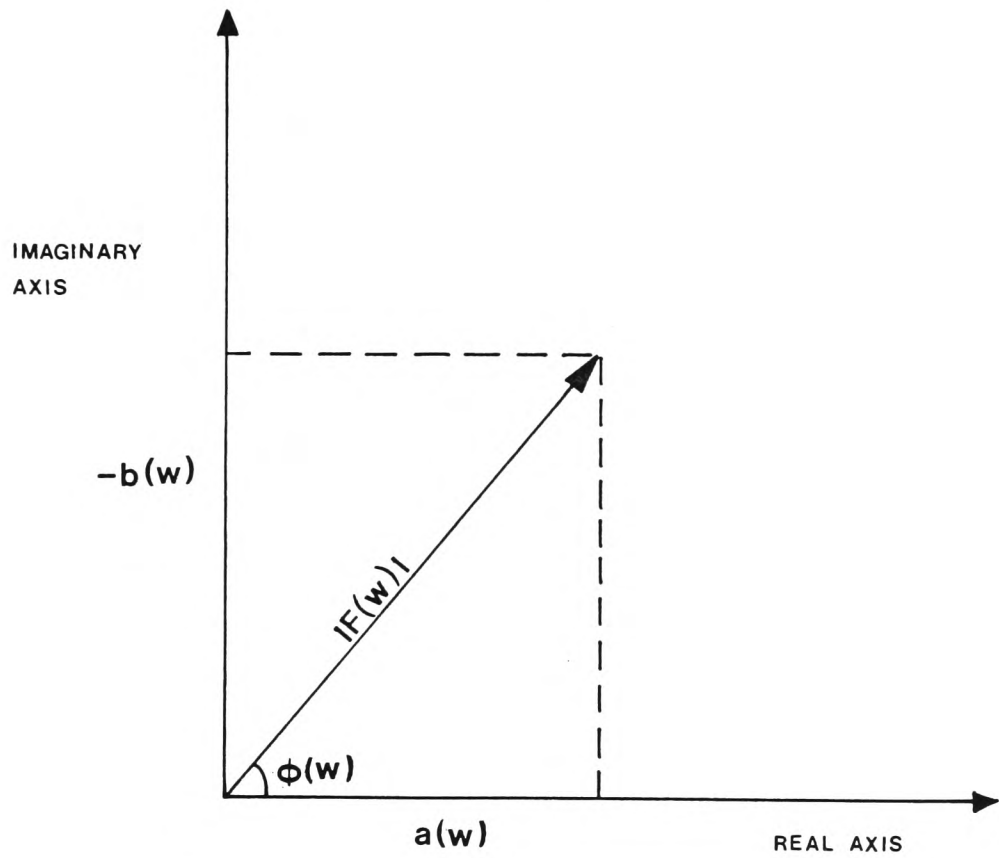


FIG (4.1) SCHEMATIC REPRESENTATION OF THE SPECTRUM
(AFTER BÅTH , 1974)

$F(\omega)$ through the Fourier transform:

$$F(\omega) = \int_{-\infty}^{+\infty} f(t)e^{-i\omega t} dt \quad (4.1)$$

$f(t)$ and $F(\omega)$ form a Fourier pair denoted by:

$$f(t) \leftrightarrow F(\omega)$$

so that the inverse transform is given by:

$$f(t) = \frac{1}{2\pi} \int_{-\infty}^{+\infty} F(\omega)e^{i\omega t} d\omega \quad (4.2)$$

Equation (4.1) expresses the Fourier Analysis of $f(t)$ while (4.2) represents the Fourier synthesis of $f(t)$. These formulas are valid for any kind of functions $f(t)$ and $F(\omega)$: real; imaginary; complex; even; odd or combinations thereof, provided they satisfy Dirichlet's conditions.

Since the Fourier method permits the representation of a large class of functions by superposition of sine and cosine and by virtue of the orthogonal properties of these trigonometric functions, the factor $e^{-i\omega t}$ in equation (4.1) acts as an operator selecting from $f(t)$ only components with frequency ω . In other words $F(\omega)$ is an average of those components of $f(t)$ over the interval of integration. In observational data this interval is limited in extent and it may be appropriate to replace the limits of integration of equation (4.1) to cover the range $-\frac{T}{2} < t < \frac{T}{2}$, where $T=2\pi$ is the fundamental period or lowest frequency. This transform is called the finite Fourier transform.

From a dimensional point of view, $F(\omega)$ has the same dimensions as $f(t)$, and the resulting amplitude spectrum is known as the

amplitude spectral density (A.S.D.) since $F(\omega)$ is referred to unit time interval. For example the dimensions of ASD for a velocity record (microns/s) will be in microns.

2.4.0 Limits of Spectra and Contamination:

Since observational data have a finite length the fundamental frequency in the spectrum is the reciprocal of record length. Therefore the longer the record, the greater is the spectral resolution, i.e: the smaller the interval between successive frequencies. At the other end of the spectrum, the upper frequency limit is defined by the sampling interval Δt . This frequency is referred to as the folding or Nyquist frequency ν_N and is equal to $1/2\Delta t$. If the seismic record contains frequencies higher than ν_N aliasing occurs and the spectrum is contaminated.

In Section 4.4.0 of Chapter 2, we established ν_N for the Rabaul and Chile data sets to be 15 and 5 Hz respectively. It will be seen later in the chapter that the former limit was generally adequate while ν_N for the Chile data was somewhat insufficient causing contamination of some earthquake spectra.

2.5.0 Discretization and the Fast Fourier Transform:

The formulae given in Section 2.3.0 only apply to continuous functions and cannot be used in discrete form. This effectively means converting a continuous integral, for finite intervals, into a summation of discrete ordinates expressing the area under the curve. Among different quadrature rules

for evaluating discrete formulas, the trapezoidal is recommended since in summation all terms have the same weight (=1) while the first and last terms have half weight.

In discrete form, equation (4.1), therefore, becomes:

$$F(\omega) = \int_{-\infty}^{+\infty} f(t)e^{-i\omega t} dt \rightarrow \frac{1}{N} \sum_{n=1}^N f(t_n)e^{-i\omega t_n} \quad (4.3)$$

A better form adapted to the discrete case is:

$$F(n) = \frac{1}{N} \sum_{v=1}^N f(v)e^{-i(2\pi n/N)v} \quad (4.4)$$

Equation (4.4) is the discrete Fourier transform (DFT), where the given time series is $f(1), f(2), \dots, f(N)$.

A more computationally efficient algorithm based on the DFT is the Fast Fourier Transform or FFT. This method of spectral calculation was first introduced by Cooley and Tukey (1965) and is sometimes known as the Cooley-Tukey algorithm.

The FFT is based on the principle that the Fourier transform of a discrete time series is calculated from the transforms of two partial series through a recursive procedure. This is done by first splitting a digital record of N observations into 2 parts; one comprising all odd digits; the other all even digits. If N is even the transforms of the two partial series is performed. In the next recursion if $N/2$ is even, the two partial series are each split inturn into 2 parts and the transform calculated for each one. This process is continued until the Fourier transform equals the reading itself. At that point the algorithm would have effectively performed the transform on N records each consisting of 1 point.

The condition that N should be even may be satisfied by selecting a number of digits such that:

$$N = 2^k$$

where k = positive integer

Therefore 2^{12} observations is a record length of 4096 points.

The most outstanding feature of this method is speed and accuracy, hence the amount of time and storage saved on the computer.

In all our spectral analyses, we made use of the FFT in the form of subroutine "COOL". A description of the relevant program, input parameters and examples of output are given later in the chapter.

Having familiarized ourselves with the basic formulas, and qualifiable criteria of the FFT, we turn to discussing practical and observational aspects of seismic spectra.

3.0.0 PRACTICAL CONSIDERATIONS

3.1.0 Difference Between Theoretical and Observed Spectra:

In general, seismic spectra are used for comparison purposes, i.e: comparing amplitudes at different frequencies or amplitudes at a given frequency in different data sets or both. In Section 2.4.0 of Chapter 3 we pointed out the fundamental elements defining a seismic spectrum, schematically shown in Figure 3.1. The general shape in the figure represents the transform of a theoretically calculated far-field displacement pulse generated by a dislocation at a specified

rupture velocity. This approximation to the seismic spectrum is vastly oversimplified. What is actually observed on the seismogram is a complex superposition of real seismic waves representing the fracture mechanism of the source and reflecting the path properties. The resulting spectrum would, therefore be complicated and rarely smooth, although its gross shape is similar to theoretical approximations. This general agreement in spectral shape between theory and observation is paramount to our thesis and forms the very basis of our assessments (see Section 3.0.0, Chapter 3).

Since our analyses involved complete seismograms rather than solitary phases, the spectra are considerably irregular. This irregularity which is primarily due to the interference between various arrivals is usually referred to as spectral "scalloping" (Johnson & McEvilly, 1974). The spiky character, therefore, makes it rather difficult to estimate spectral parameters like Ω_0 and ω_c despite the high resolution due to the inclusion of the whole earthquake record. This problem, as will be shown later is overcome by applying a smoothing procedure.

Another important consideration is that analysis of the whole seismogram has the advantage of minimizing truncation effects which could severely distort the shape of the spectrum (see Fig. 4.16). For this reason all the earthquake spectra in this research were computed from whole records with no attempt to isolate individual wave arrivals.

3.2.0 Choice of Spectral Scales:

To illustrate the general shape of the seismic spectrum with

emphasis on low frequencies we need to represent the spectral curve on abscissae that show high resolution in the low-frequency range and lower resolution in the high-frequency range. Logarithmic scales satisfy this criterion. As a consequence, longer periods are better indicated on log plots than on linear plots. This is why seismic spectra are plotted on log-log scales with the resulting shape of a "Butterworth Low-Pass Response" (Fig. 3.1). Later on in the chapter we illustrate the choice of spectral scales by giving examples.

3.3.0 P- vs S- Corner Frequency:

Recent investigations on earthquake source theory differ markedly in their predictions of ω_{cp} and ω_{cs} (subscripts cp and cs refer to P- and S- corner frequencies respectively). In most of these studies the predicted ratio of ω_{cp}/ω_{cs} amounts to a factor of 2 or more (Brune, 1970; Hanks & Wyss, 1972; Molnar et al, 1973; Sato and Hirasawa, 1973; Burridge, 1975; Madariaga, 1976). In contrast Savage (1974) and Dahlen (1974) find higher ω_{cs} than ω_{cp} by a ratio of 1.65 and 2.38 respectively.

Using his kinematical fault model, Dahlen (1974) suggests that the most obvious factor causing the predicted corner frequencies to be opposite to those of the observed spectra is due to the effect of wave scattering by inhomogenities along crustal paths. This phenomenon, in general, should tend to enrich the P-wave coda with higher frequencies relative to the S-wave coda thus resulting in higher ω_{cp} and ω_{cs} .

Savage (1974) explains this differently. He suggests that

this apparent discrepancy between predicted and observed corner frequencies is due to the fact that theoretical studies identify the true asymptotic trend in the spectra whereas observations do not extend to sufficiently high frequency range to identify this trend. This is because the bandwidth of recorded seismic waves is limited by instrumental response and background noise. As a result the observed ω_{cs} is often based on a spurious high frequency trend with the consequence of ω_{cs} being picked at too low a frequency.

Here we disagree with Savage's explanation for the simple reason that our observations, especially for distant sources, extend to frequencies above ω_{cs} . Therefore, we advocate that the loss of information of S-waves is probably due to attenuation along the travel path rather than lack of recorded bandwidth.

Peppin and Simila (1976) give a useful review of most of the above mentioned papers, in addition to pointing out that ω_{cp}/ω_{cs} may be a significant source model discriminant, its variation indicating that different models need to be applied to different source regions.

From the above, we conclude that the subject of ω_{cp} vs ω_{cs} and their ratios is still speculative and hence needs further investigation backed by much more observations. What is important, however, is the fact that a corner, whether ω_{cp} or ω_{cs} , is a measure of the width of the spectrum and is inversely proportional to fault dimension. In our analysis (see later sections), this is what we observe, i.e: a spectral shape generally similar to a "Butterworth Response" with a single

corner marking the change in trend between the Ω_0 level and the high frequency roll-off. It is, therefore, our strategy, in assessing a constructed source, to observe a tendency of this corner to move to longer periods with an accompanying build-up in Ω_0 in proportion to the number of summed records (see Section 3.2.0 of Chapter 3).

3.4.0 Source, Earth and Receiver Functions:

It is well known that an earthquake seismogram represents the convolution of the source, earth, and receiver functions. All these systems interact to attenuate or filter-out the original energy contained in an earthquake signal. Due to these effects, the seismogram will only carry part of the information released by the source.

During rupture the prevailing conditions at the source are highly non-linear and the details of the propagation pattern are extremely complex. However, due to its limited duration, the non-linear part of the disturbance rapidly decays to a level at which all further propagation is substantially and comparatively linear. For this reason and because very little is known about the details of the fracturing mechanism at its inception, the source function is assumed to be constant. This assumption seems to be reasonable and not critical especially when we take into consideration the fact that the best approximations so far, to the source, have been a linear ramp (Kanamori and Anderson, 1975) or a Heaviside unit step in time (Brune, 1973, 1976).

As far as the propagation path is concerned and since we are

analysing earthquake records believed to originate from a common source, its attenuation effect, especially in the far-field will be the same for earthquakes of all sizes. This means that we are effectively compensating for the path. Furthermore, according to our hypothesis, earthquakes originating from the same source, should carry similar spectral signature, whatever their mode of propagation. Such spectral signature will be contained in individual records and will be preserved in summation (See Chapter 3).

The transfer function of the receiver and its compensation is, however, important and must be considered. This is in fact taken care of, in the analogue stage, by the bass-lift instrument as explained in Chapter 2. Recalling our discussion on this topic and from Figure 2.5.0 we notice how the circuit effectively compensates for the roll-off of the Willmore MKII. The resulting Z/BL traces (see Figures 2.10 - 2.14) have greater resolution and clearer onsets than the Z/SP counterparts.

4.0.0 ANALYSIS SOFTWARE:

We have, thus far, outlined the basic theory behind our analysis procedure and discussed some important practical considerations. What remains is to explain the software used in analysis with some examples.

4.1.0 Transient Signal Analysis Program (TSAP):

All our analyses were performed through TSAP. This program, written by Burton and Blamey (1972), is an elaborate and

versatile software to calculate the Fourier transform of a seismic signal employing the Cooley-Tukey algorithm in the form of subroutine COOL. In addition, the program determines the group velocity and dispersion characteristics of surface waves by a multiple filtering technique based on the method of Oziewonski, et al (1969). Since we only used the Fourier transform option we will confine ourselves to describing that part of TSAP. For a comprehensive description of the program, the reader is referred to the original publication by Burton and Blamey (1972).

4.1.1 Program Procedure:

Here we adhere to the nomenclature given by the authors (loc. cit., Appendices A and B) to express the input parameters.

The program reads-in NSEIS data points of a digital time series, sampled at intervals DT. The time series is stored in the array SEIS(I), cosine tapered at both ends and fitted to a mean baseline to reduce Gibb's phenomenon, and eliminate "square wave" effects caused by a time series superposed onto a non-zero baseline. To fulfil the condition mentioned in Section 2.5.0 of this chapter, NSEIS is set to N points by adding zeroes such that: $N = 2^{k+1}$, where k is the first integer that makes: $N > NSEIS$.

The harmonic frequencies are determined by N and DT. The Nyquist is defined as:

$$FNQ = \frac{1}{2 \times DT}$$

the fundamental frequency by:

$$DF = \frac{FNQ}{NBY2} \quad \text{where } (NBY2 = N/2)$$

and the harmonic frequencies are:

$$F_{j+1} = j \times DF \quad (0 < j < NBY2)$$

These frequencies are stored in array `FREQ(I)`.

For a time series $x(t)$ of length T , sampled up to N points at DT time intervals, equation (4.4) can be re-written as:

$$X(f_j) = DT \sum_{n=0}^{N-1} x_n e^{-i2\pi j n DT} \quad (4.5)$$

It is apparent from equation (4.5) that $X(f)$ now assumes values at frequencies f_j ($|f_j| < \frac{T}{2}$).

Expanding equation (4.5) into sine and cosine transforms we have:

$$X(f_j) = DT \sum_{n=0}^{N-1} x_n (\cos 2\pi f_j n DT - i \sin 2\pi f_j n DT) \quad (4.6)$$

therefore:

$$Csp(f_j) = |\text{sign}(f_j)| DT \sum_{n=0}^{N-1} x_n \cos 2\pi f_j n DT$$

and (4.7)

$$Ssp(f_j) = \text{sign}(f_j) DT \sum_{n=0}^{N-1} x_n \sin 2\pi f_j n DT$$

If x_n is purely real then:

$$X(\pm f_j) = X^*(\mp f_j)$$

where

$$X^*(f_j) \text{ is the complex conjugate of } X(f_j).$$

Hence the real, even, or symmetrical part of x_n is the cosine

spectrum (Csp) and the imaginary, odd or anti-symmetrical part is the sine spectrum (Ssp).

Upon the call of subroutine COOL(L,Z,+1), the direct Fourier transform is performed and on return the real and imaginary transforms of SEIS(I) are stored in the complex array Z(I) as: ReZ(I) and ImZ(I). Z(I) also contains the DC component to be set to zero. During calculation the array elements are folded about the index number: NBY2P1 (= (N/2)+1) so that:

$$Z(\text{NBY2P1}+I) = Z^*(\text{NBY2P1}-I) \text{ for } I = 0, 1, 2, \dots, \text{NBY2}-1$$

This creates negative frequency components which are stored in elements NBY2P1+I up to N of the array Z(I). Expressing the amplitude and phase by means of equation (4.7) at f_j , we get the form given under (b) of Section 2.2.0 that is:

$$\begin{aligned} A_j &= (\text{Csp}^2 + \text{Ssp}^2)^{\frac{1}{2}} \\ \phi_j &= \tan^{-1}\left(-\frac{\text{Ssp}}{\text{Csp}}\right) \end{aligned} \quad (4.8)$$

The quantity measured here is amplitude spectral density because it depends on unit time interval DT (DF in the case of inverse Fourier transformation), therefore, its dimensions are: length x time, e.g: micron. second. Phase spectra, on the other hand, have the dimension of radians. These are excluded in our presentations since our prime interest is directed towards amplitude spectra.

2 Examples Illustrating Spectral Analysis using TSAP:

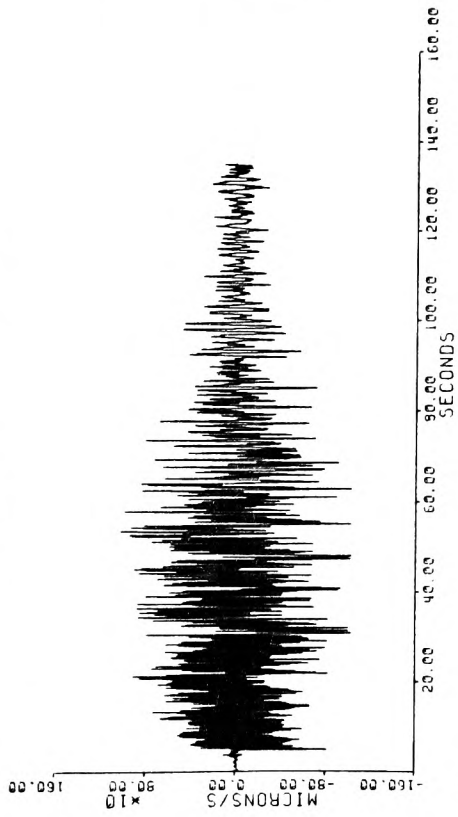
To show the Fourier transform option in TSAP we give specific examples of earthquakes from both data sources. From each

source we selected two events representing a large and small earthquake. C6001 and C6011 at S5 to show the far-field observations. RDD72 and RD068 at ETV to exemplify the local observations.

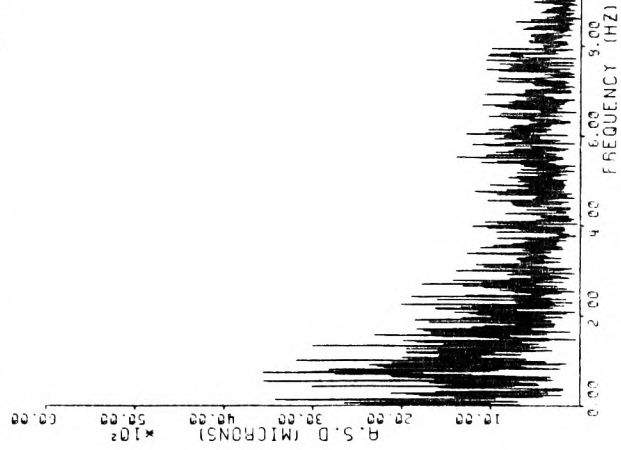
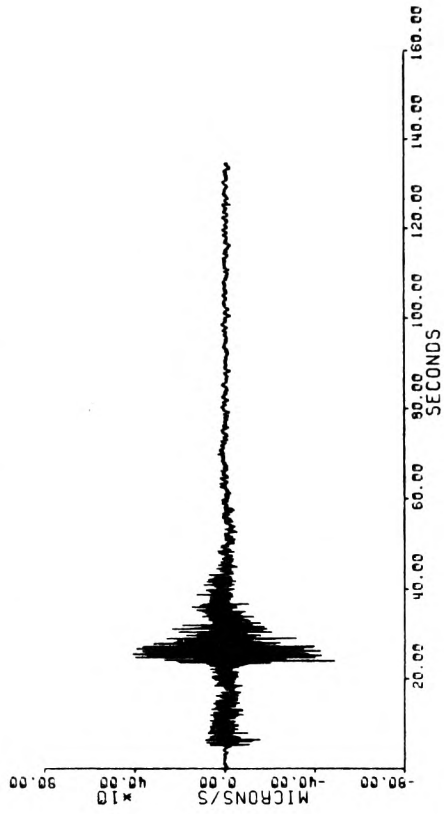
Figures 4.2 and 4.3 illustrate the Z/BL trace of these seismograms, each with the spectral amplitude plotted on linear scales below it. The amplitude spectra of the same earthquakes plotted on log-log scales are displayed in Figures 4.4 and 4.5. Comparing the linear and log plots and recalling our discussion on the choice of spectral scales we can immediately recognize the virtue of representing transforms on log-log plots, where the low frequencies are more clear and less compressed than the high frequencies. Figures 4.4 and 4.5, illustrate another aspect discussed earlier which is the spiky character of the spectrum. This is treated in the next section.

Having established that log plots are by far more useful, especially from our comparative point of view, than linear representations, we next consider the spectral differences between the Z/SP and Z/BL channels of the example events. A quick look at Figures 4.6 through to 4.9 demonstrates the considerable difference between the bass-lifted and untreated spectra particularly in the long period range. The bass-lift compensation for the low frequency components and the simultaneous suppression of high frequencies is readily noticed and looks rather impressive. Moreover, in the Z/SP plots, the overall spectral shape can hardly be made out because of its extremely irregular behaviour at all frequency bands, whereas in the Z/BL case we can recognize a more

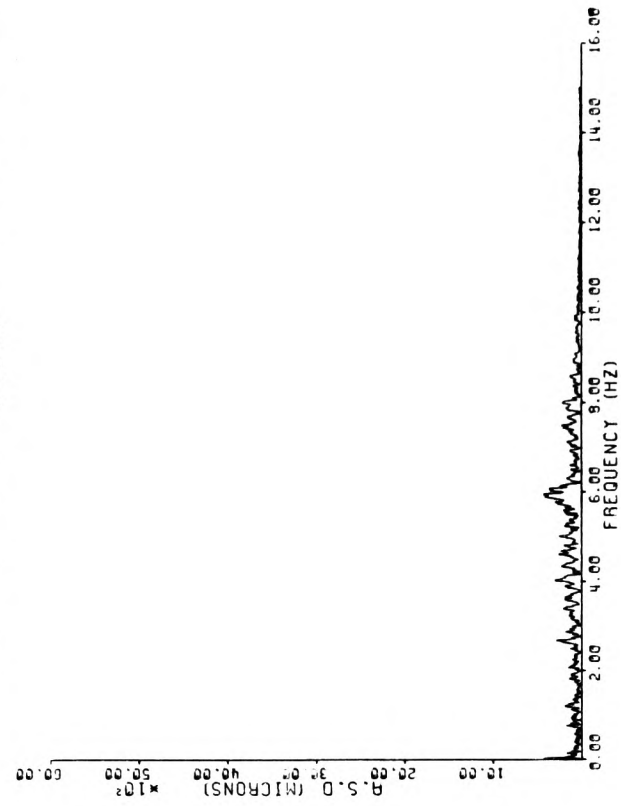
RABRUL DATA MAJOR EVENT: R0072 AT ETV MB=4.9 (Z/BL AT 5.05)



RABRUL DATA MINOR EVENT: R0069 AT ETV ML=3.0 (Z/BL AT 5.05)



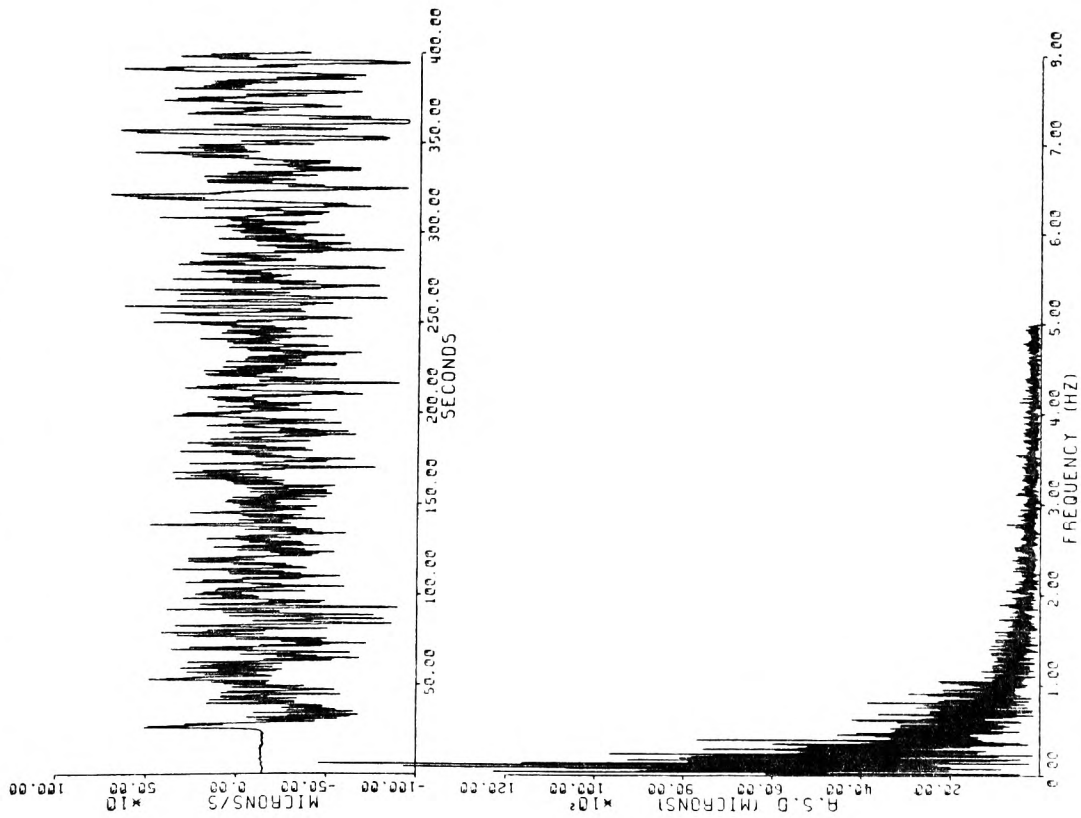
AMPLITUDE SPECTRAL DENSITY OF SEISMOG



AMPLITUDE SPECTRAL DENSITY OF SEISMOG

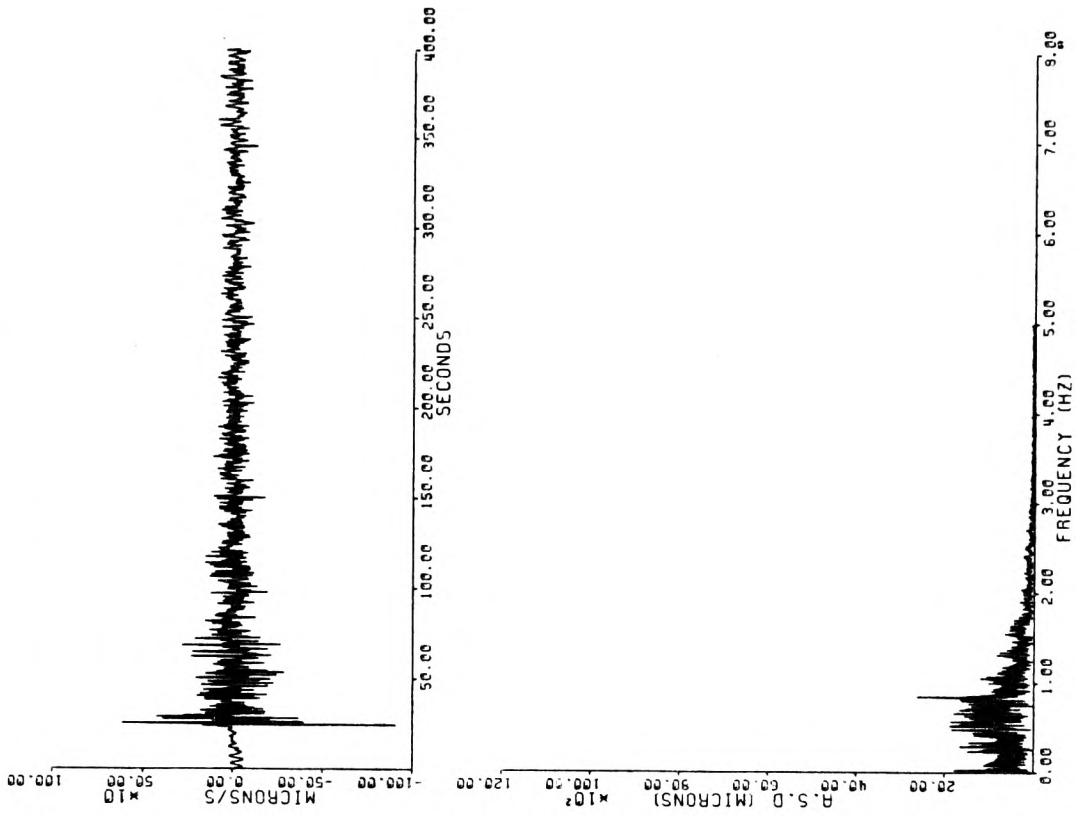
Fig. 4.2 RABRUL DATA ILLUSTRATING LINEAR SPECTRA

CHILE DATA EVENT, C8001 AT SAAS, 55 MB-6.5 (Z/BL AT 10.0S)



AMPLITUDE SPECTRAL DENSITY OF SEISMOGRAM

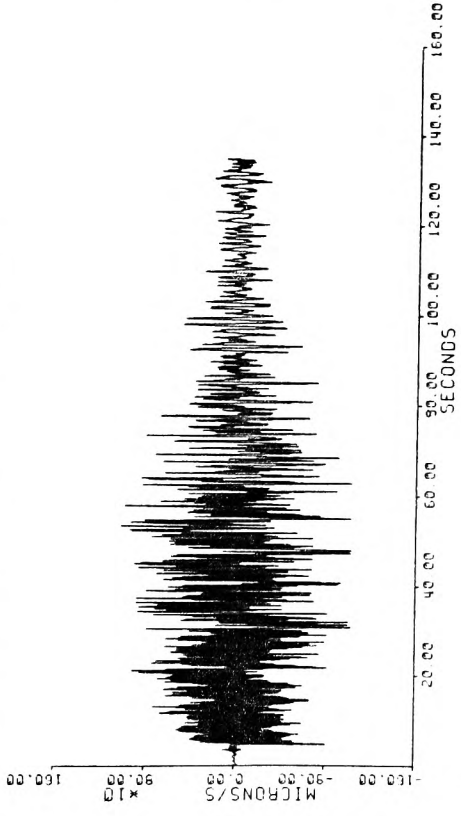
CHILE DATA EVENT, C8011 AT SAAS, 55 MB-5.3 (Z/BL AT 10.0S)



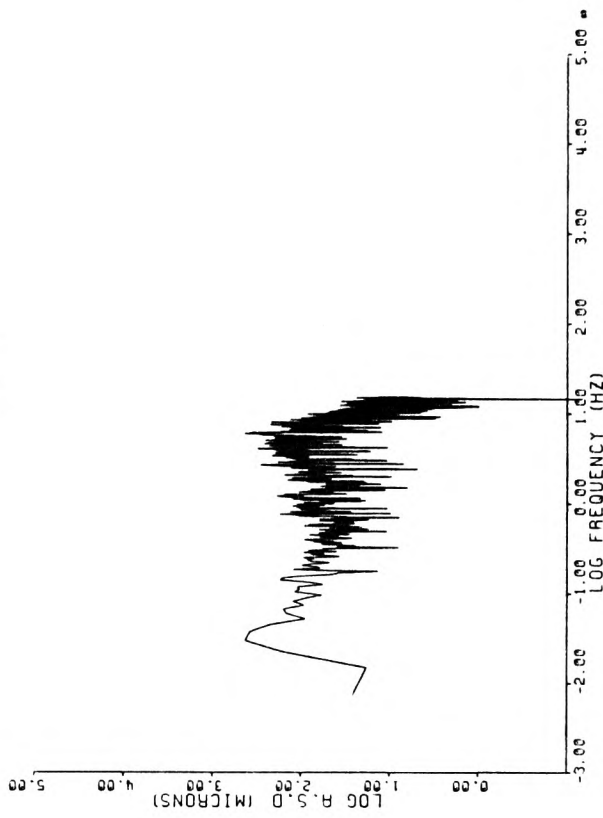
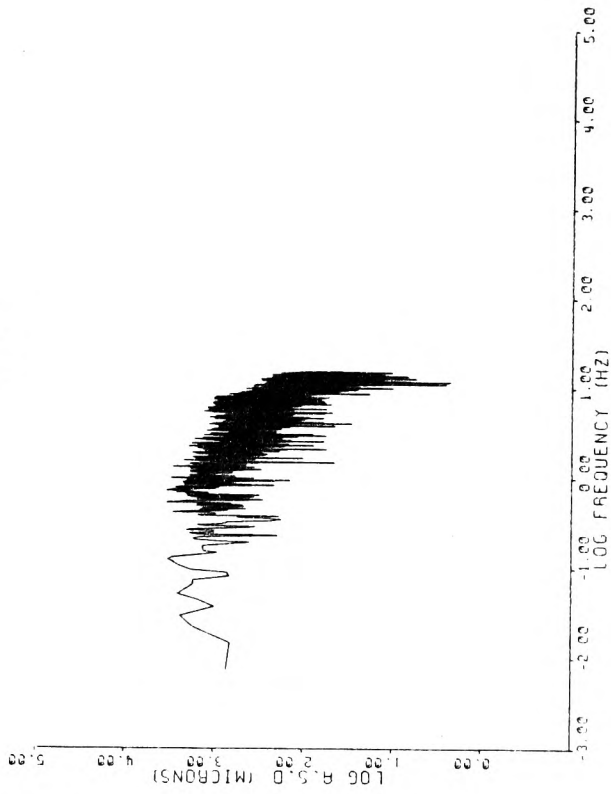
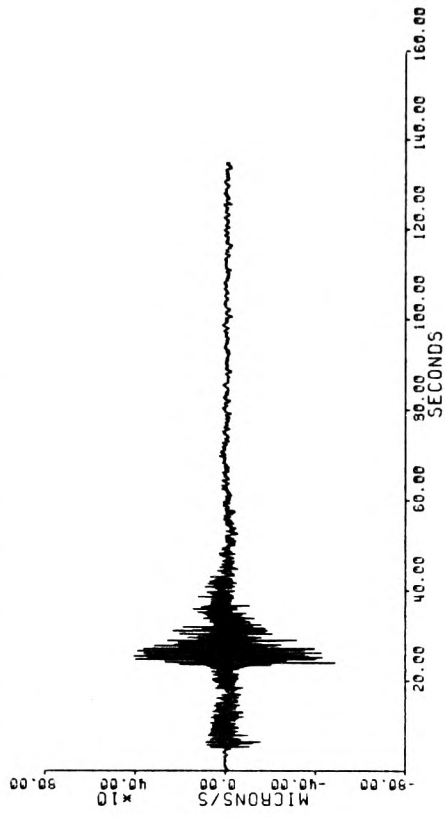
AMPLITUDE SPECTRAL DENSITY OF SEISMOGRAM

Fig. 4.3 CHILE DATA ILLUSTRATING LINEAR SPECTRA

RABAUU DATA MAJOR EVENT: R0072 AT ETV MB=4.9 (Z/BL AT 5.0S)



RABAUU DATA MINOR EVENT: R0069 AT ETV ML=3.0 (Z/BL AT 5.0S)

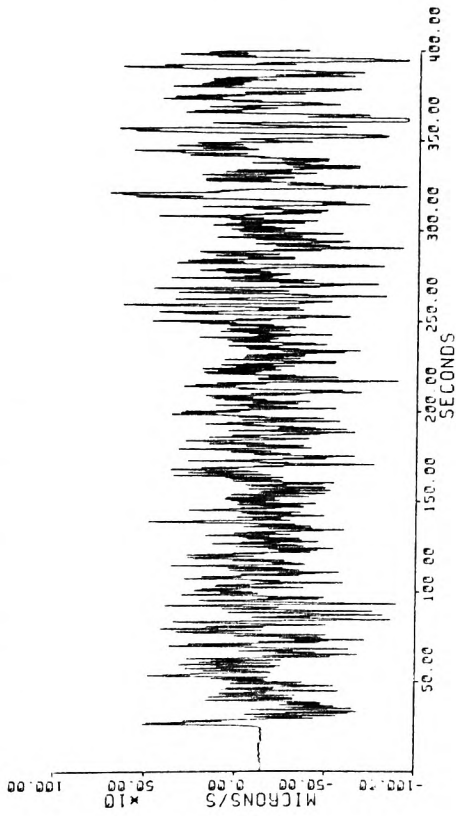


AMPLITUDE SPECTRAL DENSITY OF SEISMOG

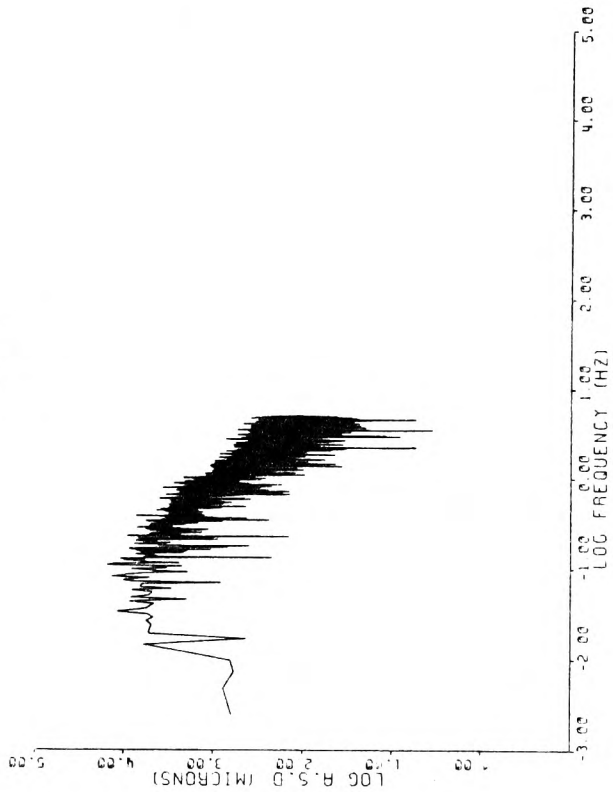
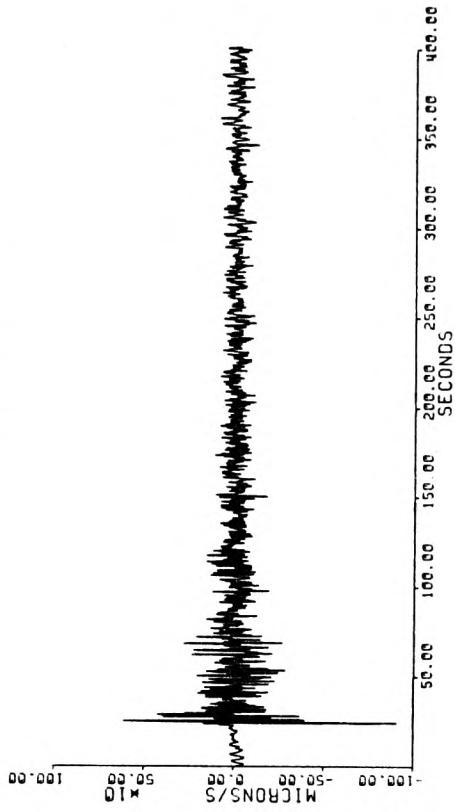
AMPLITUDE SPECTRAL DENSITY OF SEISMOG

Fig. 4.4 RABAUU DATA ILLUSTRATING LOG SPECTRA

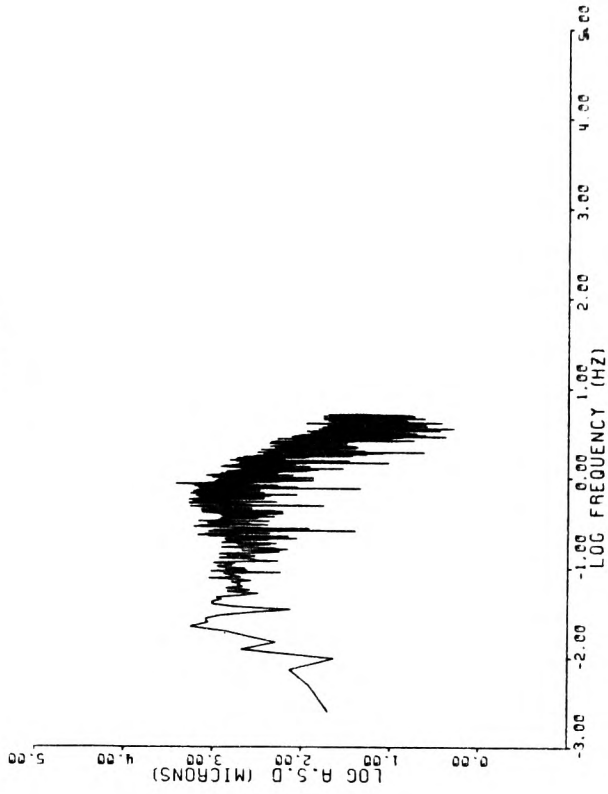
CHILE DATA EVENT: (6001) AT SARRS: 55 MB=6.5 (Z/BL AT 10.0S)



CHILE DATA EVENT: (6011) AT SARRS: 55 MB=5.3 (Z/BL AT 10.0S)



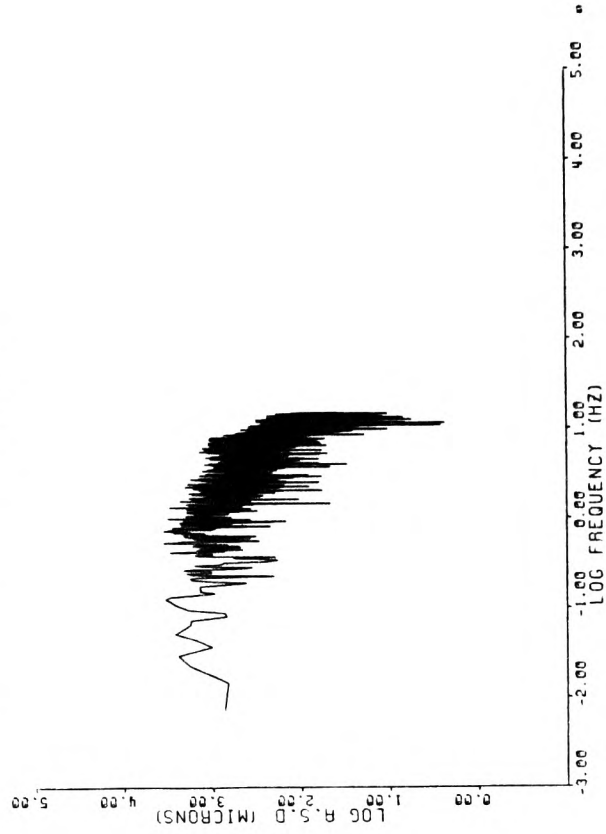
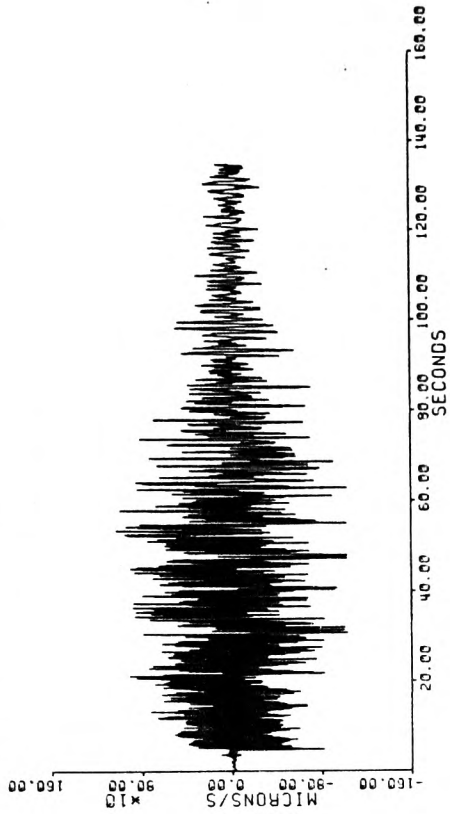
AMPLITUDE SPECTRAL DENSITY OF SEISMOGR



AMPLITUDE SPECTRAL DENSITY OF SEISMOGR

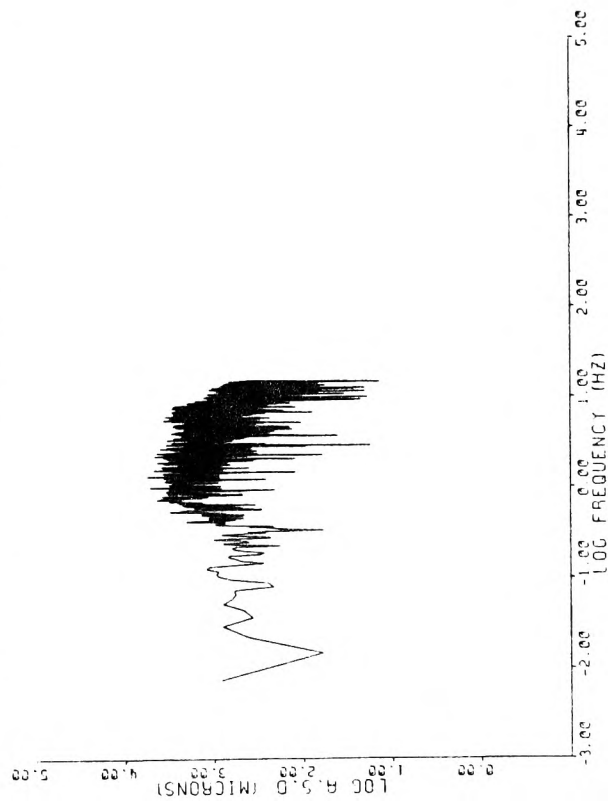
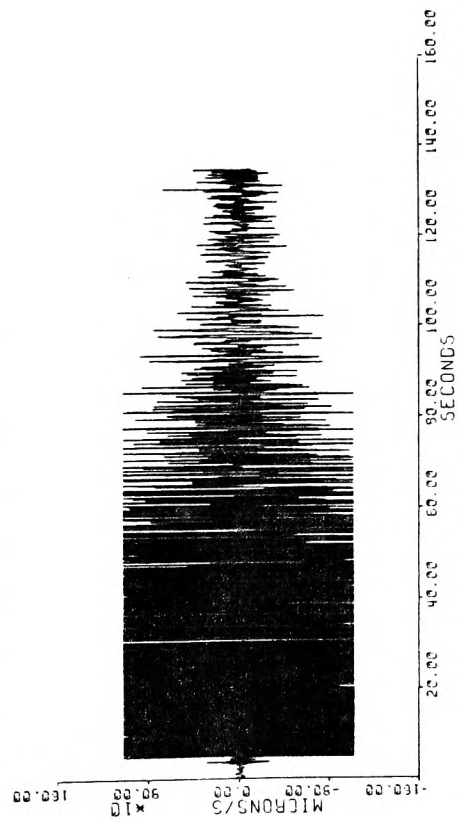
Fig. 4.5 CHILE DATA ILLUSTRATING LOG SPECTRA

RABAU DATA MAJOR EVENT: RDD72 AT ETV MB=4.9 (Z/BL AT 5.0S)



AMPLITUDE SPECTRAL DENSITY OF SEISMOG

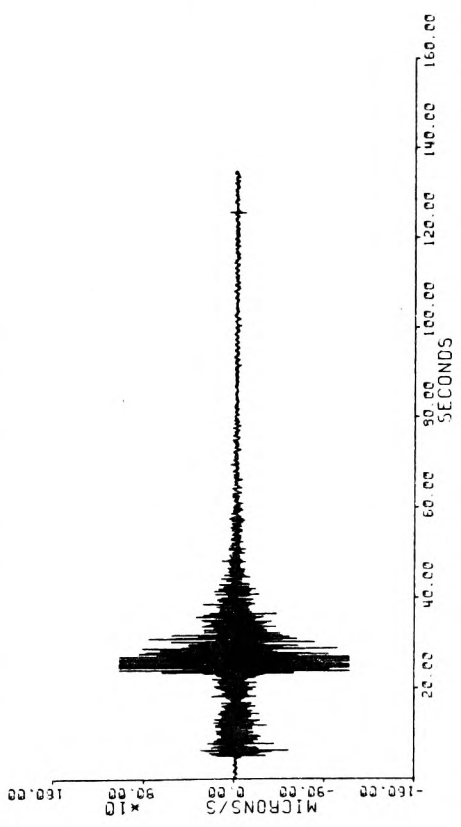
RABAU DATA MAJOR EVENT: RDD72 AT ETV MB=4.9 (Z/SP)



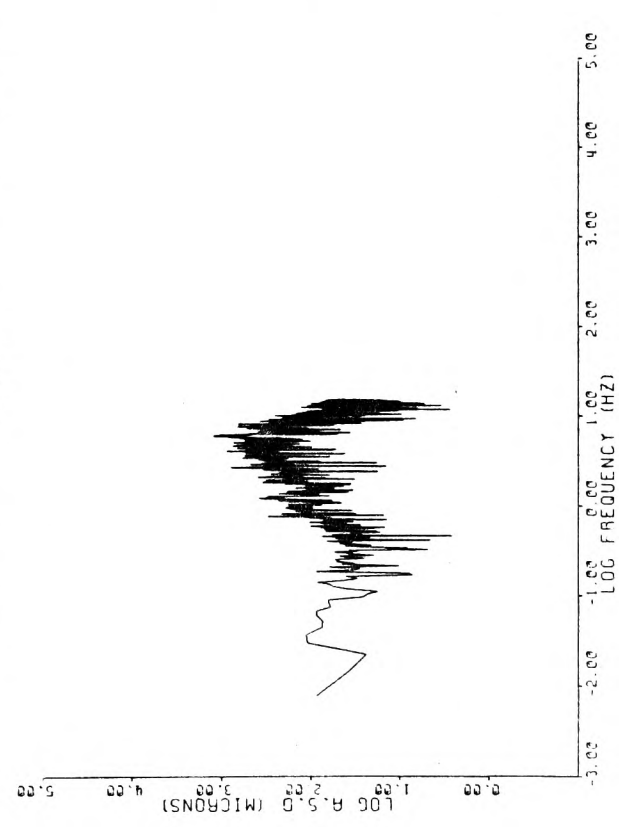
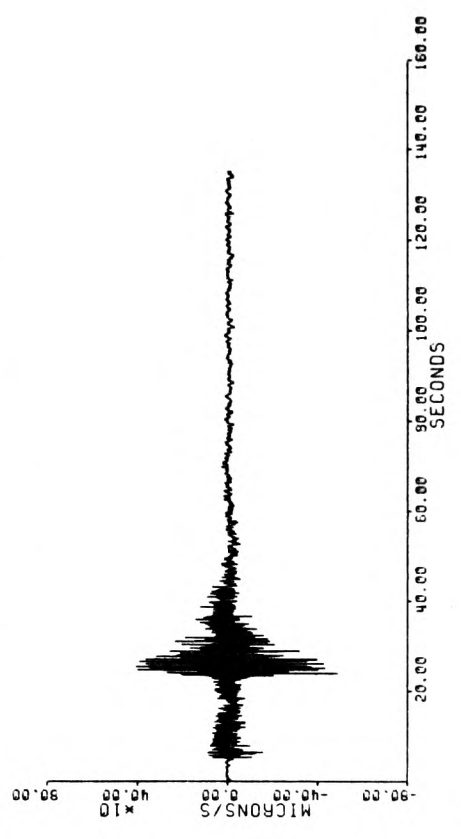
AMPLITUDE SPECTRAL DENSITY OF SEISMOG

Fig. 4.6 RABAU DATA : RDD72 ILLUSTRATING SPECTRAL DIFFERENCE BETWEEN Z/SP AND Z/BL

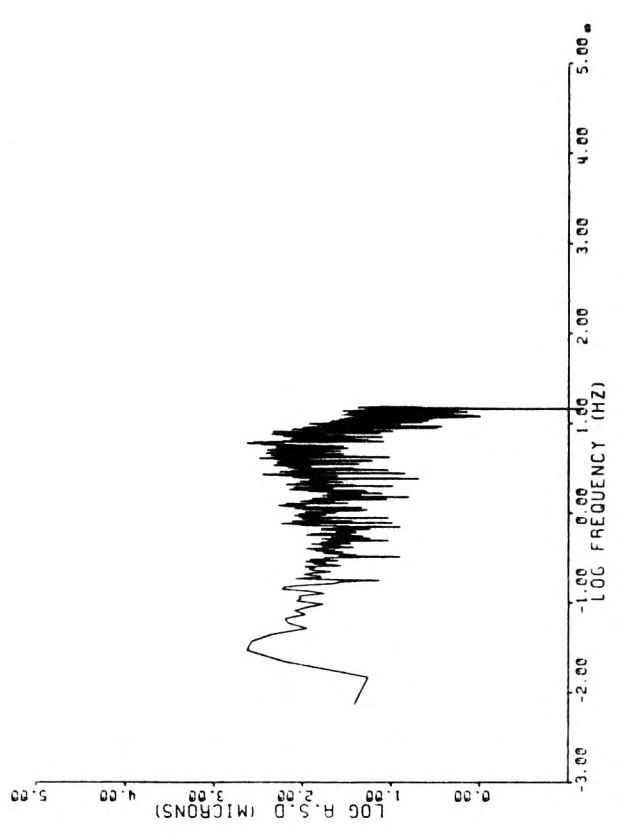
RABAU DATA MINOR EVENT, RD068 AT ETV ML=3.0 (Z/SP)



RABAU DATA MINOR EVENT, RD069 AT ETV ML=3.0 (Z/BL AT 5.0S)



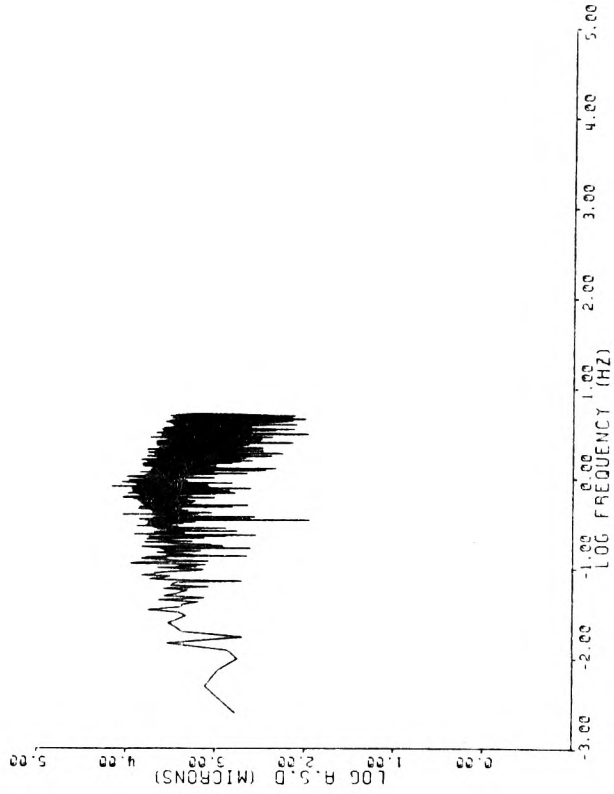
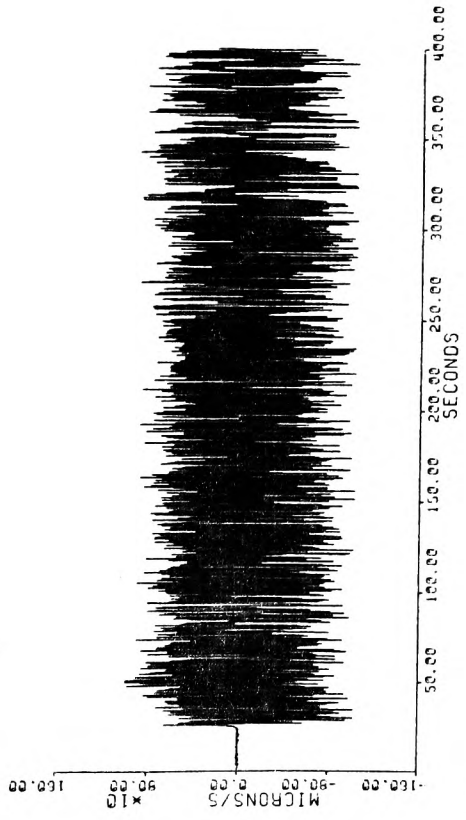
AMPLITUDE SPECTRAL DENSITY OF SEISMOGRA



AMPLITUDE SPECTRAL DENSITY OF SEISMOGRA

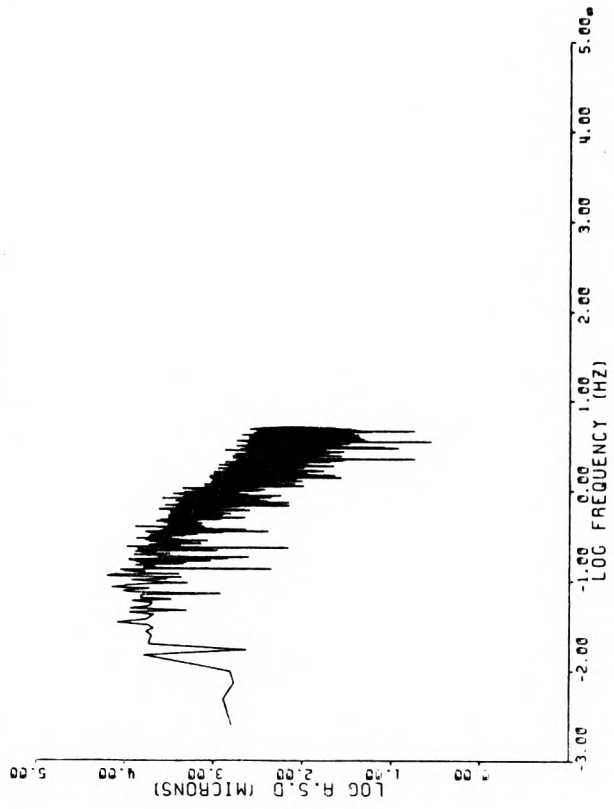
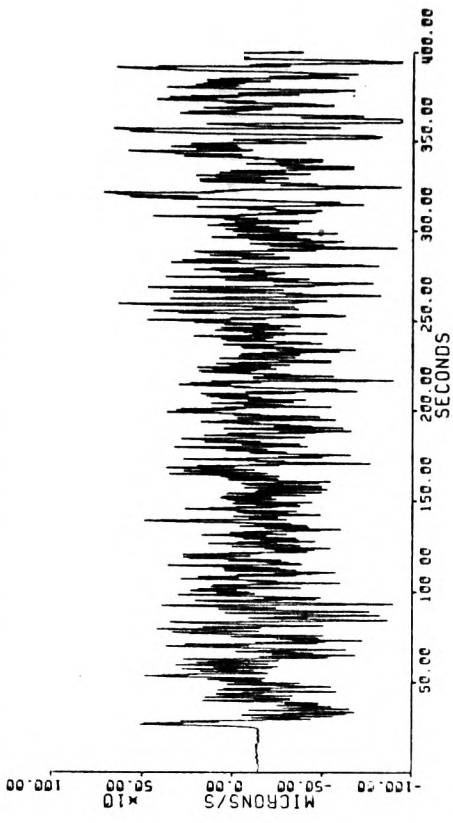
Fig. 4.7 RABAU DATA : RD068 ILLUSTRATING SPECTRAL DIFFERENCE BETWEEN Z/SP AND Z/BL

CHILE DATA EVENT: CB001 AT SACS, 55 MB-6.5 (Z/SP)



AMPLITUDE SPECTRAL DENSITY OF SEISMOGRAPH

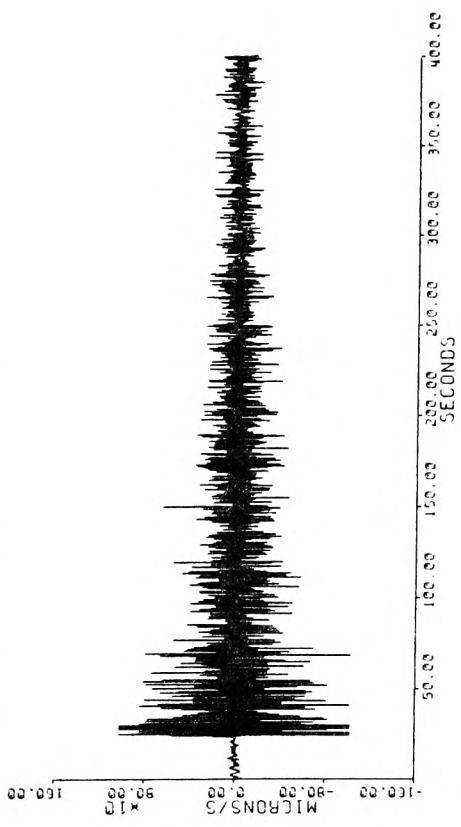
CHILE DATA EVENT: CB001 AT SACS, 55 MB-6.5 (Z/BL AT 10.0S)



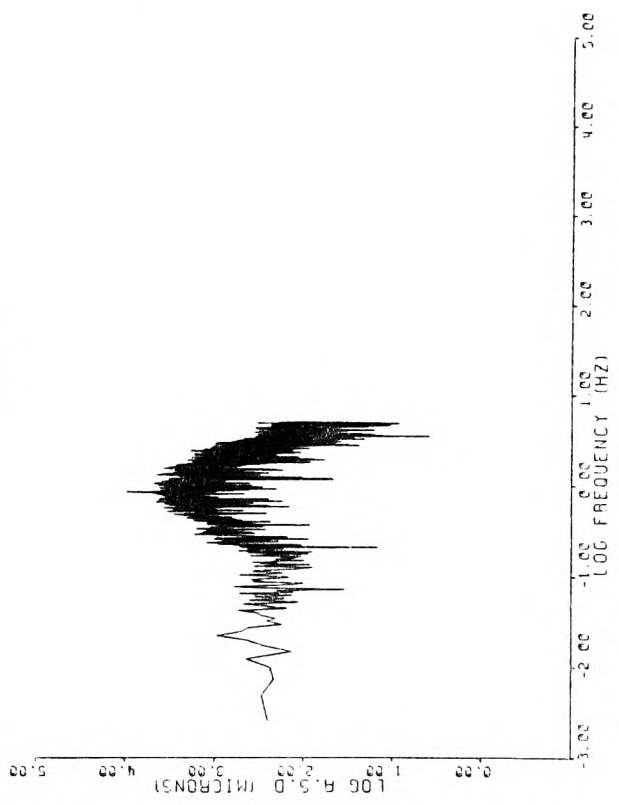
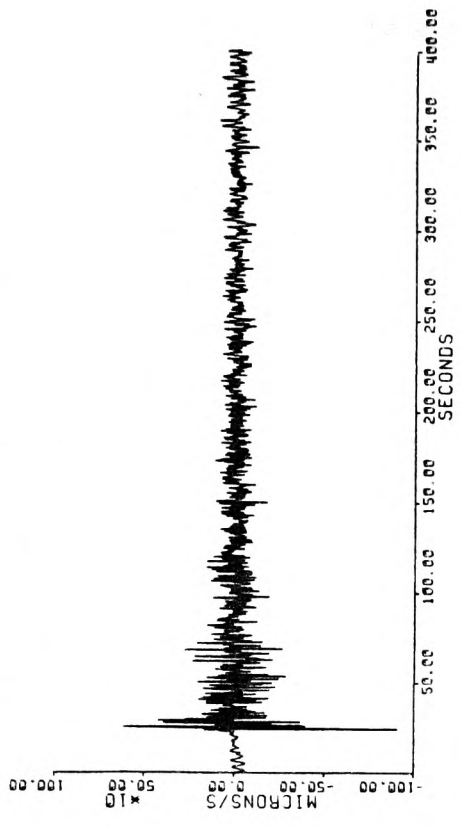
AMPLITUDE SPECTRAL DENSITY OF SEISMOGRAPH

Fig. 4.8 CHILE DATA : CB001 ILLUSTRATING SPECTRAL DIFFERENCE BETWEEN Z/SP AND Z/BL

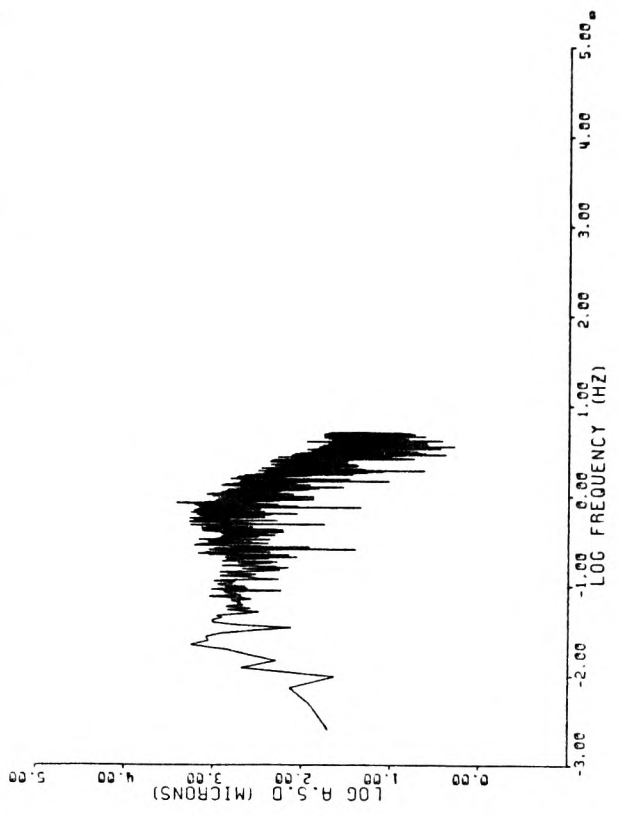
CHILE DATA EVENT: CB011 AT S99S: 55 MB-S.3 (Z/SP)



CHILE DATA EVENT: CB011 AT S99S: 55 MB-S.3 (Z/BL AT 10.0S)



AMPLITUDE SPECTRAL DENSITY OF SEISMOGR



AMPLITUDE SPECTRAL DENSITY OF SEISMOGR

Fig. 4.9 CHILE DATA : CB011 ILLUSTRATING SPECTRAL DIFFERENCE BETWEEN Z/SP AND Z/BL

definite shape over the spectral window. Here, the high frequency roll-off as well as the low frequency "flat" are more discernable compared to their Z/SP counterparts.

This spectral difference, we tend to think, could also be (at least partly) due to the non-linear part of the Z/SP records as a result of clipping. This seems to be especially true for Figure 4.6 where the complete window is overloaded.

4.2.0 Spectral Smoothing and "CUFIT":

The phenomenon of spectral "scalloping" mentioned earlier in this chapter poses a problem for our efforts to measure - with a certain degree of confidence - the seismic spectrum. A straightforward and rather crude way of estimation would be to fit, by eye, straight lines connecting the peaks within each frequency band. The Ω_0 trend will thus be a line parallel to the frequency axis while the high frequency trends will have slopes proportional to ω^{-1} , ω^{-2} , or ω^{-3} . Consequently the point of intersection of these trends will be a rough measure of the effective width of the spectrum, i.e: ω_c (see Fig. 3.1). This rough procedure was found to be insufficient and unreliable essentially because, it largely depended upon human judgment and bias which could often be misleading. Furthermore, such a qualitative approach does not systematically and numerically apply an equal-area principle. That is, replacing the observed spectrum by a smooth curve such that the area under the curve is preserved.

After a great deal of investigation and trial and error we managed to come across and successfully implement a well-known

numerical technique to smooth the seismic spectrum called the Cubic Spline fit. This technique computes a weighted least-squares approximation to the spectral curve by a cubic spline with prescribed knots. The method, incorporated in the smoothing program "CUFIT", involves forming and then computing a least-squares solution of a set of M linear equations in the coefficients C(I) where : I = 1,2,..., NCAP+3. These equations are formed using a recurrence relation of B-splines which is unconditionally stable (Cox, 1972; DeBoor, 1972) even for multiple (coincident) knots. The least-squares solution of the system of equations is obtained in a stable manner by using orthogonal transformations, viz: a variant of Given's rotations applied by Gentleman (1974, 1975). Listing of CUFIT and further details of the algorithms employed to approximate the data is given in Appendix B.

As explained in Appendix B the relevant subroutines EØ2BAF and EØ2BBF leave the choice of interior knots K(I) and the weighting parameter W(R) up to the user. The number of knots and their position with respect to the frequency values can be selected by a mixture of trial and error, experience and prior knowledge of the spectral shape (Hayes, 1974). According to Hayes (1978) this criterion stems from the observation that knots need to be more closely spaced in regions where the underlying curve exhibits rapid changes in shape than where it changes gradually. Therefore, the strategy is to arrange the knots to have a roughly equal number of data points between each adjacent pair of knots.

The other thing to consider is the weighting of data points. That is whether the co-ordinate pairs are of the same or

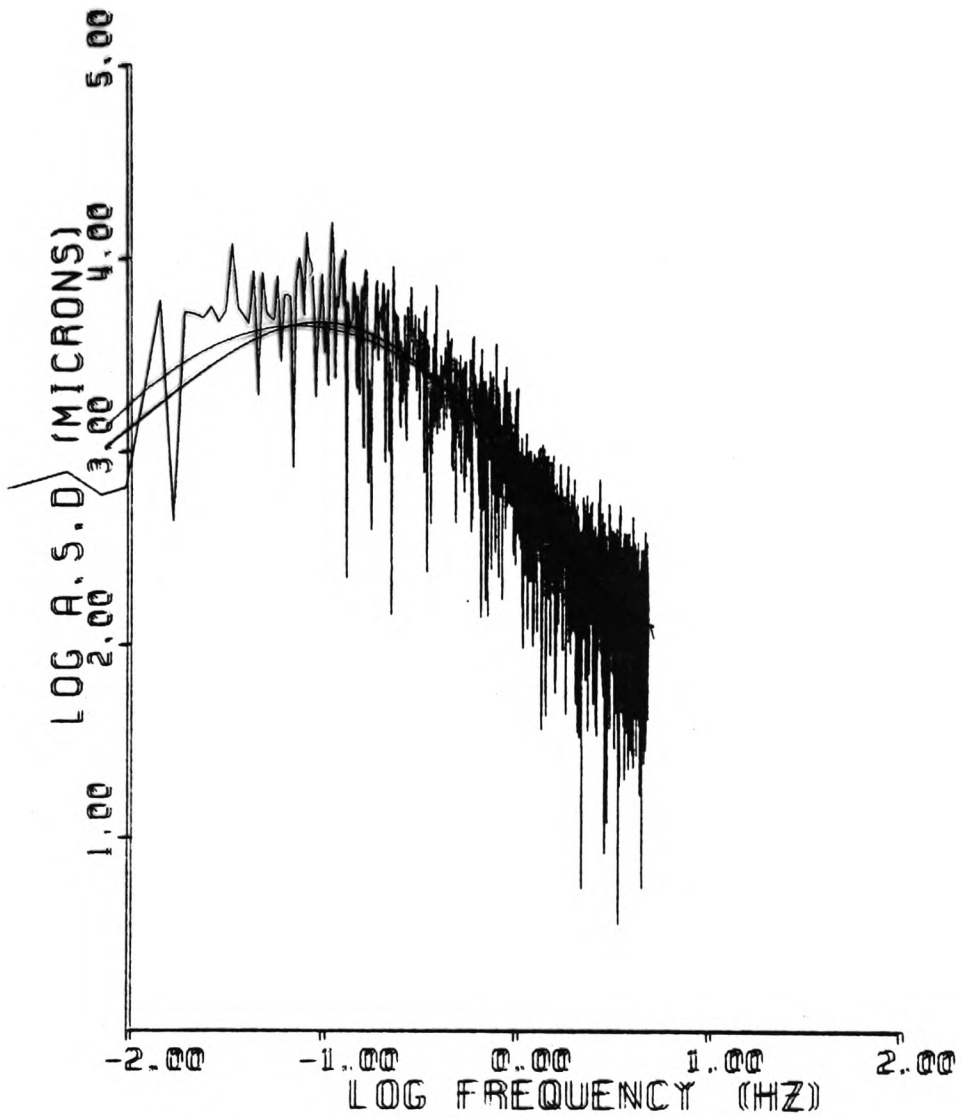
different accuracy. Here again the assignment of weights remains for the user (Cox and Hayes, 1975). It transpires, therefore, that the number of interior knots, their position and the weighting function are essential input parameters to CUFIT.

In order to be consistent and to ensure equal accuracy for all points on the spectrum we took $W(R)$ equal to unity. The choice of $K(I)$ values, on the other hand are demonstrated in Figures 4.10 and 4.11. Here both the original and smoothed versions of the spectra are portrayed on transparencies for comparison. In both figures we found that the fit is more stable at $K(I) = 2$ or 3 provided the end knots are equal or approximately equal to the smallest and largest frequency values within the spectral window. At these values and in both cases the smoothed curves are identical and seem to fit the shape of the original spectra nicely. The $K(I) = 1$ approximation, however, is rather unstable at low frequencies.

From our experience in experimenting with different K values we found that for the Chile earthquakes a good fit to their spectra is obtained with $K(I) = 2$ at frequencies of 0.1 and 4.5 Hz respectively. For the Rabaul events we selected $K = 3$ at $0.32, 1,$ and 10 Hz respectively. Therefore these K values we fixed throughout the analyses.

4.3.0 Aliasing:

The cubic spline method seems to show some promise as a reliable and numerically efficient technique for determining a smoothed approximation to the shape of a seismic spectrum

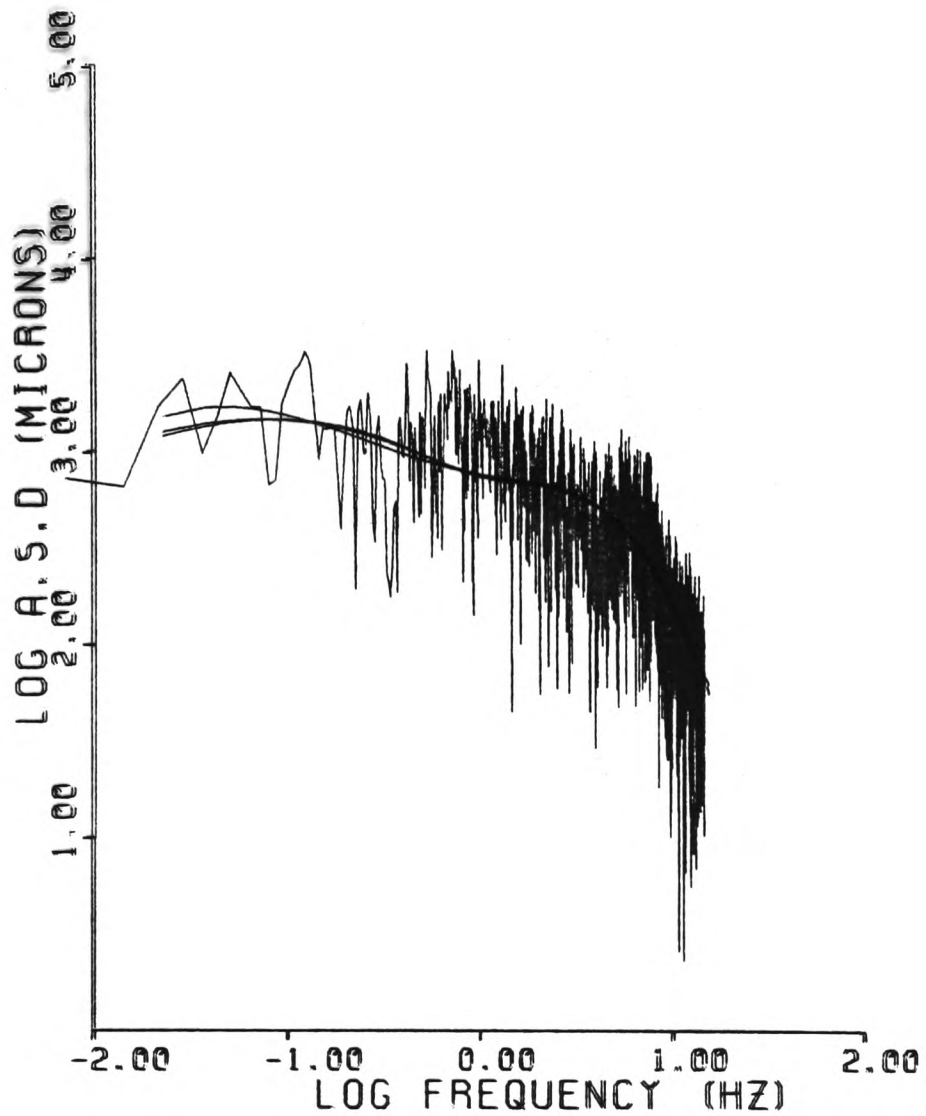


AMBLITUDSE ISPEKTRA ODENSI GMI COFSET SMOGR

CB001 AT: 55 (Z/BL)

DIFFERENT VALUES OF 'K' PARAMETER

Fig. 4.10 Chile data: CB001: Comparison between original and smoothed spectra



AMBLECTSBEIREEETRAODSBSMYCOSPECTSUNGRAM

RDD72 AT: ETV (Z/BL)

DIFFERENT VALUES OF 'K' PARAMETER

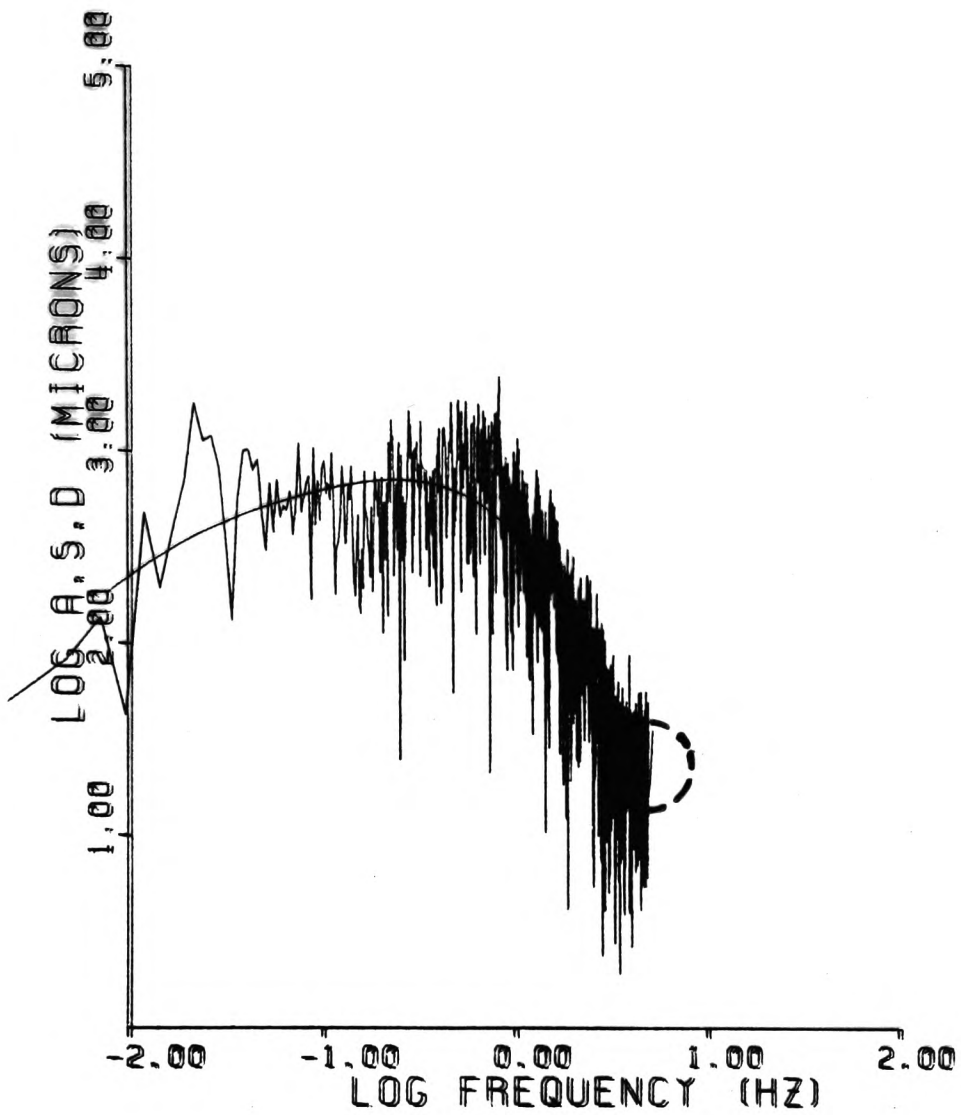
Fig. 4.11 Rabaul data: RDD72: Comparison between original and smoothed spectra

in general. What is more interesting is the technique's capability of exhibiting spectral contamination or aliasing discussed earlier. To illustrate this phenomenon we present an example from the Chile data set (Fig. 4.12) where aliasing is obvious on the smoothed version but almost passes unnoticed on the original spectrum. This example is about the most outstanding where aliasing is prominent. Fortunately, its magnitude is about 1/5 of the high frequency roll-off amounting to about 20% contamination. The basic reason for this aliasing is that for the contaminated spectra, the anti-alias filter had too high a pass-band in relation to the Nyquist frequency.

4.4.0 Influence of Frequencies Below the Bass-Lift Cutoff:

In Chapter 2 we stated that the bandwidth of interest is limited at the high frequency end by the Nyquist and at the low end by the bass-lift cutoff. Therefore our spectral calculations are only valid at this frequency range.

In Figure 4.12 we showed how frequencies above the Nyquist fold and contaminate the spectrum. At the lower frequency limit, where our attention is focused, the situation of including frequencies below the bass-lift filter is even more pronounced. This is illustrated by another Chile earthquake viz: CBO22 at S5, where the seismogram is severely overloaded in the first 50s. Figure 4.13 shows this bass-lift "ringing" (see Chapter 2) reflected on the spectrum in the form of a low frequency "hump". To eliminate this, TSAP has an option of removing such frequencies after Fourier transformation. The resulting spectrum with the Z/SP version

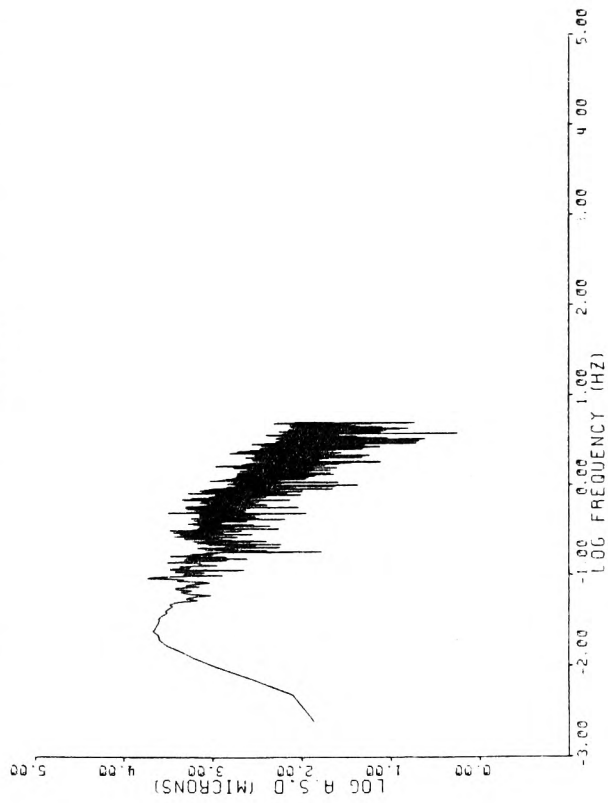
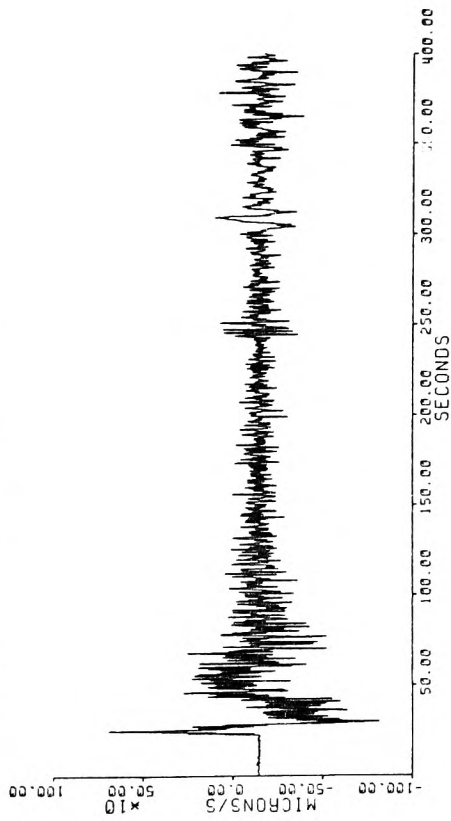


AMBUCTUDE ISREETRAUDSIES 5MY COSPETSNOGRAM.

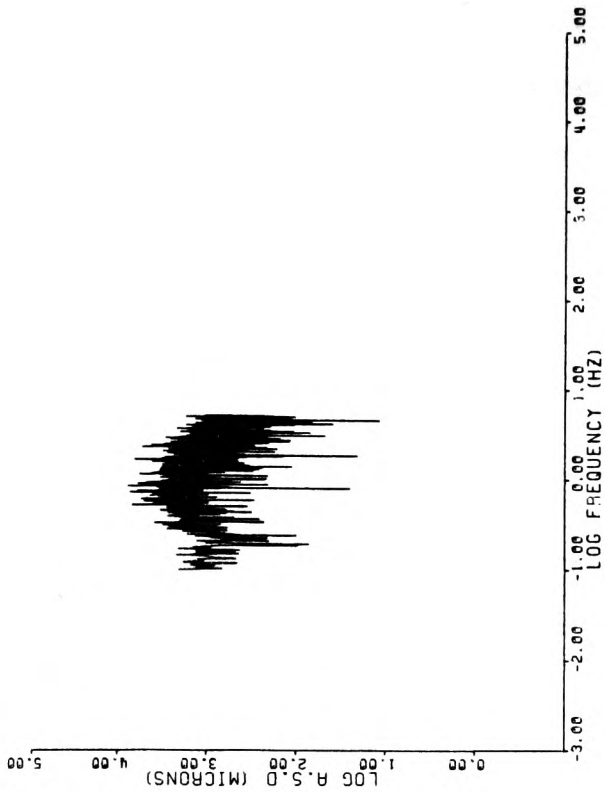
CB011 AT: 55 ILLUSTRATING 'ALIASING'.

Fig. 4.12 Chile data: CB011 showing the effect of spectral contamination.

CHILE DATA EVENT: CB022 AT SANS, 55 MB-S.7 (Z/BL AT 10.05)



AMPLITUDE SPECTRAL DENSITY OF SEISMOGRAM.



AMPLITUDE SPECTRAL DENSITY OF SEISMOGRAM.

Fig. 4.13 CHILE DATA : CB022 ILLUSTRATING Z/SP AND INFLUENCE OF FREQUENCIES BELOW Z/BL ON THE SPECTRUM

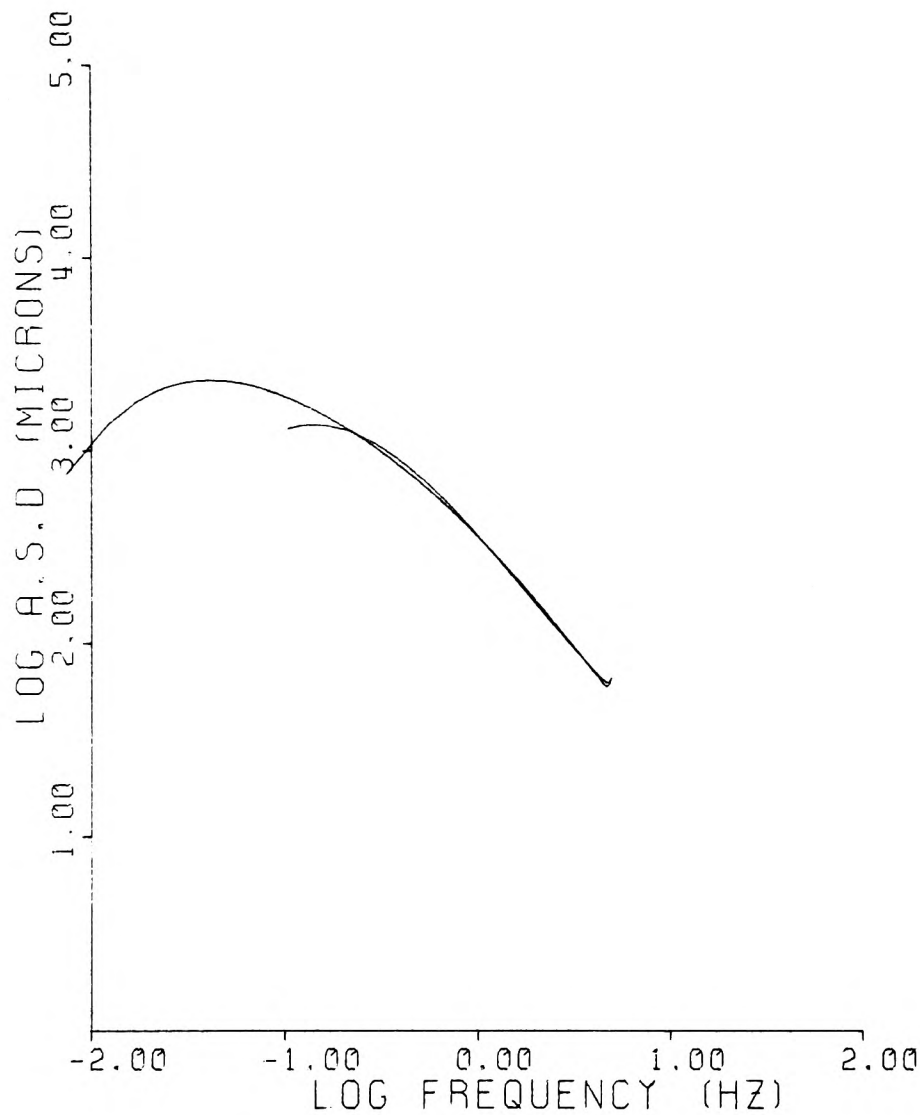
is displayed on the same figure.

The difference between the inclusion or exclusion of frequencies below the bass-lift cutoff, on smoothed spectra, is illustrated in Figure 4.14. Both curves were obtained with identical K values. At the high frequency roll-off, the spectral difference is negligible, whereas there is considerable misrepresentation at longer periods. Notice also that in the case where only the real frequency bandwidth is represented, i.e: the curve cut at 10s, a more realistic spectral shape is assumed with the "plateauing" becoming more evident at lower frequencies.

The considerable difference between the smoothed spectra of the Z/SP and Z/BL is shown in Figure 4.15. This plot seems to convincingly support our claim that the bass-lifted records are by far more useful in representing earthquake spectra of short period recordings. In other words the bass-lift circuit is not only a filter but a compensating instrument, bringing out long period contents inherent in, but unseen on Z/SP records.

An interesting speculation regarding the compensatory function of the bass-lift would be if one were to simply lift the long period end of the Z/SP spectrum by an amount equivalent to the range of bass-lift compensation. What would be the result? The answer is as follows. If we just lift the long period end, then all we are effectively doing is "flattening" the short period spectrum at the bass-lift range. As a result both spectra will not coincide because the "shoulder" is not shifted from 1.0 - 10s, neither are frequencies above 1 Hz being

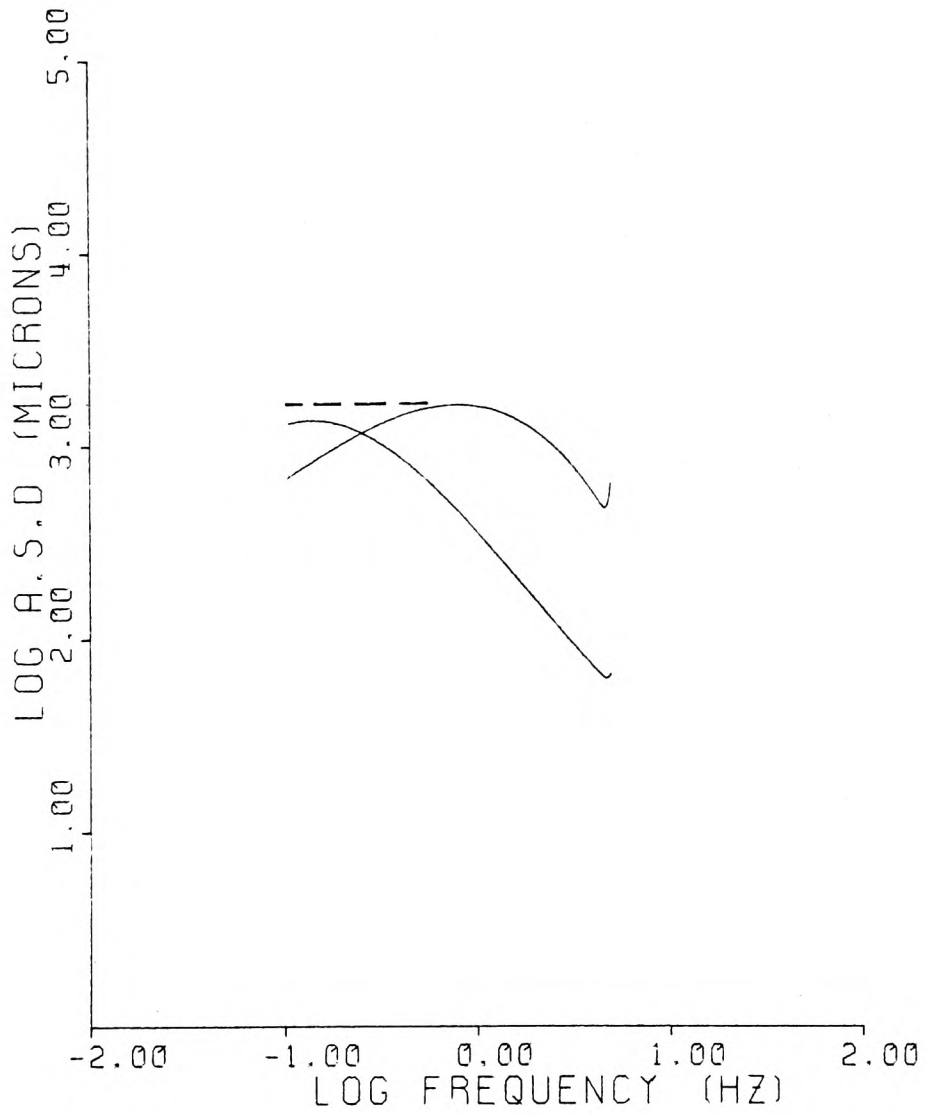
Fig. 4.14 : CHILE DATA: CB022: DIFFERENCE BETWEEN
SMOOTHED SPECTRA.



CUBIC SPLINE FIT TO SEISMIC SPECTRUM.

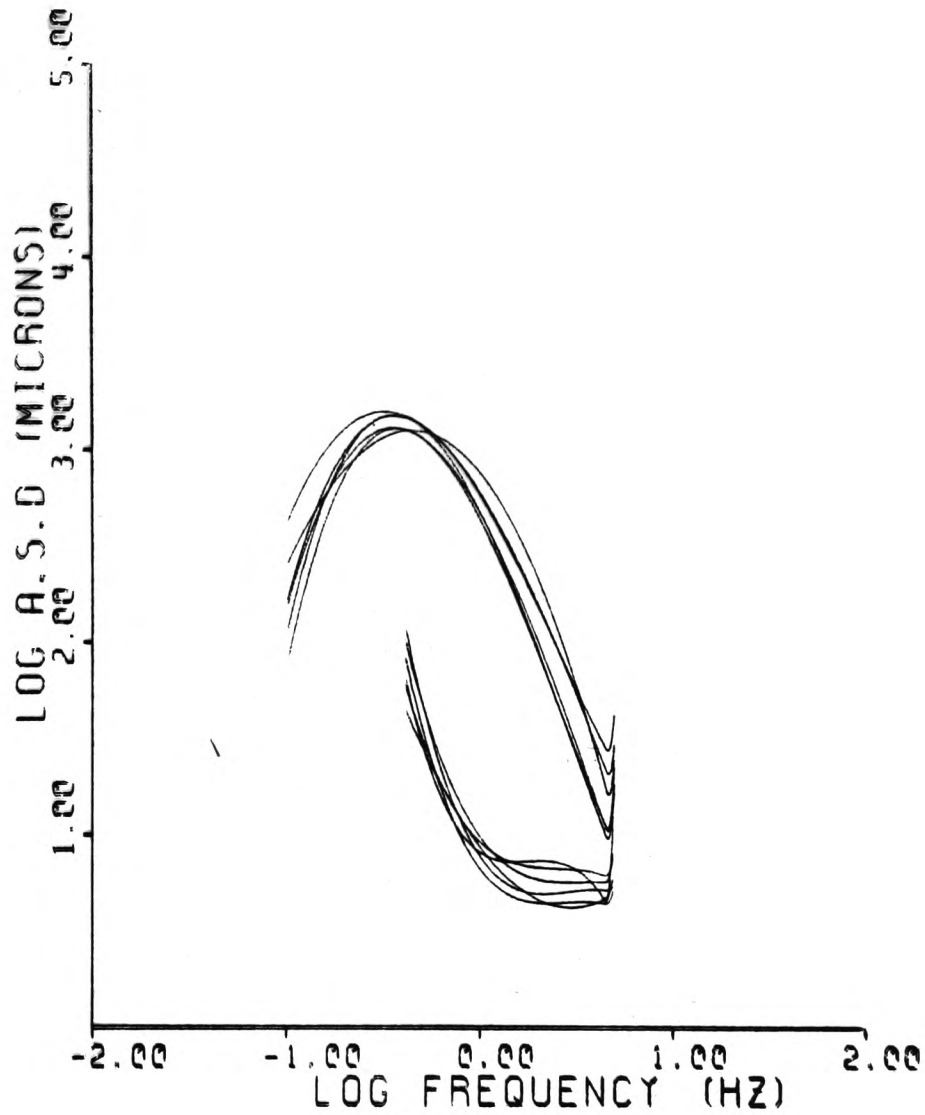
CB022 AT: S5 (Z/BL) INFLUENCE OF LOW
FREQUENCIES BELOW 10.0S ON SPECTRUM.

Fig. 4.15 : CHILE DATA: CB022: DIFFERENCE BETWEEN
SMOOTHED Z/SP AND Z/BL SPECTRA.



CUBIC SPLINE FIT TO SEISMIC SPECTRUM.

CB022 AT: S5 DIFFERENCE BETWEEN
NORMAL AND BASS-LIFTED SPECTRA.

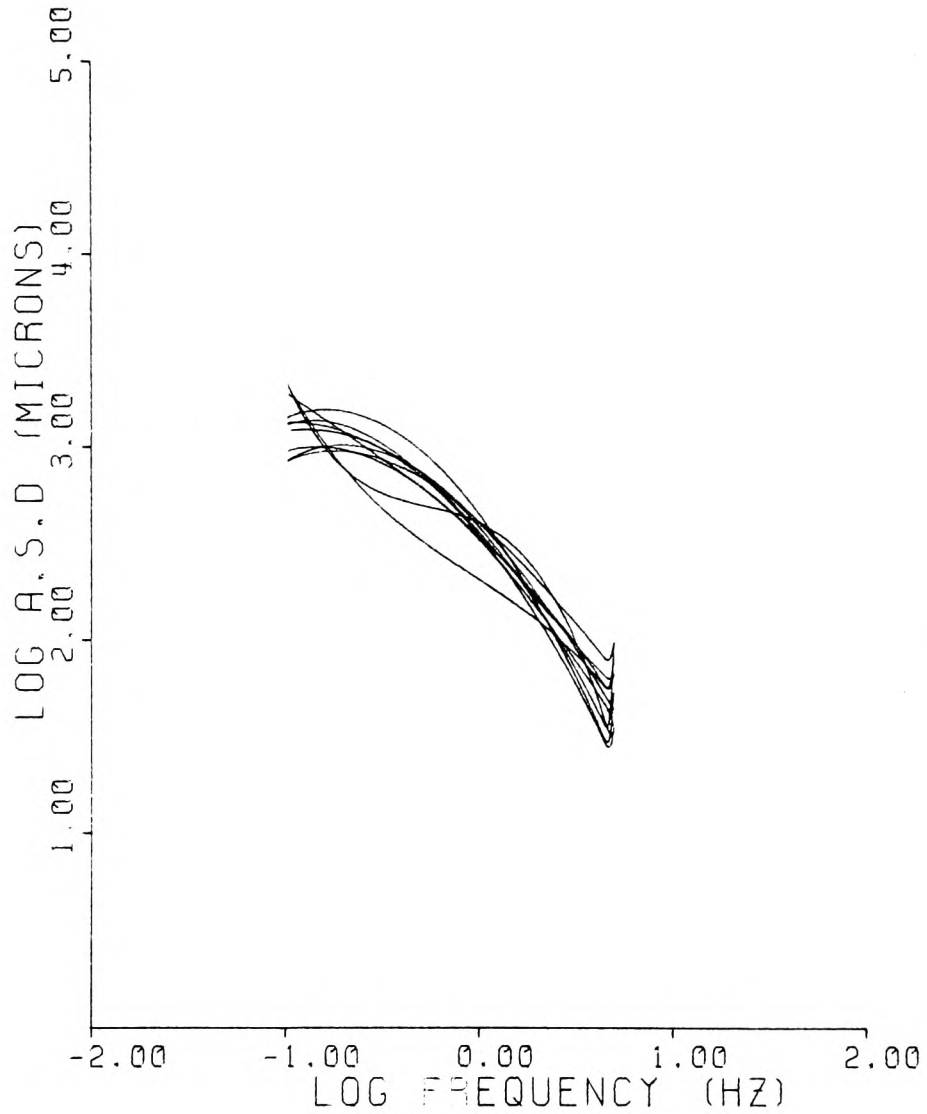


CUBIC SPLINE FIT TO SEISMIC SPECTRUM.

CB014 (Z/BL) BRESANAL NOSASSTATIONS
 @4\$@\$\$ST@PION\$AND 55

Fig. 4.16 Chile data: CB014: Spectral difference between signal and pre-signal noise at 6 array stations.

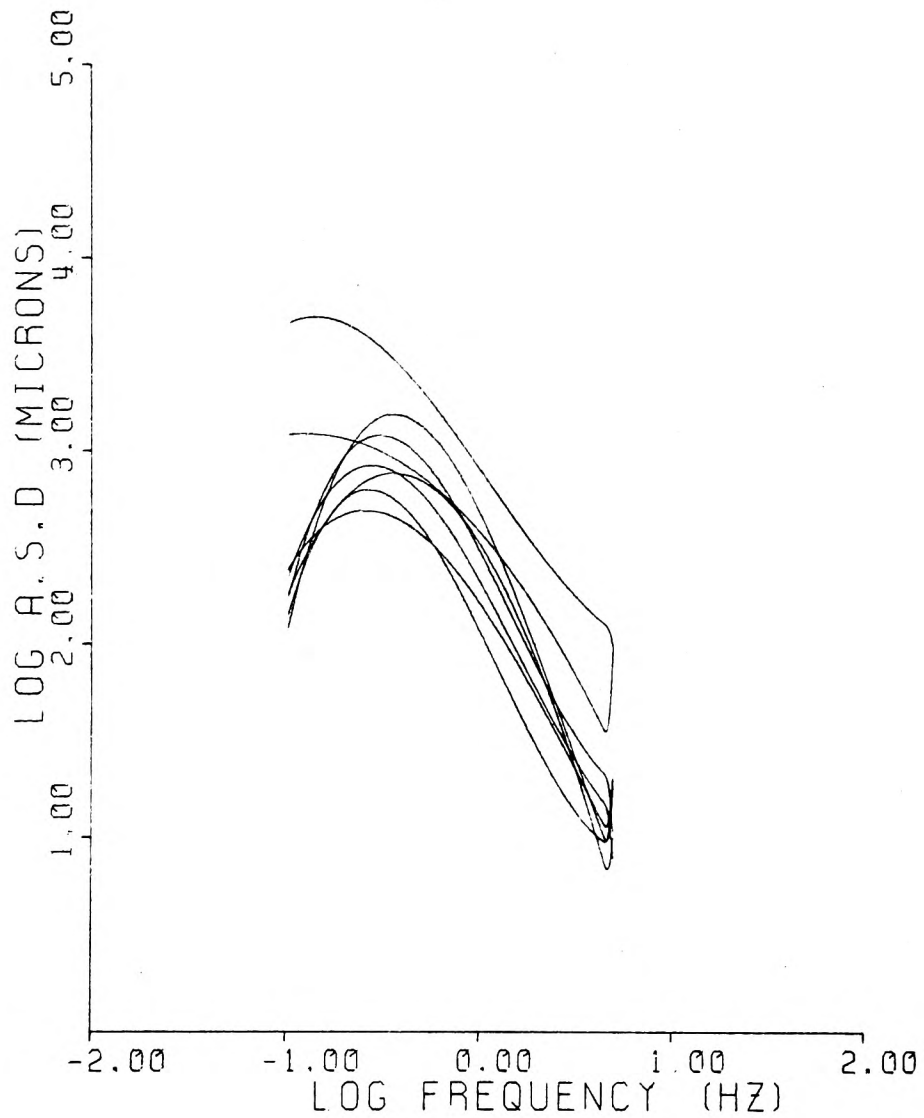
Fig. 4.17 : CHILE DATA: CB022: SMOOTHED SPECTRA
AT 10 ARRAY STATIONS.



CUBIC SPLINE FIT TO SEISMIC SPECTRUM.

CHILE DATA: CB022 (Z/BL)
SPECTRA AT 10 ARRAY STATIONS

Fig. 4.18 : CHILE DATA: ALL EVENT SPECTRA
AT A SINGLE STATION.



CUBIC SPLINE FIT TO SEISMIC SPECTRUM.

CHILE DATA: ALL EVENTS AT C.P (Z/BL)
SPECTRA OF: 01,0B,0C,22,14,11,13,18

suppressed by the same token as long periods are being lifted.

4.5.0 Pre-Signal Noise and the Final Picture:

To get an idea of pre-signal noise levels we present Figure 4.16. Despite the shorter time window of the noise preceding CB014 at the 6 SAAS stations, the signal spectra seem to be well above noise level as expected. Note that the actual noise level is beyond 1s period. Before that frequency the spectrum looks distorted - an effect, we believe, might well be due to truncation of the time sample.

In order to compare the earthquake spectra from a given source with the simulated "best fit" record constructed from their sum, we need to represent groups of such spectra on a single plot. For this purpose we wrote a simple software to perform just that. Examples of the output plots are illustrated in Figures 4.17 and 4.18 where the spectra of a single event at a number of stations and a number of events at a single station are displayed. Plots like those in Figures 4.17 and 4.18 where individual spectra are annotated along with the equivalent seismograms such as those presented in Chapter 3 will be the form in which the bulk of our results are presented in Chapters 6 and 7.

4.6.0 Discussion:

The end of this chapter marks the conclusion of the first part of this thesis which included the areas of data processing, experimental procedure and analysis techniques. What remains is to discuss the data, outline the receiving network, and

present the results arrived at employing the methods and techniques explained so far. This constitutes the second part of this thesis in which Chapters 5 and 6 are devoted to the far-field Chile Source observed from SAAS, while Chapter 7 contains our findings regarding the near-field Rabaul data set.

Before concluding this chapter, however, it is worth mentioning that there are other spectral analysis techniques namely: the 2-D Fourier Transform, the Walsh Transform and the Maximum Entropy Method which we investigated but did not implement. The main reason was the time factor involved plus our feeling that we had not yet developed a full understanding and mastery of these techniques to the extent where we can confidently base our interpretations. We, therefore, think it would be a useful piece of research to implement several analysis techniques, using our hypothesis, with the objective of establishing the most effective.

CHAPTER 5

CHILE DATA : DESCRIPTION AND OBSERVATION

1.0.0 INTRODUCTION:

The aim of the present chapter is to describe an earthquake source monitored from a seismic array. The objectives of such an investigation are:

- (a) To test the validity and extent to which the hypothesis can be applied to a relatively distant source.
- (b) To investigate the characteristics of the source and propagation effects using array records.
- (c) To explore the possibility of simulating large earthquake motions from a suitable combination of aftershock records and independent events not related in time to the main shock, but which share similar source conditions.

Among the IGS library of analogue recordings were the South American Array System (SAAS) collection of tapes. These tapes, as well as being readily available, matched the above objectives.

The source region, as will be shown later in the chapter, is one of the most seismically active regions in the World. Located between 19° - 22° S and 69° - 70° W, it forms an integral part of the Andes Mountain range occupied by Northern Chile and Southwestern Bolivia. The source-array distance is about 2270km ($\Delta=20.5^{\circ}$) at the azimuth of approximately 71° (Fig. 5.1).

The chapter is conveniently divided into 4 sections. An introduction followed by a description of the array; its layout, location, instrumentation and other characteristics. The third gives a general description of South American seismotectonics, while Section 4 is an outline of the earthquake data studied and presented in Chapter 6.

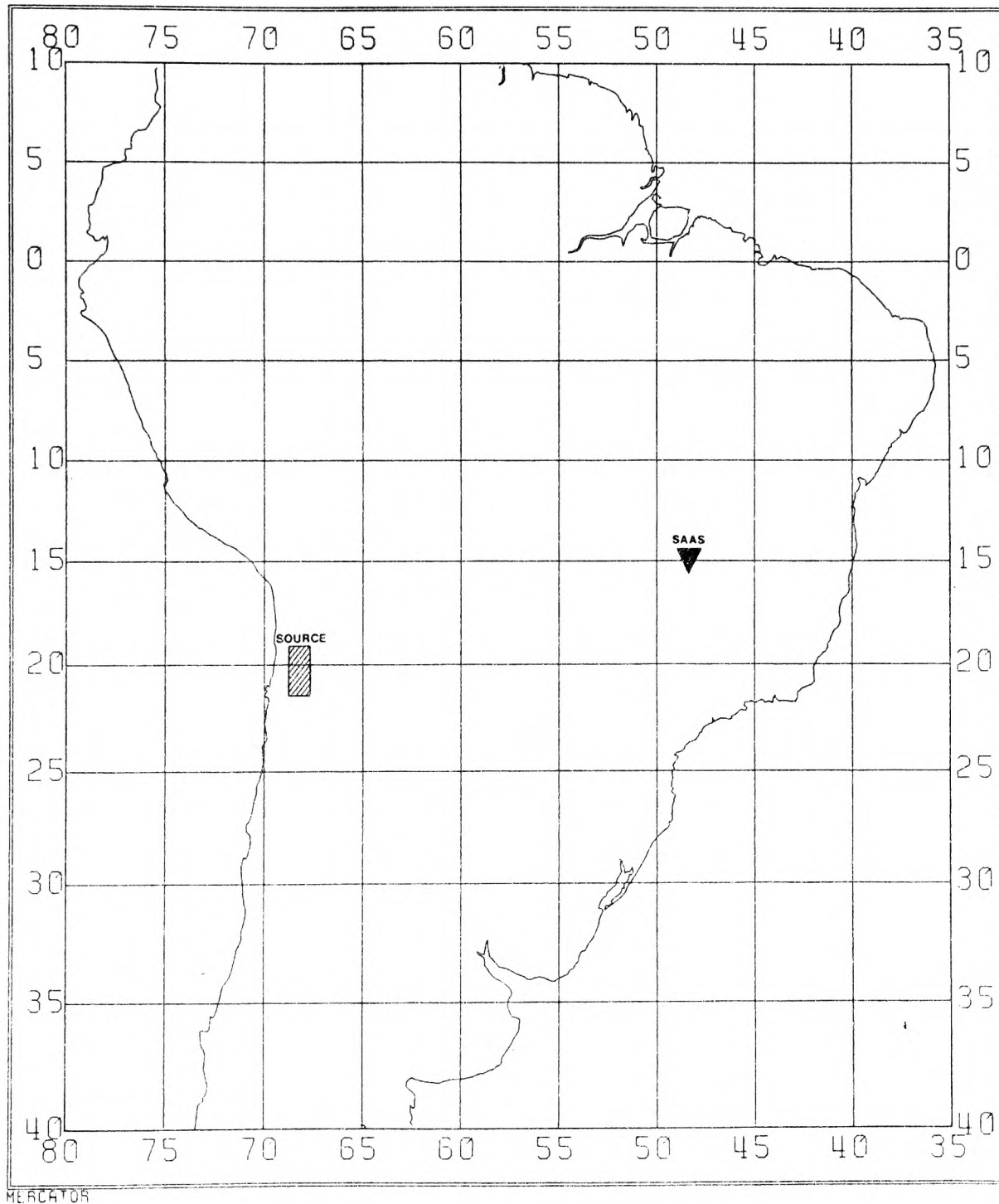


Fig 5-1 AREA OF STUDY

2.0.0 THE ARRAY:

2.1.0 SAAS Location and Layout:

The South American Array System, owned, operated and maintained by the University of Brazilia, is located on the Central Brazilian Plateau. The array consists of two linear segments perpendicular to each other forming an asymmetrical "T". The array orientation is approximately NS-EW with the central point "CP" 28km northwest of the Brazilian capital (Fig. 5.2 and Table 5.1).

The aperture of the array in EW direction is 56km. The NS line extends 37km from CP. All stations of the array except EEX, WEX, and SEX, are approximately 2.2-2.5km apart.

2.2.0 Topography and Surface Geology Occupied by SAAS:

The Brazilian Plateau lies in the middle of the Brazilian Shield, a tectonically stable region, characterised by a low level of seismicity. A few stations, notably S1, S3, and S4, have a higher level of noise because they are located on sediments in addition to their proximity to the city of Brazilia.

Topographically, the area is generally flat with few hills and small valleys. Such a morphology offers a good line of sight for radio transmission and accessibility. Most of the surface geology consists of recent, thick, unconsolidated sediments. The basement rock, mainly quartzite and other metamorphic rocks, outcrop in some places within the plateau. Stations E1, E2, E3, and E4 are situated on these outcrops.

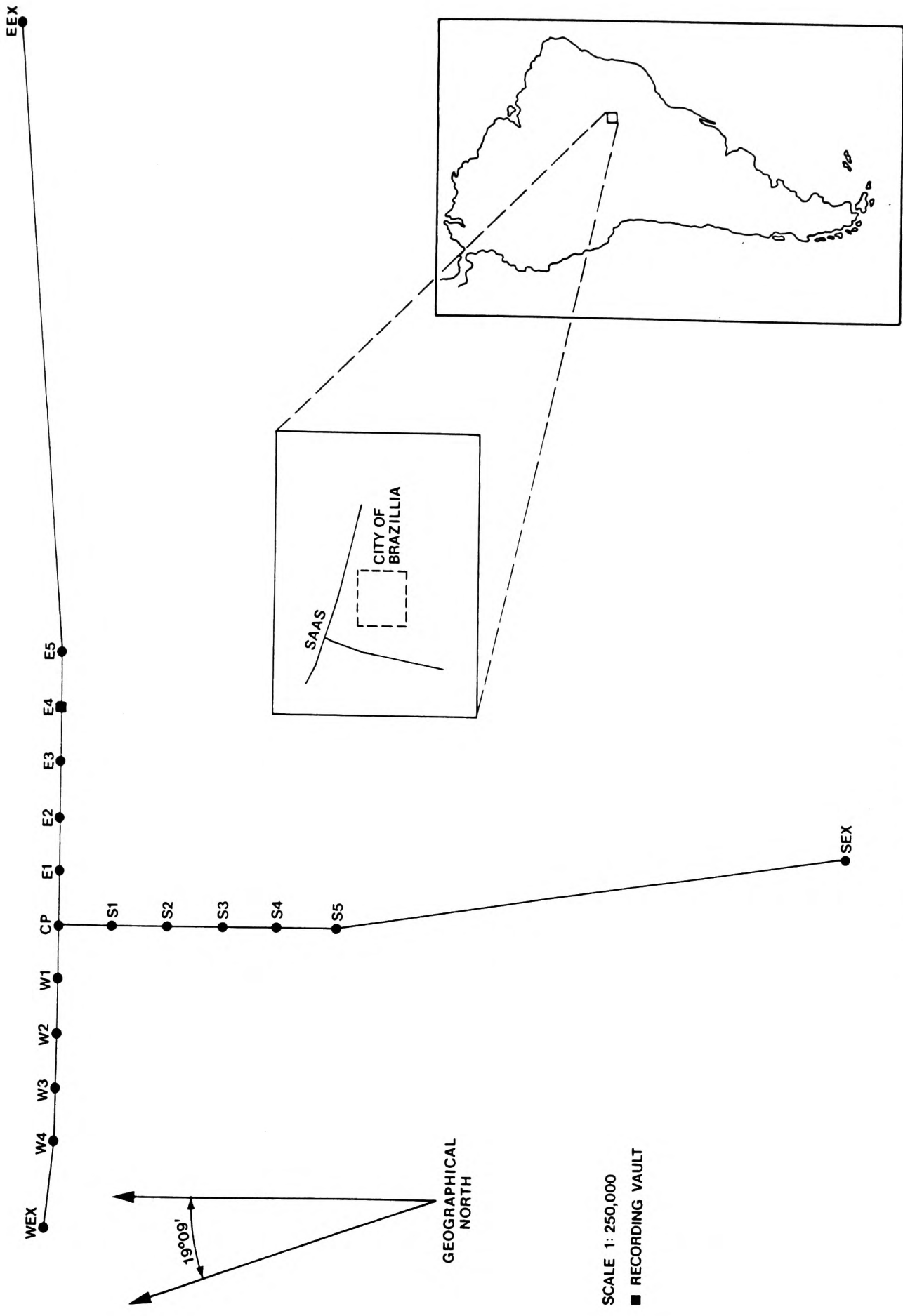


Fig 5-2 THE SOUTH AMERICAN ARRAY SYSTEM

TABLE 5.1

SAAS STATION CO-ORDINATES AND ALTITUDE

STATION CODE	LATITUDE (SOUTH)			LONGITUDE (WEST)			ALTITUDE (m)	WSSN CODE
	°	'	"	°	'	"		
CP	15	38	05.6	47	59	29.4	1211.0	BAO
E1	15	38	33.2	47	58	07.9	1187.0	
E2	15	39	00.3	47	56	49.0	1115.0	
E3	15	39	25.0	47	55	34.5	1118.0	
E4	15	39	51.1	47	54	11.2	1260.0	BDF
E5	15	40	20.9	47	52	51.2	1260.0	
EEX	15	44	18.5	47	37	11.8	1105.0	
W1	15	37	41.7	48	00	46.0	1187.0	
W2	15	37	16.7	48	02	07.0	1282.5	
W3	15	36	45.4	48	03	27.0	1253.0	
W4	15	36	18.7	48	04	46.0	1271.0	
WEX	15	35	27.4	48	04	50.0	1375.5	
S1	15	39	22.1	47	59	58.9	1127.0	
S2	15	40	40.5	48	00	25.1	1072.0	
S3	15	41	55.1	48	00	52.7	1125.0	
S4	15	43	08.9	48	01	20.2	1115.0	
S5	15	44	31.2	48	01	49.5	1142.0	
SEX	15	57	26.7	48	04	14.0	1217.0	

2.3.0 SAAS INSTRUMENTATION:

2.3.1 Detection Equipment:

Each station of the array is equipped with a short period vertical component Willmore MKII Seismometer set at 1.0S period. E4, has in addition 2 short period horizontal component seismometers, viz. N-S and E-W. These electromagnetic transducers are fitted with 3300 ohm coils giving an approximate velocity sensitivity of 5.7 volts/cm/s.

The amplifier modulator unit (Racal-Thermionic D 4980) of 210 Hz centre carrier frequency, is set at a common gain of x2000.

2.3.2 Recording Equipment:

The recording equipment, housed in an underground vault at E4, includes a Racal-Thermionic T8100 analogue recorder with 2x12 track interlaced recording heads. The 1-inch recording tapes are spooled on 8-inch diameter reels giving about 1800ft of tape or approximately 52 hrs of recording when the operating speed is 15/128 inch/s.

The recorder has 24 channels of preamplifiers and auxiliary interface circuits, 3 of which are non-seismic; 2 for flutter compensation and 1 for time. The time encoder, driven by a crystal oscillator produces second, minute, and day marks up to 32 days.

2.3.3 Instrumental Response:

A typical velocity response curve of a Willmore MKII Seismo-

meter is shown in Figure 5.3. The figure also depicts the amplitude magnification of the whole Seismographic System, incorporating a Racal-Thermionic T8100 recorder replayed at 7.5 inch/s at an Amp/Mod gain of x1000 and jet pen gain of 1v/cm.

The SAAS replay unit, similar to the IGS T8100's at Edinburgh, differ only in output gain. This difference is such that the IGS units are a factor of 10 greater than the SAAS unit when the deviation from the centre carrier frequency is 40%.

As explained in Chapter 2, the analysed data were actually replayed and processed on the EMI SELab 5000 playback unit. No magnification curve has been obtained for this system but it is maintained that the EMI amplitude response, replayed under similar conditions, is identical to the T8100 response (Houliston, personal communication).

2.4.0 SAAS Capability:

The detection capability of a seismic array is a function of many factors, most important are the following:

- (i) Location of the array relative to regional and local noise sources.
- (ii) Instrumentation employed.
- (iii) Crustal structure under the array.
- (iv) Seismic path and source characteristics.

In the previous 3 sections we briefly outlined criteria (i) and (ii). More significant are (iii) and (iv).

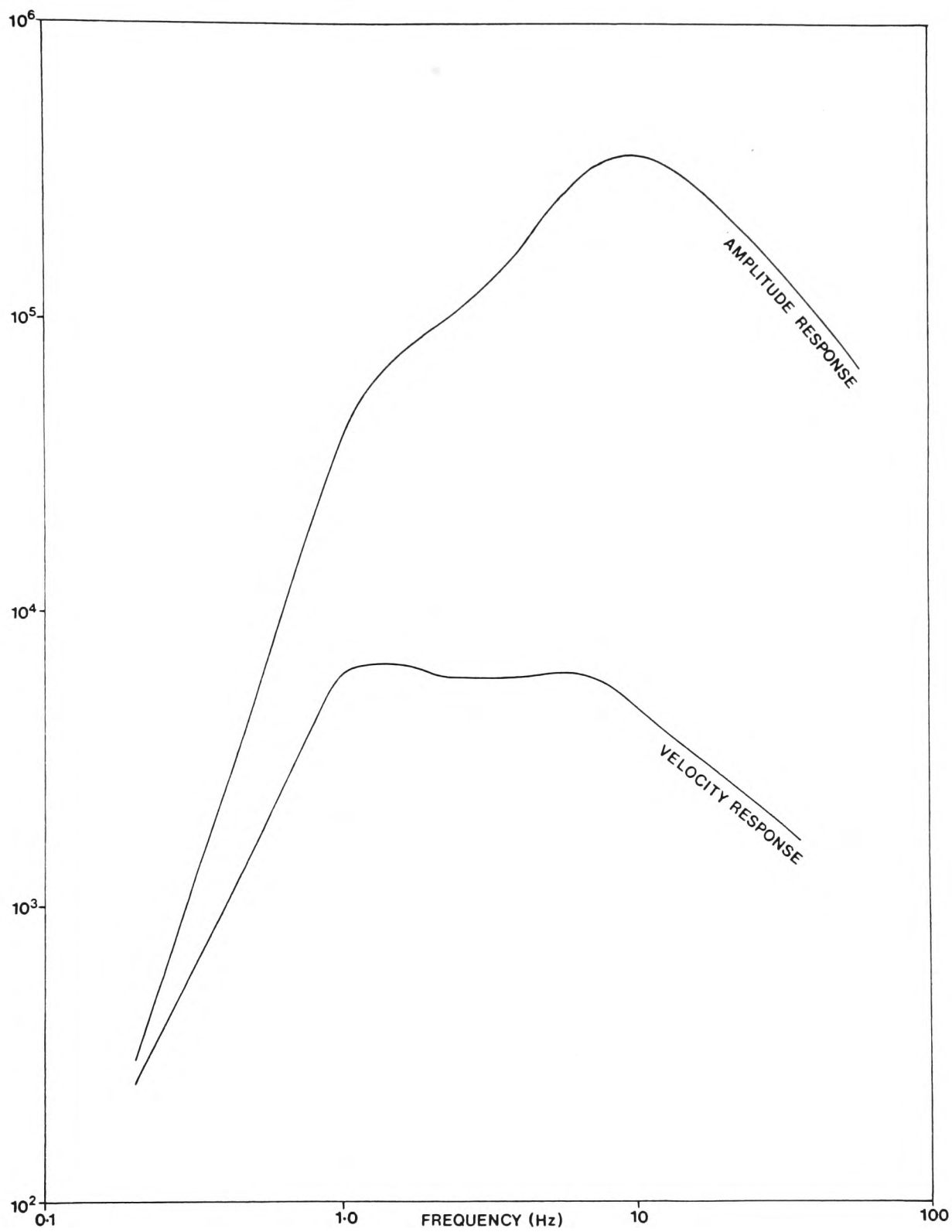


Fig 5-3 WILLMORE MK II SEISMOMETER

2.4.1 Effect of Structure Under SAAS:

Using PKIKP phases from events with $\Delta > 160^\circ$, Berrocal (1974) assessed the effect of shallow crustal structure under SAAS on the travel time of P-waves. Station corrections thus obtained varied between 0.1s for E2 and -0.01s for S1. These residuals were attributed to variations in the surface structure and topography underlying the two lines of the array. (loc.cit, Chapter 6).

The early arrivals at E2 relative to CP were explained as being due to the difference in thickness of the quartzite formation. The relatively late arrivals of the N-S stations, however, were caused by the thick recent sedimentary deposits beneath this line.

The deep crustal structure under SAAS, on the other hand, was deduced to be relatively simple with the Moho almost horizontal. Testimony for this conclusion came from two observations:

(a) The distribution of residuals in azimuth (ΔAz) and apparent velocity (ΔAV) of the 200 earthquakes studied by Berrocal (1974) differed markedly from that suggested by Otsuka (1966, Fig. 5.4). No cyclic variation in ΔAz and ΔAV was observed.

(b) Along a similar line of argument, if the Moho had a noticeable dip under the array, then opposite azimuth events should show proportionally similar relative residuals. This was not found to be the case.

Therefore the possibility of a dipping Moho under SAAS seems remote and unsubstantiated.

2.4.2 Seismic Path Properties:

Generally speaking, the Andes structure offers favourable conditions for the transmission of seismic waves in the direction of SAAS. According to Berrocal's study earthquakes originating from the source region show the following properties:

- (a) Early Arrivals (negative ΔTT).
- (b) Larger Amplitudes (positive Δm_b).
- (c) Higher Apparent Velocity (positive ΔAV).
- (d) Greater Azimuths (positive ΔAz).

Seismic waves with early arrivals and larger amplitudes than expected most probably indicate a low attenuation (high Q) propagation path. Positive ΔAV , on the other hand, is best explained by the existence of a NS high velocity horizontal discontinuity at depths of about 600km. The greater azimuth observed could well suggest a lateral discontinuity in and around the source region. Figure 5.4 illustrates the tectonic model inferred from Berrocal's study.

Part of the next chapter will be concerned with re-evaluating the kinematic and some dynamic source parameters of the earthquakes used in this research. Our observations will be shown to generally agree with the above model.

Having described the array we move on to outline the general seismotectonic "pattern" of South America, with some mention of the geology of the source region.

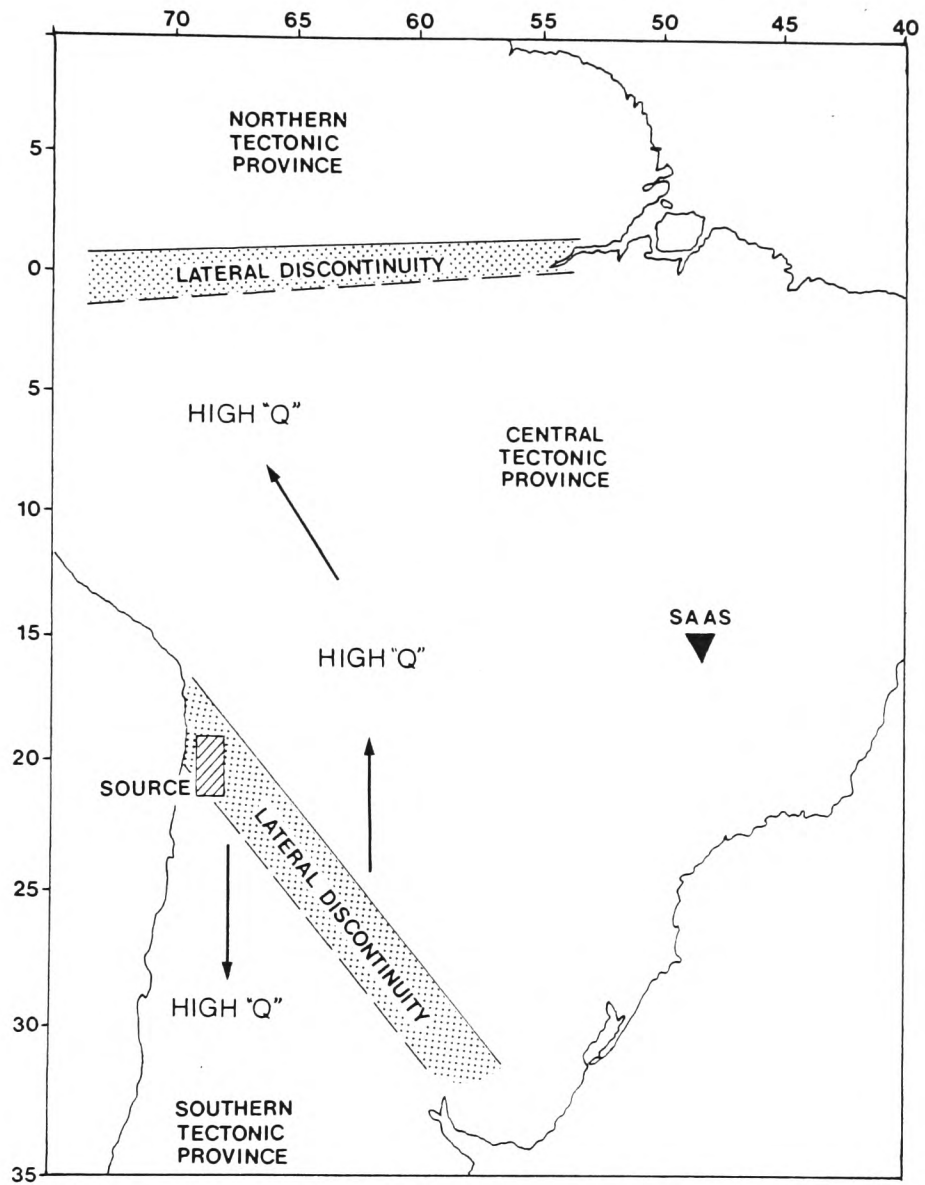


**Fig 5-4 TECTONIC MODEL OF CENTRAL SOUTH AMERICA
(AFTER BERROCAL, 1974)**

3.0.0 GENERAL SEISMOTECTONICS OF SOUTH AMERICA:

The South American Continent has a complex tectonic framework characterized by a high level of seismicity along its western margin. This seismicity is primarily related to the uplift of the Andes on the emplacement of an old Paleozoic mountain range. The stable Brazilian Shield forms the core of the Continent.

Taken as a single unit, the seismicity of the Andes Range has been said to account for 14.8% of the worlds total annual energy release (Lomnitz, 1974).

Another important tectonic feature directly related to the seismic activity of the western coast of South America is the subducting Nasca plate. The mode of subduction of this plate, recently classified as a "Chilean Type" (Uyeda and Kanamori, 1979), is characterized by a low-angle thrusting of the continental plate over the oceanic plate. This mode of subduction marks the first stage in Kanamori's Evolutionary Model (Kanamori, 1977b). A subduction of this nature provides for a wide contact zone between overriding and underthrusting plates, thus creating a strong coupling force at or near the interface. It is this part of the lithosphere that has been the sight for some of the greatest earthquakes known to civilization (Kanamori, 1978).

3.1.0 Geological Setting of Northern Chile:

The western margin of South America, as well as the whole of the Circum Pacific belt, is characterized by orogenic movements

accompanied by very active Cenozoic Volcanism. According to Lahsen (1976) the late Cenozoic Volcanism of the Andes of Northern Chile is divided into 2 principal episodes:

(i) Pre-Pliocene or Miocene Volcanism:

This episode is represented by several sheets of rhyolitic to dacitic ignimbrites and andesitic strato volcanoes. An age of at least 18.7m.y. has been suggested by Ruiz (1965) for the volcanic activity associated with the oldest unit of the sequence.

The folded ignimbrites and lava flows which occurred during late Miocene mark the last tectonic compressive phase of the Andean Orogenic cycle. During this episode volcanic activity decreased and probably ceased.

(ii) Pliocene-Quaternary Volcanism:

At the end of the Miocene Volcanic episode east-west extension began and is still occurring simultaneously with volcanism. The late Pliocene peak in volcanic activity produced differential uplift of crustal blocks along an approximately north-south fault system. Characteristic volcanic rocks of this episode include several units of ignimbrites and the andesitic stratovolcanoes that occupy the Andes summits.

Out of the 470 volcanoes of the high Andes of northern Chile, 17 are still active (Ruiz, 1965; Gonzalez, 1972). With many of the volcanoes higher than 5,500m, the elevation difference between their summits and the Chile

trench reach 12-14km over a distance of 350-400km. The distribution of late Cenozoic volcanism and the principal morphostructural units generated by the extension process are shown in Figure 5.5.

3.2.0 Seismicity and Spatial Distribution of Earthquakes Around the Source:

During the past decade or so, many investigators focused their attention on the seismic activity of the western margin of South America (see for example: Santo, 1969; Isacks and Molnar, 1971; James, 1971; Kelleher, 1972; Stauder, 1973; Sacks and Okada, 1974; Swift and Carr, 1974; Barazangi and Isacks, 1976).

Since the more recent work of Barazangi and Isacks (1976) is based on a good quality large data sample, it serves as a useful guide in giving a recent and clear picture about the seismicity of the Nasca plate beneath Northern Chile. From their investigation, the following are worth noting:

- (a) There is a peak in earthquake activity between depths of about 100-130km. Most of these intermediate depth events occur between about 17° - 24° S near the major bend in the coastline between Peru and Northern Chile (loc.cit, Fig. 5.1).
- (b) Under this region the descending Nasca plate is estimated to have a dip of $25-30^{\circ}$, with the asthenosphere forming a wedge separating the oceanic plate from the continental plate (Fig. 5.6). This asthenospheric material has been the source of the Quaternary volcanism outlined in Section 3.1.0.

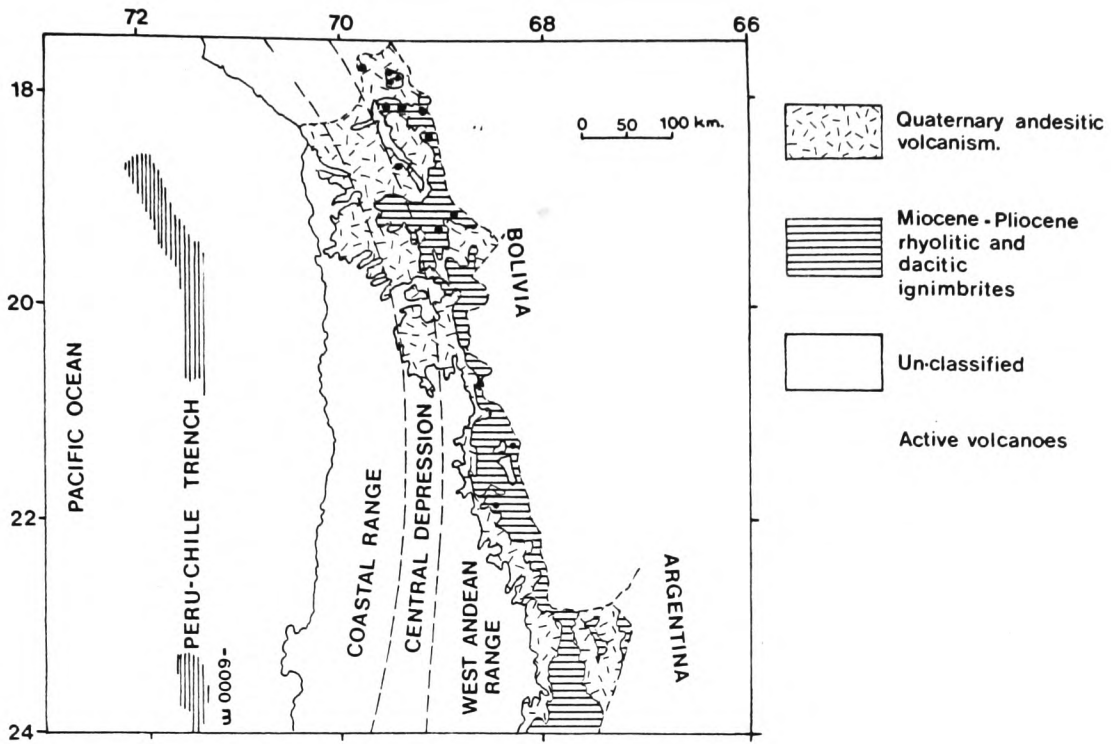


Fig 5-5 LATE DISTRIBUTION OF CENOZOIC VOLCANISM IN NORTHERN CHILE (AFTER LAHSEN; 1976)

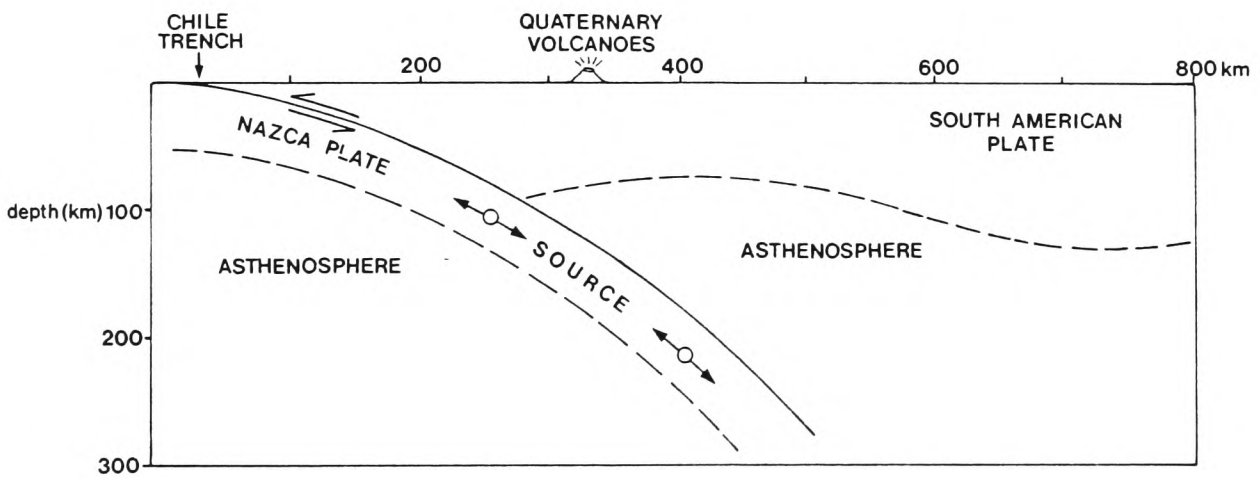


Fig 5-6 INFERRED GEOMETRY OF DESCENDING NAZCA PLATE UNDER NORTHERN CHILE (AFTER BARAZANGI & ISACKS, 1976)

(c) At its line of convergence with the oceanic plate, the South American plate is estimated to have a thickness of less than 130km.

(d) The major dynamic forces interacting to produce these intermediate depth earthquakes are extensional in nature with the stress axis parallel or sub-parallel to the dip of the Nasca plate.

3.3.0 Mechanism of Earthquakes Near the Source:

One of the most comprehensive and authoritative investigations of earthquake mechanisms around the source region is that of Stauder (1973). His work involved focal mechanisms of P and S wave data for 61 earthquakes ($m_b > 5.0$) that occurred in Northern and Central Chile during the years 1962-1970.

Stauder classified the 47 North Chilean events into 3 groups: coastal earthquakes or those of normal focal depth; those of intermediate depth, and those of deep focus. The following is a summary of his study:

(i) 25 coastal earthquakes ($30 < h < 60$ km) show one nodal plane dipping steeply ($65^\circ - 85^\circ$) to the west, with the other dipping gently ($15 - 20^\circ$) in a general easterly direction (loc.cit, Fig. 5.3).

Taking the gently dipping plane to be the fault plane, the average solution corresponds to an underthrusting of the oceanic plate in a direction $N85^\circ E$. The dip of the thrust plane at this depth is about 20° .

(ii) 14 intermediate-depth earthquakes ($100 < h < 120 \text{ km}$) show one nodal plane tending to be steeply inclined with a NW-SE strike and a second plane of relatively small dip inclined to the west or southwest (loc.cit, Fig. 5.4). The preferred motion is a normal type faulting along the steep plane.

(iii) 8 deep-focus earthquakes ($500 < h < 600 \text{ km}$). The mechanism of this group show one nodal plane steeply dipping towards the west or southwest. The second plane, of smaller dip, is inclined to the east or southeast. This suggests a compressional stress along the subducting plate.

The dip of the plate around these great depths becomes much steeper, about 60° (loc.cit, Fig. 5.9).

In Chapter 6, we present the P-nodal solutions for the earthquakes analysed in this research. The average solutions obtained will be seen to agree, in general, with the intermediate group outlined above.

4.0.0. THE DATA:

In contrast with an history of large and destructive earthquakes, the seismic zone surrounding the source has lacked a major earthquake during this century. Therefore, there is increasing likelihood that this stored tectonic strain will be released by a large event (Kelleher et al, 1973).

In line with the above prediction Yegulalp and Kuo's (1974) statistical technique point towards an expected maximum magnitude shock exceeding 8.6 within the next 100 or so years.

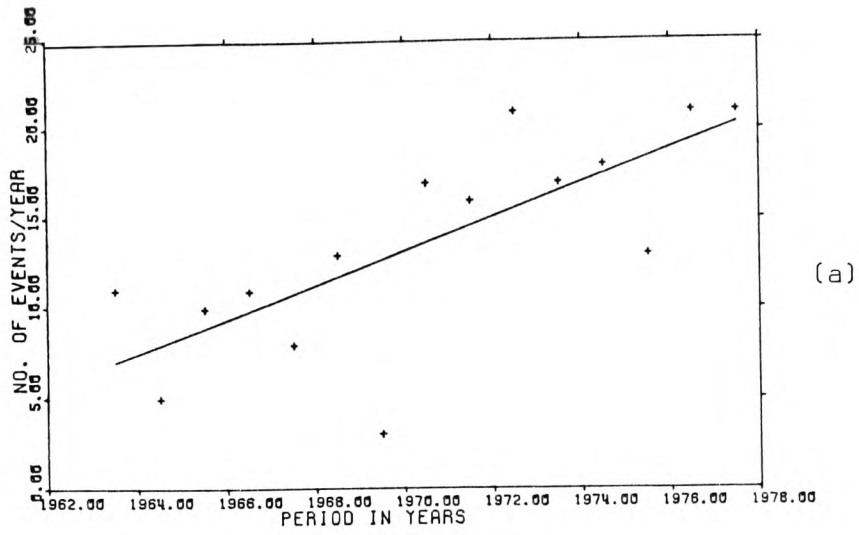
To get a clear idea of the earthquake activity within the locality of the source, we made our own assessment. For earthquakes with $M_s \geq 4.0$, a search was made into the IGS World Seismicity File. The period of search covered the years 1963-1977. Despite the apparent incompleteness of the file down to this relatively low magnitude (Burton, 1978) and although the search reflected a short time sample it nevertheless revealed remarkable features. (See Fig. 5.7).

The M_s values used to construct Figures 5.7a and 5.7b were either reported observations or converted values from m_b estimates through the application of Marshall's (1970) M_s - m_b relation. In Figure 5.7c we used the magnitude-energy conversion formula of Bath (1958).

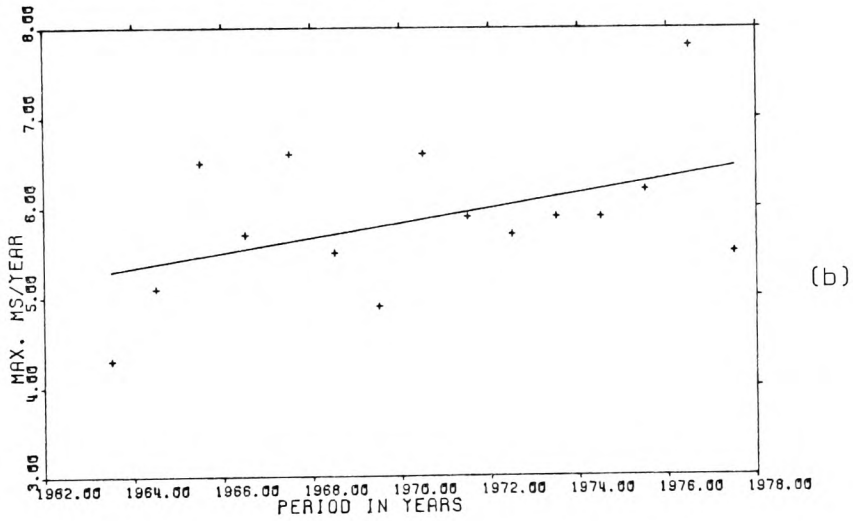
From the general character of the 3 diagrams, it is evident that a substantial rise in seismic activity occurred within the area of the source.

Along this line of thought we may put forward the argument that we are probably evidencing the development of a foreshock sequence which may have culminated in a major energy release during 1976. On the other hand, we could equally well argue that this process has not in fact subsided or ceased but that it is probably still continuing and would ultimately give way to a larger scale rupture in the form of a "Great" earthquake as was suggested by earlier predictions.

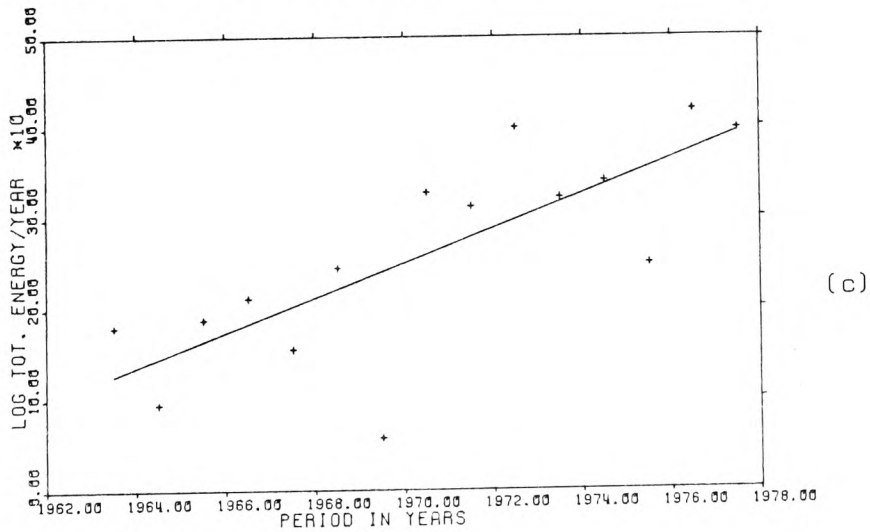
With this general introduction to the seismic activity of the source, we proceed to outline the earthquakes studied, analysed and presented in Chapter 6.



ANNUAL NUMBER OF EVENTS (1963-1977)
CHILE SOURCE REGION:19-22S;67-70W



ANNUAL MAX MAGNITUDE EVENT (1963-1977)
CHILE SOURCE REGION:19-22S;67-70W



TOTAL ANNUAL ENERGY RELEASE (1963-1977)
CHILE SOURCE REGION:19-22S;67-70W

Fig. 5.7 Seismicity of the source region

4.1.0 The Main Shock:

On 30th November 1976 at 00 40 56.5 a large earthquake ($m_b=6.5$) struck Southwestern Bolivia and Northern Chile in the Cordillera Occidental near Salar de Uyuni.

According to NEIS reports, 1 person was killed and 13 injured with considerable damage at Iquique-Pozo Amonte area, Chile. The shock registered a maximum intensity of VIII on the M.M. scale with felt intensities of V-VI throughout Tarapaca and Antofagasta Provinces. Respective intensities of IV and II were reported at Arequipa, Peru and La Paz, Bolivia.

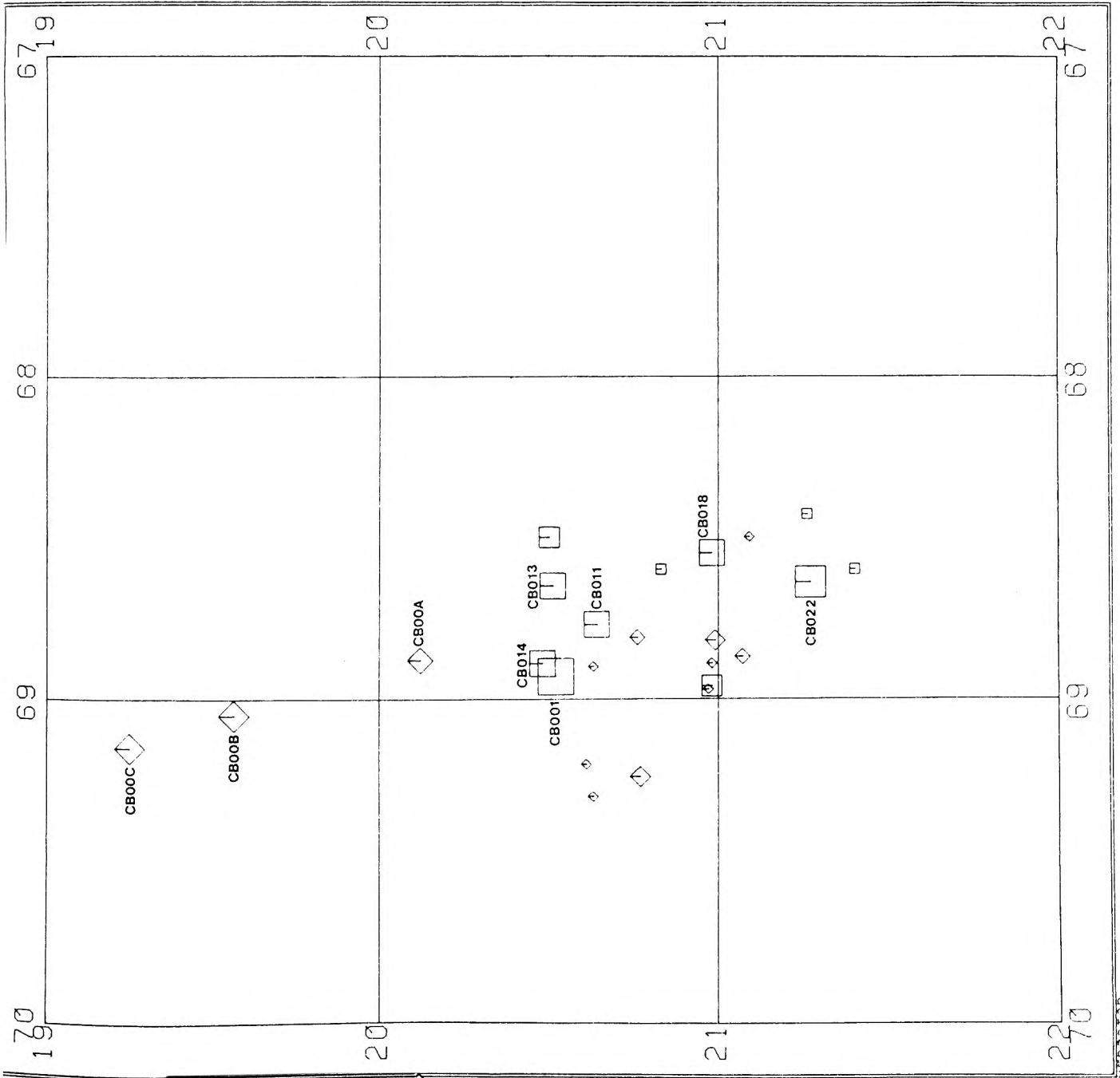
4.2.0 The Aftershock Sequence:

The main shock of 30th November was followed by a series of some 22 aftershocks during December 1976. Both NEIS and ISC give these aftershocks a range of m_b between 4.0 and 5.7. Figure 5.8 shows the epicenters of these aftershocks with respect to the main source.

Out of the 22 aftershocks reported by NEIS and ISC, only 5 were recorded at SAAS. Table 5.2, lists in chronological order, all the events with their kinematic parameters as determined by ISC.

4.3.0 Three Additional Events:

Preliminary investigation into this relatively small sample of aftershocks proved inadequate from the point of view of experimental procedure. The problem is a two-fold one and may be stated as follows:



KEY TO SYMBOLS	
DEPTHS (SYMBOL TYPES)	
+	UP TO 30.00
*	30.00 TO 60.00
□	60.00 TO 100.00
◇	100.00 TO 200.00
△	200.00 TO 300.00
○	300.00 TO 400.00
	400.00 OR GREATER
MAGNITUDE (SYMBOL RADIUS)	
·	UP TO 4.00
·	4.00 TO 4.50
·	4.50 TO 5.00
·	5.00 TO 5.50
·	5.50 TO 6.00
·	6.00 TO 6.50
·	6.50 OR GREATER

Fig 5-8 ISC LOCATIONS OF EARTHQUAKES STUDIED

MERCATOR

(a) Insufficiency of the earthquake sample:

A basic pre-requisite of the hypothesis as outlined in Chapter 1 is to acquire enough earthquake records to sample the focal region of the major earthquake source. The 5 aftershocks proved insufficient in this respect.

The problem was further augmented by the fact that at the time of recording of most of these events, approximately 1/3 of the array stations were out of order. This placed a crippling limitation on record quantity.

(b) Restriction of the Technique to Aftershock records:

Assuming that the aftershocks were enough in quantity to affect the desired progression in record simulation, then the ultimate result would, by implication, be restricted to a relatively short time sample. The resulting simulated source would then represent an earthquake rupture that excludes the stress-time history of the neighbourhood region. This in turn would render the hypothesis weaker and of less substance.

To try and remedy or at least minimize these two disadvantages, 3 additional earthquakes were selected and included in the data set. The times of occurrence of these events are not related to the 1976 main energy release, but their location relative to the main source, suggests an empirical tectonic relationship.

Note that the numbering of the main source and aftershocks in Figure 5.8 and Table 5.2 follow the sequence of their

TABLE 5.2

KINEMATIC PARAMETERS OF EARTHQUAKES STUDIED

EVENT	DATE	ORIGIN TIME	LATITUDE (SOUTH)	LONGITUDE (WEST)	DEPTH (KM)	m_b
CB00A	10/10/1972	22 42 16.0	20.12	68.88	103	5.5
CB00B	12/05/1974	10 05 54.6	19.57	69.05	107	5.6
CB00C	25/08/1975	21 42 08.5	19.26	69.15	101	5.7
CB001 (MAIN)	30/11/1976	00 40 56.5	20.52	68.93	70	6.5
CB011	03/12/1976	05 27 33.6	20.64	68.77	88	5.3
CB013	04/12/1976	05 06 40.0	20.51	68.65	95	5.1
CB014	04/12/1976	12 32 32.1	20.48	68.89	87	5.5
CB018	17/12/1976	20 23 08.1	20.98	68.55	76	5.4
CB022	28/12/1976	13 51 56.2	21.27	68.64	85	5.7

occurrence. Similarly the lettering given to the 3 independent earthquakes.

4.4.0 Discussion:

As mentioned earlier in this chapter, part of Chapter 6 will be concerned with re-evaluating the kinematic and some dynamic source parameters of the data of Table 5.2.

For the present, however, we focus our attention on Figure 5.8 and point out certain salient features that are worth noting:

- (a) All 5 aftershocks seem to cluster to the east and south-east of the main epicenter. The sequence of occurrence broadly indicates that the pattern of tectonic strain released in the aftershocks migrated in a southeasterly direction.
- (b) The location of the 3 independent epicenters (viz. CBOOA, CBOOB, and CBOOC) relative to the main epicenter suggest a continuation of the general fracture zone to the north-west.

This particular feature could be explained from a different standpoint. If we could conveniently call these events foreshocks, then we could envisage the whole process as a crack extending from NW to SE.
- (c) All events except CBOOC, lie within a radius of 100km from the main source, an indication of common stress pattern.
- (d) The depths of all the shocks show that they originated from an intermediate zone, possibly related to the tectonic

stresses acting at the interface of or within the subducting Nazca plate. (See Fig. 5.6).

Finally, we conclude this chapter with the presentation of Table 5.3. This table depicts the final picture of the studied data against each SAAS station. Those marked "X" indicate that the record was utilized in the experimental procedure and analysis. Excluding the main event, viz. CBO01, the total number of component records ready for simulation is found to be around 80 traces.

EVENT	E1	E2	E3	E4	E5	EEX	CP	W1	W2	W3	W4	WEX	S1	S2	S3	S4	S5	SEX
CB00A	X	X	X	X	X				X				X		X	X	X	
CB00B	X		X	X	X		X			X				X		X	X	
CB00C	X	X	X	X	X		X			X			X	X	X	X	X	
CB001 (MAIN)	X			X	X		X		X	X			X		X	X	X	
CB011	X			X	X		X		X	X			X		X	X	X	
CB013	X			X	X		X		X	X			X		X	X	X	
CB014	X			X	X		X		X	X			X		X	X	X	
CB018	X			X			X						X			X	X	
CB022	X			X			X	X		X			X	X		X	X	

TABLE 5.3

THE SELECTED EARTHQUAKES

CHAPTER 6

CHILE DATA : SOURCE PARAMETERS AND SEISMOGRAM ANALYSIS

1.0.0 INTRODUCTION:

In Chapter 5 we presented an observational and descriptive account of the Chile data source, the transmission path and the receiving array. In this chapter we report the results obtained for the far-field observations, through the application of the methods and techniques developed in the first part of this thesis.

The chapter begins with re-evaluating some of the important kinematic and dynamic source parameters including relocation, body wave magnitudes, source dimensions of the main shock, and focal mechanisms.

In the seismogram analysis section we discuss phase identification around the 20° -discontinuity. Apparent velocities and azimuths and their estimations is next discussed with examples. This is followed by a discussion of the summation scheme which includes a description of the concept of array transposition to the source. The direction and sequence of trigger is explained with examples.

The final section consists of presenting the results in the time and frequency domains, i.e: the seismograms and their equivalent spectra for the various summations.

2.0.0 SOURCE PARAMETERS:

2.1.0 Event Relocation:

2.1.1 "SPEEDY":

We start our re-evaluation of parameters by relocating the Chile earthquakes. For this purpose we used a simple and effective location program often used in GSU practice known as "SPEEDY" (Douglas, et al, 1974). The logic behind the algorithm is based on Geiger's method for estimating the standard errors of determining the focal co-ordinates and joint confidence regions for epicentral location. The method consists of linearizing and solving by iteration the non-linear least squares location problem. In computing, the confidence regions constructed in the linearized problem become exact asymptotically as the number of recording stations used gets larger (Flinn, 1965).

SPEEDY computes the epicenter, depth and origin time of a seismic event, given the arrival times of the P-phases at 4 or more stations. If the arrival times are available from only 3 stations, then either depth or origin time must be restrained (kept constant) to some initial value. For less than 3 arrivals no solution is possible.

Using the J-B (1967) or Herrin (1968) P-travel time tables, the program employs the equation of condition:

$$\delta T_j = \delta H + \delta h \frac{\partial T}{\partial h} - x \cos \alpha_j \frac{\partial T}{\partial \Delta_j} - y \sin \alpha_j \frac{\partial T}{\partial \Delta_j}$$

where: $\delta T_j = A_j - H - T_j$

and H is the approximate origin time of the event.

h is the approximate depth of the event.

Δ_j , α_j are the distance and azimuth respectively from the approximate epicenter to the jth station.

A_j, T_j are the P-phase arrival and travel time respectively from the approximate epicenter to the j th station.

$\partial T / \partial \Delta_j$ is the partial derivative of the travel $T (= f(\Delta_j, h))$ with respect to distance at the point (Δ_j, h) . $\partial T / \partial h$ is the partial derivative of the travel time T with respect to depth at the point (Δ_j, h) . Both of these derivatives are obtained from the mentioned travel time tables. The unknowns $x, y, \delta h$, and δH are the corrections to latitude, longitude, depth and origin time respectively.

The condition matrix of normal equations are solved by matrix inversion. Given a set of condition equations of the form:

$$(X) \vec{\beta} = \vec{y}$$

where (X) is the matrix of coefficients of the condition equations.

$\vec{\beta}$ is a vector of corrections to trial estimates.

\vec{y} is the vector of residuals.

SPEEDY computes estimates $\hat{\vec{\beta}}$ of $\vec{\beta}$ by least squares, hence:

$$\hat{\vec{\beta}} = (S)^{-1} (X)' \vec{y} \quad (6.1)$$

where $(S)^{-1}$ is the inverse matrix of $(X)' (X)$

and $(X)'$ is the transpose of (X)

$$(S) \hat{\vec{\beta}} = (X)' \vec{y}$$

are called the normal equations.

According to Lilwall (1969) poorly determined solutions of equation (6.1) occur when the determinant of the matrix approaches zero. This is reflected in abnormally large confidence limits on the least squares solution. The reason for this is that the confidence limits depend on the square root of the diagonal elements of the inverse $(S)^{-1}$ (Douglas, 1966), and since the elements of $(S)^{-1}$ are proportional to $1/\text{DET}(S)^{-1}$, therefore a small determinant tends to lead to a large confidence region.

The program incorporates a simple form of rejecting inconsistent data based on the method of Herrin et al (1968). By the first iteration the standard deviation σ is calculated and the data truncated at $\sigma=2$ about the median and not the mean. This helps eliminate skewness (Lilwall, 1969). σ is then recomputed, corrected for truncation (Freedman, 1966) and the original sample truncated as before but using the new σ . This process is repeated until successive iterations yield changes small enough to be neglected.

2.1.2 Results:

The P-arrivals, epicenters and depths of the Chile earthquakes input to SPEEDY were those reported by ISC. Table 6.1 lists the new latitudes and longitudes with the 95% confidence limits and the standard deviations. Figure 6.1 shows the relocated events.

Comparing Figure 6.1 with the original ISC locations of Figure 5.8 we see that the relocations have more or less the

TABLE 6.1 Re-evaluation of Kinematic Parameters

EVENT	DATE	ORIGIN TIME	LATITUDE (SOUTH)	LONGITUDE (WEST)	DEPTH (km)	STANDARD DEVIATION (S)	Number of Degrees of Freedom	95% Confidence area (km ²)
CB00A	10/10/1972	22 42 18.1	20.045	68.722	103	0.546	45	81.41
CB00B	12/05/1974	10 05 57.1	19.451	68.889	107	0.443	88	42.93
CB00C	25/08/1975	21 42 10.7	19.240	69.004	101	0.387	61	30.05
CB001 (MAIN)	30/11/1976	00 40 58.3	20.474	68.810	70	0.477	136	30.32
CB011	03/12/1976	05 27 36.2	20.476	68.689	88	0.483	63	79.71
CB013	04/12/1976	05 06 42.4	20.513	68.868	95	0.471	42	99.25
CB014	04/12/1976	12 32 34.0	20.335	68.639	87	0.424	75	60.36
CB018	17/12/1976	20 23 10.3	20.950	68.431	76	0.430	47	58.18
CB022	28/12/1976	13 51 58.5	21.140	68.543	85	0.460	109	35.25

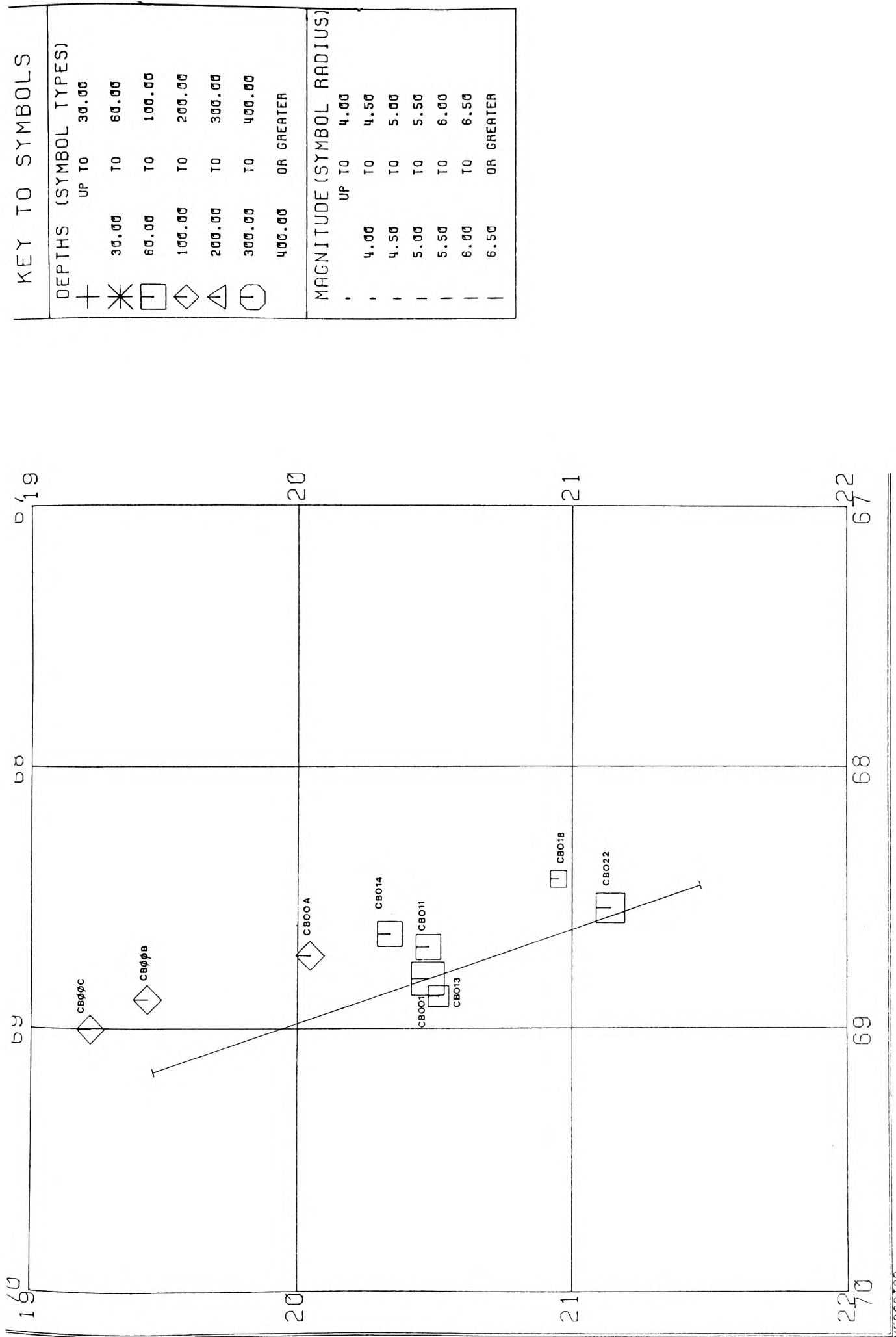


FIG (6.1) RELOCATION OF THE CHILE EARTHQUAKES

MERCATOR

same configuration as before. The new epicenters seem to be shifted as a whole to the NE by about 10-15km with the relative locations of individual events, especially those of the after-shocks, slightly more drawn nearer the major shock.

In the preliminary runs of SPEEDY we found that not restraining depth resulted in unstable solutions. The results listed in Table 6.1, therefore represent the most likely fit using Herrin (1968), restraining depth values to those reported by ISC from pP-P observations and rejecting residuals $> 0.9s$.

The resulting values of " σ " (about 0.5s) include all the variations of world wide travel times in various azimuths. However we derived some reassurance from the list of the 95% confidence regions which are well within the accepted practical uncertainty in epicentral location. According to Flinn (1965) an ellipse on the earth's surface with an area of $470km^2$ is regarded as a good solution.

2.2.0 Observation of P-Wave Residuals:

We mentioned in Chapter 5 that according to Berrocal (1974) earthquakes originating from the source region generally show earlier P-arrivals than expected, i.e: negative $\Delta T.T$ at most SAAS stations. To investigate this we selected SAAS: E4 and S5 at which all the Chile earthquakes were recorded. The P-arrivals were picked to within 0.01s using maximum paper speed, maximum jet pen gain and a bandpass of DC-10Hz. Table 6.2 lists the calculated arrivals using Herrin (1968), those observed and the resulting residuals at E4 and S5. The

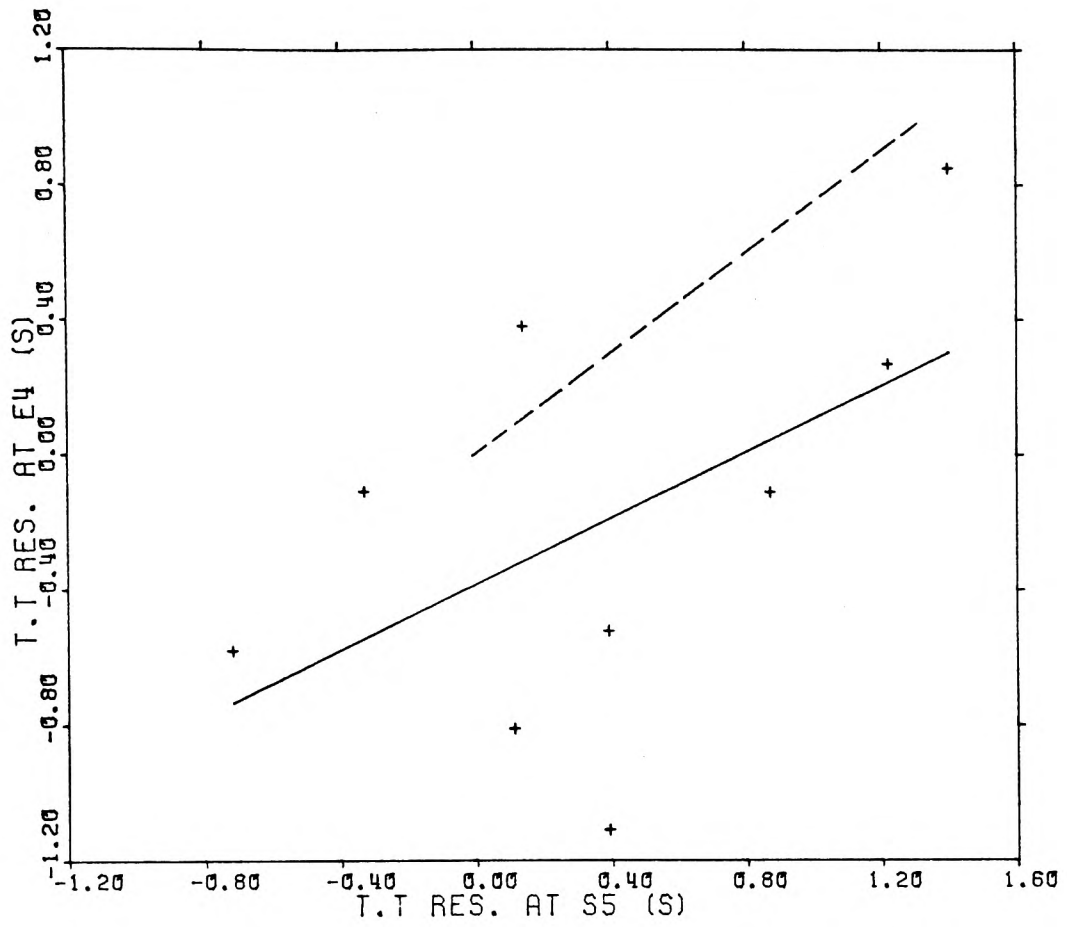
TABLE 6.2 P-Residuals at SAAS : E4 and E5

EVENT	DATE	ORIGIN TIME	E4				S5								
			CALCULATED P-ARRIVAL	OBSERVED P-ARRIVAL	Δ (deg)	$\Delta T.T$ (s)	CALCULATED P-ARRIVAL	OBSERVED P-ARRIVAL	Δ (deg)	$\Delta T.T$ (s)					
CB00A	10/10/72	22 42 18.1	22 46 45.43	22 46 44.38	20.3	-1.11	22 46 43.18	22 46 43.63	20.1	0.39					
CB00B	12/05/74	10 05 57.1	10 10 25.09	10 10 24.34	20.4	-0.81	10 10 22.94	10 10 23.11	20.2	0.11					
CB00C	25/08/75	21 42 10.7	21 46 39.16	21 46 40.07	20.4	0.85	21 46 37.44	21 46 38.90	20.3	1.40					
CB001	30/11/76	00 40 58.3	00 45 29.08	00 45 28.56	20.4	-0.58	00 45 28.01	00 45 27.44	20.3	-0.72					
CB011	03/12/76	05 27 36.2	05 32 04.55	05 32 04.09	20.3	-0.52	05 32 03.48	05 32 03.93	20.2	0.39					
CB013	04/12/76	05 06 42.4	05 11 12.37	05 11 12.32	20.5	-0.11	05 11 11.30	05 11 11.03	20.4	-0.33					
CB014	04/12/76	12 32 34.0	12 37 02.43	12 37 02.76	20.3	0.27	12 37 00.28	12 37 01.56	20.1	1.22					
CB018	17/12/76	20 23 10.3	20 27 38.47	20 27 38.42	20.2	-0.11	20 27 36.30	20 27 37.23	20.0	0.87					
CB022	28/12/76	13 51 58.5	13 56 27.08	13 56 27.52	20.3	0.38	13 56 26.00	13 56 26.20	20.2	0.14					
						Mean $\Delta T.T$ = -0.190s					Mean $\Delta T.T$ = 0.386s				
						Standard Deviation = 0.62					Standard Deviation = 0.69				

appropriate station corrections given by Berrocal were applied (loc. cit, Table 8). Source and ellipticity corrections were neglected since both are assumed to be constants.

The mean of $\Delta T.T$ indicate earlier arrivals at E4 while at S5 the arrivals are late. The standard deviations are comparable at both stations but their high values reflect the considerable scatter in readings. Figure 6.1a shows a plot of the $\Delta T.T$ values at E4 against those at S5 for all shocks. The distribution of data points seems to reflect the source map of Figure 6.1 with a definite trend. The regression line has a slope of about 0.5 and a y- intercept of about -0.4.

The contrast in arrivals between E4 and S5 which amount to approximately 0.6s appear to correlate with the subsurface geology beneath the two sites (see Section 2.2.0, Chapter 5). More importantly, however, is the local structure under E4 and S5. If the structure under every point of SAAS were similar, if the Moho was horizontal, and if the altitude of the stations were the same, then the observed arrival times should ideally be identical to the expected ones (i.e: almost simultaneous arrivals, with small allowances for azimuth and range). This would be portrayed by the broken line of Figure 6.1a which passes through the origin and has unity slope. Since the possibility of a dipping Moho under SAAS was discounted (see Section 2.4.1, Chapter 5) and because the difference in altitudes between E4 and S5 can only account for a fraction of the observed 0.6s relative residual, the major contributing factor to the anomaly has to be attributed to the difference in thickness between the formations underlying the two stations.



CHILE DATA: P-WAVE RESIDUALS
AT SAAS: E4 AND S5

Fig. 6.1a P-Wave Residuals

Obviously the true dimensions depend on the P-wave velocity distribution of the layers involved and our small sample is not sufficient to give such a detailed picture. It would, therefore, be valuable to investigate the effects of local structure under SAAS through measurements of large samples of teleseismic P-phases (see for example: Niazi, 1966; Cleary et al, 1968; Corbishley, 1970; Wright et al, 1974), or by crustal studies in the vicinity of the array (Agger and Carpenter, 1964).

2.3.0 Estimation of Body-Wave Magnitude " m_b ":

Here we attempt to re-evaluate m_b from the short period vertical components of the Chile events. For this we employ the Gutenberg-Richter (1956) formula:

$$m_b = \log_{10} (A/TK) + Q(\Delta, h) + \delta(s, p, r)$$

where: A is the peak to trough ground amplitude (mm).

T is the P-wave period (s).

K is the magnification in thousands at T.

$Q(\Delta, h)$ is the distance-depth factor.

$\delta(s, p, r)$ is the source - path - receiver correction.

In applying the above formula the term $\delta(s, p, r)$ was omitted since very little is known about these corrections. For the seismograms where the major portion of the P-coda is saturated, it was difficult to measure amplitudes. The only other option open to us was to try and reconstruct that part of the waveform by "filling-in" the clipped peaks and troughs. Extra care was taken in reconstructing the measured P-phases

making sure that the amplitudes, periods and arrivals were consistent across the array.

The uncertainty in reconstruction and in reading appears to be within practical limits as evidenced by the standard deviation and number of observations listed along side the m_b estimates in Table 6.3. The table also includes the ISC estimates of m_b with the resulting residuals Δm_b . On average, Δm_b indicates that our estimates are greater than the ISC values by less than $\frac{1}{2}$ a unit. This supports Berrocal's findings regarding the larger amplitudes recorded at SAAS, which were explained as being due to a high Q path. This may well be a contributing factor. But what Berrocal had not speculated upon, at this distance range, however, is the possibility of the existence of a 20° -discontinuity around depths of about 400km (Julian and Anderson, 1968; Lehmann, 1974, 1970). We therefore are inclined to suggest that the observed large P-amplitudes observed at SAAS as compared with ISC estimates are probably due to the coupled effect of a low attenuation path and the refraction of these waves at a deep high velocity layer.

Unfortunately our insufficient data sample plus the restriction of the distance range to the threshold of the 20° -discontinuity offers inconclusive evidence in support of our claim.

An interesting investigation would be to collect a large sample of ΔT and Δm_b from earthquakes at a distance range of at least $10-30^\circ$ in the direction of SAAS with the view of studying source and path properties in order to establish whether the suggested discontinuity exists or not.

TABLE 6.3 Body Wave Magnitudes and Residuals at SAAS

EVENT	SAAS			ISC		Δm_b
	m_b	σ	n	m_b	n	
CB00A	6.08	0.05	7	5.50	35	0.58
CB00B	6.06	0.07	6	5.60	56	0.46
CB00C	6.19	0.11	7	5.70	39	0.50
CB001	6.89	0.13	8	6.50	61	0.39
CB011	5.61	0.10	8	5.30	28	0.31
CB013	5.23	0.15	8	5.10	17	0.13
CB014	5.86	0.08	8	5.50	48	0.36
CB018	5.01	0.13	8	5.40	34	0.39
CB022	6.30	0.09	7	5.70	64	0.60

TABLE 6.4 Surface Wave Magnitudes and Energies

EVENT	m_b	M_s	E_s ($\times 10^{22}$)
CB00A	6.08	7.00	2.0893
CB00B	6.06	6.95	1.7378
CB00C	6.19	7.22	4.3652
CB001	6.89	8.68	549.5400
CB011	5.61	6.02	0.0813
CB013	5.23	5.23	0.0059
CB014	5.86	6.54	0.4571
CB018	5.01	4.77	0.0013
CB022	6.30	7.45	9.3325

(see Section 3.1.0 for further discussion).

2.4.0 Surface-Wave Magnitude-Energy Estimation:

As shown in Chapter 2, most of the surface waves for the large Chile earthquake viz: CB001 is overloaded. Therefore a similar waveform reconstruction was applied to 20s surface waves at 5 SAAS stations viz: E4, CP, S1, S4, and S5. M_s was estimated from the IASPEI (Prague-Moscow, 1962) formula:

$$M_s = \log_{10}(A/TK) + 1.66 \log_{10} \Delta + 3.3$$

where: A is the amplitude (mm) of 20s surface waves

T is the period

Δ is the epicentral distance (degrees)

An additional depth correction was applied using the Czechoslovak Geophysical Institute formula (WDC-A, Report SE-8, 1977, p.19):

$$dM_s = 0.007 (h-20) \text{ for } \Delta \approx 20^\circ, h < 100\text{km}$$

Our readings gave an M_s value of 8.57 averaged over the 5 stations. To check this result we substituted the equivalent m_D value into Marshall's (1970) formula:

$$M_s = 2.08 m_D - 5.65$$

This gave $M_s = 8.68$ which is about 0.1 of a unit higher than our estimates. Such a result encouraged us to use Marshall's formula to the other shocks. The results are listed in Table 6.4.

To assess from M_s how the total energy released by the Chile

earthquakes compares with that of CB001 we used Bath's (1958) formula:

$$\log_{10} E_s = 1.44 M_s + 12.24$$

The results are also listed in Table 6.4. It is clear from these estimates that the sum of total energies released by the individual "foreshocks" and aftershock sequence is only about 3% of the total energy radiated by CB001. This is expected and follows the exponential relationship governing earthquake size and energy (see Section 2.7.0).

2.5.0 Source Dimensions of the Large Shock:

Having obtained M_s estimates we proceed to assess the source dimensions of CB001. For this purpose we make use of some empirical relationships published by Kanamori and Anderson (1975) which incorporate source parameters like M_0 and S .

According to this work an inter-plate large earthquake such as CB001 would probably - on average - have an apparent stress " σ_a " = 10 bars and a stress drop " $\Delta\sigma$ " = 30 bars, assuming a medium of rigidity " μ " = 3×10^{11} dyne/cm². Taking these parameters as a first approximation we find that a large earthquake of $M_s \approx 8.5$ has:

$$M_0 = 10^{29} \text{ dyne-cm} \quad (\text{loc. cit. Figure 4})$$

and

$$S = 27 \times 10^3 \text{ km}^2 \quad (\text{loc. cit. Figure 5})$$

Using the above parameters in the empirical relation:

$$\bar{D} = \frac{M_0}{\mu S}$$

We obtain an average dislocation \bar{D} of about **12.3 μ m**

From the estimated fault area it is possible to deduce the fault length L (along the strike) by assuming that:

$$L = 2W$$

This approximation has been shown to give the best agreement with observational data (see for example: Abe, 1975; Geller, 1976). Employing this relation we find that:

$$L \approx 232\text{km}$$

Unfortunately we have no geological information to compare our results with. The object of the exercise, however, is merely to give an idea of the rupture dimensions. This, drawn to scale, is shown in Figure 6.1, with the fault length centred on the location of CB001 and along its deduced strike. With the exception of CB00C, all epicenters appear to fall within the major fault line. A better picture is shown in Figure 6.2.

2.6.0 Focal Mechanisms:

Using P- first motions reported by ISC we determined the focal mechanism plots for the Chile group of shocks. Figure 6.2 schematically illustrates these solutions. The detailed diagrams are given in Appendix (C) stereographically projected on the lower hemisphere. Table 6.5 lists the strike " ϕ " and dip " δ " of both the fault plane and auxiliary plane.

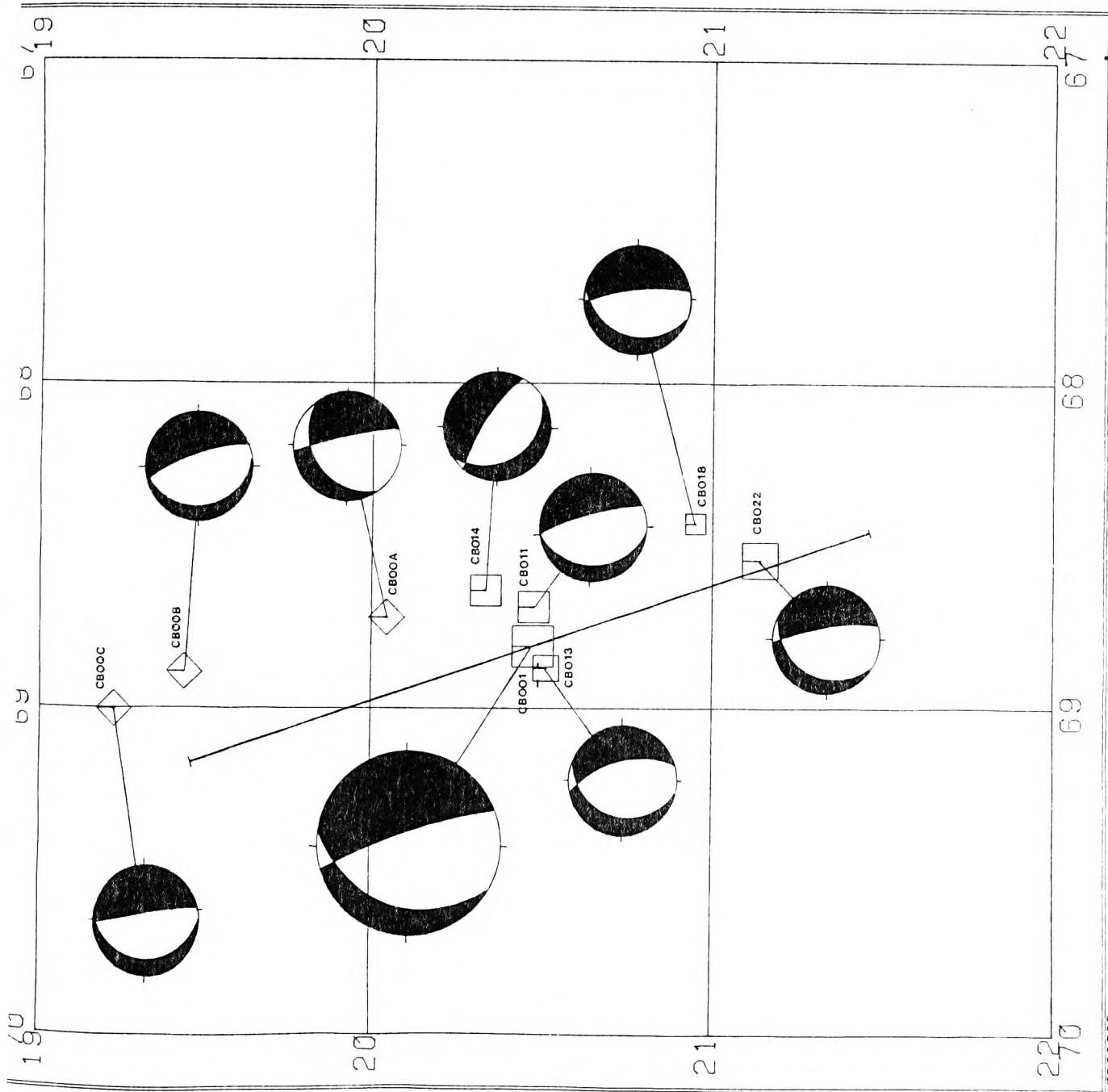


FIG (6.2) FOCAL MECHANISM OF THE CHILE EARTHQUAKES

KEY TO SYMBOLS

DEPTHS (SYMBOL TYPES)	
UP TO 30.00	
+	30.00 TO 60.00
*	60.00 TO 100.00
□	100.00 TO 200.00
◇	200.00 TO 300.00
△	300.00 TO 400.00
○	400.00 OR GREATER

MAGNITUDE (SYMBOL RADIUS)	
UP TO 4.00	
—	4.00 TO 4.50
—	4.50 TO 5.00
—	5.00 TO 5.50
—	5.50 TO 6.00
—	6.00 TO 6.50
—	6.50 OR GREATER

EVENT	FAULT PLANE		AUXILIARY PLANE	
	ϕ_1°	δ_1°	ϕ_2°	δ_2°
CB00A	N12W	82	N49E	12
CB00B	N16W	73	N-S	17
CB00C	N10W	80	N6E	10
CB001	N19W	80	N9E	11
CB011	N18W	84	N7E	6
CB013	N21W	70	N21E	24
CB014	N47W	76	N32W	14
CB018	N6W	80	N9E	10
CB022	N6W	80	N28E	12

TABLE 6.5 Focal Mechanism Parameters

From Figure 6.2 and Table 6.5 it is apparent that with the exception of CB014 all earthquake solutions generally show one nodal plane steeply dipping with a NW-SE strike, while the second plane shows a small dip inclined in a northwesterly direction.

Recalling our discussions regarding the general seismicity and earthquake mechanisms of the source region (Section 3.0.0, Chapter 5), we notice that our solutions agree well with those of Stauder (1973). The strike and dip of the steeply inclined nodal plane is therefore taken to represent the fault surface. The distribution of first motions suggests a normal type-faulting along this preferred surface.

2.7.0 Discussion:

We have so far re-evaluated the kinematic and some dynamic source parameters of the Chile data. The following points thus become apparent:

- a) From the point of view of event relocation it seems that, in general, our earlier discussion regarding the locations of these events (Section 3.4.0, Chapter 5) and the deductions made thereof are still valid. In other words, the general re-evaluated tectonic framework, as evidence by relocation, essentially remains the same.
- b) The observed P-wave travel time residuals suggest that the anomalies are probably due to local structure and geology rather than to path effects. The body-wave magnitude residuals, on the other hand, seem to imply the probable

existence of a 20° -discontinuity in the travel time curve, coupled with the presence of a high velocity discontinuity at about 400km depth, although this is not conclusive.

- c) Estimated surface-wave magnitudes and energies suggest that the total energy release of the "foreshock" and aftershock sequence amounts to only about 3% of that released by CB001.

According to Bath's (1958) $E_s - M_s$ formula it appears that in order to "regenerate" the energy of an $8.5M_s$ earthquake we require around 145 events of $7.0M_s$ and about 4000 with $6.0M_s$.

As will be shown later in this chapter we do not need so many to reconstruct the major portion of the spectral signature of the main source.

- d) Using empirical formulas we have deduced an approximate fault length of 232km for the main source. This length appears to cover most of the focal region of the smaller shocks.

- e) The determined P- mechanism solutions generally indicate a NW-SE fracture steeply dipping to the NE. The radiation pattern of all the events, particularly of the aftershocks is in general agreement with that of CB001 thus indicating normal-type faulting. This similarity in radiation between the main shock and aftershock sequence supports other observations elsewhere (see for example: Stauder and Bollinger, 1966; McEvelly and Casady, 1967; Page, 1968; Brady, 1976 for theoretical treatment).

3.0.0 SEISMOGRAM ANALYSIS:

3.1.0 The 20° -Discontinuity and Phase Identification:

At first glance, the seismograms of the Chile earthquakes (Figures 6.3a-d and 6.4a-e), indicate that their reading is not straightforward. At this distance range the complication in phase arrivals is due to a combination of factors, the most important of which are source structure and path effects.

In this section we attempt to identify the prominent phases observed and relate them to the 20° -discontinuity. Before doing so, however, it is appropriate to give a brief explanation of this phenomenon.

At short distances and in most regions the ray parameter " $dT/d\Delta$ " is about $13.8s/^{\circ}$. This value gradually decreases to 12.3 between $18-19^{\circ}$, but drops sharply to 10.4 between $20-21^{\circ}$. On the P-travel time curve, this is manifested by an abrupt change in slope at around 20° , corresponding to a ray having its lowest point at depths of about 400km. Furthermore, at this range, the P-wave amplitudes are exceptionally large. These observations indicate that between the depths reached by rays emerging at 20° , there is a "discontinuous" increase in the P-wave velocity accompanied by a decrease in the value of $dT/d\Delta$ for first arrivals by about 20%. This phenomenon came to be known as the 20° -discontinuity (Lehmann, 1934; Jeffreys, 1939; Lehmann, 1961, 1962, 1964, 1970).

According to Jeffreys (1976), the most likely interpretation is that the P-wave velocity increases continuously with depth

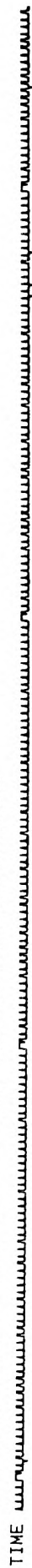
and especially rapidly over a certain depth range ($\approx 400\text{km}$) to give triplication. The time curve would then have a continuous slope, but would curve strongly around 20° . It, therefore, follows that the large P-wave amplitudes are probably due to these phases being refracted in a high velocity layer at depths of about 400km.

3.1.1 Observation of P-Phases:

Figures 6.3a-d show the first 3.5 minutes of events: CB018, CB013, CB011, and CB014 plotted to the same scale. Both Z/N and Z/BL traces are illustrated to aid in identifying the P-phases. Figure 6.3e is a plot of the observed P, PP, and PPP travel times. They seem to agree reasonably well with the J-B times shown as broken lines. The P-pP intervals also correlate with depths of 75-100km. Of course ISC depths were obtained from this interval.

Most interesting of all, however, are the phases marked P_1 and P_2 in Figure 6.3f. These generally have a separation of 2-3s. The phases are exceptionally clear on the Z/BL trace of CB011 and CB014 but less obvious on CB013 and CB018. We found that normalizing the traces to that of CB014 does not help in identification since the overall P-signals on the seismograms of CB013 and CB018 are weak. On the array records of CB014, however, the phases are much more obvious (Fig. 6.3g) and appear to follow through on most Z/BL traces. A more or less similar kind of identification may be made on the seismograms of the larger earthquakes (Figs. 6.4a-e) although these phases are extremely obscured by overloading.

CHILE DATA: CB018 AT SAAS; E4 (P-PHASES) (150/900/2100/0.00005/0.001)

TIME 

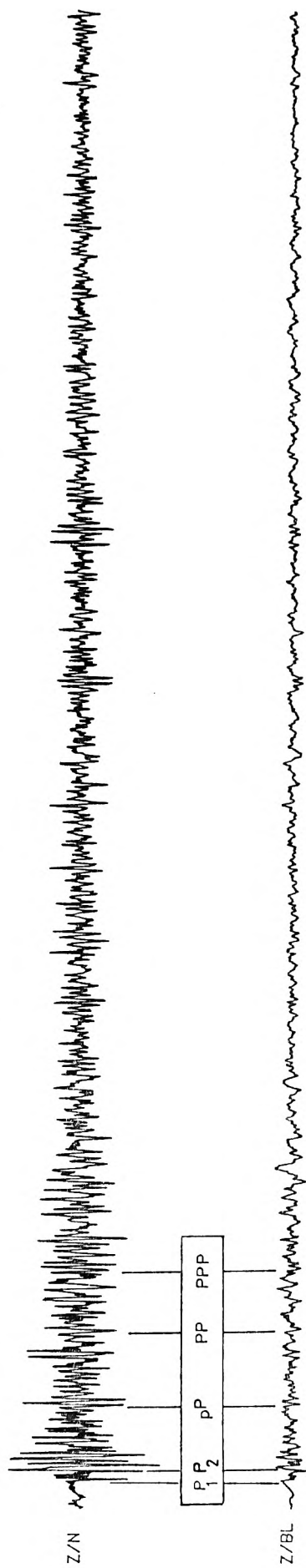


Fig. 6.3a CB018

CHILE DATA: CB013 AT SAMS, E4 (P-PHASES) (150/470/2100/0.00005/0.001)

TIME

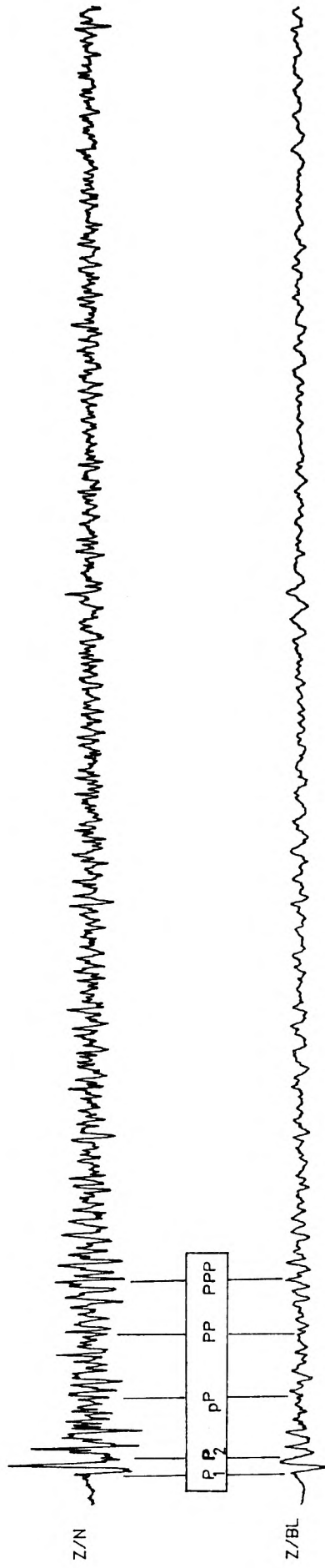


Fig. 6.3b CB013

CHILE DATA: CB011 AT SAAS, E4 (P-PHASES) (150/80/2100/0.00005/0.001)

TIME

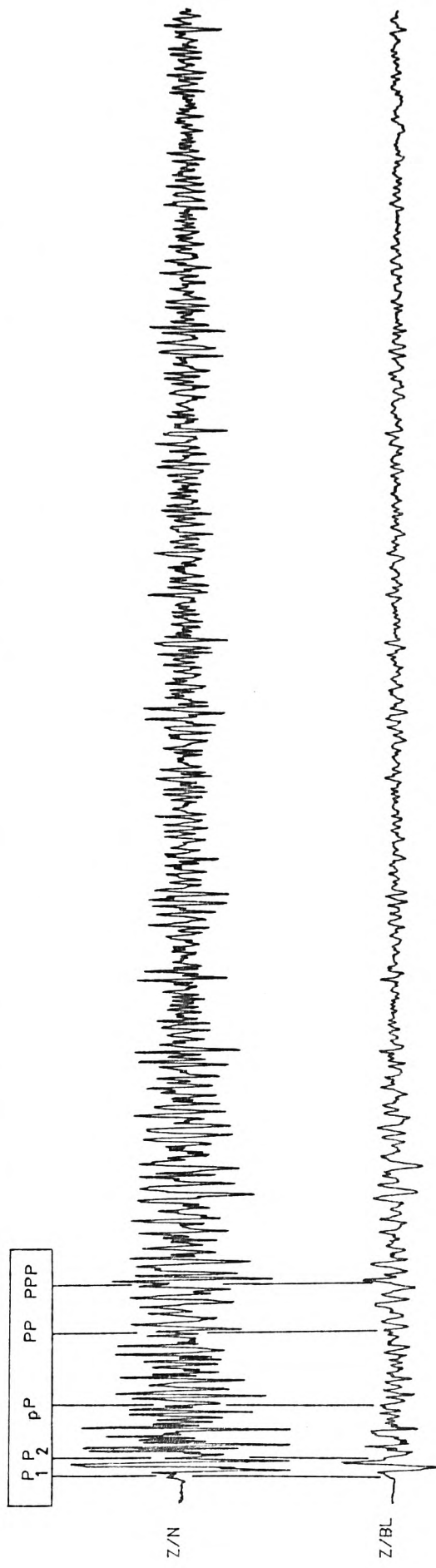


Fig. 6.3c CB011

CHILE DATA: CB014 AT SAAS, E4 (P-PHASES) (150/970/2100/0.00005/0.001)

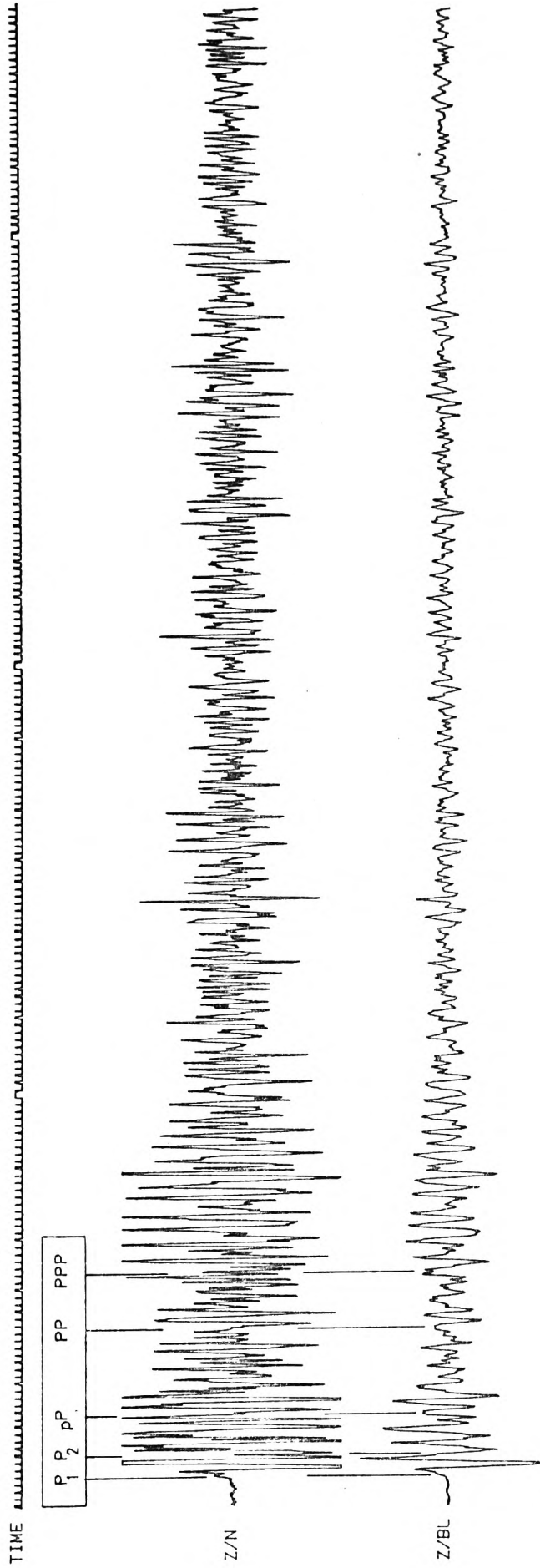
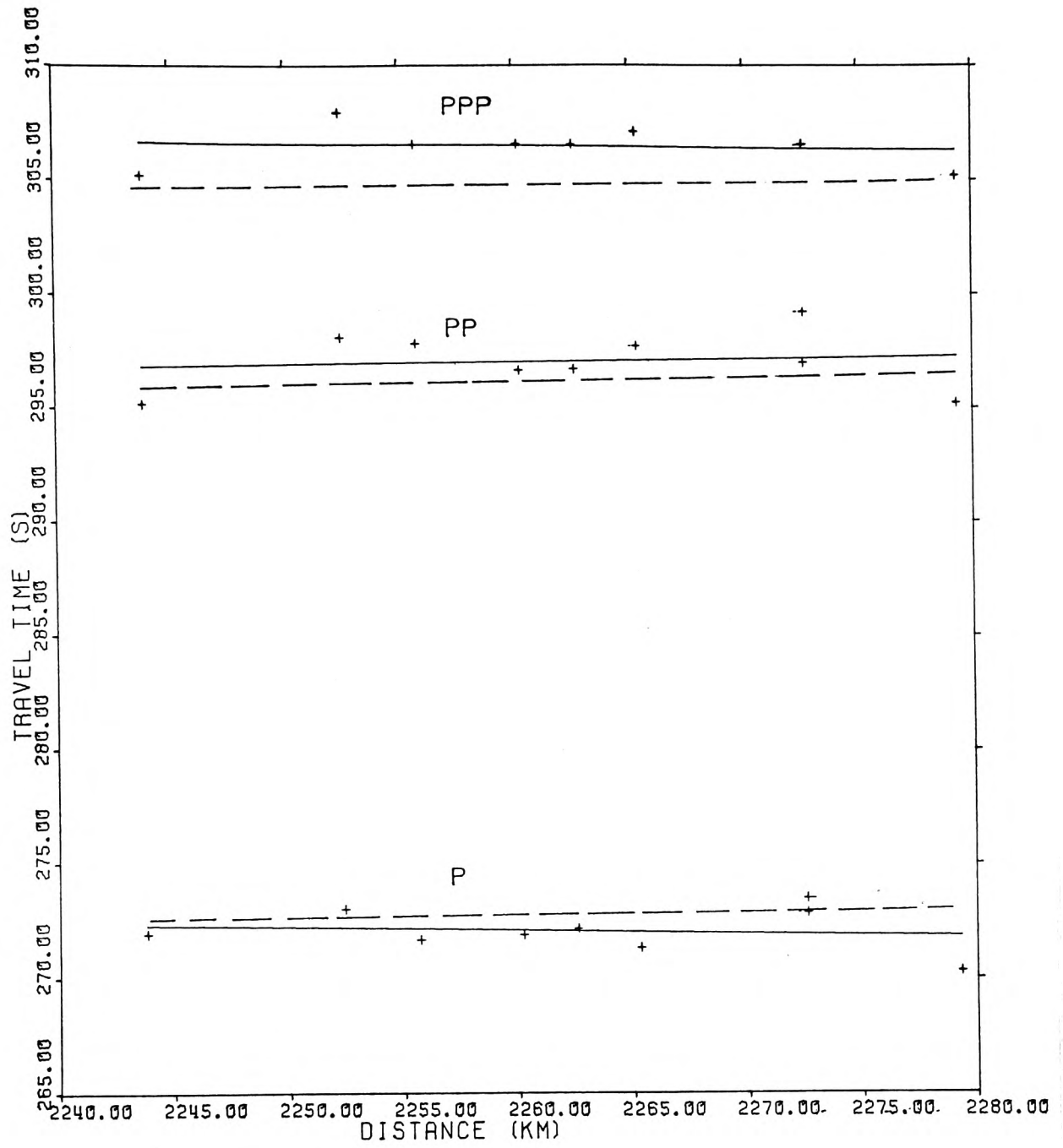


Fig. 6.3d CB014



TRAVEL TIME PLOT OF OBSERVED
P, PP, AND PPP PHASES AT SAAS: E4

Fig. 6.3e : P, PP, PPP Phases

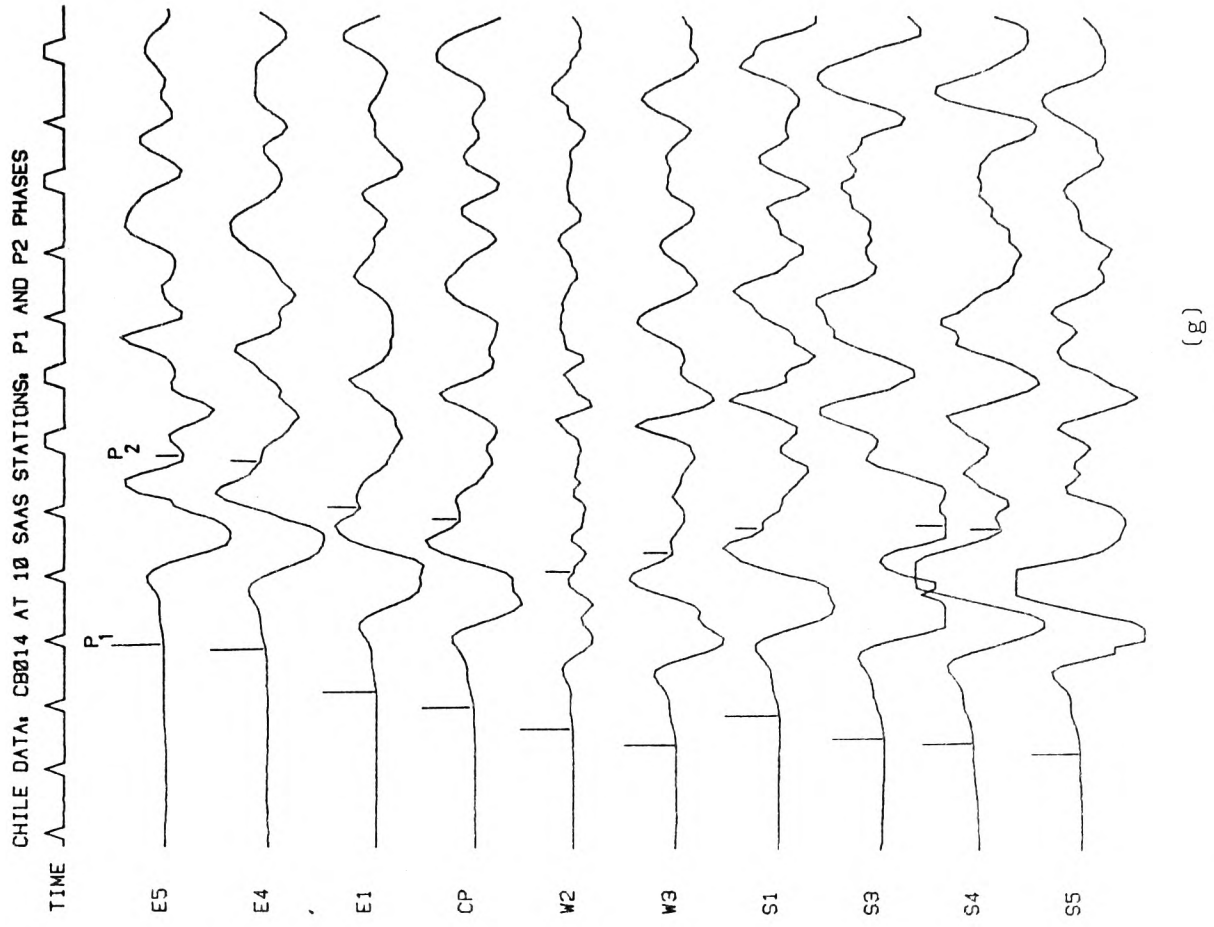


Fig. 6.3f and g : P₁ - P₂ Phases

The $P_1 - P_2$ phases identified here appear to be similar to those originally suggested by Lehmann (1970, p.363) on explosions in North America. With a separation of about 3s and almost identical velocity these phases correlate exceptionally well with those published (loc. cit, Fig. 5). It transpires therefore that these observations plus the Δm_b anomaly discussed earlier are both in favour of the suggested presence of a discontinuity in travel time and depth in the direction of SAAS.

Unfortunately our distance range as evidenced by the farthest SAAS station to the nearest and farthest epicenter amounts to only about 53km (see Fig. 6.11). This in addition to the fact that the array almost faces the fault broadside, inevitably means that if we were to construct travel time curves for P_1 and P_2 we would get limited resolution but not enough to observe their behaviour with distance. This is the reason for the suggestion made in Section 2.3.0 of this chapter.

3.1.2 Observation of S- and Surface Phases:

The large earthquake seismograms of Figures 6.4a-e show the S- and surface phases more clearly. Here again the S arrivals are in general agreement with the published tables. The core phase PcP is also discernable on most of these seismograms.

The large amplitude phase, on the other hand, identified as LQ (continental first Love, Simon, 1969, p.96) is quite remarkable especially on the seismograms of CB001 and CB002. The phase has periods of 7-12s and corresponds to a velocity

CHILE DATA: CB001 AT SAAS: E4 (P & S-PHASES) (150/670/3500/0.0002/0.001)

TIME

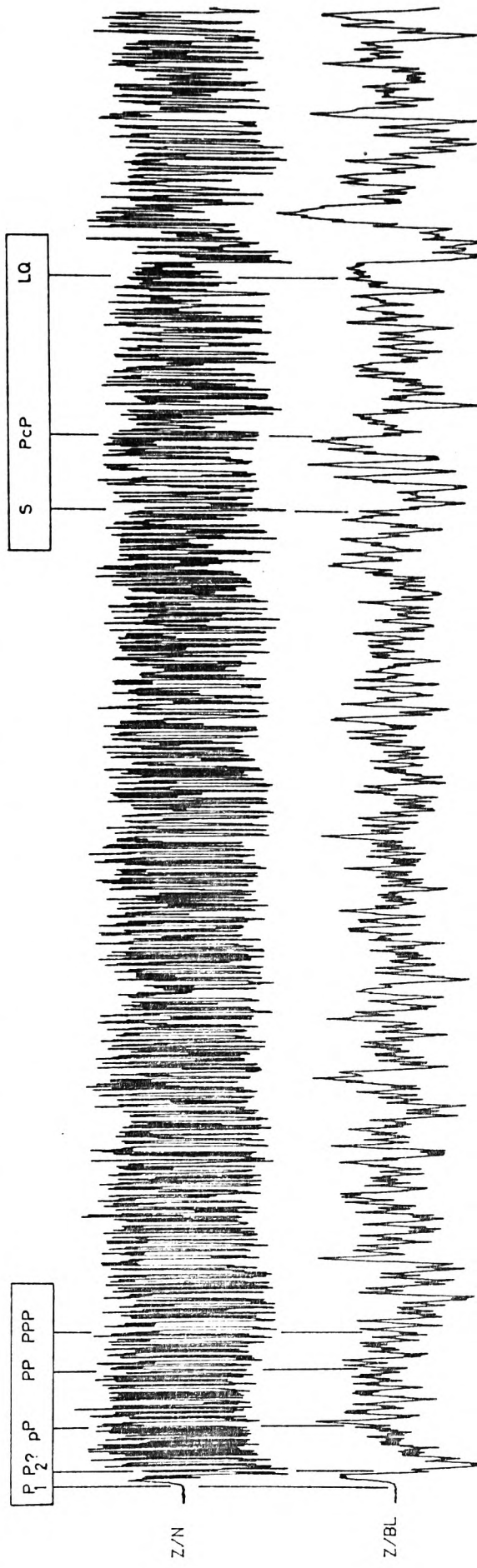


Fig. 6.4a CB001

CHILE DATA: CB022 AT SAAS, E4 (P & S-PHASES) (250/500/3500/0.0002/0.001)

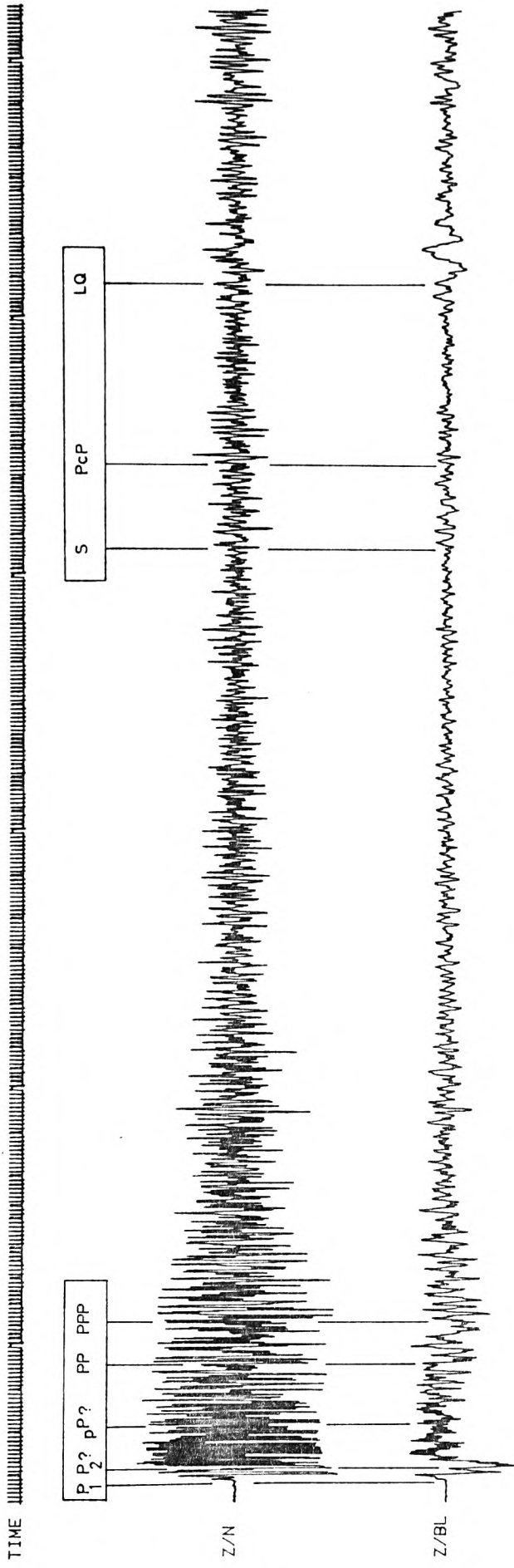


Fig. 6.4b CB022

CHILE DATA: CB00A AT SAAS: E4 (P & S-PHASES) (250/770/3500/0.0002/0.001)

TIME

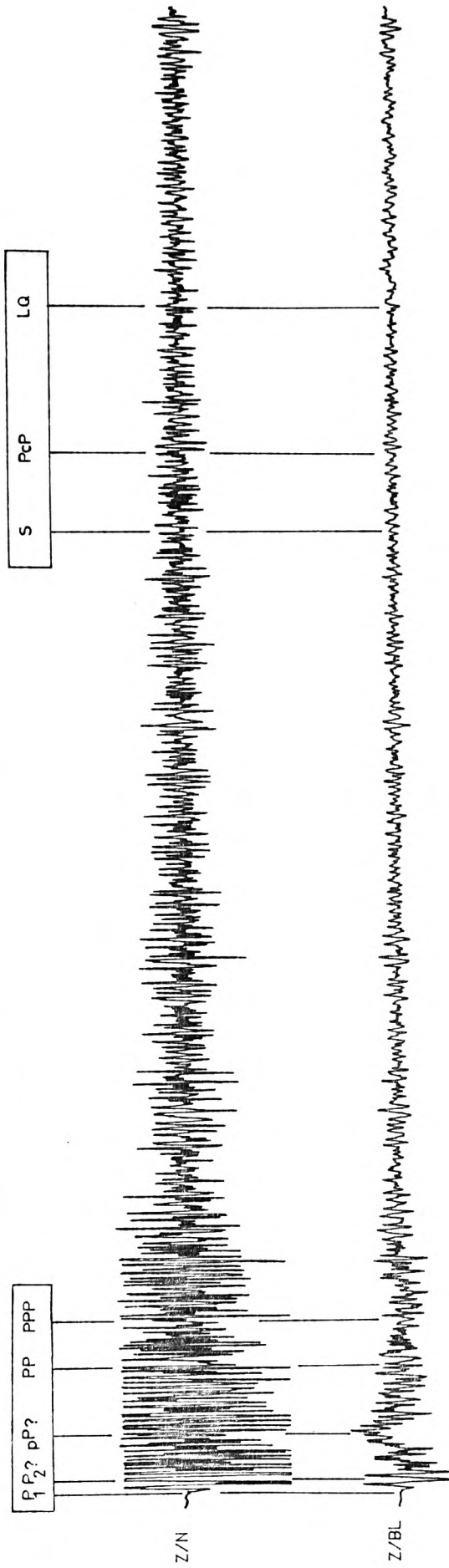


Fig. 6.4c CB00A

CHILE DATA: CB00B AT SAAS: E4 (P & S-PHASES) (250/570/3500/0.0002/0.001)

TIME

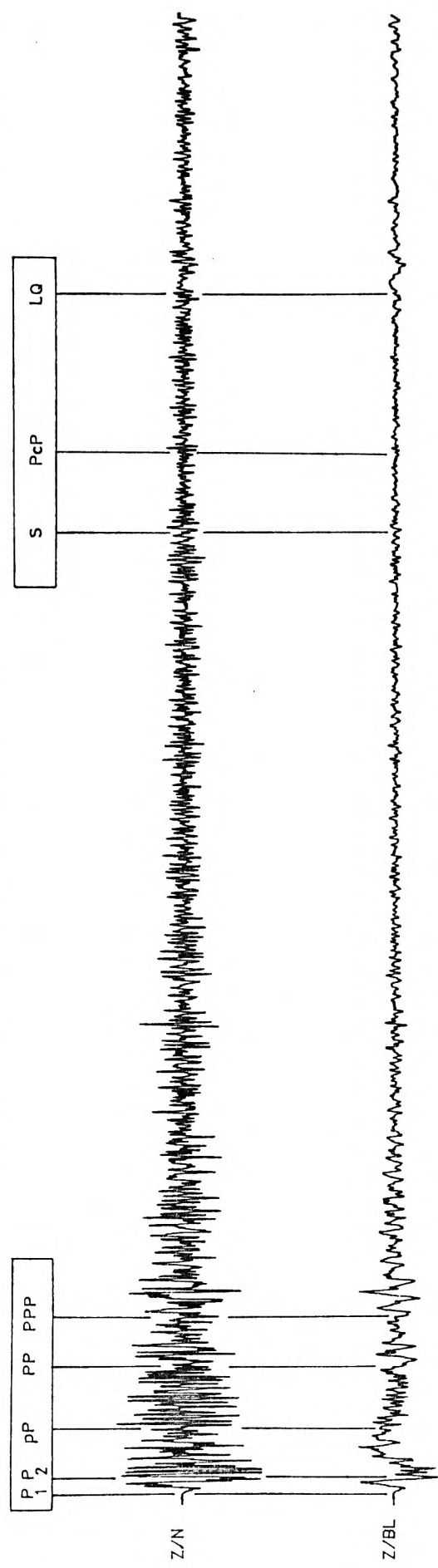


Fig. 6.4d CB00B

CHILE DATA: CB00C AT SAAS, E4 (P & S-PHASES) (250/520/3500/0.0002/0.001)

TIME

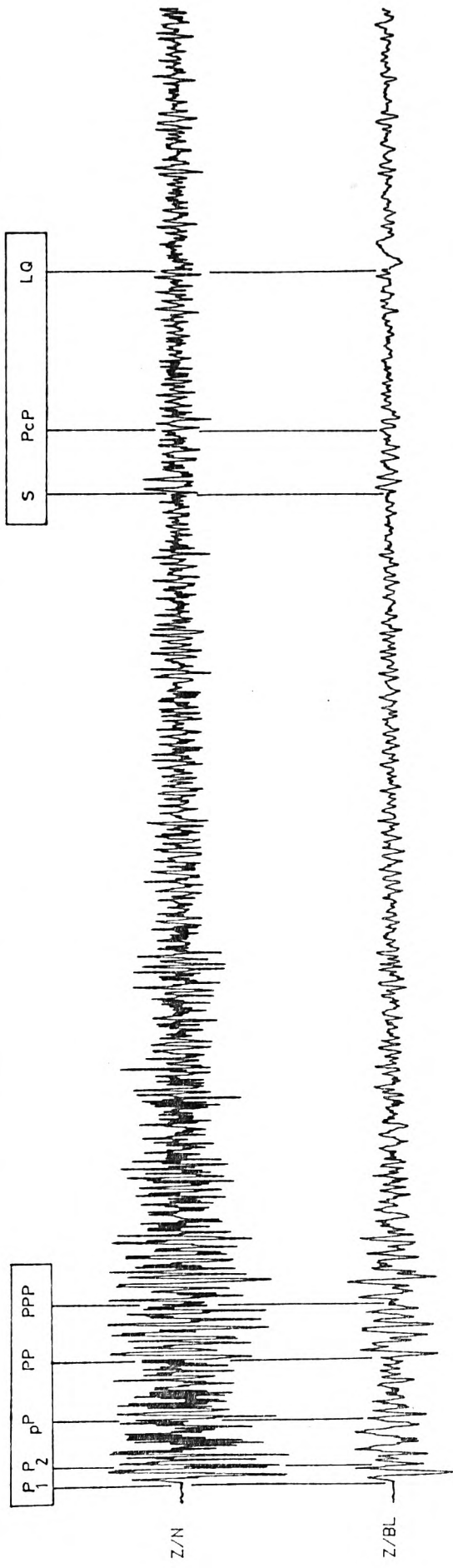


Fig. 6.4e CB00C

of about 4km/s. These properties are more or less similar to the Lg-phase originally identified by Press and Ewing (1952) as being a unique phase characteristic of continental paths at short distances. The presence or absence of this conspicuous phase is therefore an indication of the presence or absence of a completely continental path since as little as 2° intervening oceanic crust is sufficient to eliminate the phase entirely (Ewing et al, 1957). Although the precise mechanism of Lg propagation is not fully understood, it is thought to involve predominantly transverse motion which may be accompanied by appreciable vertical components, multiply reflected within a superficial sialic layer (loc. cit, p.219). It is this vertical component of the particle motion of Lg we believe we are observing. Obviously the sharpness of the phase depends on how the incoming energy is partitioned into vertical and horizontal motions. For instance, the motion of Lg on the seismogram of CBOOA is mostly horizontal and therefore the vertical component is inconspicuous.

3.2.0 Estimation of Apparent Velocity and Azimuth:

In estimating station or epicentral azimuths we used a straight forward calculation incorporating the relocated epicenters and the array station co-ordinates. The resulting Az values are therefore supplementary. In practice, however, and because of the possible existence of a lateral discontinuity around the source region (Section 2.4.2, Chapter 5) plus the minor contribution of the earth's ellipticity, azimuth may not supplement station back-bearing. But since our observations

are at a short distance range and originate from a common source, both values of Az are assumed to supplement. This reduces our calculations and as was shown in the example runs of "BEAM" in Chapter 3, azimuth does not adversely affect our ultimate results.

For apparent velocity estimates we used the observed phase velocities for P and S published by Birtill and Whiteway (1965). According to these curves (loc. cit. Fig. 1) the P-wave velocity around 20° is about 10.1km/s while that for S is about 6.5km/s. In Section 4.5.1 of Chapter 3 it was shown that these phase velocities were sufficient to give significant construction especially for the P-phase.

In order to obtain a representative velocity for the sum - across the array - of the short and long period wave components we present two examples of runs for CB014 and CB022 shown in Figures 6.5 and 6.7 (see also Section 3.3.0 for further discussion). Taking the respective calculated azimuths and selecting a range of AV between 3-12km/s for both events (Figs. 6.6 and 6.8) it is evident that at 10km/s the short period P-phases are significantly enhanced compared to the long period waves. Moving down to a phasing velocity of 4km/s we find that the amplitudes of the short period phases are substantially reduced while those of the long periods hardly change. This phenomenon is expected in phased array outputs and the reason is as follows:

In order to reject or accept a signal of a particular period it is necessary to ensure that it is rejected or accepted over

CHILE DATA: CB014 AT 10 SAAS STATIONS (409/960/5726/0.00005/0.00004)

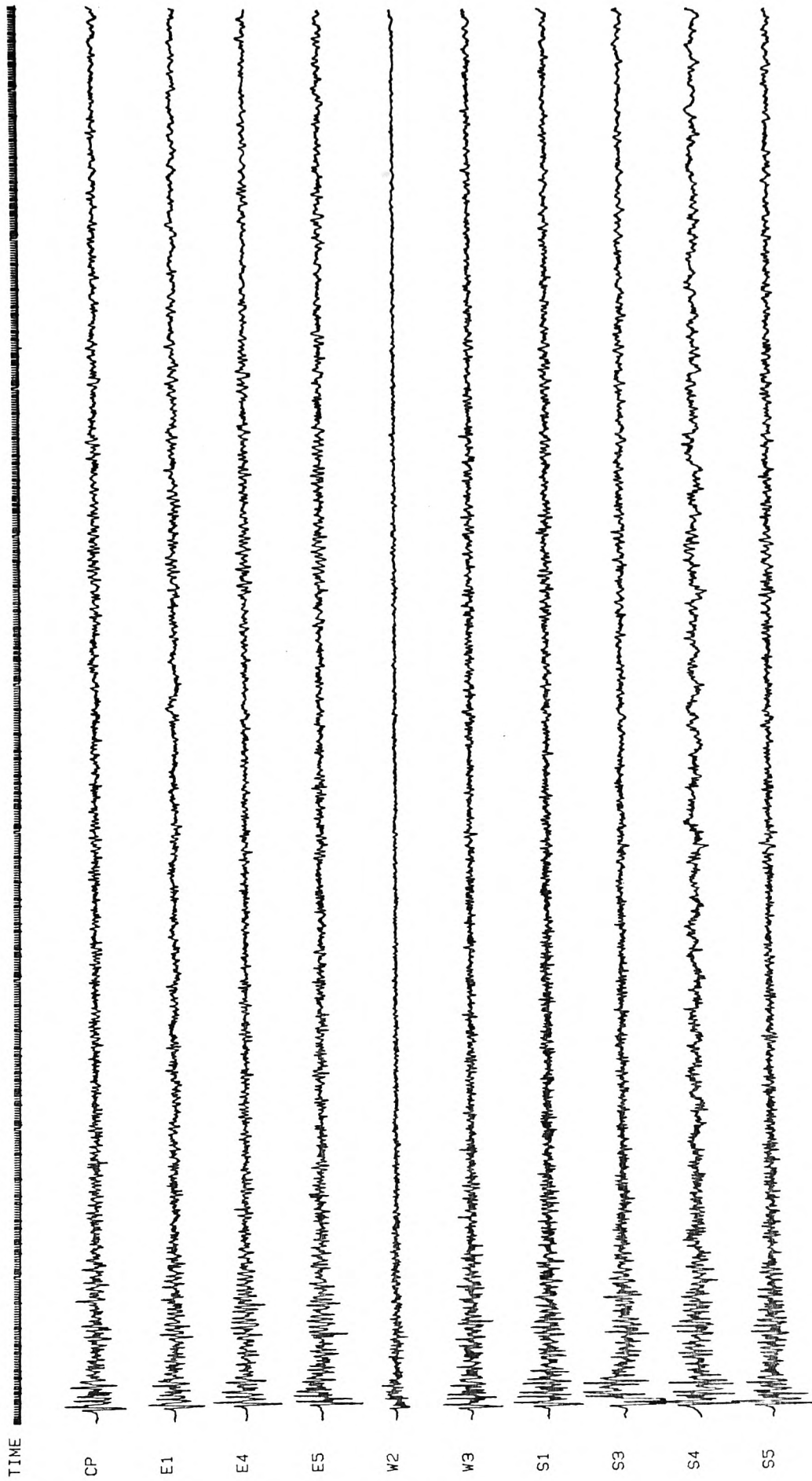


Fig. 6.5 CB014

CHILE DATA: CB014 SUM OF 10 SAAS STATIONS (AZ=252/AV=3-12) (409/0.0001)

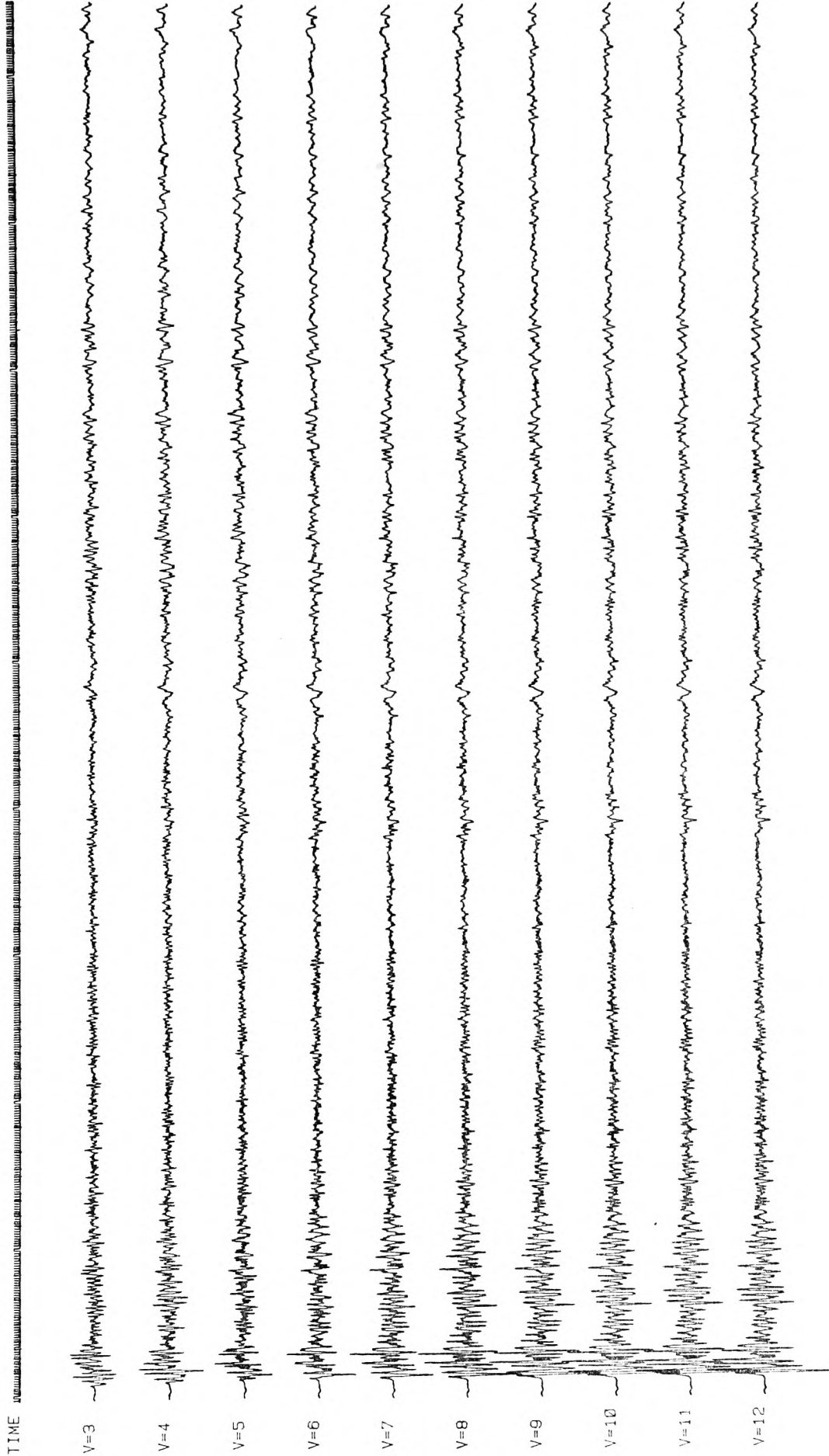


Fig. 6.6 Sum of CB014

CHILE DATA: CB022 AT 10 SAAS STATIONS (409/500/5726/0.0001/0.0004)

TIME

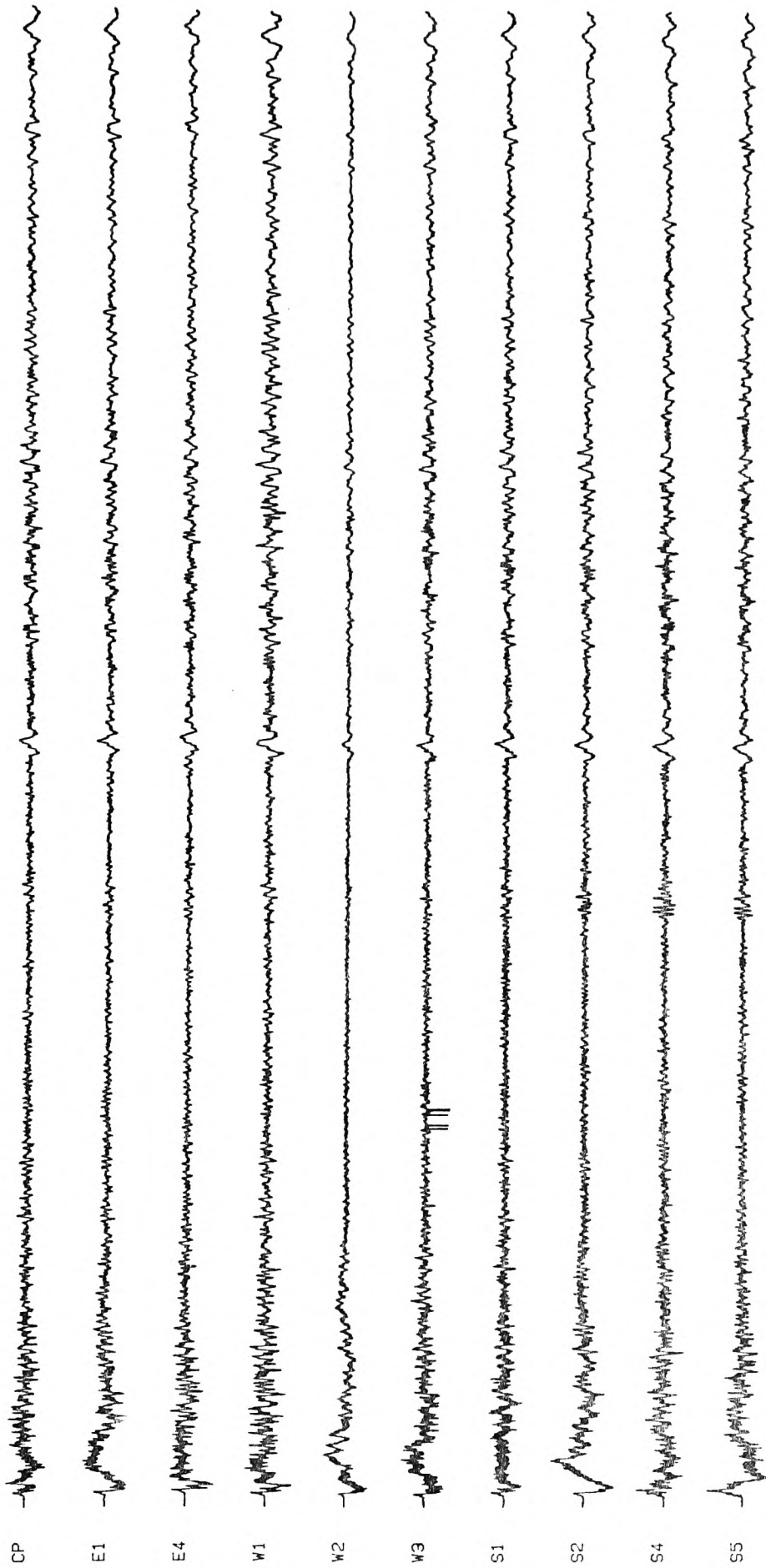


Fig. 6.7 CB022

CHILE DATA: CB022 SUM OF 10 SAAS STATIONS (AZ=250/AV=3-12) (409/0.0001)

TIME

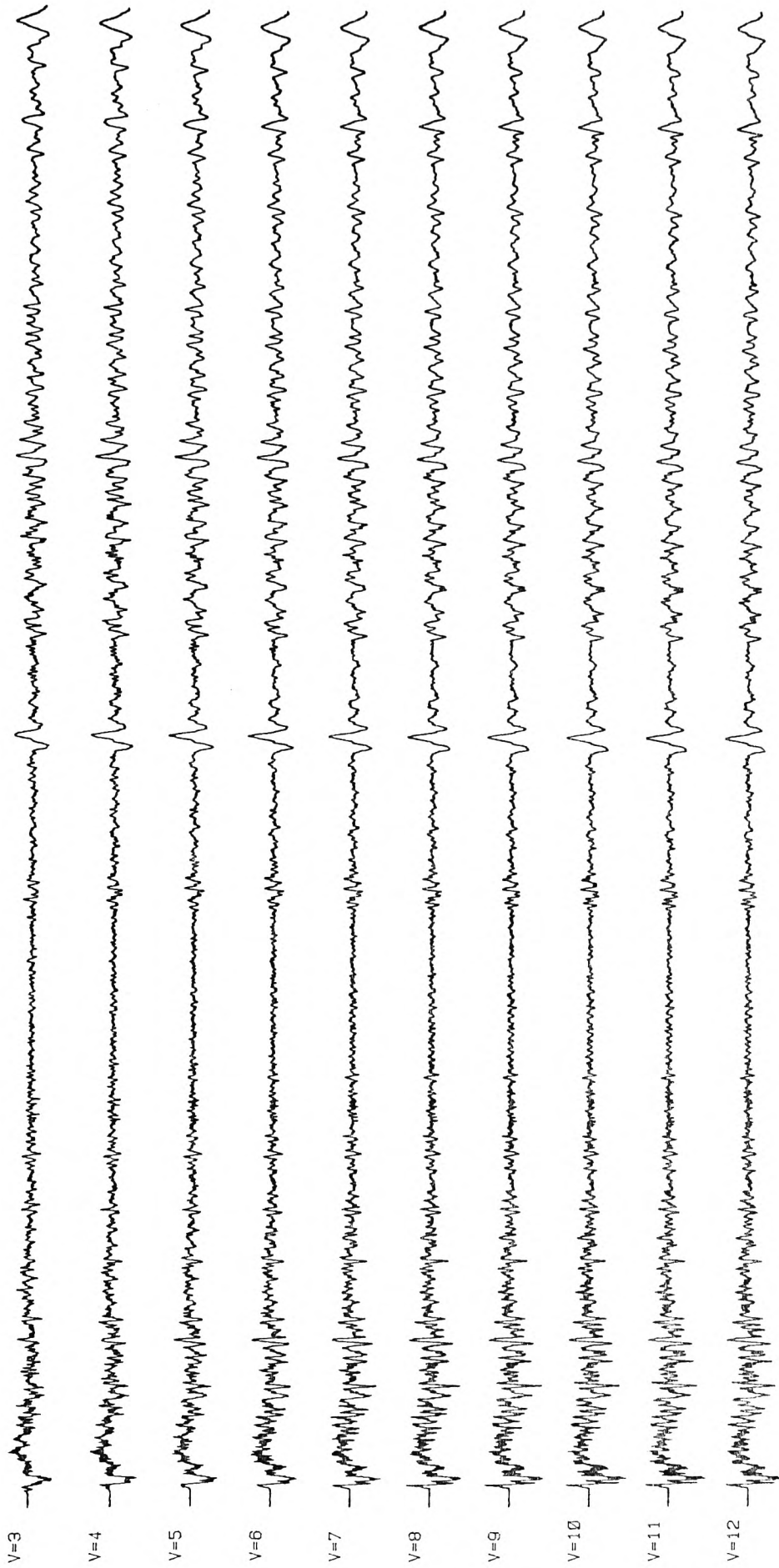


Fig. 6.8 Sum of CB022

the range of frequencies in which it has significant energy. If parameters like seismometer separation, azimuth, and velocity are all constants, then the phase shift will be proportional to frequency and in turn inversely proportional to wavelength. Thus when the apparent wavelength of a particular phase is substantially larger than the array dimensions, the total summed response output for that phase will not be affected. Bearing this in mind we find that for the short period P-phases at a range of about 20° , an apparent velocity of about 10km/s, and frequencies between 0.5-1 Hz will have corresponding wavelengths between 10-20km. For the longer period phases such as the LQ, on the other hand, we get wavelengths of the order of 30-50km.

Now to see how these wavelengths and their direction of arrival compare with SAAS dimensions we require a formula relating the above parameters to the total summed response E_n . One such relation (Willmore, personal communication) is:

$$E_n = E_0 e^{i(\omega t + (n-1)\alpha/2)} \frac{\sin n\alpha/2}{\sin \alpha/2}$$

where: E_0 is the response for a single seismometer

$$\alpha = \frac{2\pi d \cos \phi}{\lambda}$$

and: d is the seismometer spacing

λ is the seismic wavelength

ϕ is the angle of arrival of the wavefront

Note that in the above equation, the complex part describes

the phase shift as a function of frequency, while the real part specifies amplitude. Therefore a plane wavefront from the Chile source will arrive at angles of $\phi = 38^\circ$ and 52° at the EW and NS arms of SAAS respectively. Our array dimensions will then reduce to:

$$17.5 \cos 38 = 13.8\text{km} \quad \text{along the EW line}$$

$$12.5 \cos 52 = 7.7\text{km} \quad \text{along the NS line}$$

It immediately follows from the above that the shorter period waves whose wavelengths are comparable to the array size will be directly influenced by the velocity filtering procedure, while those of much larger wavelengths remain unaltered. Therefore, in order to provide adequate resolution for longer periods, arrays extending over several wavelengths are necessary.

It is interesting to note that the arrival following the LQ phase especially on Figure 6.8 corresponds to a continental LR with velocity of about 3km/s. This is an encouraging feature because we are in fact constructing longer periods which are beginning to match the phases on the large earthquake record of CB001 in both arrival and period.

3.3.0 The Summation Scheme:

In the previous section we observed that for a range of input phasing velocities the long period content is not affected whereas the summed short period response is substantially altered. In this section we attempt to relate the phasing velocity at the receiver with the rupture velocity and

triggering sequence determined by the assumed initial dislocation which sweeps the fault area in a given direction. Before going further, however, it is appropriate to ask two questions, the answers to which would aid in clarifying later sections:

(a) Which earthquake are we attempting to construct and which events are our elementary "building bricks"?

(b) Having answered (a), what is the extent of difference in appearance in the waveform or on the spectrum which we desire to eliminate or alternatively construct?

The answer to the first is that we will be seeking to reconstruct the earthquake mechanism of the main shock CB001 as seen by a single array station. For this purpose we will be utilizing all SAAS records of all "foreshocks" and after-shock sequence. The answer to (b) therefore follows. Our objective will be a simulated seismogram and spectrum which reflects the frequency content and amplitude build-up that has the closest possible resemblance to the record and spectral signature of CB001. Here is where rupture velocity and triggering pattern play a major role.

3.3.1 Rupture Velocity at the Far-Field:

In Section 2.6.0 of Chapter 3, we stated that in the far-field a fault may be approximated by a point double couple. This may be explained with reference to Brune's (1970) paper in which he discussed both near- and far-field spectra.

According to Brune, as the range of observation increases, diffraction and scattering reduces the long period or static spectrum. In other words the static field decays at a higher order of distance than the dynamic field (or roll-off). Therefore at large distances and for wavelengths greater than the source dimensions, the effect of the opposing side of the fault diffracts around the dislocation and differentiates the far-field spectrum. This gives the long period, large distance equivalent source as a double couple (Maruyama, 1963; Burridge and Knopoff, 1964).

Bearing this concept in mind and recalling our discussion in Section 3.2.0 of Chapter 3 in which we mentioned that the appropriate time delays introduced in the summation process must account for rupture propagation and travel times of seismic waves, and is determinable by the input apparent velocity, we can recognize the important difference between a wavefront crossing an array of detectors at a given apparent velocity and that of a rupture assumed to propagate along a fault surface. The ultimate target would then be to incorporate an assumed rupture velocity with an observed seismic velocity in order to construct the most likely "trigger factor", which, at a given direction would resemble a simulated rupture process approximating that produced by the main source.

In our brief outline of dislocation theory (Section 2.3.0, Chapter 3) we mentioned that a dislocation is assumed to propagate along the fault at a constant rupture velocity " v_R " dependent on the S-wave velocity " β ". The ratio of " v_R/β " is

called the Mach number "M" and is usually taken to be subsonic in nature, i.e. $M < 1.0$ for most kinematic source models.

The implication of the Mach number or "trigger factor" was studied by Boore et al (1971) in a discussion of propagating 2-dimensional edge dislocations. They showed that the maximum motion in the normal component produced by a dislocation of unit amplitude and unit rise time increases with the Mach number and is a particularly strong function for M close to unity (loc. cit, Fig. 9). This result was confirmed by the near-field investigations of Boore and Zoback (1974a) and used by the same authors to model the strong motion recordings at the Pacoima Dam of the San Fernando earthquake of 1971 (Boore and Zoback, 1974b). It is worth noting here that no equivalent studies of rupture propagation in the far-field have been reported. We therefore have to assume that the above discussion extends to a distance range comparable to our observations. If this was taken as an acceptable extrapolation then our guide will be the S-wave velocity at the source structure. This at depths of 75-100km is about 4.36km/s, therefore a phasing velocity of 4km/s would correspond to $M = 0.92$. As a higher M alternative, we sum at 10km/s along the fault. This would give near-optimum phasing of P-waves from a single source as seen from SAAS but would correspond to $M = 2.29$ referred to the β -value in the focal region. The reasons for such a choice are:

- (a) The long period construction at subsonic M is quite promising and shows encouraging preliminary results (Fig. 6.8).

(b) It is conceivable that a fault propagating subsonically could give rise to supersonic "bow" waves in an overlying low-velocity layer as suggested by Aki (1968a) and Boore et al (1971).

(c) The respective velocities of 4 and 10km/s give the best construction of the low (static) and high (dynamic) range of frequencies on the far-field spectrum.

In Section 3.3.3 of this chapter we explain how these velocities are incorporated with the directions and sequence of trigger.

3.3.2 Transposition of Array to Source:

As we pointed out in Chapter 5, one main objective in utilizing array records is to have numerous earthquake samples which could be appropriately phased and summed to produce a large-earthquake seismogram. In this context we can imagine each station of SAAS as representing a point source of that particular earthquake. The E-W line would then simulate a fault line, at that direction and of comparable dimension, consisting of a sequence of point source equivalent to the number of recording stations. A similar argument is applied to the N-S arm of SAAS.

To assess the number of point sources available, i.e: the number of seismograms, their relative positions and directions of spread with respect to the fault dimensions of the major shock we employ what we have come to call the principle of array - source transposition (similar to the idea of arrays and

co-arrays introduced by Haubrich, 1968). This basically involves translocating the central point of the array to the hypocenter of each earthquake.

The method is fairly straightforward for a single station-multievent case (see Chapter 7). For an array of stations, however, the operation involves translocation between parallel horizontal or inclined planes at the same level or at different levels in a uniform medium. The array map will therefore be inverted on the source map and the central point of the array coinciding with the earthquake hypocenter. Figure 6.9 illustrates this principle.

Translocation leaves all source-array vectors unchanged. There will, however, be some vertical distortion if the ray paths are in a heterogeneous stratified earth. The method would be ideal if the fault surface was horizontal. Between a horizontal array and a dipping fault, on the other hand, the simple imagery fails to reproduce the model. This is because the array image does not lie in, or is not parallel to the fault plane and hence if one were to swing the N-S line to coincide with the fault surface at that dip, one would introduce extra paths unaccounted for. As a consequence we are limited to the option of imagining the ray paths swinging in azimuth about CP to give a virtual source transposed horizontally along the fault to coincide with the hypocenter. The resulting imagery would therefore introduce a "thickness" to the fault determined by the extent and slants of the E-W and N-S lines from the fault surface. This is shown schematically in cross section in Figure 6.10 and the equivalent map is

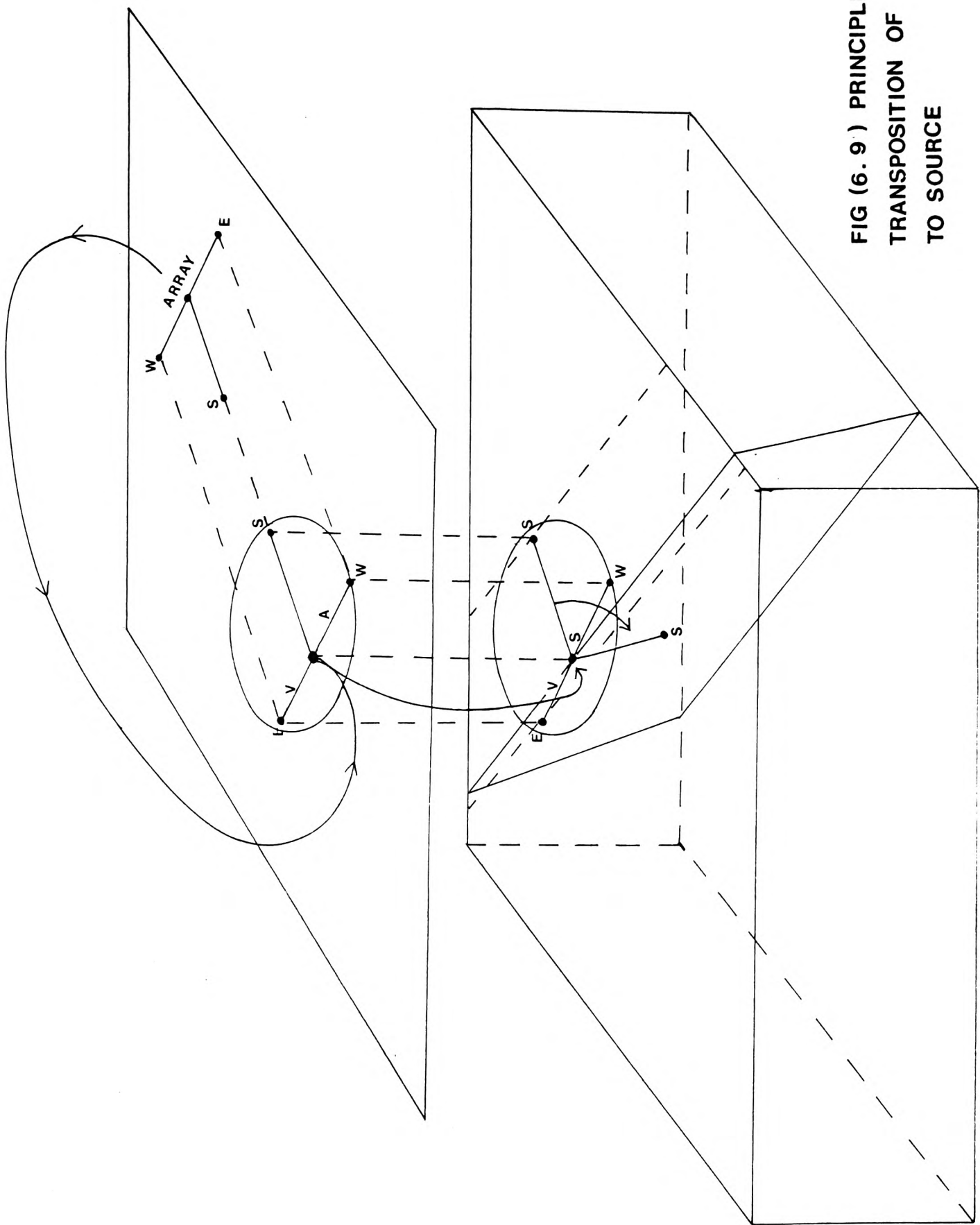
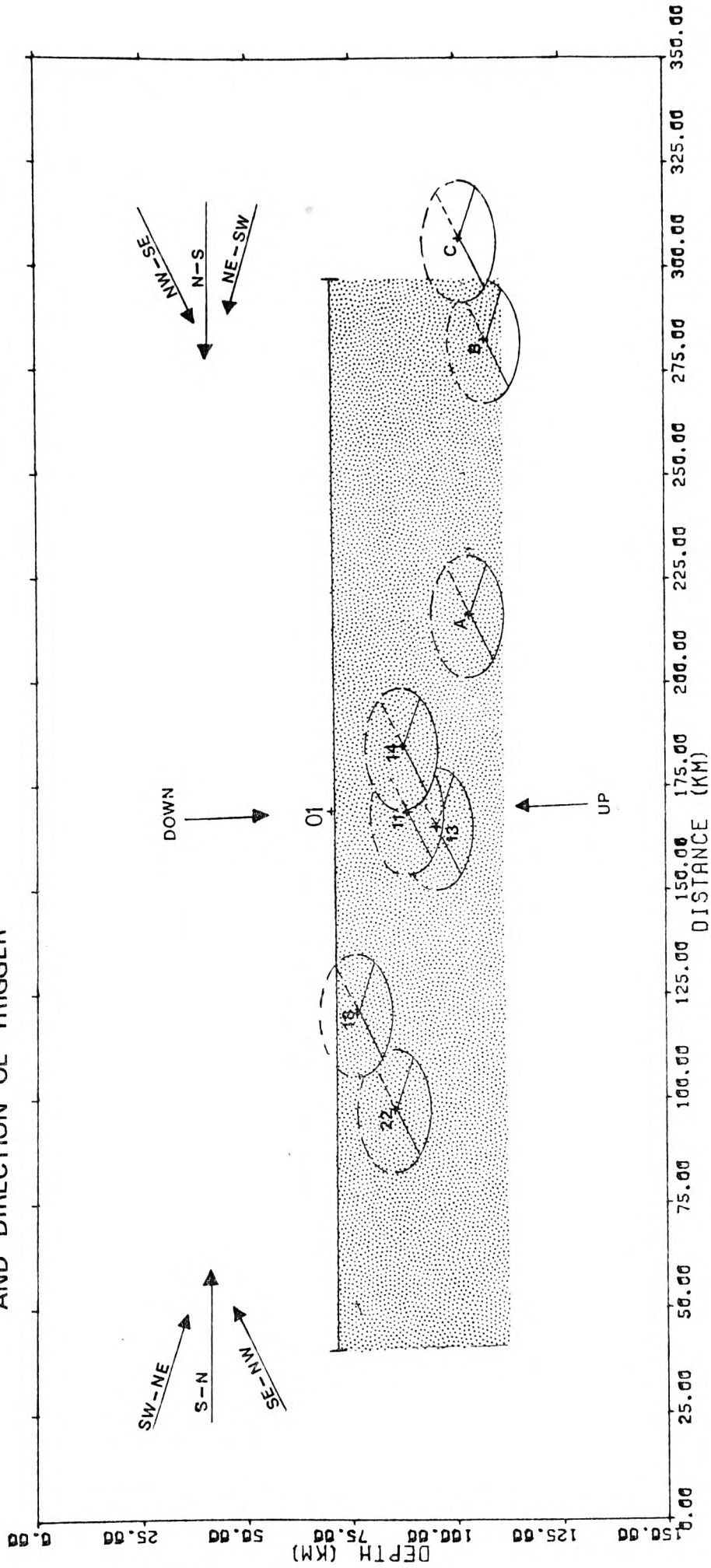


**FIG (6.9) PRINCIPLE OF
TRANSPPOSITION OF ARRAY
TO SOURCE**

FIG(6.10) CROSS SECTION ALONG FAULT STRIKE
 SHOWING POSITION OF HYPOCENTRES
 AND DIRECTION OF TRIGGER



CHILE DATA : TRANSPOSITION OF ARRAY
 TO FAULT SURFACE

illustrated in Figure 6.11.

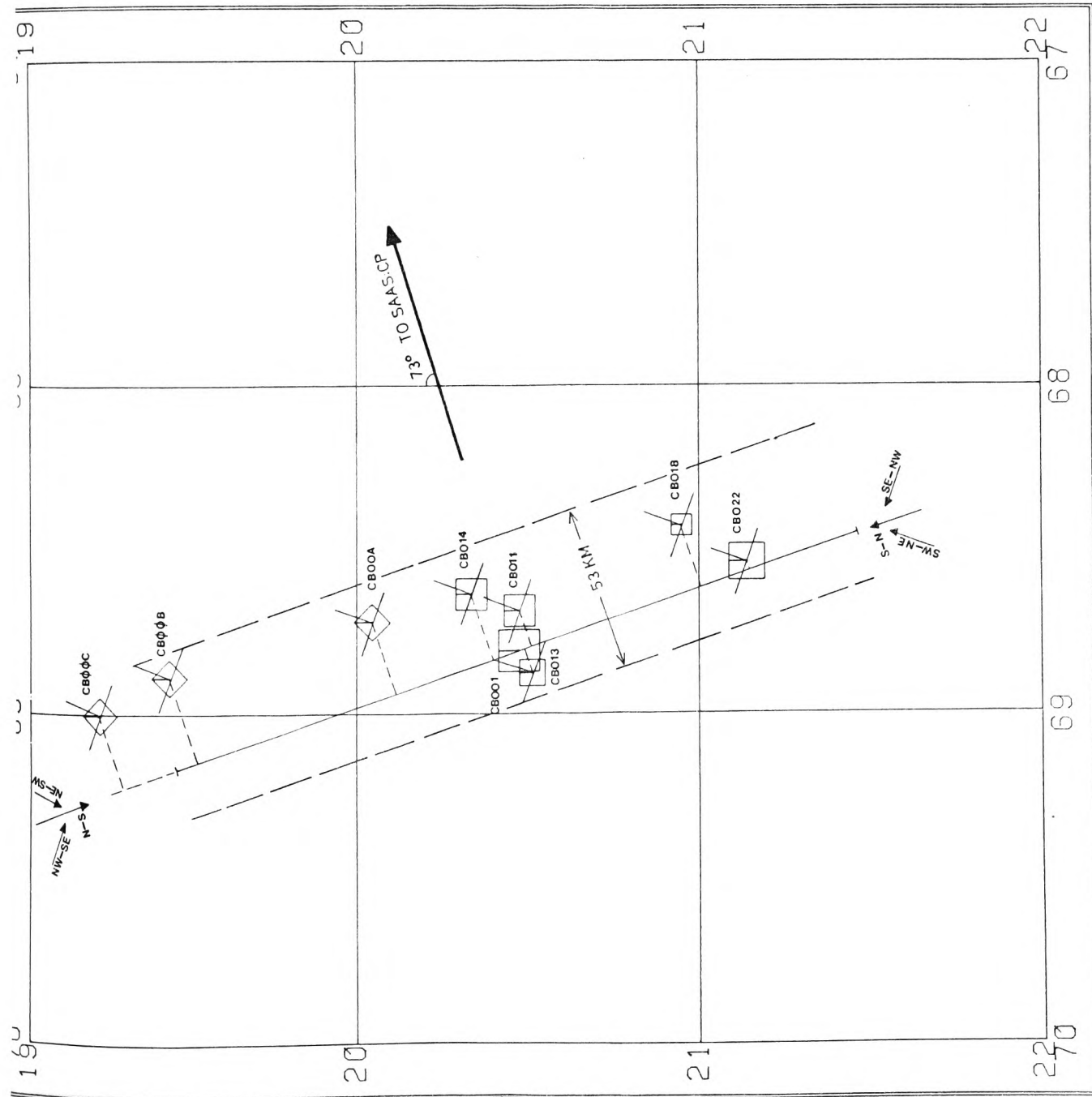
3.3.3 Direction and Sequence of Trigger:

In the previous two sections we discussed rupture velocity and array translocation to the source. What remains to discuss is possible fracturing directions or sequence of trigger available under the constraints of array transposition method.

In Section 2.6.0 of this chapter we found that the focal mechanism solutions of all the events suggest a normal-type faulting generally trending NW-SE. This indicates that the ambient stresses responsible for these shocks are extensional (see Section 3.2.0, Chapter 5). Bearing this in mind it is possible to suggest the following cases to account for the direction and hence triggering sequence of the initial displacement:

- CASE (1) Along fault surface (strike) in a N-S direction.
- " (2) " " " " " " S-N "
- " (3) Oblique to fault surface in a NW-SE direction.
- " (4) " " " " " " NE-SW "
- " (5) " " " " " " SW-NE "
- " (6) " " " " " " SE-NW "
- " (7) Along fault surface (dip) in a downward direction.
- " (8) " " " " " " an upward "

Cases (1), (2), (7), and (8) involve all SAAS stations of all event records since the direction of trigger is along the fault surface (in the strike or dip directions) and summation is carried out with respect to the central point of the array:



KEY TO SYMBOLS

DEPTHS (SYMBOL TYPES)	UP TO	TO
+	30.00	30.00
*	30.00	60.00
□	60.00	100.00
◇	100.00	200.00
△	200.00	300.00
⊖	300.00	400.00
○	400.00	OR GREATER

MAGNITUDE (SYMBOL RADIUS)	UP TO	TO
·	4.00	4.00
·	4.00	4.50
·	4.50	5.00
·	5.00	5.50
·	5.50	6.00
·	6.00	6.50
·	6.50	OR GREATER

FIG (6.11) TRANSPOSITION OF SAAS TO SOURCE REGION

MERCATOR

CP. Cases (3) and (6) involve only the E-W line of SAAS for all events because the dislocation is assumed to propagate oblique to the fault surface and its direction will be determined by the transposed E-W arm of the array. Similarly cases (4) and (5) involve only the N-S line of stations.

The propagation direction of the initial dislocation combined with the rupture velocities discussed earlier will evidently determine the sequence and speed of trigger and hence the sequence of summation and input velocities. Examining Figures 6.10 and 6.11 closely we notice that the 8 cases described above fall into 3 sequence categories as shown below:

	AF/N-S (CASE 1)→	←AF/S-N (CASE 2)
(1)	C + B + A + 14 + 13 + 11 + 18 + 22	
	OB/NE-SW (CASE 4)→	←OB/SW-NE (CASE 5)
	OB/NW-SW (CASE 3)→	←OB/SE-NW (CASE 6)
(2)	C + B + A + 13 + 14 + 11 + 22 + 18	
	AF/UPWARD (CASE 8)→	←AF/DOWNWARD (CASE 7)
(3)	B + A + C + 13 + 11 + 14 + 22 + 18	

To illustrate what we have discussed so far we give examples of summed outputs assuming the array records of a single event are involved. The examples shown in Figures 6.12 and 6.13 are events: CB014 and CB022 plotted to the same scale. The lettering: SL, SE, and SS signify: ALL, E-W and N-S summed outputs respectively at input velocities of 4 and 10km/s which

CHILE DATA: CB014 SUMS OF ALL, EW, NS SAAS STATIONS (AV=4 & 10) (409/0.0001)

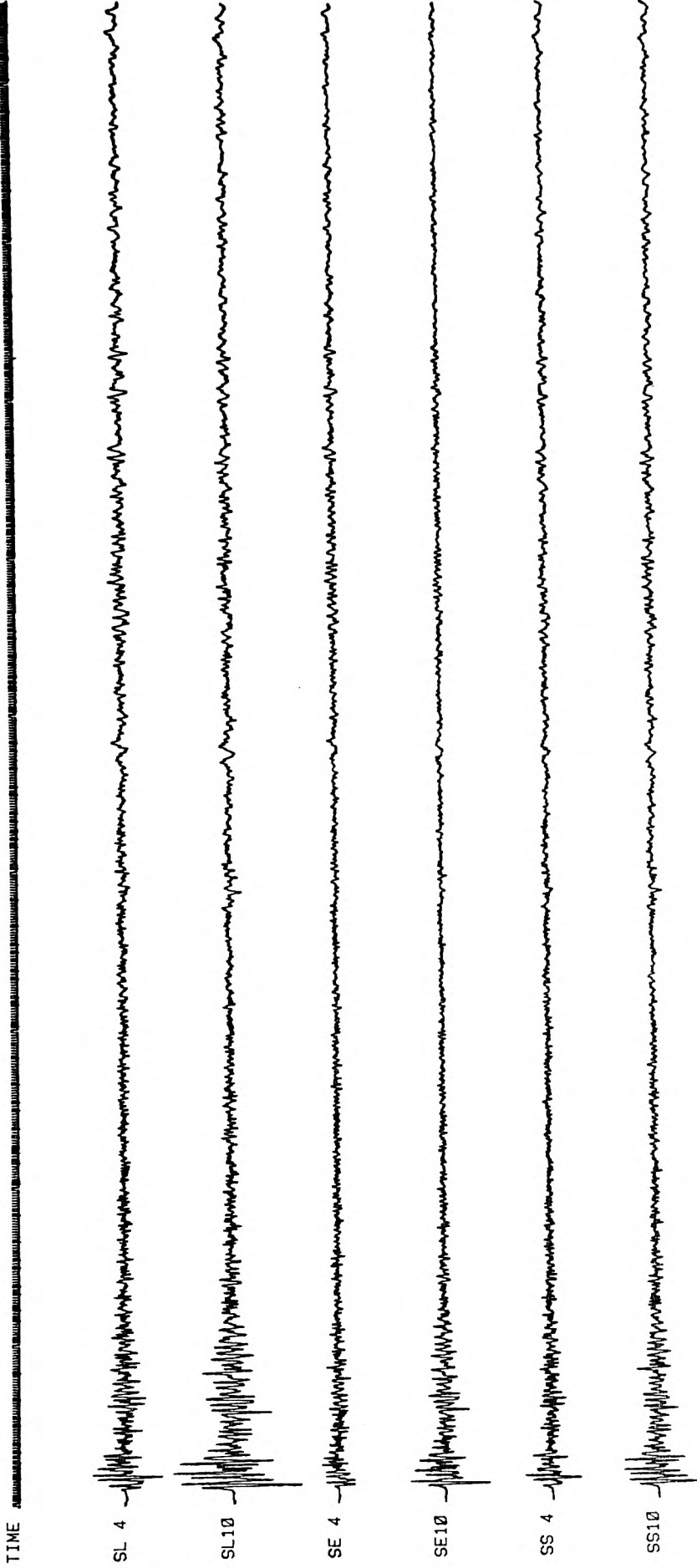


Fig. 6.12 CB014 : Sum at short and long period ranges

CHILE DATA: CB022 SUMS OF ALL, EV, NS SAAS STATIONS (AV=4 & 10) (409/0.0001)

TIME

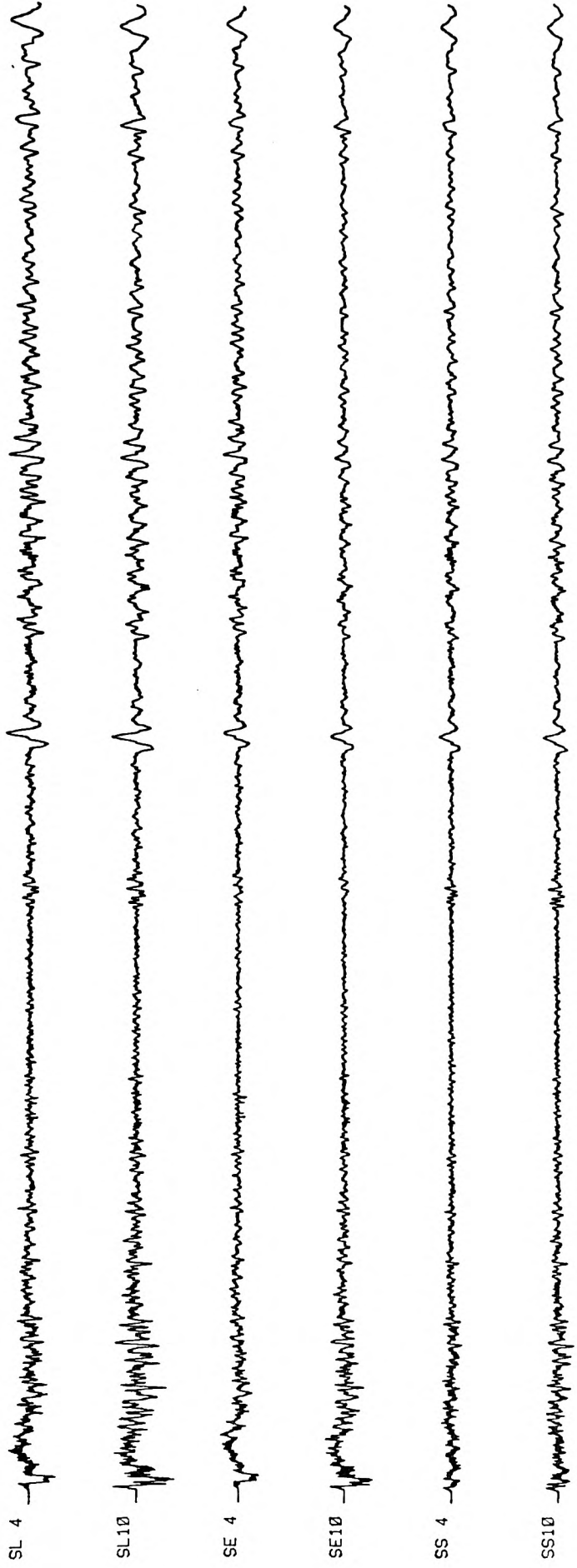


Fig. 6.13 CB022 : Sum at short and long period ranges

pertain to average Mach numbers of 0.92 and 2.29. It is clear from the figures that for subsonic rupture propagation involving ALL summed outputs the results are impressive in the long period range. This is especially true for the larger event CB022 of Figure 6.13.

4.0.0 RESULTS AND DISCUSSION:

In this section we report the results of our summations according to the scheme discussed in the previous section comparing and pointing out similarities and differences.

4.1.0 Comparison of ALL, EW, and NS Individual Event Sums:

Recalling our discussion at the beginning of Section 3.3.0 we stated that our target is to construct the source of CB001 at a single station. To show the "target" and "building bricks" we present the seismograms of all the Chile earthquakes at E4 (Fig. 6.14) and their respective spectra (Fig. 6.15). The hatched area under the spectral curve of CB001 should, therefore be ideally filled by enough samples from a suitable combination of all other events in such a way as to bring the simulated spectrum to match that of CB001. If this were accomplished then we would have met our primary target and constructed a source with similar fracturing mechanism to the main shock as observed from a single station.

We start by considering the spectral differences between the summation of each component event at: ALL, EW, and NS SAAS stations with subsonic and supersonic rupture propagation. Figures 6.16a and b through to 6.18a and b illustrate the sums

CHILE DATA: ALL EVENTS AT SAAS: E4 (409/70/5726/0.0001/0.0005)

TIME

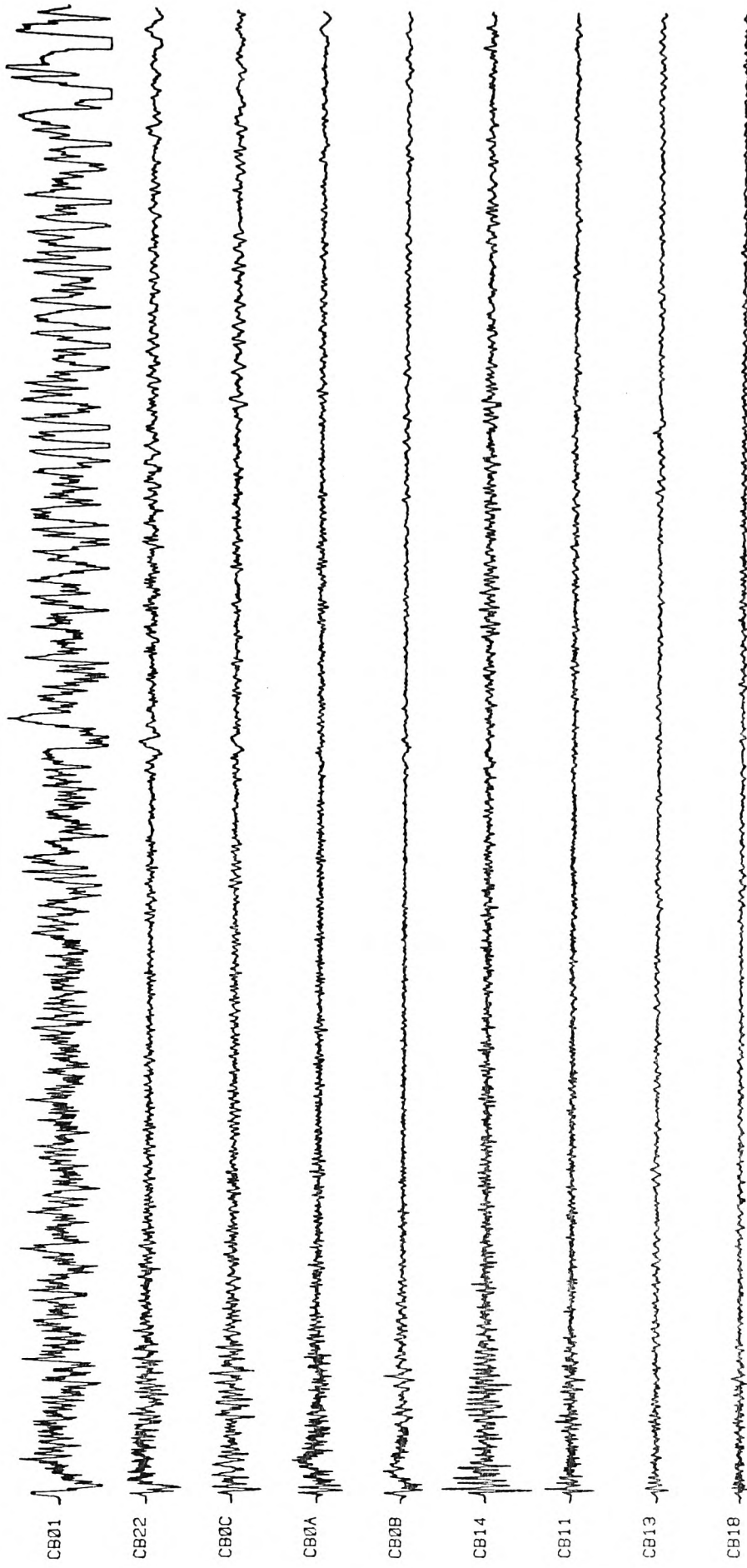
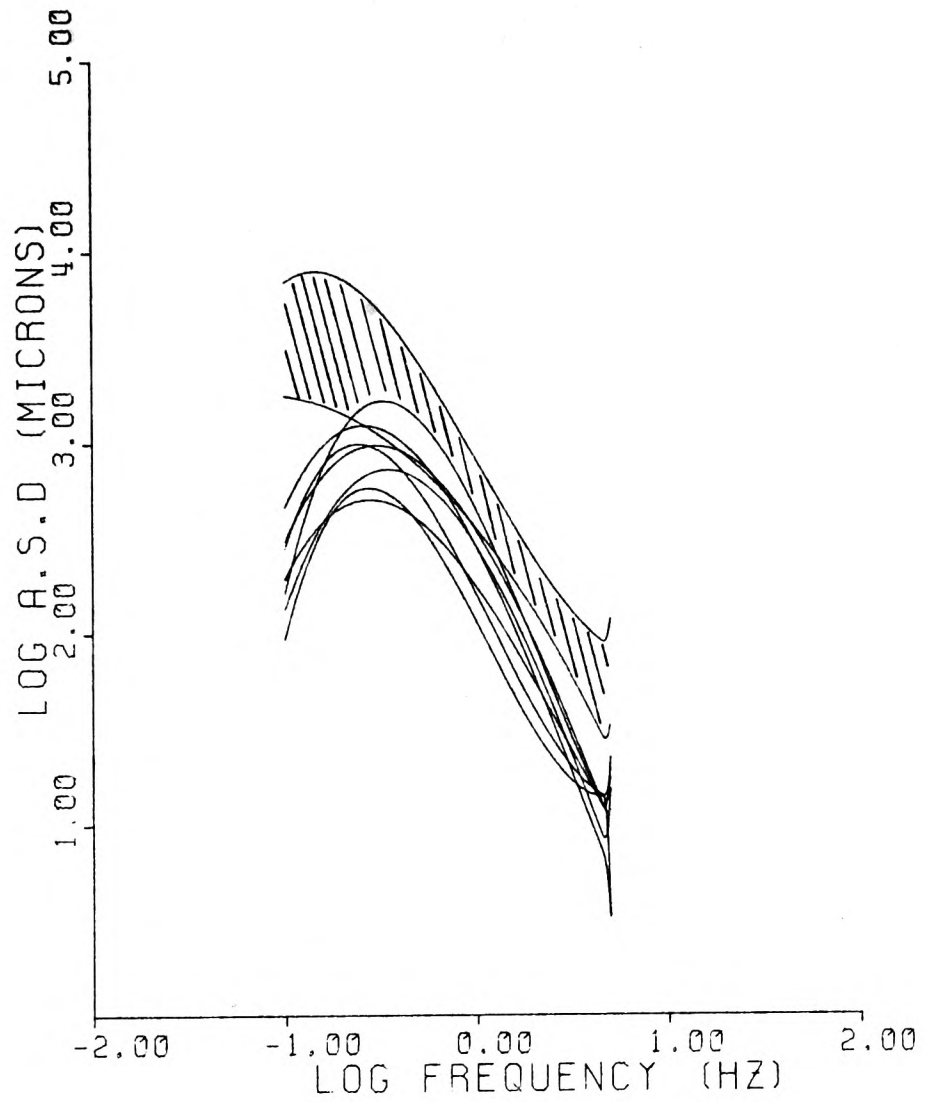


Fig. 6.14 All events at SAAS : E4



CUBIC SPLINE FIT TO SEISMIC SPECTRUM.

CHILE DATA: ALL EVENTS AT SAAS: E4
 SPECTRA OF: 01,22,C,B,A,14,11,13,18

Fig. 6.15 Spectra of all events at SAAS : E4

CHILE DATA: ALL EVENTS AT ALL SAAS STATIONS: SUM ALONG FAULT (AF/N-S) AV=4 KM/S

TIME

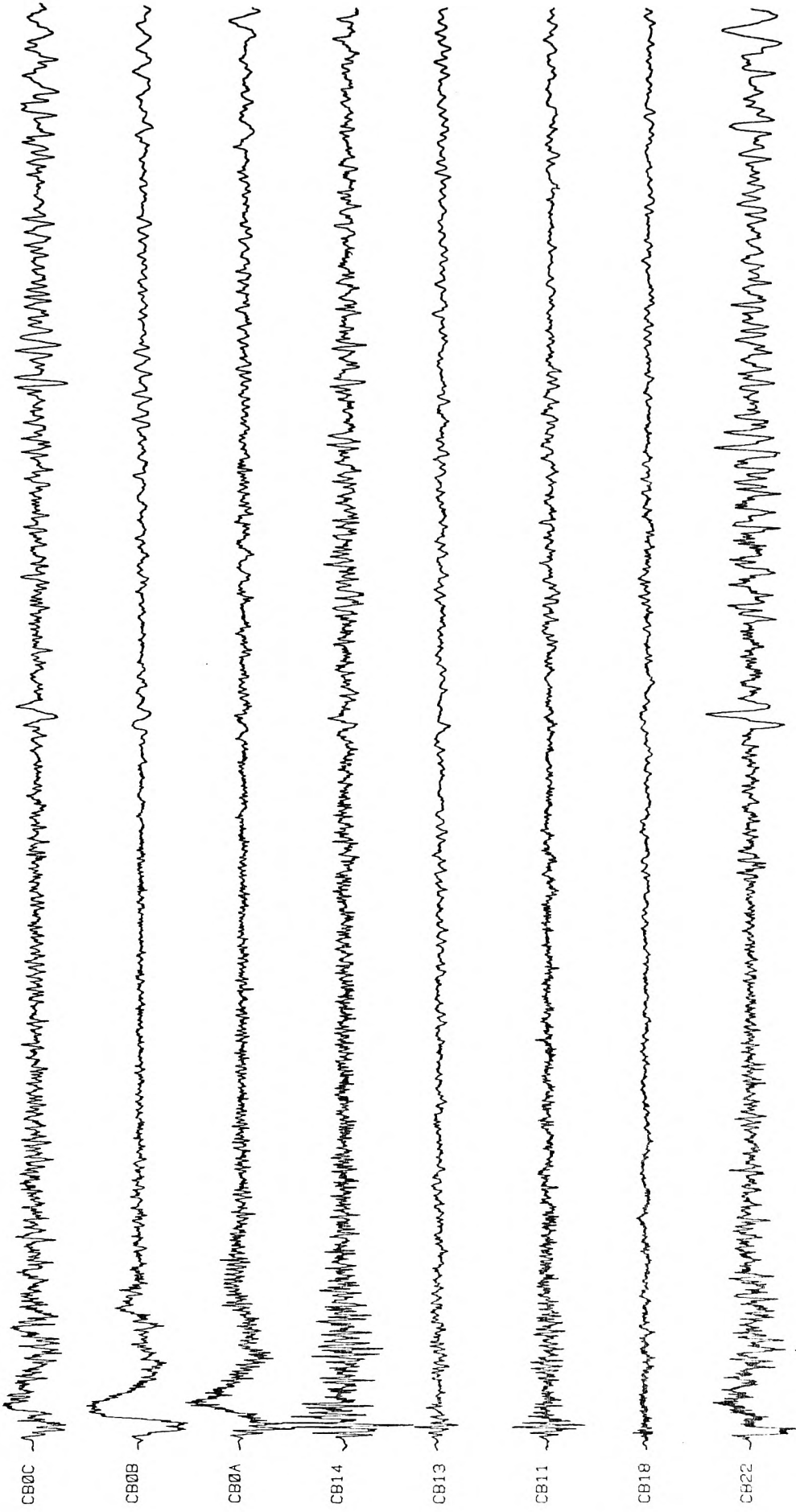


Fig. 6.16a : AF/N-S : 4km/s

CHILE DATA: ALL EVENTS AT ALL SAAS STATIONS: SUM: AF/N-S (AV=10 KM/S)

TIME

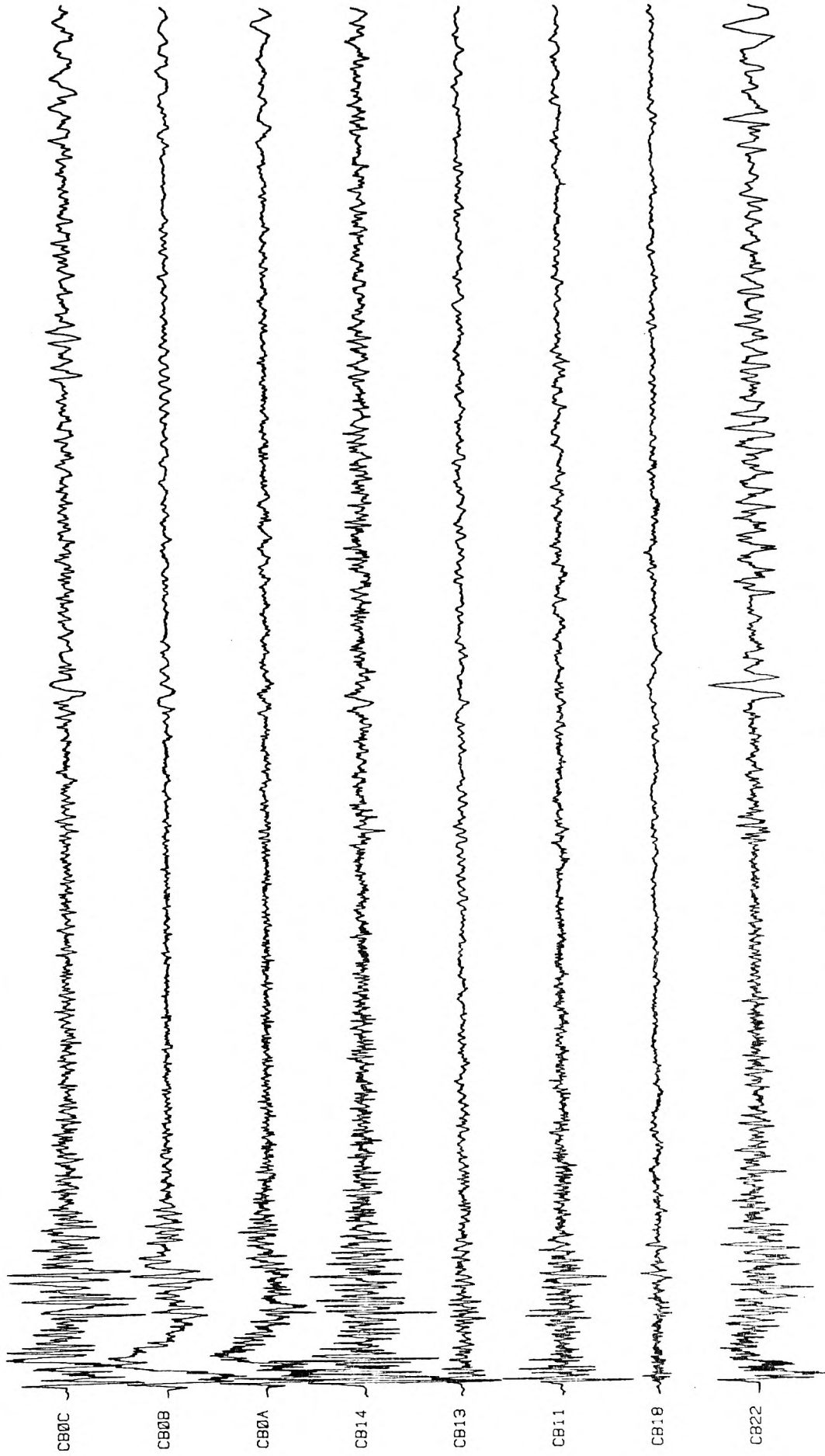


Fig. 6.16b : AF/N-S : 10km/s

CHILE DATA: ALL EVENTS AT E-W SAAS STATIONS: SUM, OF/NW-SE (4 KM/S)

TIME

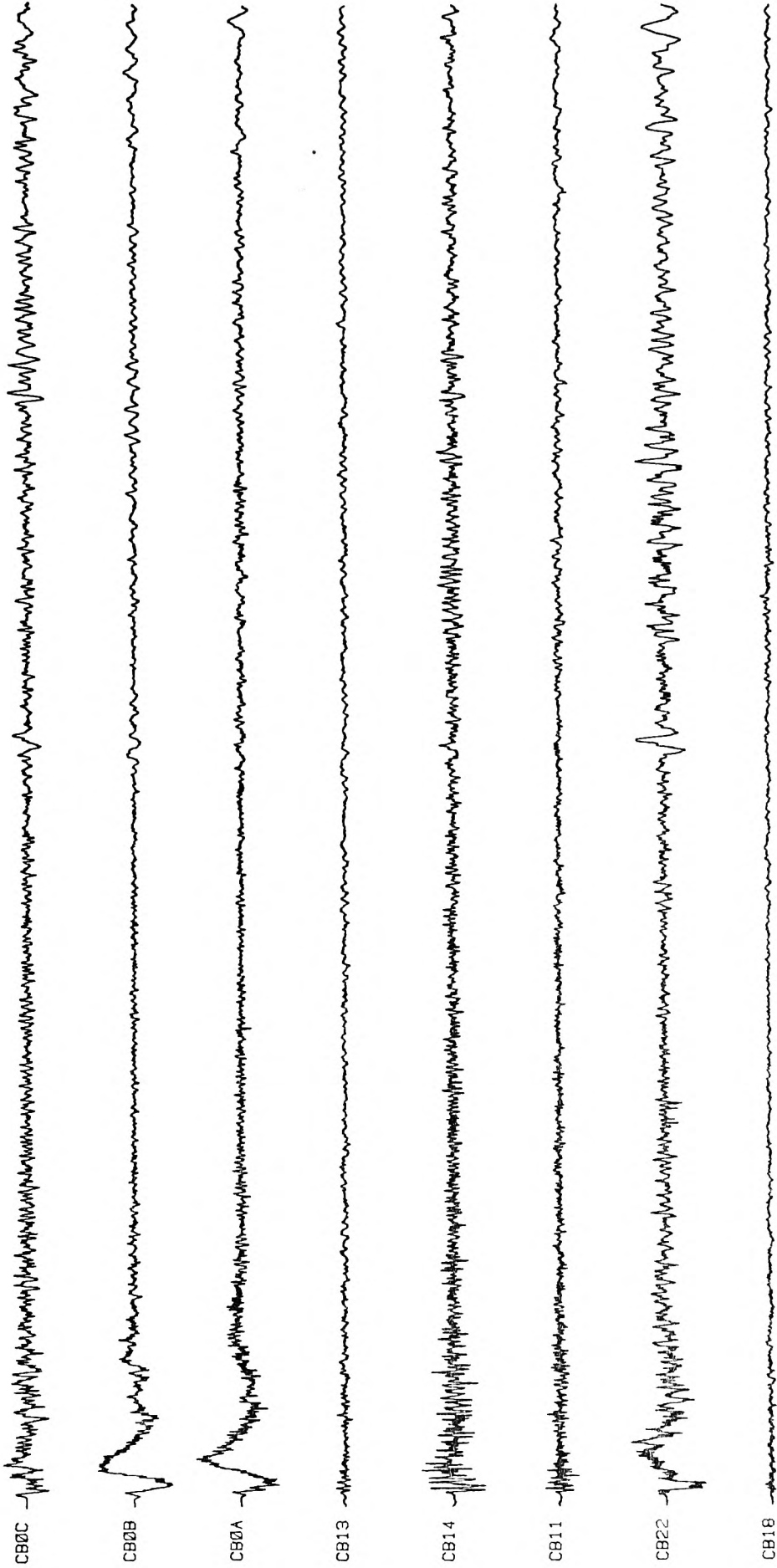


Fig. 6.17a : OF/NW-SE : 4km/s

CHILE DATA: ALL EVENTS AT E-W SAAS STATIONS; SUM; OF/NW-SE (10 KM/S)

TIME

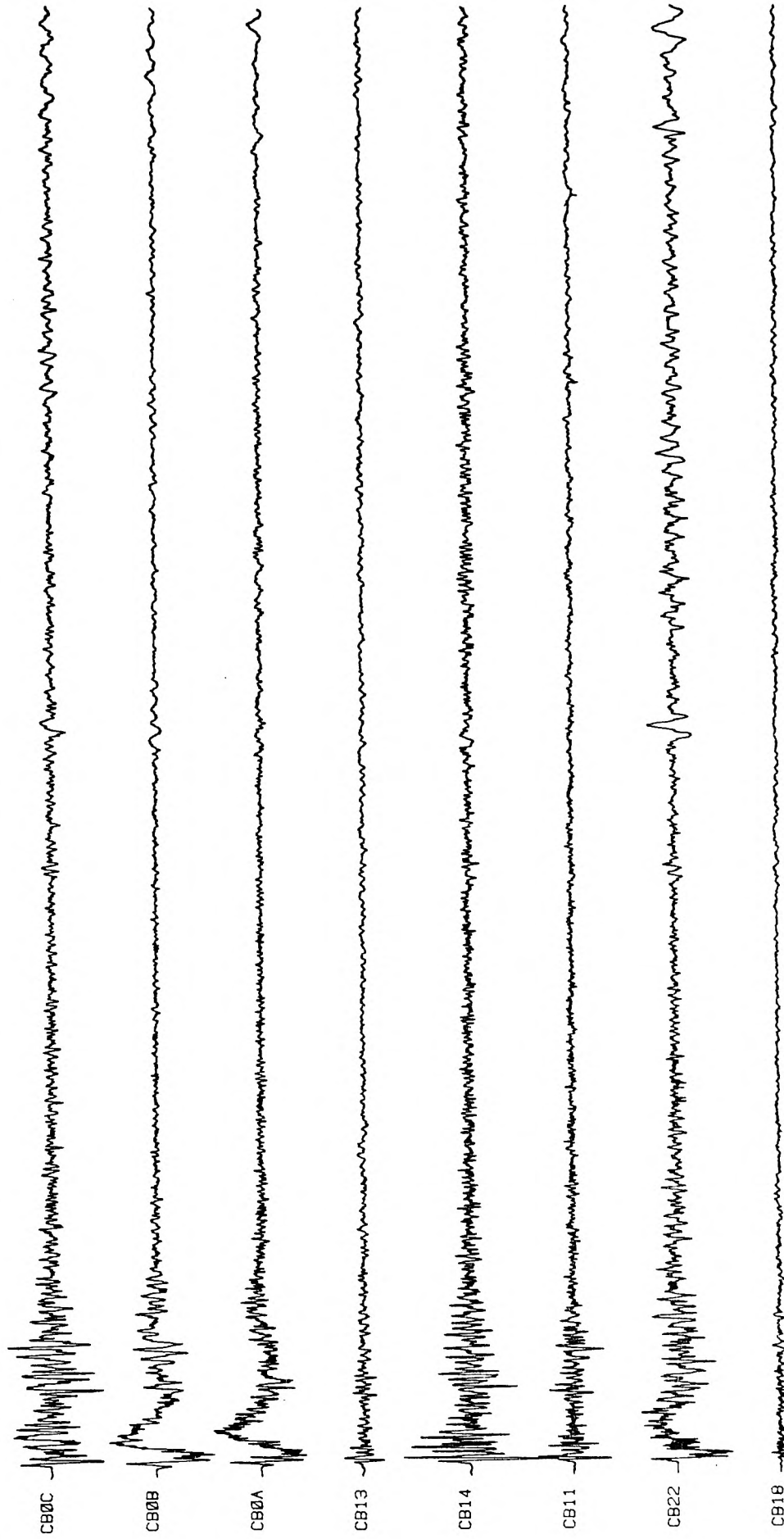


Fig. 6.17b : OF/NW-SE : 10km/s

CHILE DATA: ALL EVENTS AT N-S SAAS STATIONS; SUM; OF/NE-SW (4 KM/S)

TIME

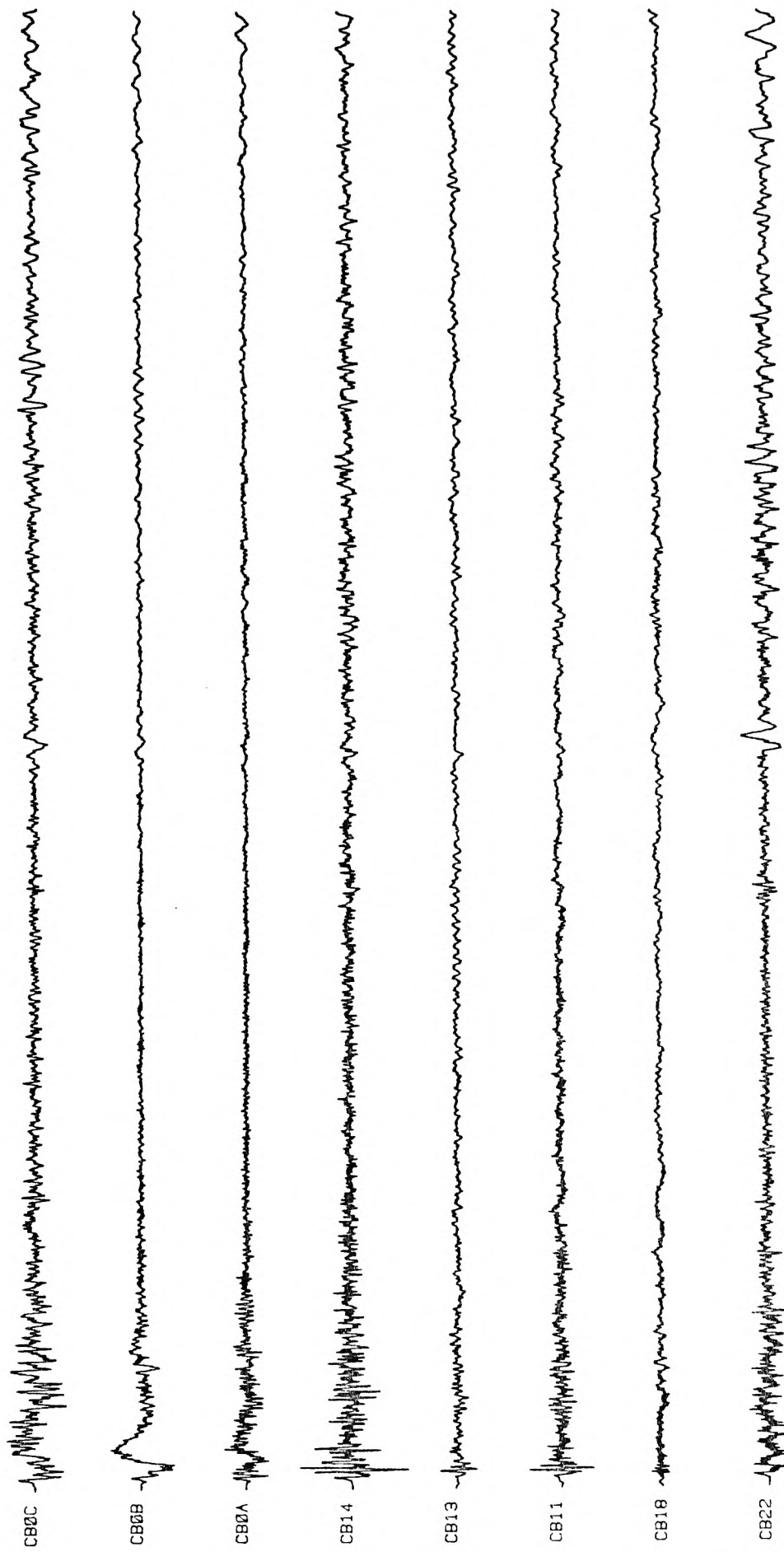


Fig. 6.18a : OF/NE-SW : 4km/s

CHILE DATA: ALL EVENTS AT N-S SAAS STATIONS: SUM: OF/NE-SW (10 KM/S)

TIME

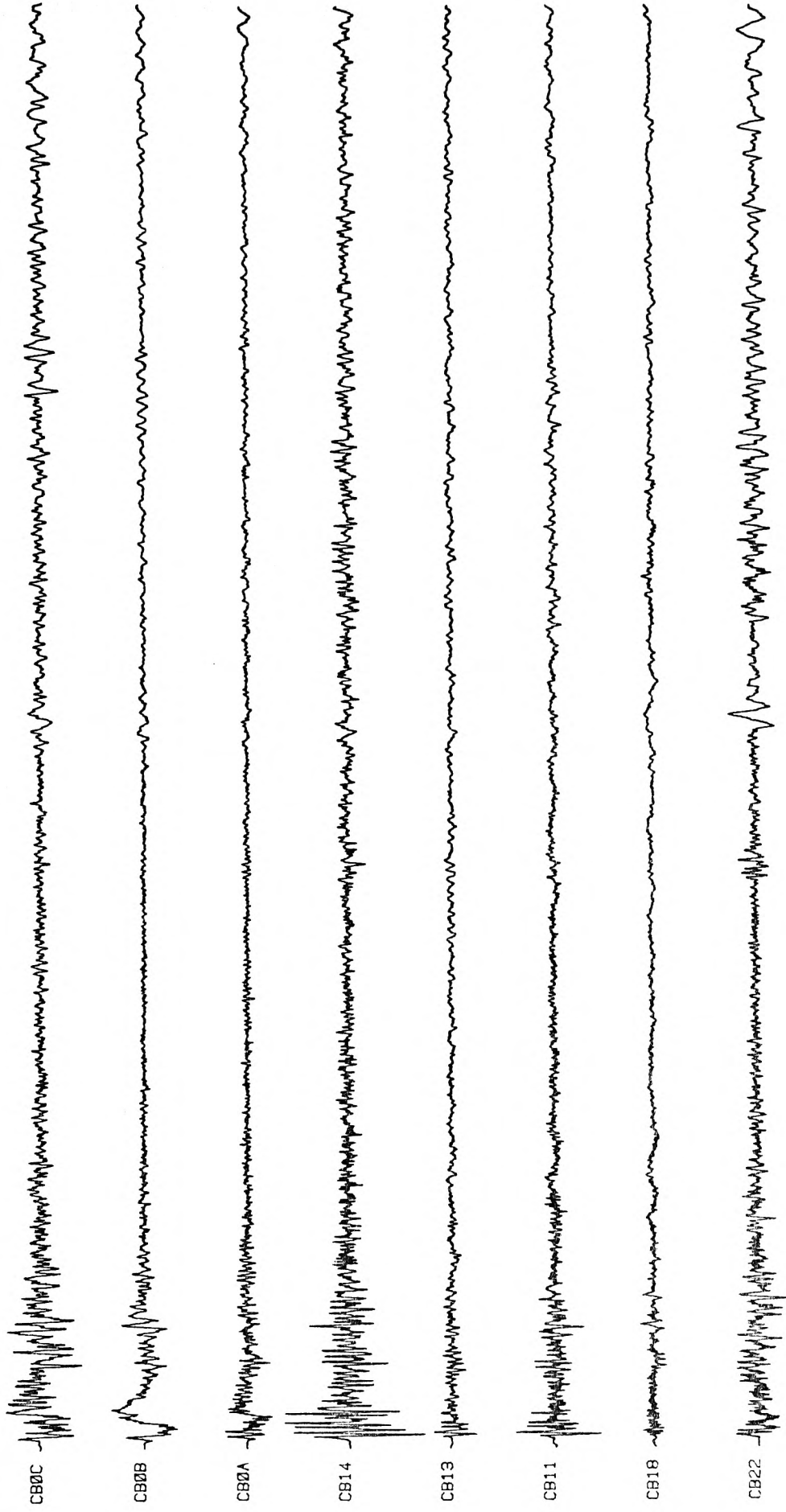


Fig. 6.18b : OF/NE-SW : 10km/s

of all events plotted to the same x-y scale with a N-S direction of trigger along the fault (AF) and oblique to the fault (OF). That is: AF/N-S (ALL SAAS stations), OF/NW-SE (E-W SAAS stations) and OF/NE-SW (N-S SAAS stations) at average Mach numbers of 0.67 (i.e: AV=4km/s) and 1.65 (i.e: AV=10km/s). The equivalent spectra are collectively displayed in Figures 6.19 and 6.20. The spectrum of CB001 is marked on all plots.

The first impression from the spectral plots of Figures 6.19 and 6.20 is that some of the spectra are well below that of the major shock while others are above especially in the dynamic part or roll-off. If we look closely, however, it is possible to decipher only 2 spectral curves that seem to coincide with the major part of the CB001 spectrum. These curves are marked by solitary arrows. Searching through individual spectral plots we found that these correspond to events CB00C (Fig. 6.19) and CB00B (Fig. 6.20). The spectral approximations are shown in Figure 6.21a and the equivalent seismograms are displayed in Figure 6.21b.

Examining Figures 6.21a and 6.21b we note the following:

- 1 - The constructed long period amplitude from the 12 array records of CB00C resembles that of CB001 more closely than that of CB00B. This is most certainly due to:
 - a) Size of the input event.
 - b) Record quantity.
 - c) Selected rupture velocity.

- 2 - The shapes of the equivalent simulated spectra compare

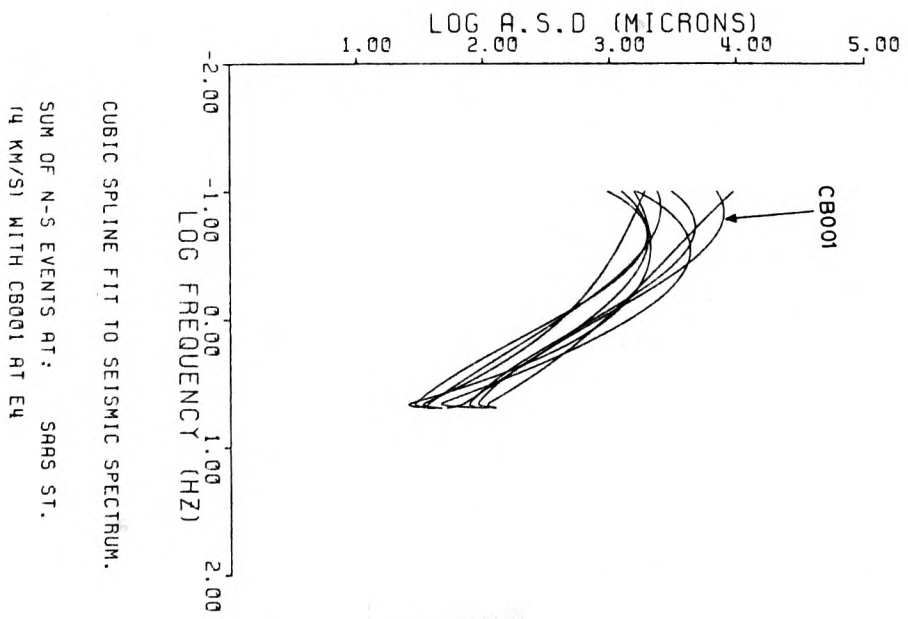
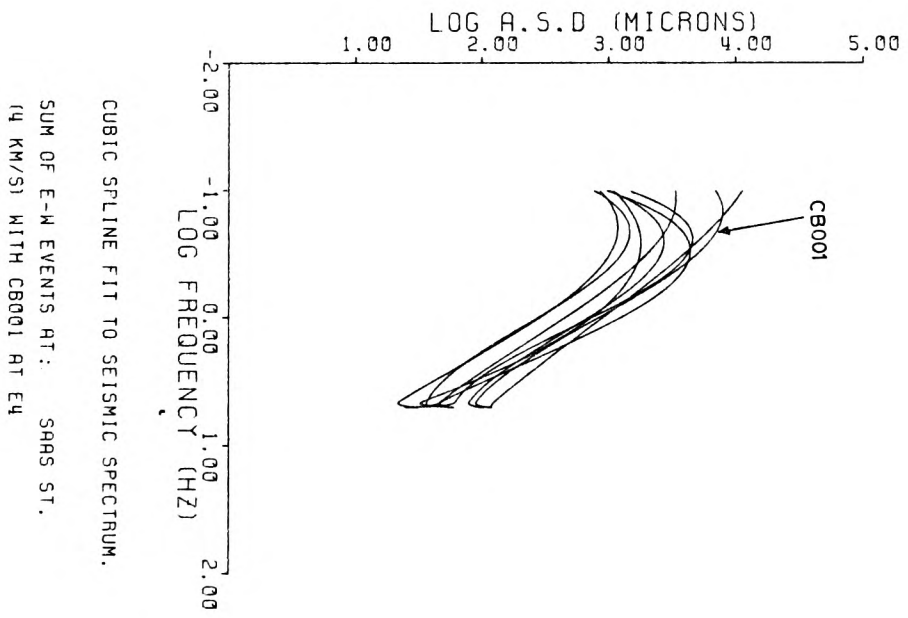
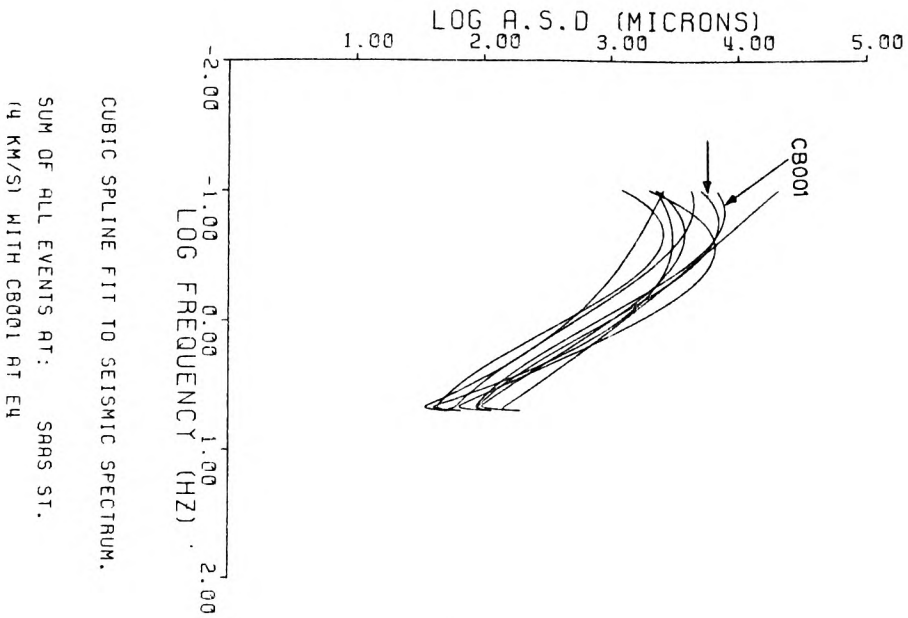


Fig. 6.19 Spectra of sums at 4km/s

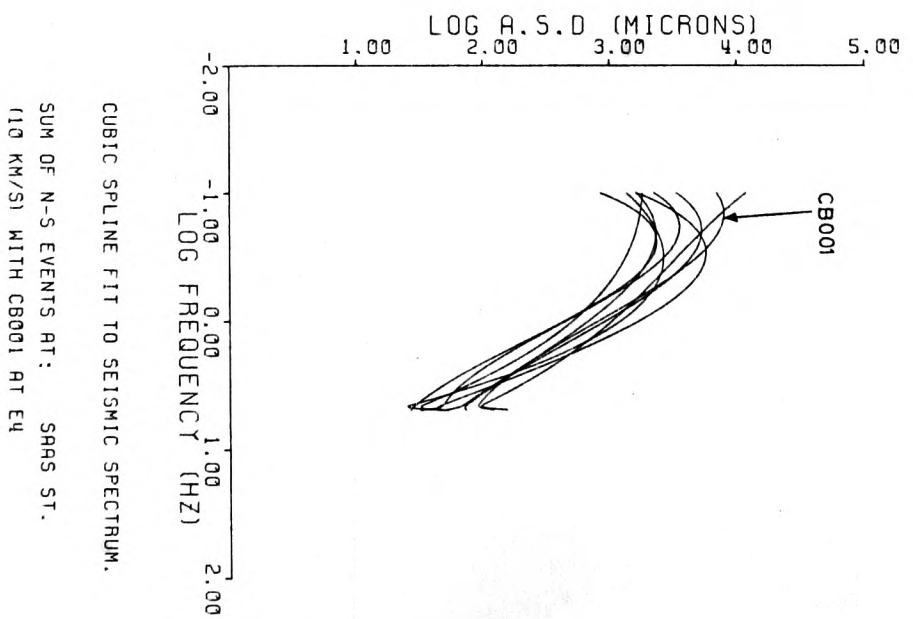
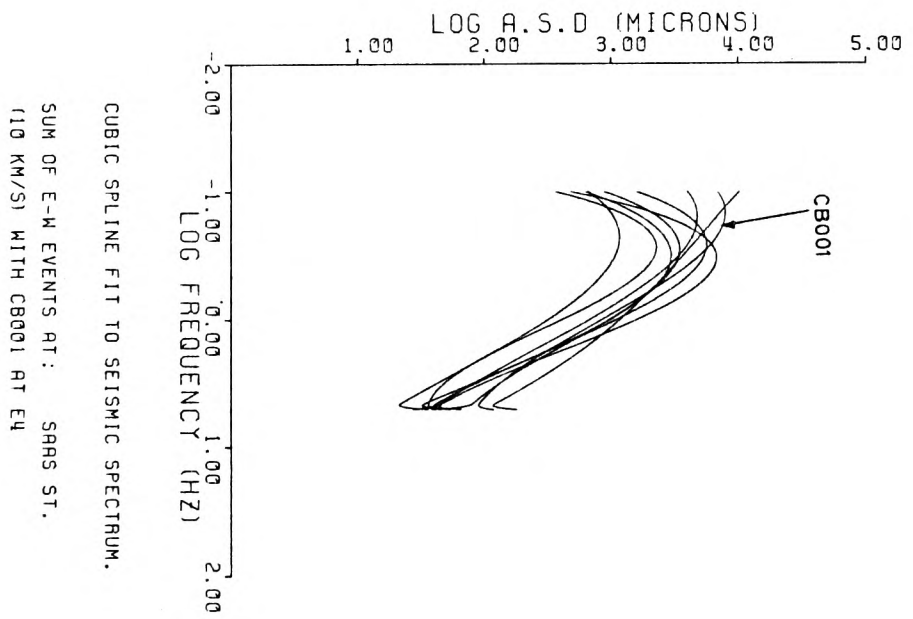
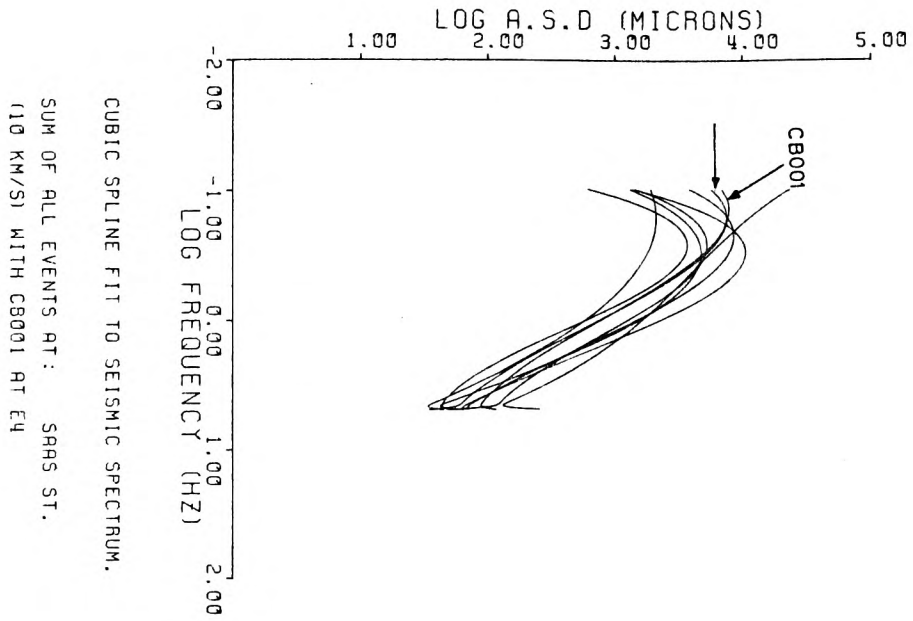


Fig. 6.20 Spectra of sums at 10km/s

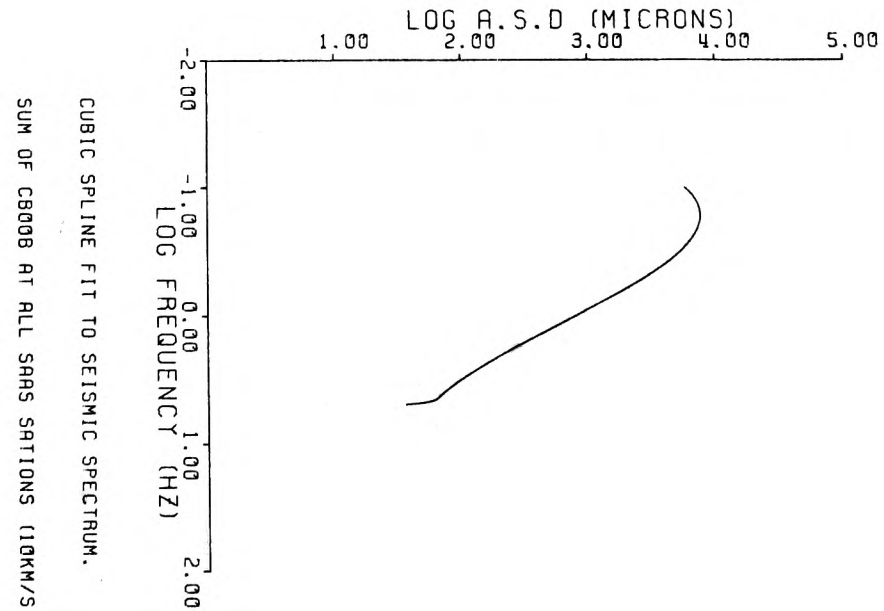
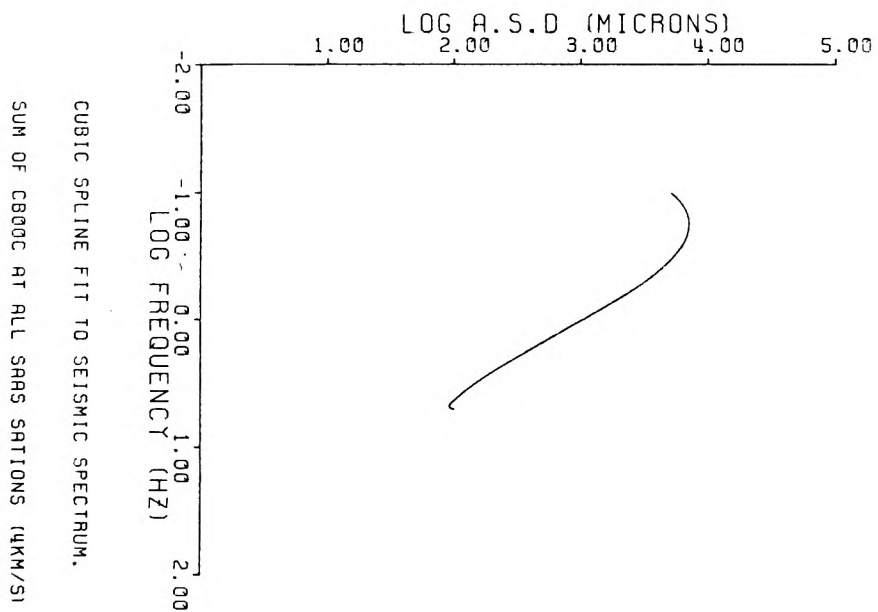
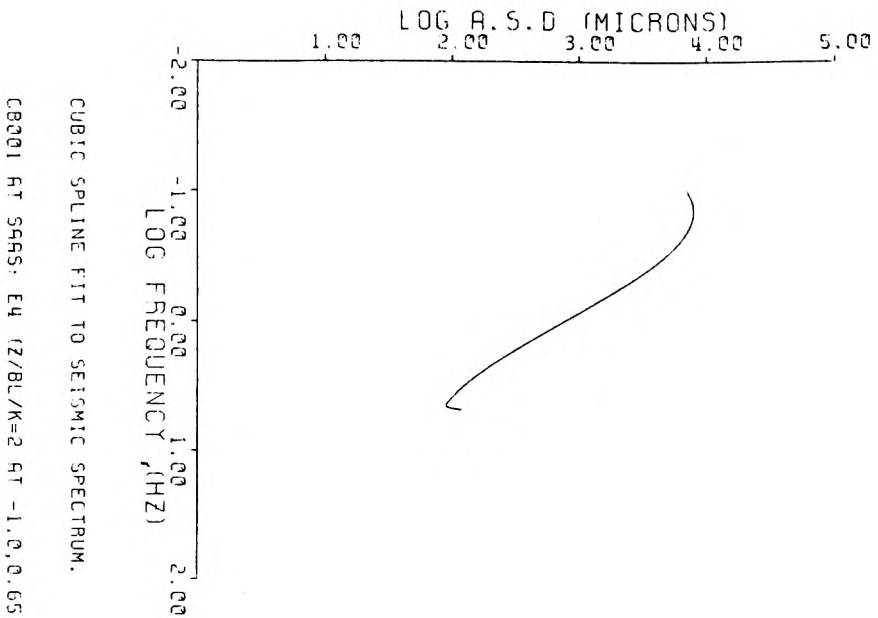


Fig. 6.21a Spectral comparison of approximate fits

CHILE DATA: COMPARISON BETWEEN CB001 AT E4 AND SUMS OF CB00C AND CB00B

TIME



SUM OF CB00C AT 12 SAAS STATIONS

TIME



SUM OF CB00B AT 10 SAAS STATIONS

TIME

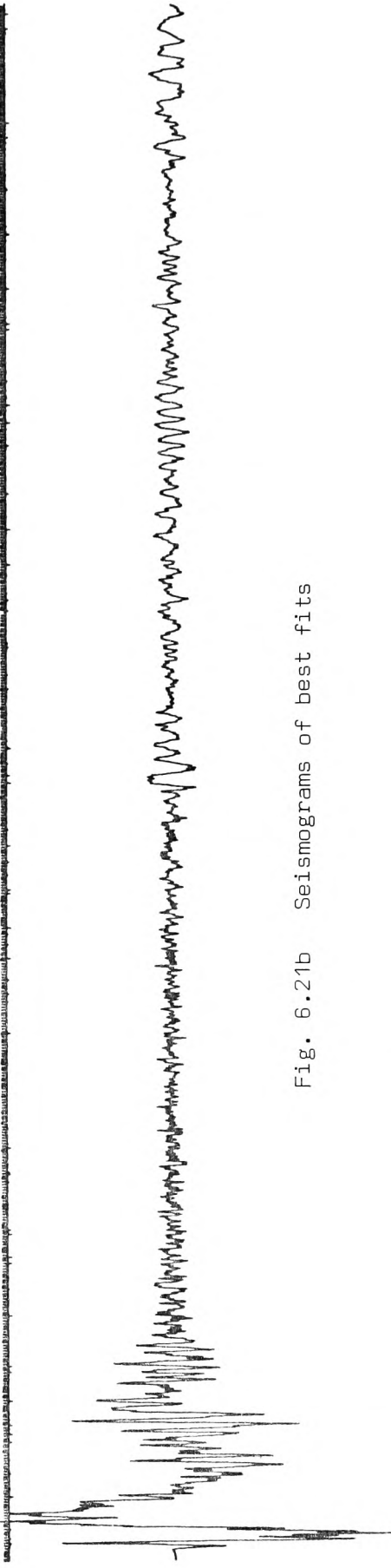


Fig. 6.21b Seismograms of best fits

remarkably well with that of CB001. Both, however, are clearly below the static or long period Ω_0 level of CB001.

As a preliminary interpretation of this result we may state that we have in fact reconstructed a source very much similar in spectral shape to an actual large earthquake spectrum.

Comparing the results, it is possible to point out the following facts:

- 1) Clearly the trigger direction along the fault plane where all array records are incorporated seems a better approximation than a direction oblique to the fault.
- 2) The subsonic rupture speed used to construct the simulated long period motion from the array records of CB00C appear to be more realistic for the simple reason that a better waveform fit is observed.
- 3) As we mentioned in our rupture velocity discussion, it could happen that subsonic rupture at the fault surface may generate in an overlying low velocity layer, waves travelling at supersonic speeds. This could be the case with the result obtained from the summation of 10 array records of CB00B at $M \approx 2.29$. This highly hypothetical and tentative situation, however, seems unlikely because the simulated seismogram from CB00B records shows long period phases much lower in amplitude than that displayed by the sum of CB00C records.
- 4) In relation to (3) above, and because our assumed source model is a 2-dimensional kinematic Haskell-type fault (see

Section 3.3.0, Chapter 3), it seems remotely possible that rupture speeds exceed Mach numbers > 1.0 . (See for example Boore et al, 1971).

4.2.0 Attempting to Construct a Larger Source:

Having obtained what appears to be a significant result in constructing the large earthquake motion of CB001 at a single station, we ask the question of what would be the outcome if we incorporate the initial sums given in the previous section according to the 8 cases described in Section 3.3.3? The appropriate answer would be that since we have already constructed an approximation to the motion and spectral signature of CB001 at one station, there is enough prima facie reason to expect the reconstruction of an even larger source by combining the initial sums. We proceed to investigate this possibility.

Before doing so, however, if we look back at the seismograms of the initial sums shown in Figures 6.16a and b to 6.18a and b we notice how the ringing effect of the bass-lift circuit is being augmented at this stage of summation. This feature is particularly true for the CB00A and CB00B sums. We therefore expect that in the final sums of the 8 cases this effect would build-up even more. This in fact turns out to be the case as illustrated in Figure 6.22. Although this problem is taken care of in the analysis stage (see Chapter 4) and does not adversely affect our ultimate results, it nevertheless is worth attempting to remedy this digitally and observe what happens to seismic wave amplitudes and periods. For this purpose we applied a simple unipolar digital filter to the

CHILE DATA: SUM OF ALL EVENTS; ALONG FAULT STRIKE IN N-S DIRECTION CASE (1)

TIME

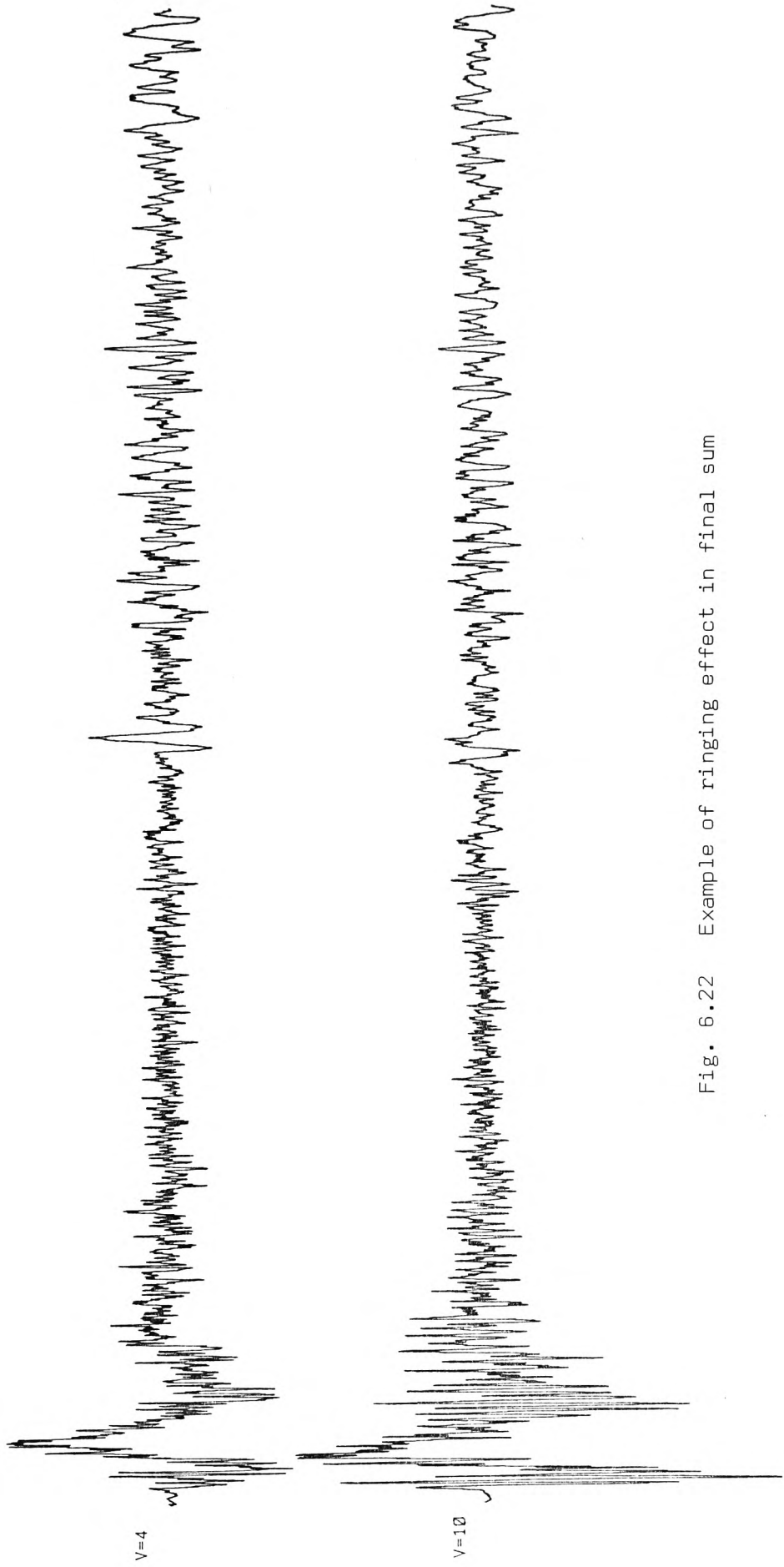


Fig. 6.22 Example of ringing effect in final sum

upper trace of Figure 6.22. The filtered outputs at three amplitude ratios are shown in Figure 6.23. At a ratio of 0.8 maximum we notice that the ringing is almost eliminated but that the long period content is severely suppressed and phase shifted by nearly 2π . Applying such a filter to our summed outputs would consequently mean that we lose most of the significant part of the seismogram. As a final resort and for purely display purposes we present the 8 cases with a substantial part of the ringing cut out.

On this basis we present the seismograms and respective spectra in the sequence outlined in Section 3.3.3. Thus each final summed case is plotted to the same scale for the subsonic and supersonic rupture propagation respectively (Figures 6.24, 6.25, 6.27, 6.28, 6.30, 6.31, 6.33, and 6.34). The equivalent spectral plots each with the spectrum of CB001 at E4, included for comparison, are shown in opposite trigger directions, i.e.: cases (1) and (2), (7) and (8), (3) and (6), (4) and (5) (Figures 6.26, 6.29, 6.32, and 6.35).

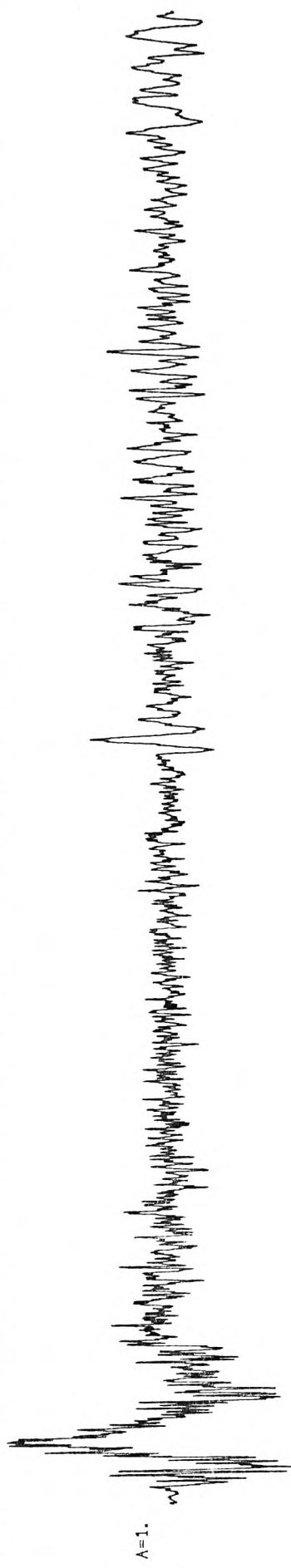
As expected the spectral differences are quite clear. In all the spectral plots the curve with a "hump" (produced by the larger amplitudes around the frequency range of 0.5-5 Hz) corresponds to supersonic rupture velocity. The lowest curve is that of CB001 and the middle curve corresponds to subsonic ($M = 0.92$) propagation.

Studying the 8 cases we make the following observations:

1. In cases (1), (2), (7) and (8) we recognize the substantial step-up in the static (long period or Ω_0) level as

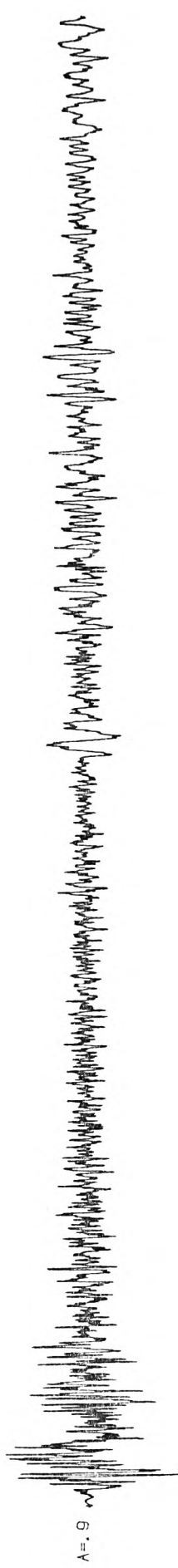
CHILE DATA: SUM OF ALL EVENTS CASE (1) ELIMINATION OF RINGING BY DIGITAL FILTER

TIME



AA=0.9

TIME



AA=0.8

TIME

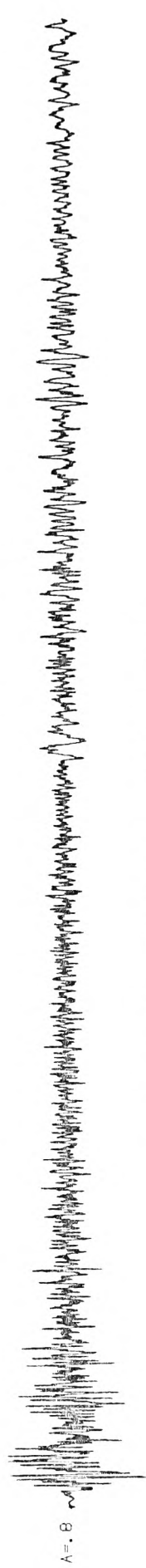


Fig. 6.23 Eliminating ringing effect

CHILE DATA: SUM OF ALL EVENTS: ALONG FAULT STRIKE IN N-S DIRECTION CASE (1)

TIME

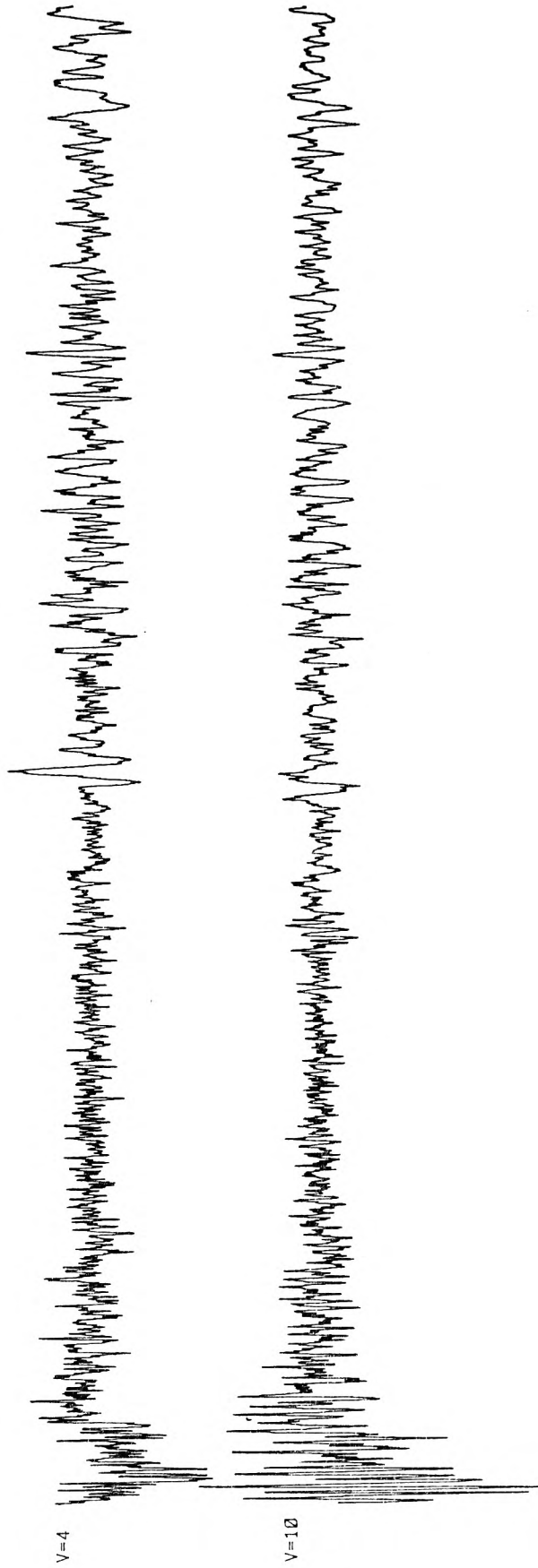


Fig. 6.24 Case (1)

CHILE DATA: SUM OF ALL EVENTS: ALONG FAULT STRIKE IN S-N DIRECTION CASE (2)

TIME

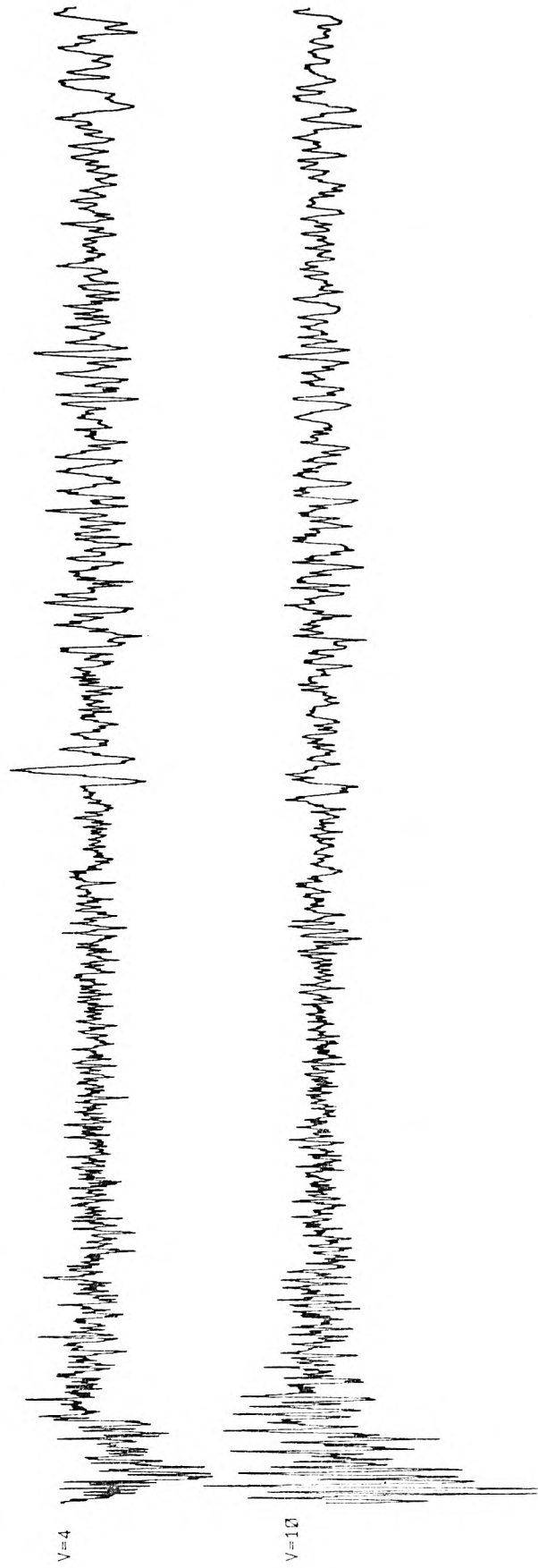


Fig. 6.25 Case (2)

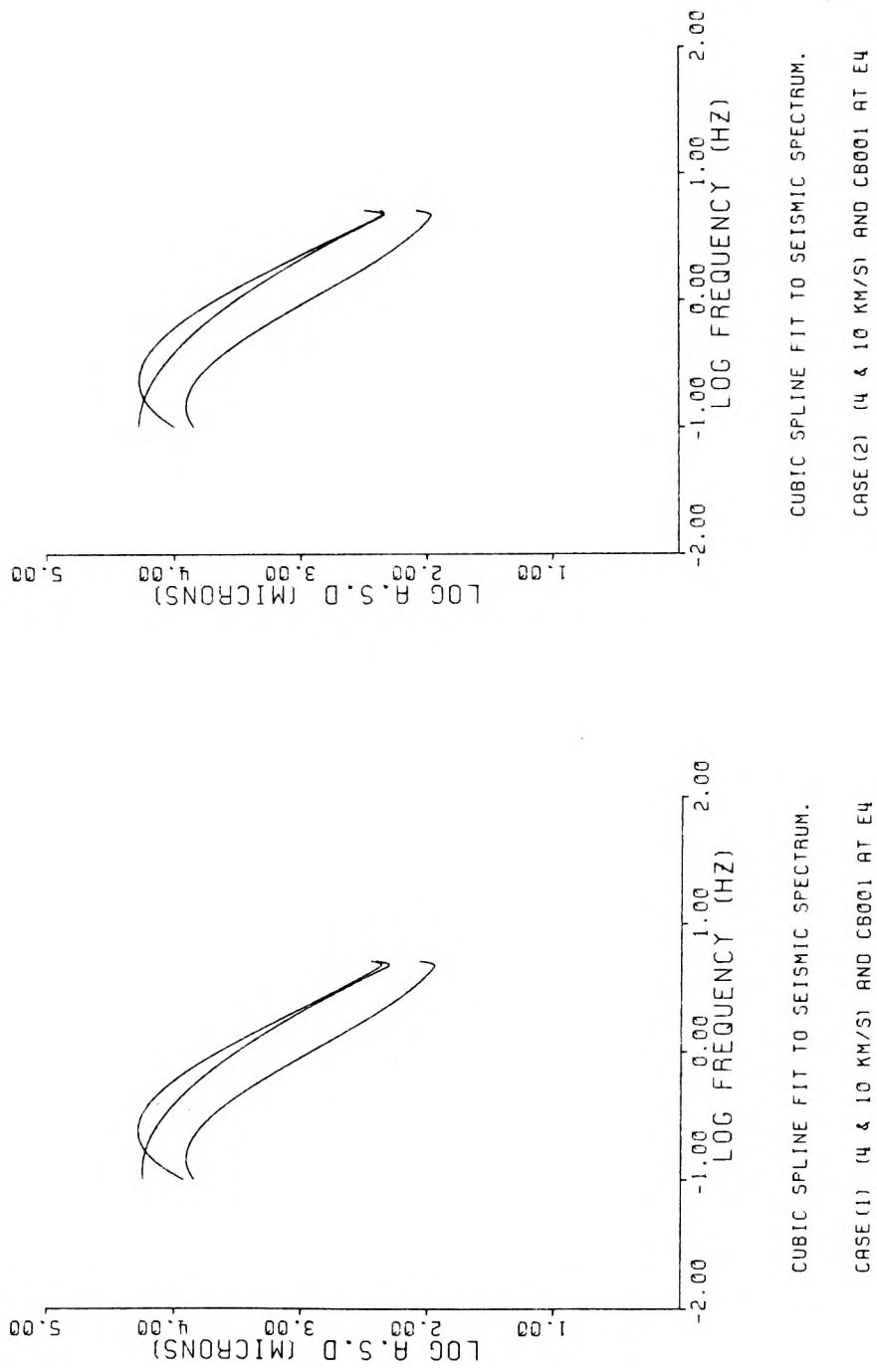


Fig. 6.26 Spectra of Cases (1) and (2)

CHILE DATA: SUM OF ALL EVENTS, ALONG FAULT DIP IN DOWNWARD DIRECTION CASE (7)

TIME

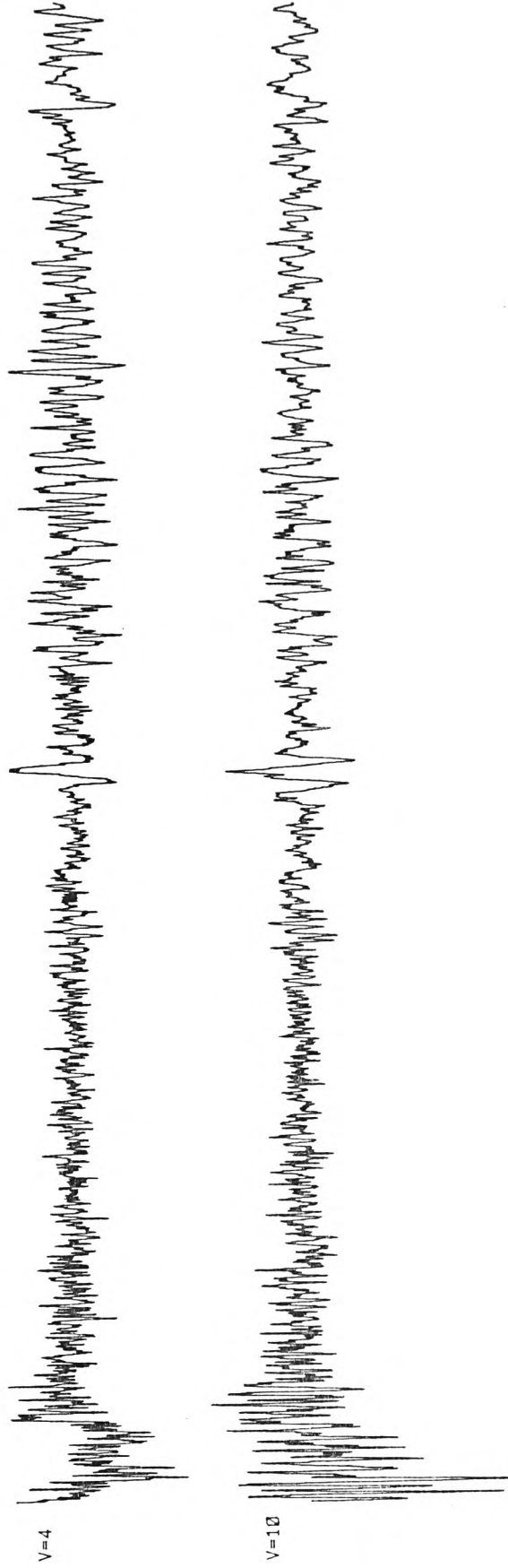


Fig. 6.27 Case (7)

CHILE DATA: SUM OF ALL EVENTS ALONG FAULT DIP IN UPWARD DIRECTION CASE (8)

TIME

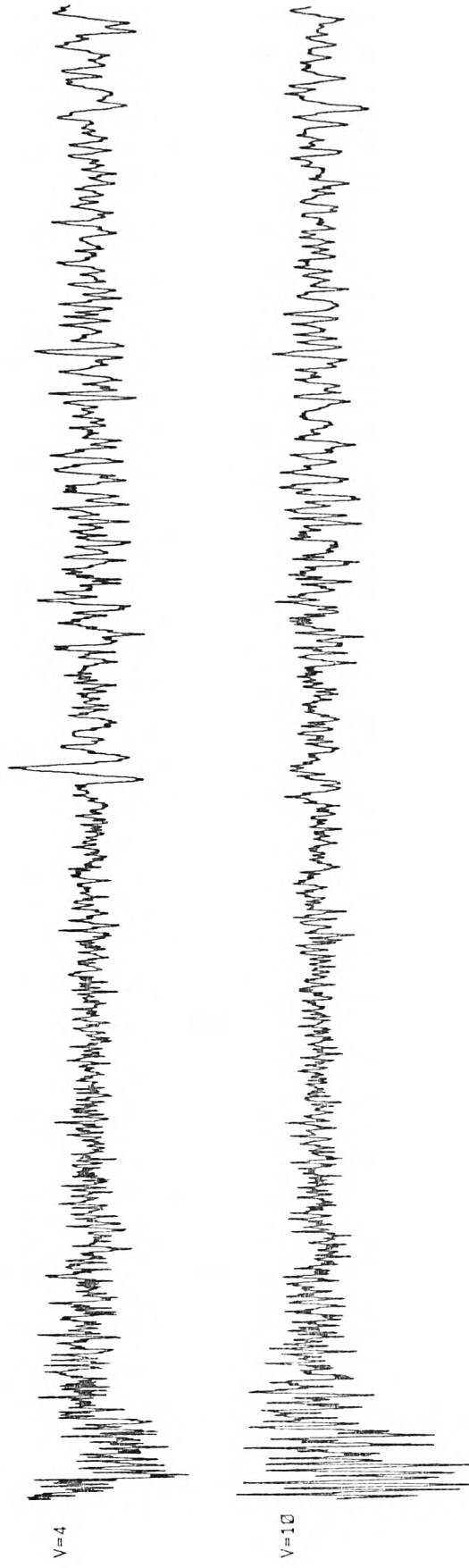
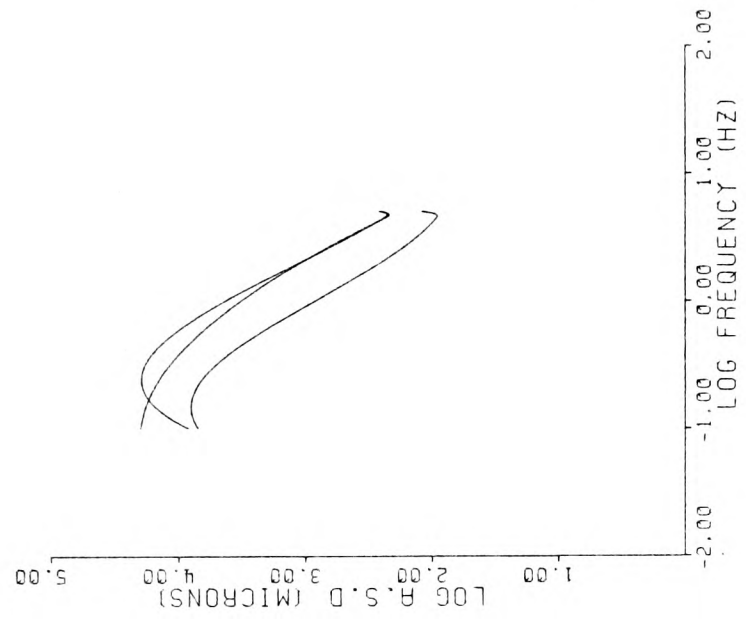
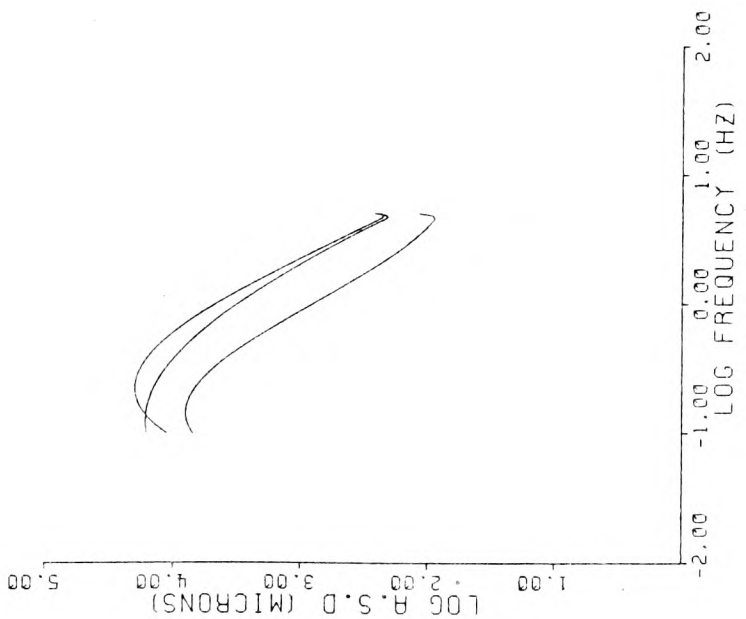


Fig. 6.28 Case (8)



CUBIC SPLINE FIT TO SEISMIC SPECTRUM.
CASE (7) (4 & 10 KM/S) AND C6001 AT E4



CUBIC SPLINE FIT TO SEISMIC SPECTRUM.
CASE (8) (4 & 10 KM/S) AND C6001 AT E4

Fig. 6.29 Spectra of Cases (7) and (8)

CHILE DATA: SUM OF E-W EVENTS OBLIQUE TO FAULT IN NW-SE DIRECTION CASE (3)

TIME

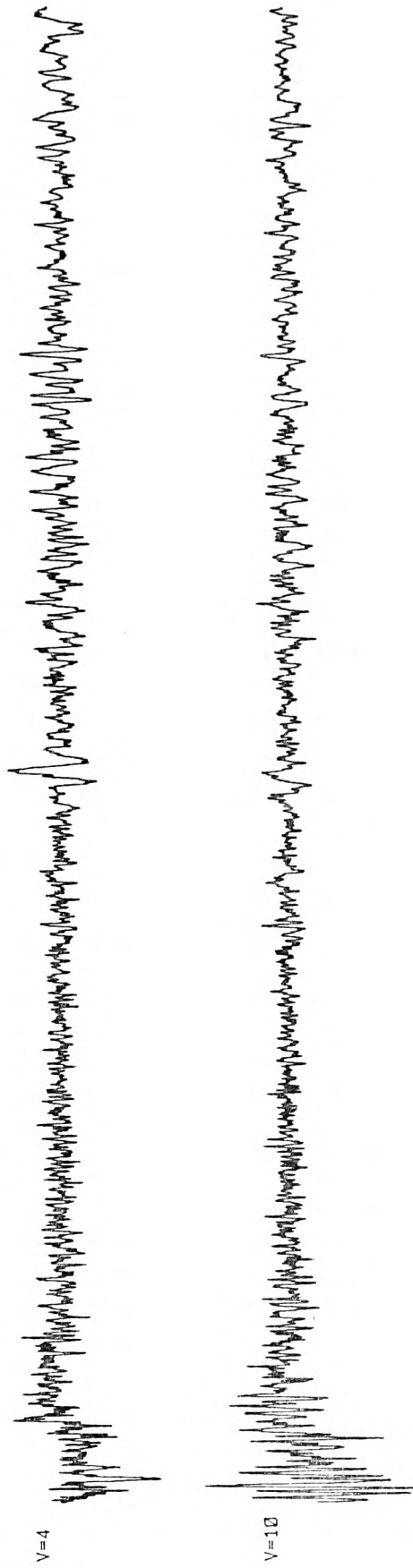


Fig. 6.30 Case (3)

CHILE DATA: SUM OF E-W EVENTS OBLIQUE TO FAULT IN SE-NW DIRECTION CASE (6)

TIME

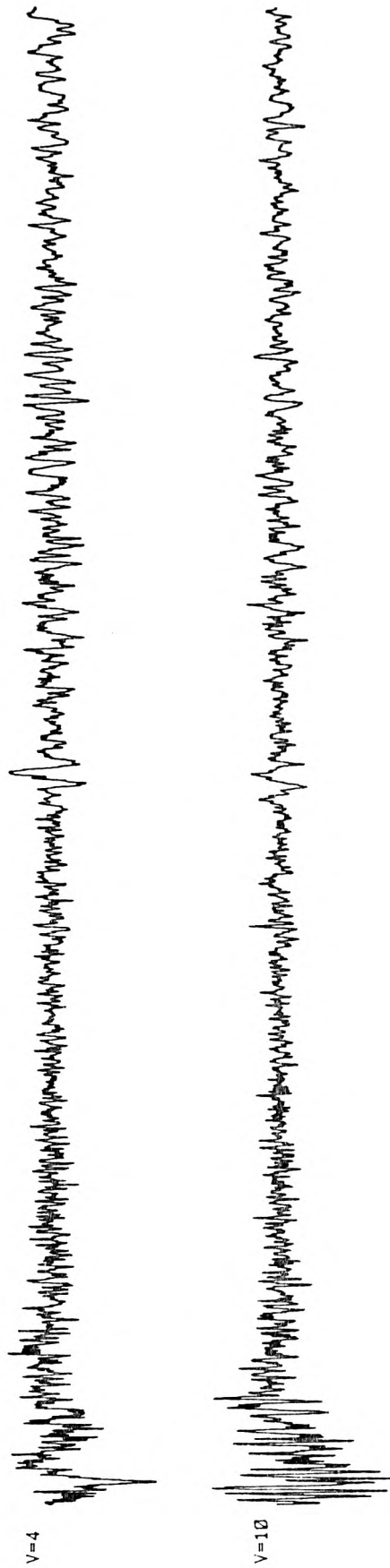
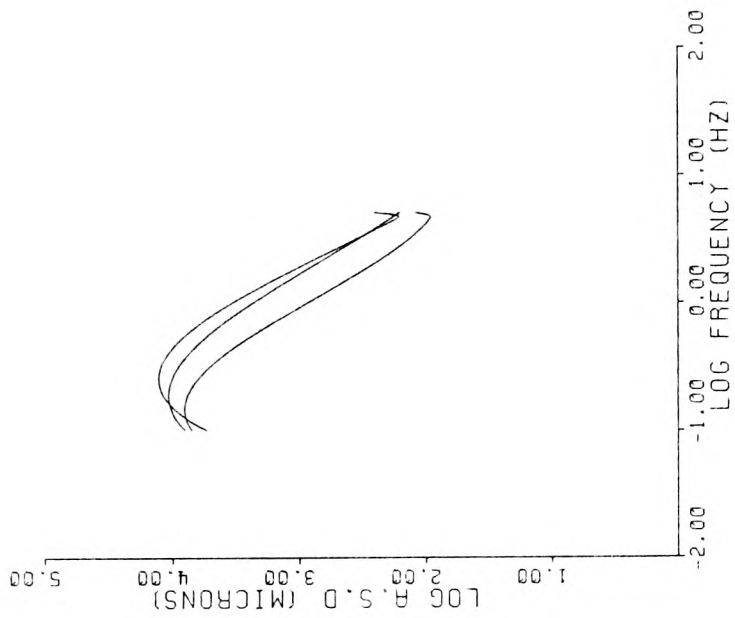
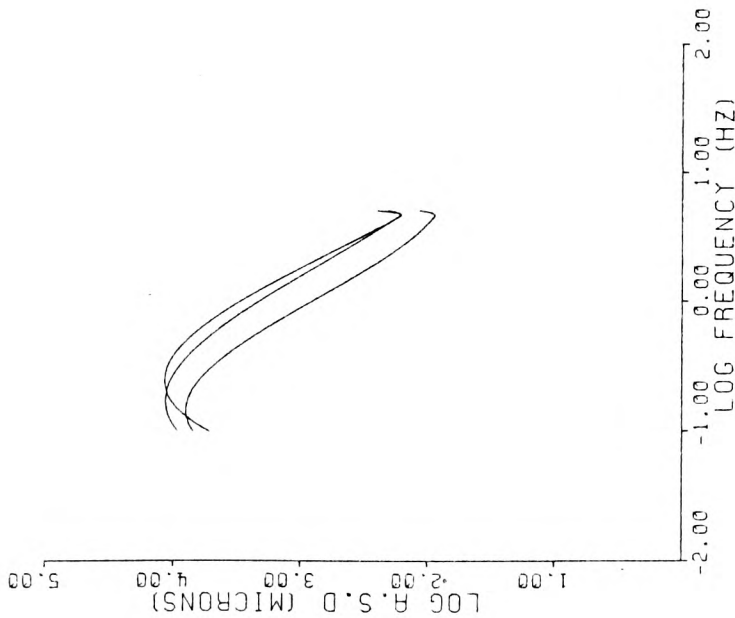


Fig. 6.31 Case (6)



CUBIC SPLINE FIT TO SEISMIC SPECTRUM.

CASE (6) (4 & 10 KM/S) AND C6001 AT E4



CUBIC SPLINE FIT TO SEISMIC SPECTRUM.

CASE (3) (4 & 10 KM/S) AND C6001 AT E4

Fig. 6.32 Spectra of Cases (3) and (6)

CHILE DATA: SUM OF N-S EVENTS OBLIQUE TO FAULT IN NE-SW DIRECTION CASE (4)

TIME

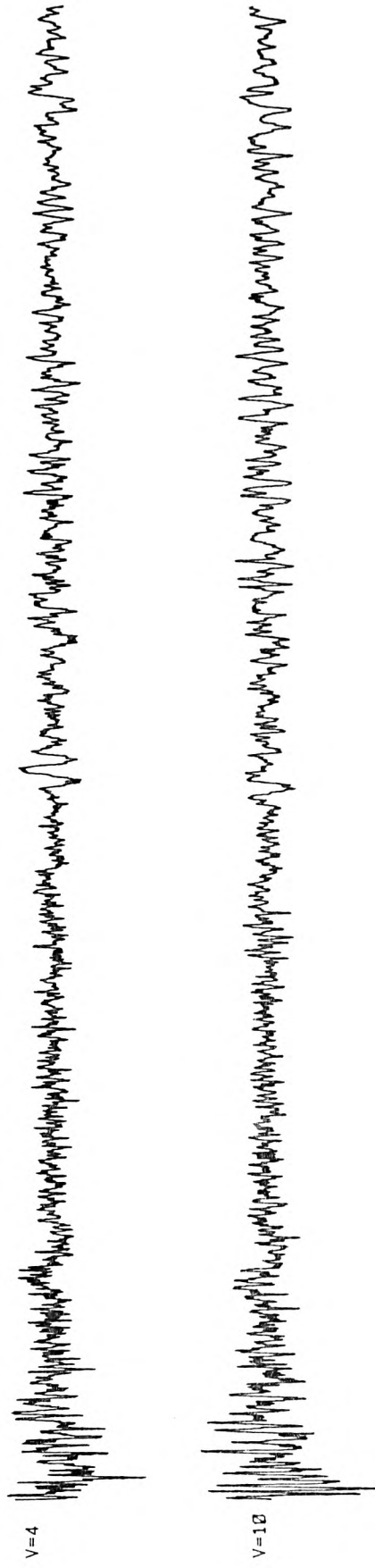


Fig. 6.33 Case (4)

CHILE DATA: SUM OF N-S EVENTS OBLIQUE TO FAULT IN SW-NE DIRECTION CASE (5)

TIME



V=4



V=10

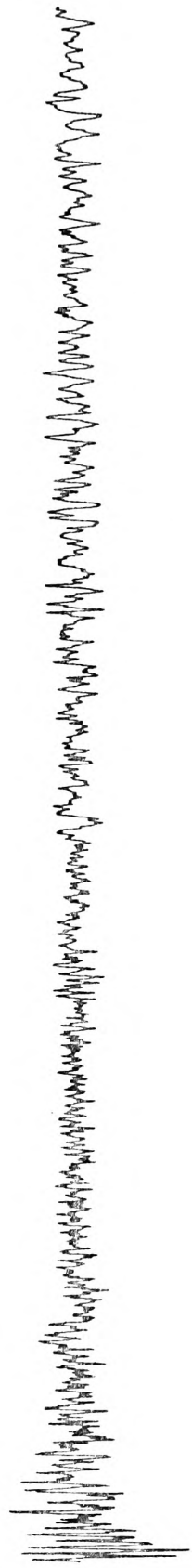
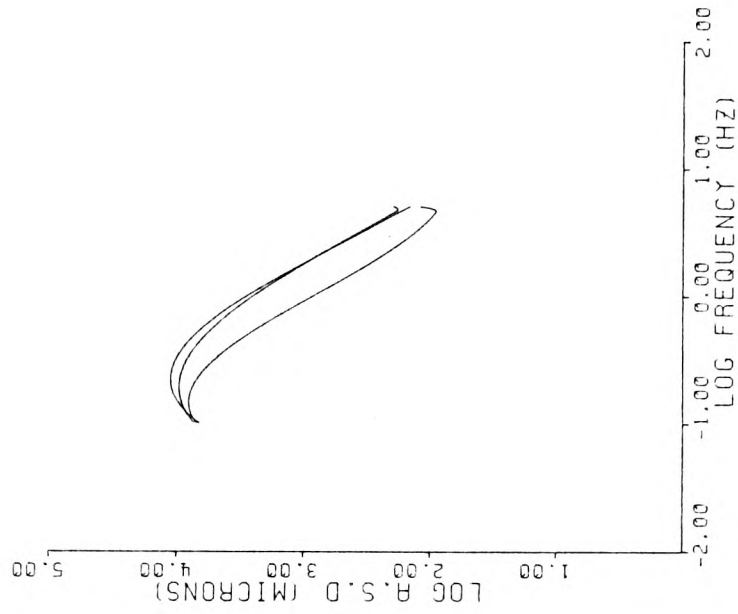
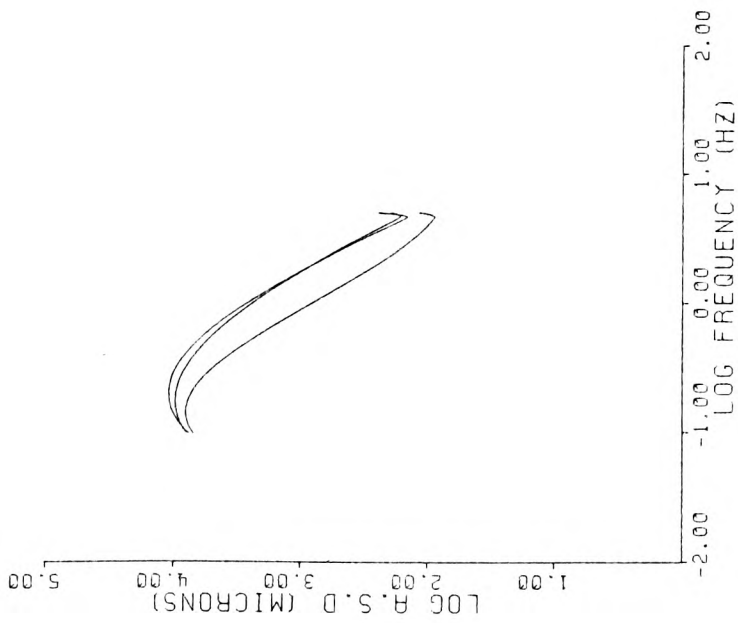


Fig. 6.34 Case (5)



CUBIC SPLINE FIT TO SEISMIC SPECTRUM.

CASE (4) (4 & 10 KM/S) AND C6001 AT E4



CUBIC SPLINE FIT TO SEISMIC SPECTRUM.

CASE (5) (4 & 10 KM/S) AND C6001 AT E4

Fig. 6.35 Spectra of Cases (4) and (5)

compared to that of CB001, while in cases (3), (4), (5), and (6) the static level has a smaller degree of enhancement over the CB001 spectrum.

2. Generally, the shape of the spectra constructed from subsonic rupture propagation for the 8 cases is similar to the spectral shape of CB001. It is, however, clear from Figures 6.32 and 6.35 that even with subsonic speed the long period level does not match that of CB001 in frequency. If anything these spectra seem to plateau to the Ω_0 level before CB001, thus indicating that their corner frequencies are slightly higher.
3. Cases (1), (2), (7) and (8) show more realistic results. This is mainly because the plateauing of the simulated spectra at subsonic rupture seem to occur at periods longer than that at which CB001 attains the Ω_0 level. Therefore the constructed corner frequencies are lower indicating a larger source. This is particularly clear for cases (2) and (8) although most of the constructed static level lies outside the lower frequency limit of our plots.

From the above observations we conclude the following:

- 1 - As with the individual sums, the dislocation direction along the fault surface is more favoured. This combined with the large number of input records (about 75) has enabled us to construct a source larger than CB001.
- 2 - It appears that subsonic rupture propagation is the most likely speed with which the dislocation spreads.

- 3 - From the second observation, and because the constructed corner frequencies for cases (3), (4), (5) and (6), at subsonic rupture, are slightly higher than CB001, we conclude that these cases do not represent a larger source.
- 4 - Out of the remainder of cases only cases (2) and (8) appear to show corners lower than CB001. Therefore these cases are the closest simulations to a source larger than CB001.

5.0.0 GENERAL CONCLUSIONS:

From the investigations reported in this chapter we conclude the following:

- 1 - Calculations of m_b residuals and observations of the P_1 - P_2 phases on the seismograms of the Chile earthquakes indicate the probable existence of a 20° -discontinuity in travel time coupled with a discontinuous increase in P-wave velocity at around 400km depth. We however, require further observations and a larger sample in order to support or deny this claim.
- 2 - Estimations of M_s and energies generally support the exponential relationship between earthquake size and energy release. We, however, did not require more than 10-12 seismograms to construct the major portion of CB001.
- 3 - P- first motions suggest a faulting regime similar to that found for the main shock. Empirical formulas give a length of 232km.

- 4 - From apparent velocity estimates we showed that the shorter period waves whose wavelengths are comparable to SAAS dimensions are directly influenced by velocity filtering, while those of much larger wavelengths remain unaltered.
- 5 - Setting our target to be the reconstruction of the source mechanism and large earthquake motion of CB001, and recognizing the implication of rupture propagation we selected Mach numbers of **0.92** and **2.29** for subsonic and supersonic propagation respectively.
- 6 - We have introduced and applied a method involving simple geometry whereby the array dimensions may be translocated to a particular hypocenter without unduly changing source-array vectors.
- 7 - Based on the focal mechanism solutions and the general fault motion obtained, and by the use of array transposition we have deduced various triggering directions for the assumed dislocation.
- 8 - From individual event sums and at both subsonic and supersonic "trigger factors" we have constructed seismograms similar in appearance to the wave motion of the large earthquake seismogram of CB001. The spectral signatures of these simulated records also show remarkable resemblance to that of CB001. The construction obtained from the summation of 12 records of CB00C at subsonic rupture speed, triggered in a direction representing propagation along the fault, appears to be the most likely

situation bearing in mind that our fault model is a 2-dimensional kinematic source where rupture propagations greater than sonic are theoretically unsubstantiated.

- 9 - In our attempts to construct a source larger than CB001 we have tested 8 cases of trigger at both rupture speeds. The static level or long period construction at subsonic propagation along the fault surface, for cases (2) and (8) seem to indicate this possibility.

6.0.0 DISCUSSION:

It appears that the most important overall conclusion regarding this study is the fact that it is possible to reconstruct or simulate the wave motion and consequently the spectral signature of a large earthquake source such as CB001 from the suitable summation of smaller earthquake seismograms located in the same focal region.

The results reported in this chapter are a first attempt and although they might be convincing enough they lack quantification. By this we mean assessing the simulated spectra through numerical measurements of source parameters like ω_c and Ω_0 . These would directly give source dimensions. A task like this is not simple and we do not know of any investigation that has attempted this especially with real earthquake spectra. We therefore feel that an essential and complementary part of our research would be to search for and develop scientifically sound criteria for the precise measurements of real as well as simulated source parameters.

From the point of view of fracturing mechanism and rupture propagation we feel that our methods are primitive and insensitive to dynamic factors such as differential stress drop, rise time and slip vectors along the fracture surface. S-wave solutions, which were extremely difficult to obtain in our case, would have greatly facilitated our conception of stress release and consequently would have given us stronger grounds for favouring triggering directions over others.

Another main disadvantage is the fact that we had no prior knowledge of geological or geodetic data from the main Chile shock. Information provided by such data could have included total fault offset. This in turn would have given an idea as to how and where the initial fracture developed.

The assumption of a kinematic 2-dimensional fault model and edge dislocation could well have been an oversimplified approximation to our source. Furthermore we simply assumed that unidirectional subsonic propagation is extendable to the far-field without considering other far-field terms such as the starting and stopping effects of a propagating rupture.

CHAPTER 7

RABAUl DATA : EXAMPLE ON NEAR-FIELD OBSERVATIONS

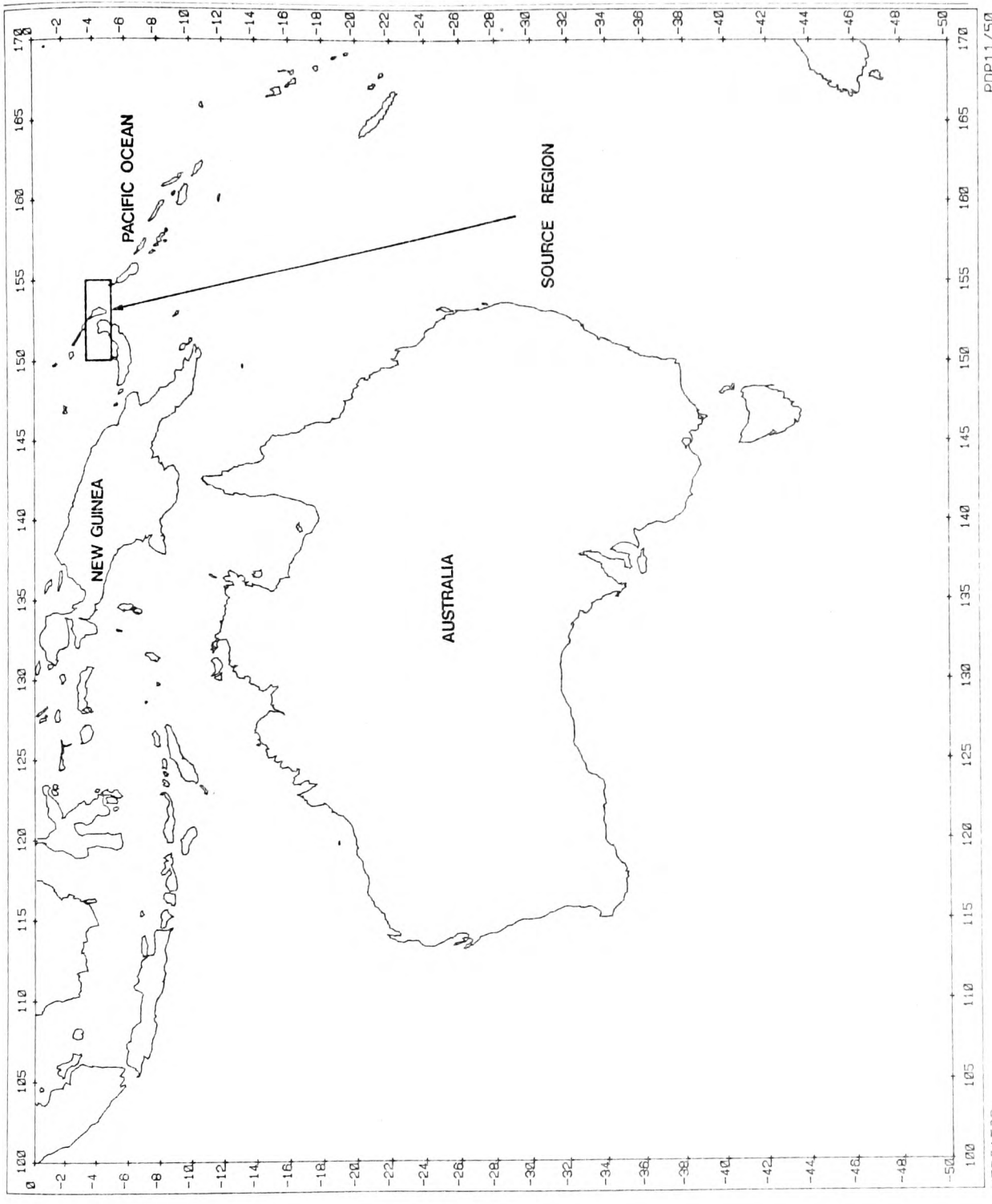
1.0.0 INTRODUCTION:

In this chapter we report our findings with respect to the near-field Rabaul data set. The general approach, methodology, and analysis is similar to that followed in Chapter 6 for the far-field Chile source. The basic aim, therefore, of this chapter is to apply the hypothesis to small shocks monitored from a local network with the view of constructing a larger earthquake source.

The source is the New Britain - New Ireland region located between $4-5^{\circ}\text{S}$ and $152-153^{\circ}\text{E}$ (Fig. 7.1). The source-receiver distance ranges between 40-160km. With an extremely high level of seismic activity both regionally and locally, the area is ideal for our near-field example.

As will be seen later all our observations were made from one station viz: ETV within the Rabaul Network and hence fall into the category of a single station-multievent case.

The chapter begins with a description of the general seismotectonics, geology, seismicity, and focal mechanisms of the source region. This is followed by a brief outline of the receiving network and the selected data. In Section 4.0.0 and we attempt to locate the selected earthquakes and estimate their local magnitude. Next we discuss phase identification, apparent velocity and azimuth followed by the summation scheme and how the data was grouped. Finally the chapter is concluded with the presentation of the results in the time and frequency domains.



PDP11/50

FIG (71) AREA OF STUDY

MERCATOR

2.0.0 GENERAL SEISMOTECTONICS:

Papua New Guinea and the Solomon Islands constitute part of a zone of late Tertiary to Recent tectonic activity that encircles the Pacific Ocean. The region has characteristic features including island arcs, mountain chains, and contemporary volcanic and seismic activity (Curtis, 1973). Recurrent orogeny, erosion and faulting with displacements of great magnitude, have to a certain extent, obscured the stages of its evolution, although according to Thompson and Fisher (1965) there is evidence that the area has been an unstable zone of interaction between the Australian plate on the southwest and the Pacific plate to the north and east since Lower Cretaceous.

2.1.0 Geology and Surface Structure of New Britain and New Ireland:

A comprehensive account of the geology of New Britain and New Ireland is given by Ryburn (1971). The following description is therefore mainly taken from the above reference and from Curtis (1973).

New Britain and New Ireland have a history of volcanism and tectonism dating back to Lower Tertiary. Their geology resembles that of the Solomon and New Hebrides Islands and to some extent that of the Huon Peninsula in mainland New Guinea. The geology of the two islands is similar in many respects (Fig. 7.2). However, New Ireland and the Gazelle Peninsula seem to have been modified by Quaternary crustal movements associated with the northwest Solomon Islands trend and now constitute a separate tectonic province from the rest of New

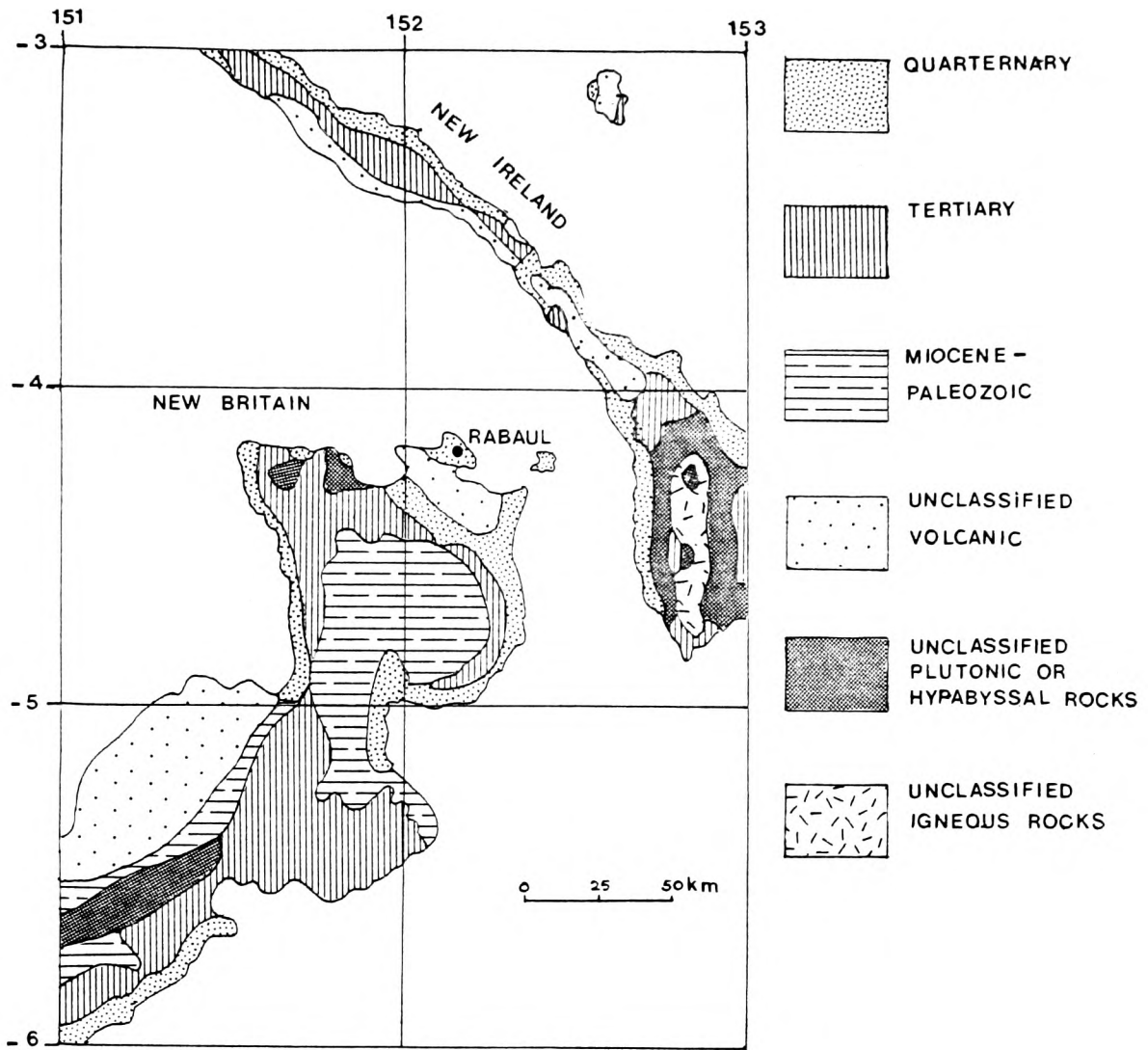


FIG (7.2) GEOLOGY OF NEW BRITAIN AND NEW IRELAND (FROM: GEOLOGICAL SURVEY OF AUSTRALIA 1963)

Britain.

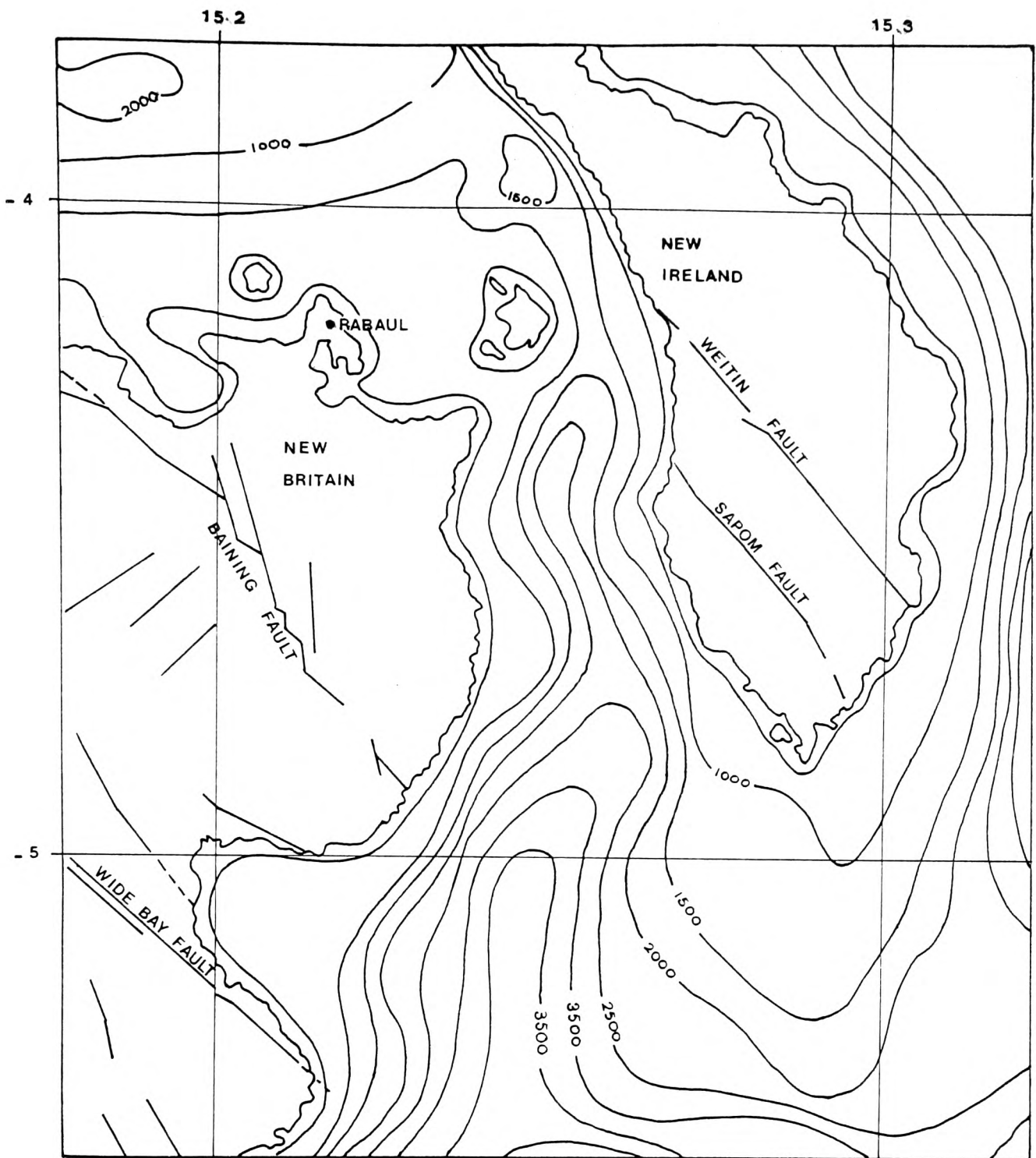
2.1.1 New Britain Arc:

The geological evolution of New Britain seems to have begun in the Eocene with an episode of island arc volcanism producing what Macnab (1970) termed as "Baining Volcanics". These volcanics are overlain by mainly Upper Oligocene to Lower Miocene interbedded pyroclastics, tuffs and volcanic conglomerates, and intruded by large basic to intermediate plutons along the axis of the island. Above this system are considerable thicknesses of Middle Miocene limestone deposited during a period of slow subsidence followed by Upper Miocene andesitic and basaltic lavas in the Gazelle Peninsula, and Upper Miocene to Pliocene terrestrial and marine sediments west of the Baining Fault (Fig. 7.3).

In central New Britain, Upper Tertiary unconsolidated intermediate to acid tuffs and tuffaceous sediments overlie the Baining Volcanics or, in places, Middle Miocene limestone. The mountainous topography of New Britain appears to be the result of block-type faulting and regional uplift which began around Pleistocene or the end of Pliocene times, and is probably continuing today. Volcanism has been almost continuous since early Pleistocene.

2.1.2 Admiralty Arc:

This arc consists of New Ireland, New Hanover, Mussau and Manus Islands from which only New Ireland is outlined.



**FIG(7.3) SURFACE FAULTING AND BATHYMETRY OF
NEW BRITAIN AND NEW IRELAND
(FROM: GEOLOGICAL SURVEY OF AUSTRALIA, 1963)**

Like New Britain, New Ireland is underlain by a thick sequence of agglomerates, tuffs and volcanic sediments. The age of deposition of these volcanics appears to be Upper Oligocene rather than Eocene, as in New Britain. Along much of New Ireland, the Oligocene volcanics are intruded by numerous plutonic and hypabyssal rocks. South New Ireland is dissected by a major northwest trending fault known as the Weitin fault which has undergone left-lateral strike slip movement.

In general New Ireland as well as the other group of islands, are all characterized by pre-Miocene dioritic plutonic centers, now exposed to deeply eroded mountain blocks which have been covered or flanked by Tertiary andesitic pyroclastics, shallow-water limestones and clastic sediments.

2.2.0 Seismicity and Focal Mechanism of the Source Region:

Recent investigations into the seismicity and tectonics of the New Guinea - New Britain - Solomon Arc indicate that the region has an extremely complex history due to the interaction of 2 major plates and several sub-plates (Denham, 1969; Isacks and Molnar, 1971; Johnson and Molnar, 1972; Everingham, 1974).

According to Isacks and Molnar (1971) deep sea trenches, belts of volcanoes, and inclined zones of shallow- and deep-focus earthquakes form island-arc structures parallel to the New Britain and Solomon Islands. These two structures meet and form a sharp corner east of the southeastern tip of New Ireland (Fig. 7.4). Like the New Hebrides arc farther east and unlike all other Circum-Pacific arcs, the New Britain and

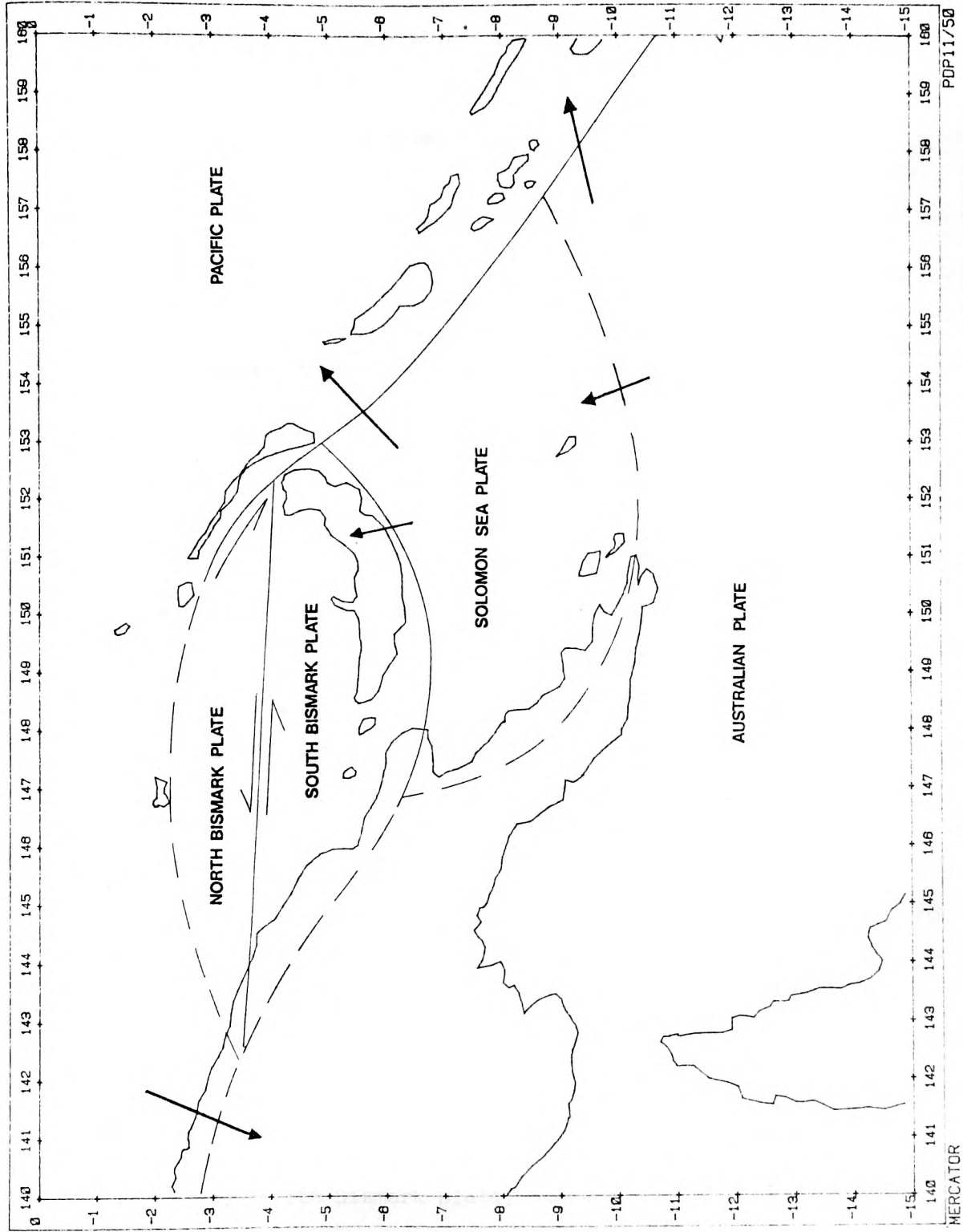


FIG (7.4) INFERRED PLATE MOTIONS NEAR THE SOURCE REGION (AFTER JOHNSON & MOLNAR, 1972)

Solomon arcs are convex to the south and face away from the Pacific basin. Apparently, the lithosphere beneath the Coral and Solomon Seas is being consumed at these arcs. Southwest and west of New Britain subcrustal earthquakes occur beneath New Guinea, but the distribution of hypocenters is not well defined.

Several additional zones of shallow seismicity are present in the region. The most striking is a well-defined linear alignment of shallow epicenters that cross the Bismark Sea north of New Britain. Another follows the Bismark archipelago, while a third appears to cross the Solomon Sea from the southeastern end of New Guinea to the Solomon Islands. These zones suggest that in this region the boundary between the large Australian and Pacific plates is complex and probably includes 3 or more additional small plates.

Johnson and Molnar (1972) made a study of focal mechanisms of earthquakes occurring in the New Guinea - New Britain - Solomon region. The solutions obtained required the existence of at least 2 additional plates, viz: the south Bismark and Solomon Sea plates, between the Pacific and Australian plates and possibly a third, viz: the north Bismark plate (Fig. 7.4).

The data of Johnson and Molnar suggest that the Solomon Sea plate moves in a NW direction with respect to the Australian plate and in a NE direction with respect to the Pacific plate. The north Bismark plate, however, appears to be moving SE with respect to the Pacific plate, but the low seismic activity suggests a relatively low rate of motion. The South Bismark plate, on the other hand, is moving east with respect to the

north Bismark plate, SSE with respect to the Solomon Sea plate, and approximately SW with respect to the Australian plate.

In the New Guinea - Solomon region, Everingham (1974) studied 152 earthquakes with $M_s > 6.9$ which occurred between 1900-1972. From his investigations the following merit noting:

- a) Magnitude/frequency results show a b-value of 0.97 in the range of $6.1 < M_s < 7.9$ for shallow earthquakes. This decreases to 0.5 for $M_s < 6.1$ and increases to 1.62 for $M_s > 7.9$.
- b) Lithospheric plate slip rates calculated from seismic moments are extremely low ($\approx 1.5\text{cm/yr}$) in northwest New Guinea and very high (up to 20cm/yr) in the northern Solomon Sea seismic zone.
- c) Temporal cumulative summation of seismic moment curves indicate a periodicity of seismic activity of approximately 25 years at the triple plate junction. Elsewhere the rate is aperiodic.

With this outline of the seismotectonic pattern of the source region we next consider the receiving network and the earthquakes studied.

3.0.0 THE NETWORK AND DATA:

3.1.0 The Rabaul Seismic Network:

Following the recommendations of Latter (1969, 1970), the IGS

Global Seismology Unit launched a seismic project during 1970-1973. According to Jones (unpublished report) the initial aim of this project was to set up and operate a network of a number of remote stations on the New Britain and New Ireland Islands to investigate the temporal and spatial distribution of earthquake foci occurring in the region with the objective of establishing a relationship between the seismicity and volcanicity of the area.

The network consists of one base station (ERB) at the Rabaul Volcanological Observatory plus 6 out-stations. Figure 7.5 shows the location map of the network, and Table 7.1 lists the co-ordinates and attitudes of the stations.

The detecting and recording equipment consisted of a 3-component Willmore MKII at ERB, and similar vertical instruments at all out-stations. The seismometers were all set to 1.0s period and 0.6 critical damping. In addition a low gain component was installed at ERB in 1972 to record strong motion activity (Jones, 1976). The amplifier-modulator units (Thermionic MKI) of the out-stations were set to a common gain of X400, while the 3-component set had a gain of X200. The Thermionic T8100 recording and playback units are identical to those described in Section 2.3.0 of Chapter 5.

3.2.0 The Data:

During approximately 3 years of operation, the Rabaul Network produced some 80 1-inch tapes which are stored at the IGS magnetic tape library. According to Jones (personal communication) the 33 tapes of the RB/F series covering the period

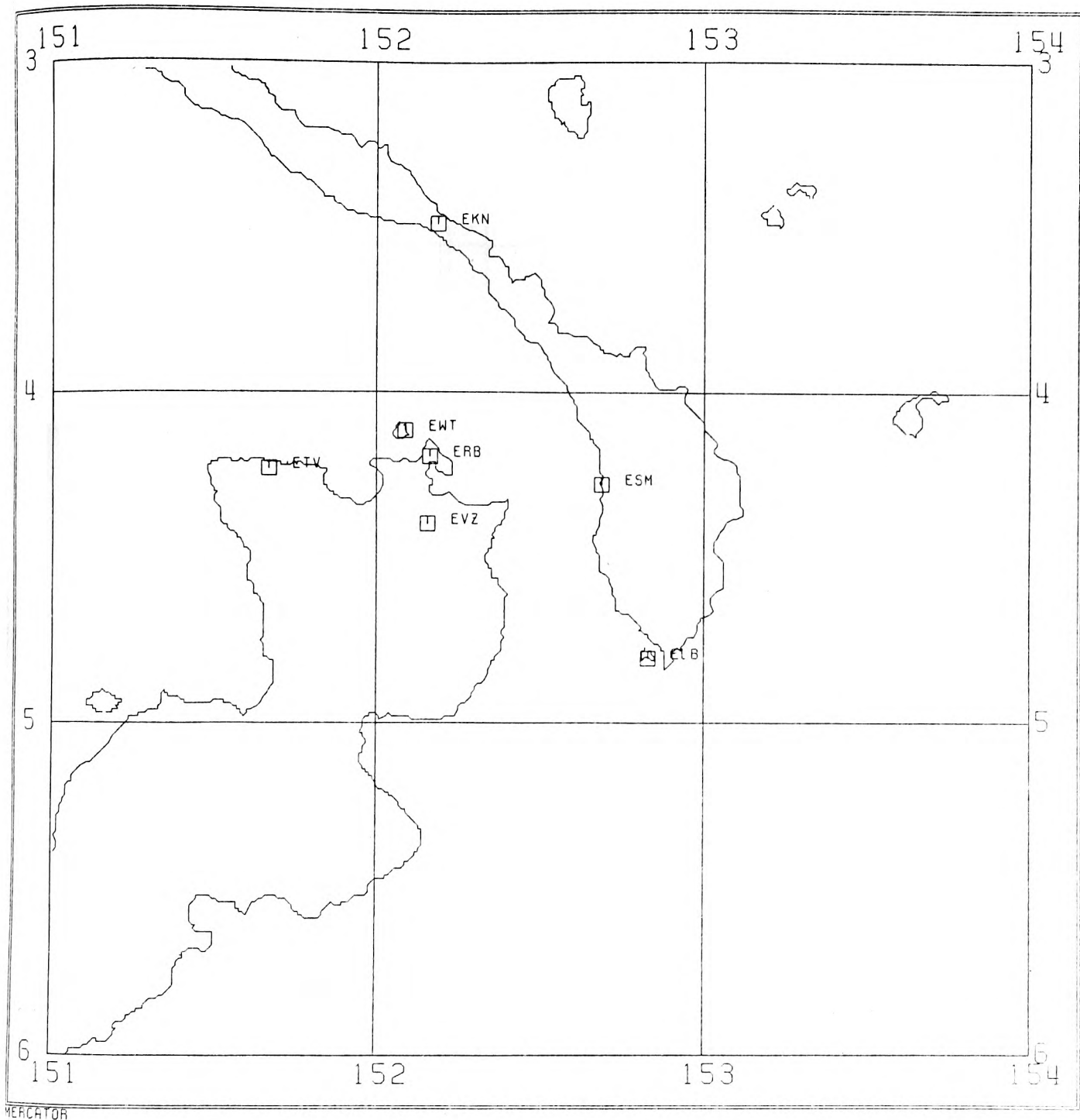


FIG (7.5) LOCATION OF RABAUL NETWORK
1970 - 1973

STATION CODE	NAME	LATITUDE (SOUTH)			LONGITUDE (EAST)			ALTITUDE (m)	WSSN CODE
		°	'	"	°	'	"		
ERB	RABUL	4	11	35.4	152	09	45.0	180.0	RAB
EWT	WATOM ISL	4	06	54.0	152	05	15.0	40.0	WAT
EVZ	MT. VARZIN	4	23	45.6	152	09	19.2	597.0	VAZ
ELB	LAMBOM ISL	4	48	13.8	152	49	48.0	10.0	LAM
ESM	SEMALU	4	16	37.2	152	41	10.8	50.0	CNI/SEM
EKN	KONOGOGO	3	29	19.8	152	11	06.0	270.0	KON
ETV	TOVANAKUSS	4	13	45.0	151	40	33.0	140.0	TOV

Table 7.1 Rabaul station co-ordinates and Altitudes

December 1972 - March 1973, are the most appropriate set, since during that time there was optimum instrumental operation.

Out of this collection of tapes we managed to select about 100 local events. General selection criteria included amplitude contrast of the P- and S-phases, S-P interval and the frequency content of the earthquakes. In addition, 2 large events were selected, viz: RDM73 and RDD72 with ISC m_b values of 4.9 and 5.7 respectively.

We made our observations from ETV because this station had a very low background noise level throughout the period compared to the other stations within the network plus the fact that numerous local shocks were recorded, which could be related to the possible activity of the nearby Baining fault system. Including the two large shocks, a total of 56 earthquakes were locatable, 32 of which were used in analysis (see later sections).

4.0.0 SOURCE PARAMETERS:

Under this section we attempt to locate the selected events and estimate Richter's local magnitude M_L . Since the shocks were very localized no data were available for focal mechanism determination. Even for the large events, the reported ISC first motions were too few to permit a solution.

4.1.0 Event Location:

In locating the Rabaul data we used an IGS program known as "RLOC", the basic logic of which is similar to "SPEEDY"

outlined in Chapter 6.

RLOC can be run interactively, is faster and has the option of inserting the appropriate local velocity structure. The program is used in day-to-day epicentral location of local earthquakes recorded by LOWNET and is claimed to give convergent and relatively accurate solutions. The accuracy of RLOC was deduced from the comparative runs with "FAMG" (Crampin, 1973) for surface explosions of known parameters (Neilson, personal communication).

RLOC proved sufficient for our purposes as evidenced by the standard deviations listed in Table 7.2. The relocated events are shown in Figure 7.6. It must be pointed out here, that the program has no means of rejecting insufficient data. Therefore the locations obtained could well contain a network bias since azimuthal coverage is extremely poor. Nevertheless, the located epicenters seem to occur to the south of the network and generally correlate with the tectonic pattern outlined earlier. Note that no solutions were possible for events reported by 2 stations only. This curtailed the initial number of selected earthquakes to nearly half.

It is worth pointing out here that P-velocity-depth structure used in locating the data is a smoothed version of that given by Finlayson et al (1972) (Browitt and Jones, personal communication).

4.2.0 Magnitude Estimation:

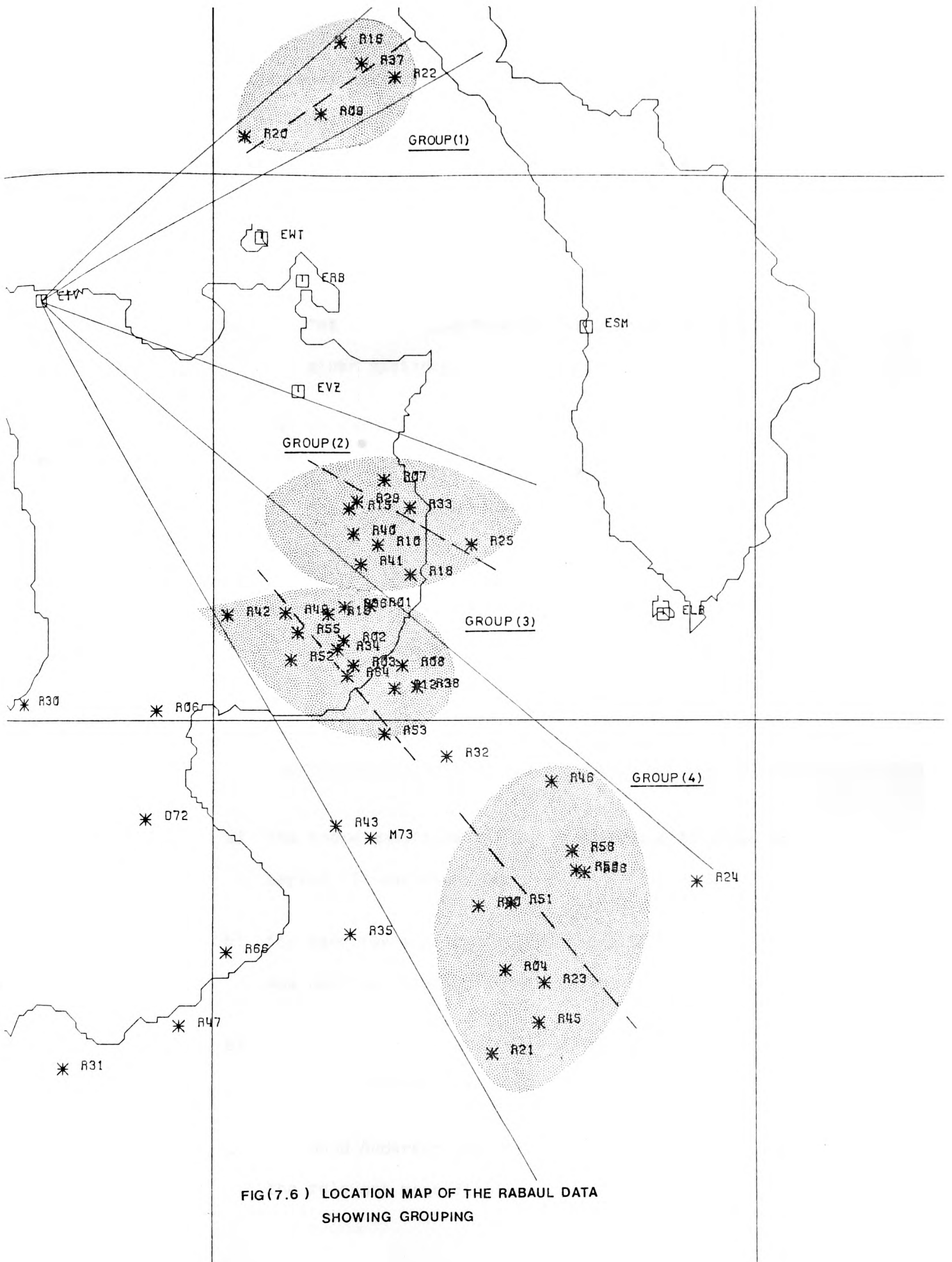
Since there are few P- first motions available for focal

Table 7.2 Kinematic Parameters and Local Magnitudes

EVENT	DATE	ORIGIN TIME	LATITUDE (SOUTH)	LONGITUDE (EAST)	DEPTH (km)	S.D	Δ (km)	M_L
R01	23/11/1972	08 52 21.0	4.789	152.286	75	0.013	93.6	2.4
R02	"	13 13 52.9	4.858	152.238	40	0.019	93.6	2.3
R03	24/11/1972	01 23 26.0	4.899	152.256	50	0.007	98.8	2.1
R07	26/11/1972	12 08 55.7	4.558	152.311	8	0.102	79.6	2.1
R08	"	13 18 52.8	4.899	152.346	50	0.011	105.8	2.5
R09	27/11/1972	10 57 54.3	3.885	152.196	31	0.004	69.1	2.4
R10	"	18 34 50.9	4.677	152.301	7	0.056	85.3	1.7
R12	"	20 37 21.9	4.941	152.332	60	0.056	107.2	2.3
R15	28/11/1972	05 12 53.4	4.611	152.248	16	0.142	71.7	2.4
R18	"	12 54 47.1	4.732	152.361	30	0.010	94.5	2.6
R19	"	13 54 48.3	4.805	152.210	46	0.007	87.5	2.2
R20	"	18 36 42.4	3.929	152.057	7	0.043	53.4	2.1
R21	"	22 55 27.3	5.610	152.514	17	0.038	168.8	2.9
R22	29/11/1972	20 47 32.9	3.861	152.332	29	0.059	83.5	2.2
R23	30/11/1972	03 25 58.4	5.481	152.610	14	0.021	172.8	2.6
R25	"	08 02 33.5	4.676	152.474	9	0.036	100.6	2.6
R29	02/12/1972	19 29 18.3	4.598	152.263	9	0.009	71.7	2.4
R33	18/12/1972	17 22 52.2	4.609	152.360	29	0.006	84.8	2.5
R34	23/12/1972	02 38 43.0	4.870	152.227	49	0.016	94.5	2.6
R36	27/12/1972	05 27 39.4	4.791	152.240	41	0.010	87.5	2.4
R37	29/12/1972	03 13 43.5	3.791	152.271	49	0.007	82.2	2.1
R38	"	21 37 06.2	4.939	152.374	41.0	0.067	110.7	2.6
R41	02/01/1973	23 02 52.9	4.713	152.270	5	0.035	84.8	2.4
R42	04/01/1973	13 20 20.2	4.806	152.026	63	0.006	75.7	2.2
R45	11/01/1973	02 06 22.1	5.553	152.600	25	0.010	178.8	3.0
R46	13/01/1973	17 04 14.6	5.113	152.623	29	0.083	143.9	2.8

Table 7.2 (continued)

EVENT	DATE	ORIGIN TIME	LATITUDE (SOUTH)	LONGITUDE (EAST)	DEPTH (km)	S.D	Δ (km)	M_L
R49	19/01/1973	13 12 08.5	4.802	152.132	44	0.007	81.3	2.6
R51	26/01/1973	13 53 21.2	5.336	152.548	22	0.006	157.5	2.9
R55	29/01/1973	15 00 52.5	4.838	152.154	47	0.005	85.3	2.3
R56	15/02/1973	14 20 58.4	5.276	152.669	29	0.179	160.1	2.9
R58	28/02/1973	18 50 47.1	5.240	152.661	31	0.055	157.0	3.0
R68	26/03/1973	17 48 49.9	5.280	152.684	25	0.032	100.2	2.8
RDD72	25/12/1972	03 32 25.0	5.181	151.877	62	0.243	107.8	4.9 _b
RDM73	14/03/1973	11 25 48.9	5.216	152.289	28	0.211	129.1	5.7 _b



FIG(7.6) LOCATION MAP OF THE RABAUL DATA
SHOWING GROUPING

mechanism studies the only other source parameter which could be estimated for this data set is Richter's (1935) local magnitude:

$$M_L = \log_{10} a - (-\log_{10} a_0) \quad (7.1)$$

where a is the maximum trace amplitude recorded by the "standard" Wood-Anderson torsion seismometer at a given distance.

a_0 is the amplitude that would be recorded on the same instrument at the same distance from a "standard shock" of $M_L=0$.

Because our seismograms were recorded by the Willmore MKII vertical short period seismometers, we are restricted to measuring the maximum SV-phase observed. We must also allow for the difference in magnification between the Willmore and Wood-Anderson instruments. Thus the following procedure was used:

- a) The trace amplitude "A" for the maximum SV-phase at period "T" was measured.
- b) For each reading, the Willmore amplitude response curve was used to obtain the magnification "M" at "T".
- c) To get the ground amplitude we divided A/M making sure the units of "A" are in mm.
- d) The Wood-Anderson response curve was consulted to obtain the relevant magnification "m" at "T".

e) The "a" term in equation (7.1) will therefore be:

$$a = A/M \cdot m$$

f) The epicentral distance listed in Table 7.2 is then used to obtain the equivalent $-\log a_0$ from Richter (1958) page 342.

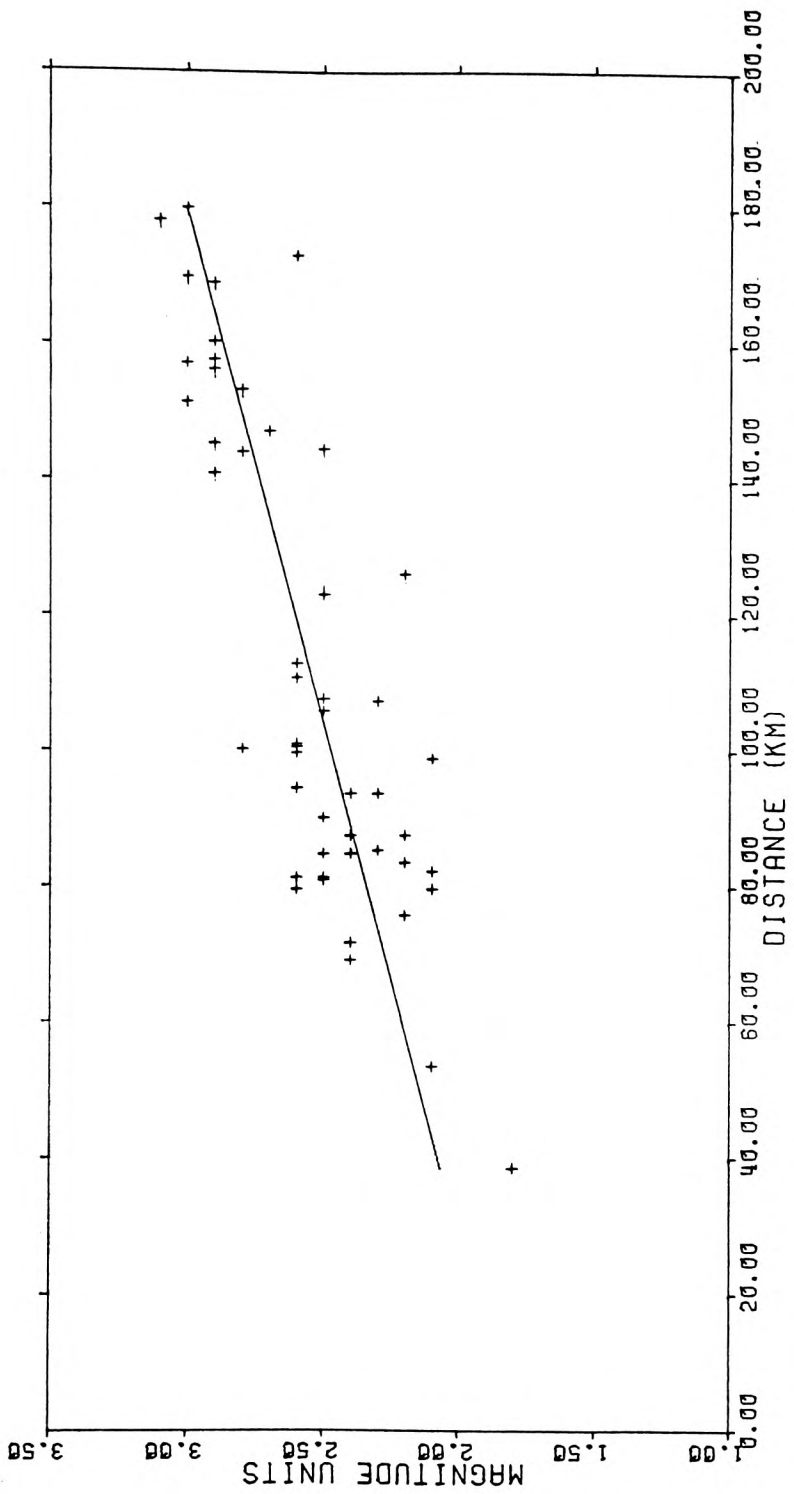
The results of M_L plotted against epicentral distance for all the locatable events given in Table 7.2 are shown in Figure 7.6a. The regression line clearly indicates the increase of M_L with distance as measured from ETV.

The problems regarding the application of this scale are clearly pointed out by the comprehensive investigation of Jacob and Neilson (1977). The most outstanding are:

- 1) Our measurements of amplitude were done on vertical and not horizontal components.
- 2) The difference between the amplitude response curves of the two instruments.

The first problem is not so serious especially when we take into consideration the fact that our measurements - for all events - were performed on SV. In other words our data are internally consistent as far as the component of motion is concerned. The second problem, however, is more critical and should be investigated.

Allowing for the difference in response curves between the Wood-Anderson and Willmore instruments can best be described by citing the following paragraph in Willmore and Karnik



PLOT OF RICHTER'S MAGNITUDE 'ML'
AGAINST EPICENTRAL DISTANCE.

Fig. 7.6a Rabaul Data : M_L from ETV

(1970, PAR3-3.2):

"In performing this operation, note that any differences between the shapes of the two response curves will affect the relative amplitudes of earthquake phases of different period. It may therefore happen that the largest amplitude recorded by the available seismograph may not correspond to the same phase as that which would give the largest record on the Wood-Anderson. For this reason, several phases should be read, and the one which gives the largest converted amplitude should be used."

Based on this argument we set out to justify our calculations of M_L . For this purpose we selected 4 shocks from each group shown in Figure 7.6 which amounted to nearly half of the total sample. In each of the selected seismograms and within the S wavetrain we read-off 4 different values of amplitudes corresponding to 4 different periods. As expected, the results of our calculations generally showed that the "a" term from which we obtained the M_L values were indeed the largest values recorded. We therefore conclude that our M_L values are reliable in so far as they represent rough estimates of local magnitude. Evidently, if there were data available from underwater explosions, it would have been possible to deduce a local magnitude scale for the area as was performed by Jacob and Neilson (1977) for LOWNET in Scotland.

From Figure 7.6a we noticed that M_L gets larger as epicentral distance increases. The question to be asked here is whether

this feature is consistent throughout the network. To check this we selected 10 shocks from all the groups of Figure 7.6 and searched through all the network stations. Unfortunately the selected events were only recorded on 2 other stations viz: ESM and EVZ. The resulting plots are shown in Figure 7.6b. Although the sample is rather small and has a gap in range, we nevertheless tend to suggest that what we are observing appears to be a genuine increase in the size of shocks as the range becomes larger.

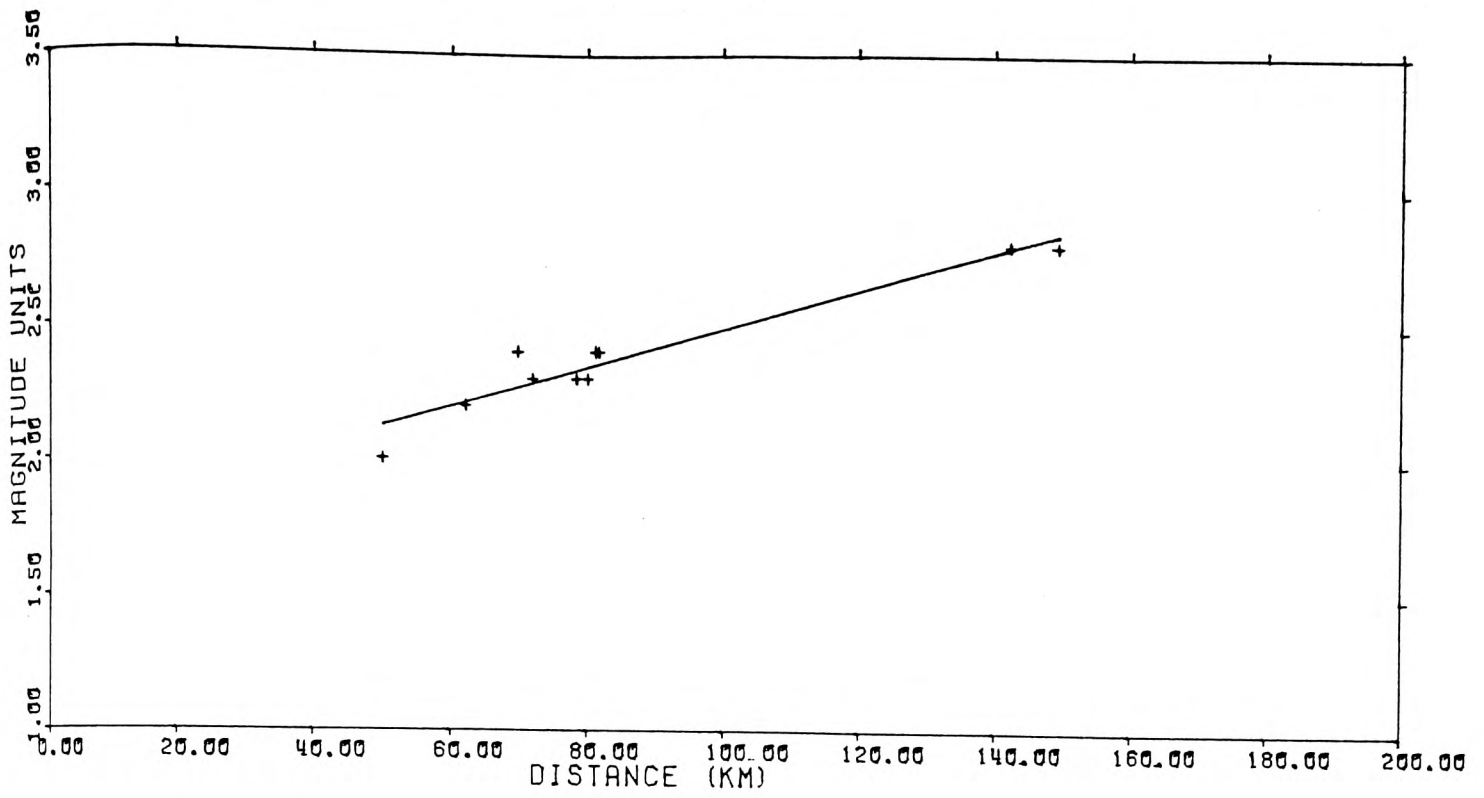
5.0.0 SEISMOGRAM ANALYSIS:

Along more or less similar lines to those followed in Chapter 6 we discuss in this section phase identification and apparent velocity estimation.

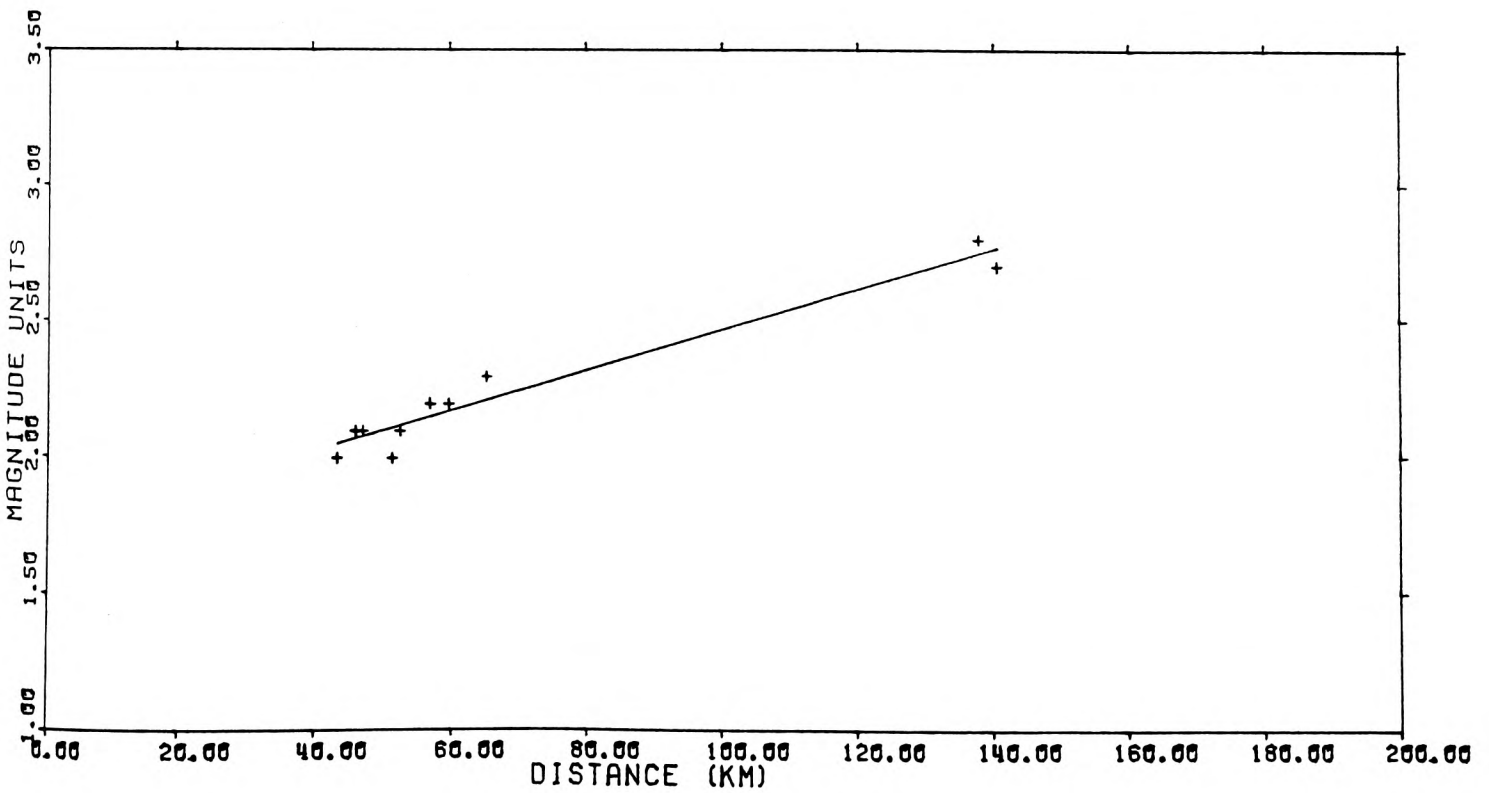
5.1.0 Phase Identification:

At this short range, crustal phases become important, and the contrast between P and S is remarkable. A first glance at the phase arrivals especially within the P-wave group of these local earthquakes shows that they are not so easily interpreted. This is most certainly due to complexity in crustal structure around the source, within the path and beneath the receiving network. Such complexity in phase arrivals is evident in the S-wave group but less acute because of their relatively larger amplitudes.

Searching through our records we noticed some degree of similarity in the S-wave train shared by most shocks. This is an encouraging feature since we will be focusing our



PLOT OF RICHTER'S MAGNITUDE 'ML'
AGAINST EPICENTRA DISTANCE (ESM)



PLOT OF RICHTER'S MAGNITUDE 'ML'
AGAINST EPICENTRAL DISTANCE (EVZ)

Fig. 7.6b Rabaul Data : M_L from ESM & ETV

attention of S-wave construction.

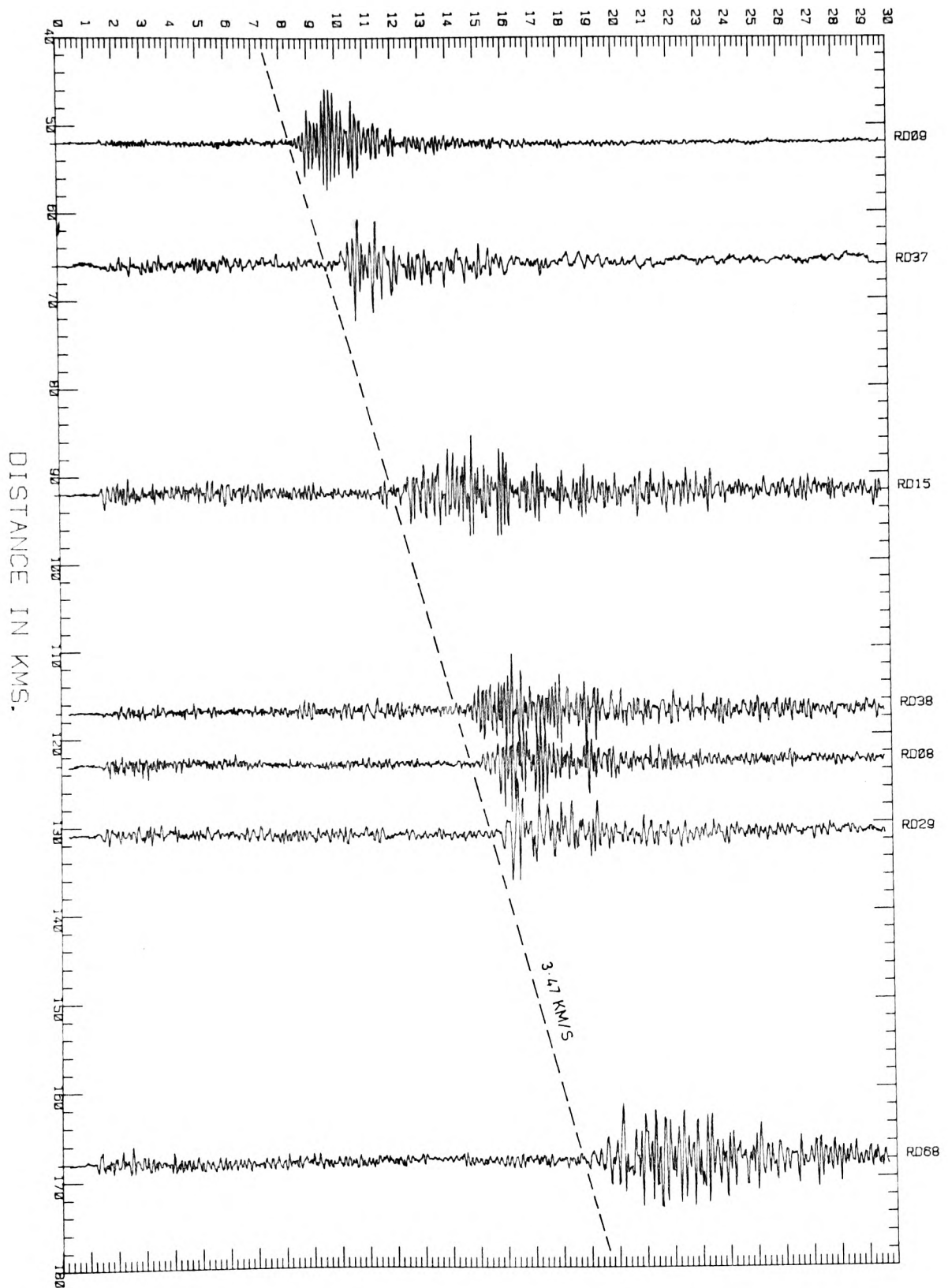
In order to identify the first onset of S and later on to estimate apparent velocities we proceeded to generate record sections based on what seemed to be the S-P interval for each shock and its respective epicentral distance from the observing station ETV. The selection and plot programs viz: "HDPICK" and "SEISEG" (Booth, personal communication) were used for this purpose. "SEISEG" assumes horizontal crustal layers and a Poisson ratio of 0.25. From the groups of events shown in Figure 7.6 we selected a few shocks well spaced and spreading between a distance of 50-170km. The record section is shown in Figure 7.7 plotted to a reduced velocity of 8.0 km/s. The broken line joining the S-wave onsets indicates a velocity of about 3.5km/s. This S-P distribution seems to correlate with the published crustal structure beneath the Gazelle Peninsula of New Britain (Finlayson et al, 1972).

5.2.0 Estimation of Apparent Velocity and Azimuth:

The procedure followed in calculating azimuths is identical to that adopted in Chapter 6 and a similar reasoning regarding azimuth and back-bearing is applied.

As mentioned in the previous section our prime target is to construct the S-wave group (see Section.5.3.2). This plus the fact that we will be using different earthquake records observed from one station means that our summation procedure requires accurate collating of seismograms and good estimations of apparent velocities for S-waves. To get apparent velocities we applied the same record section technique used in Section

REDUCED TIME IN SECS



R. V. B. D.

Fig. 7.7 Rabaul Data : Record Section

5.1.0 and selected a few earthquake records from the groups shown in Figure 7.6. Figures 7.7a to 7.7d illustrates this. The slopes of the broken lines in Groups(1), (2) and (4) agree reasonably well and give velocities ranging between 3.1-3.4 km/s. The only outstanding velocity is that of Group (3). Our immediate impression is that the input parameters for this group might be in error or conversely that the S-waves of this group indeed have a faster velocity. The only argument against this is the fact that the location of the shocks of Group (3) are close enough to those of the other groups especially Groups (2) and (4) (see Fig. 7.6), and in fact have a range of distance intermediate between them. This means that this high value of velocity is suspect. The only other method we could use to check this result is by using S-wave arrivals at other network stations. This simple method, often used in GSU practice (Neilson, personal communication) is based on the assumption of a plane wavefront, a flat earth and a homogeneous horizontal crustal structure. Given the relative onsets of a particular phase arriving at a network of 2 or more stations, we may calculate, by simple geometry, the apparent velocity of that wavefront at the desired or reference station.

Allowing for error in picking phases, the method proved to be consistent and effective. The results obtained for the first S-wave onset of Group (3) and for some of the shocks from the other groups varied between 3.20-3.48km/s. This result agrees remarkably well with the velocities shown in the record sections in general. As far as the assumptions of this method and those for the construction of record sections go, we may state that

REDUCED TIME IN SECS

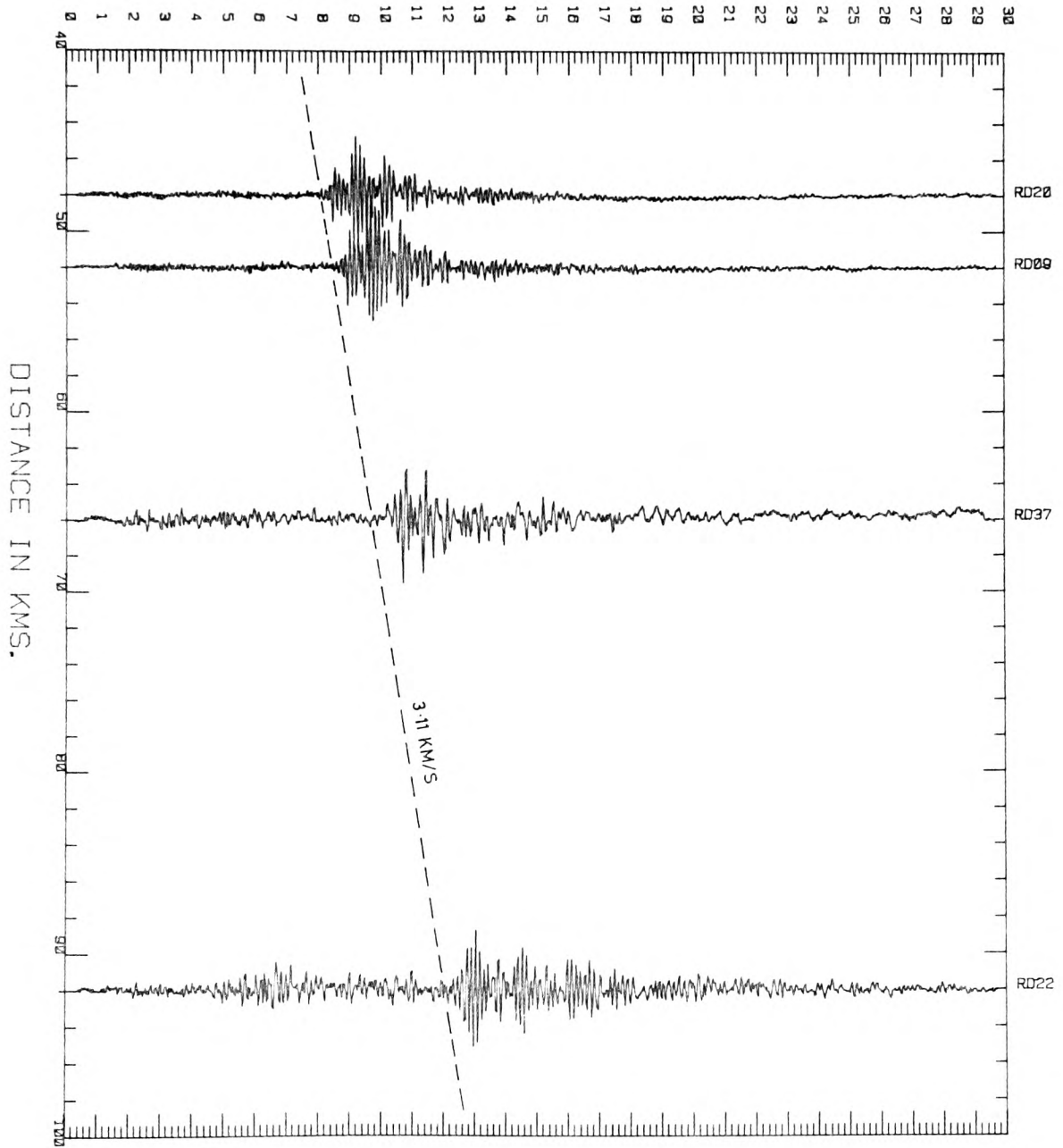


Fig. 7.7a : Record section of Group (1)

REDUCED TIME IN SECS

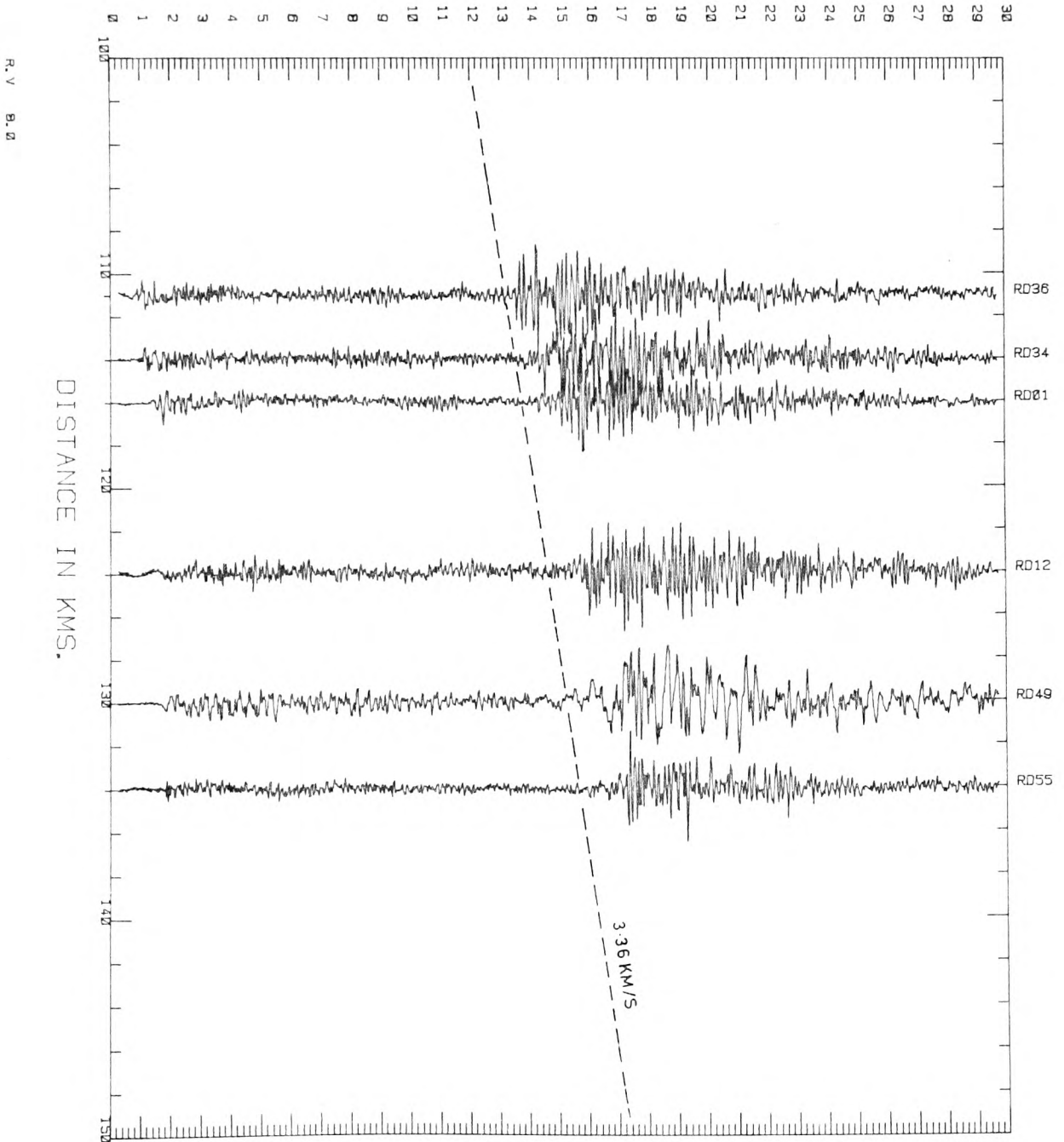


Fig. 7.7b : Record section of Group (2)

REDUCED TIME IN SECS

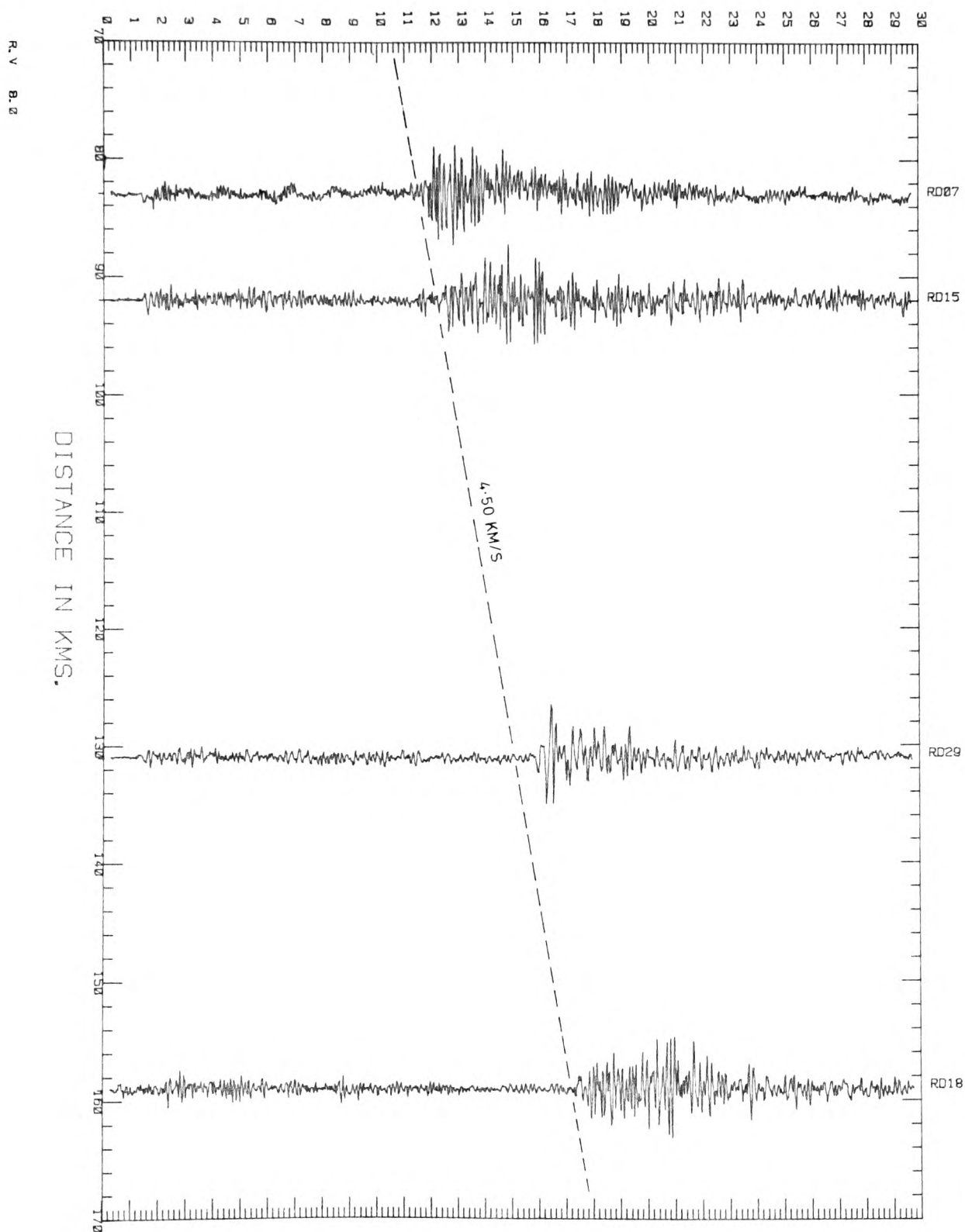
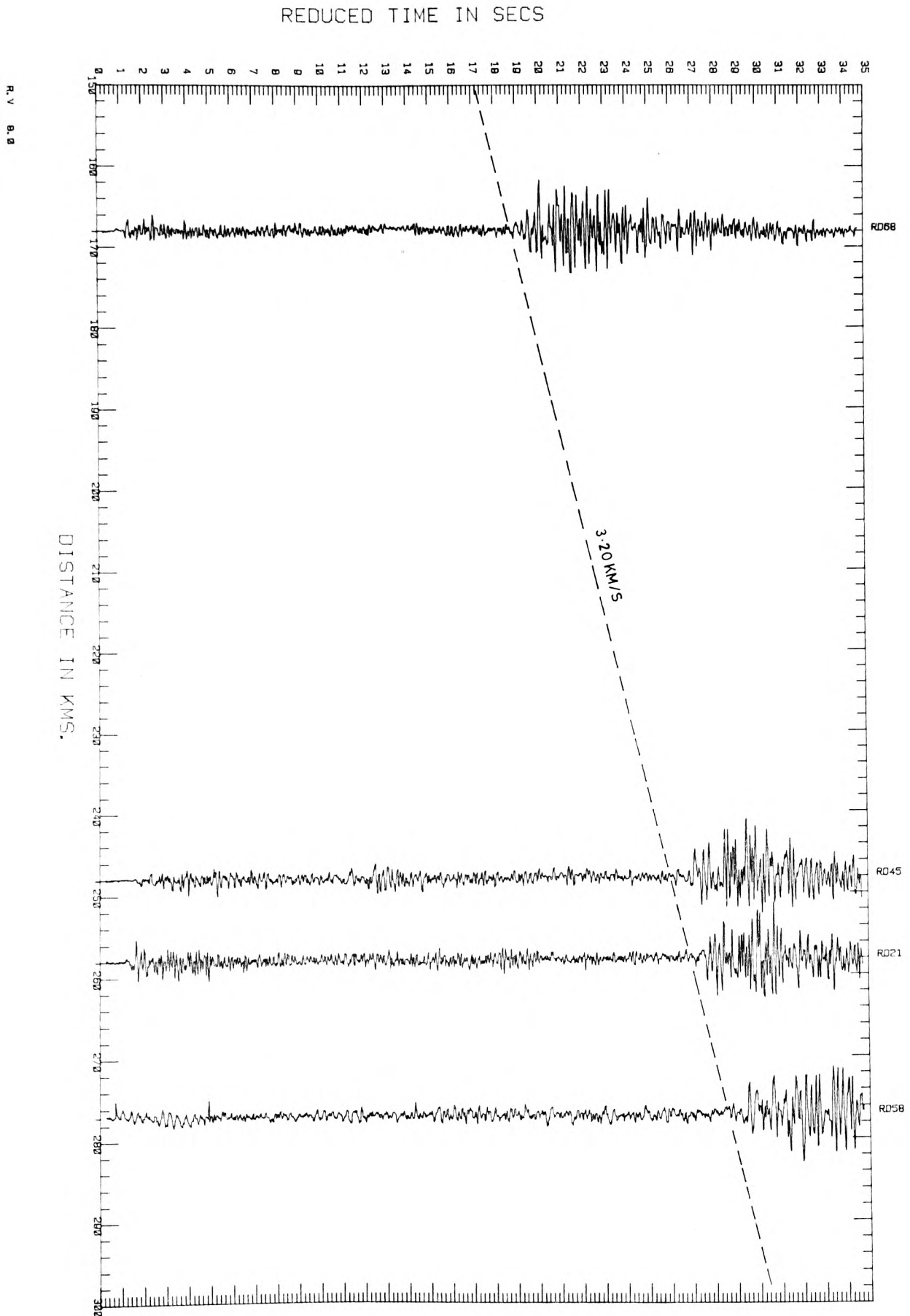


Fig. 7.7c : Record section of Group (3)

Fig. 7.7d : Record Section of Group (4)



the value of 4.5km/s found for Group (3) was in error. It is worth noting here, that according to this simplified procedure the P-wave velocity ranged between 6.2-7.0km/s. Here again, these velocities appear to agree with the data reported by Finalyson et al (1972, Fig. 6).

5.3.0 The Summation Scheme:

In this section as in its counterpart for the far-field source of Chapter 6 we attempt to relate the obtained apparent velocities to the rupture speed with which the assumed dislocation is triggered in a particular direction.

Recalling our discussion in Section 3.3.2 of Chapter 6 regarding array translocation we stated that in the case of a single-multievent situation, the operation is straightforward. This is because the single station location is directly inverted onto the source map at the hypocenter of each earthquake thus giving an identical image of the station records at the virtual source. Having established this we next consider rupture propagation and triggering sequence for the 4 groups (Fig. 7.6).

5.3.1 Event Grouping and Trigger Sequence:

At short distance range as in our case azimuth becomes important. Assuming that our locations are accurate enough, we may use azimuth to segregate the events into 4 distinct groups shown by the shaded areas in Figure 7.6. This grouping is further justified (again if the depths from epicentral locations are accurate) by looking at the depth sections of

Figure 7.8 which were obtained by projecting the hypocenters of each group on to the broken line of Figure 7.6. These sections thus correspond to azimuths of 50° , 120° , and 140° respectively. As a consequence the total number of 56 locatable events was reduced to 32 which were later used in summation.

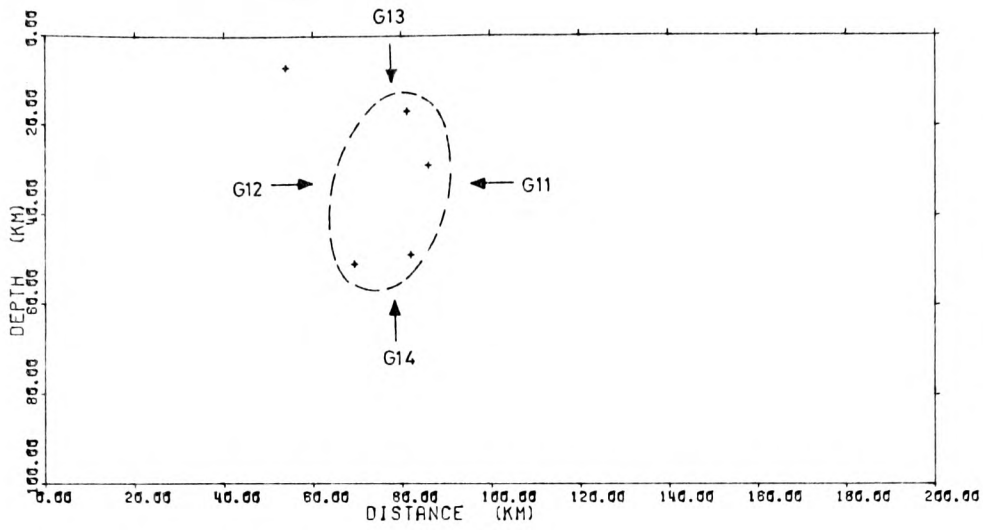
Having grouped the shocks according to azimuth and depth we next consider the direction and sequence of trigger. In order to do this we must consider the available facts:

(1) The surface structure map of Figure 7.3 generally indicates that the major faulting systems seem to have a NW-SE trend. Although not to the same scale, we can still compare Figure 7.3 with Figure 7.6 and suggest that the shocks of Group (3) could well be related to the Baining fault system. The other groups, however, do not correlate with the local structure simply because there is no surface evidence of faulting as is the case with Group (2) or because the epicenters are located off-shore as in the case of Groups (1) and (4).

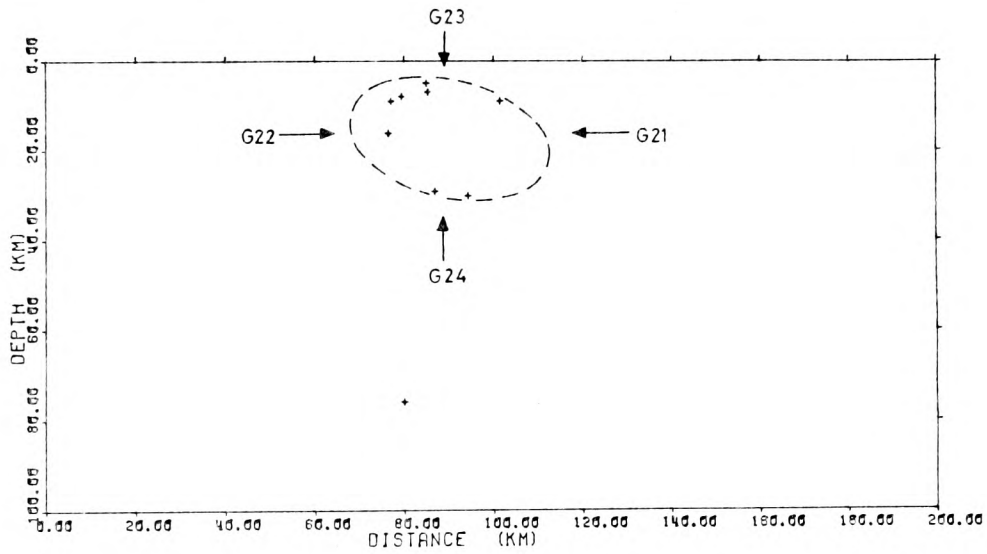
(2) The only source of mechanism studies for earthquakes occurring in the crust or upper mantle east of New Britain is that of Isacks and Molnar (1971). According to their solutions the tension axes are parallel to the dip of the seismic zone and the null axes are parallel to the strike of the zone (loc. cit, Table 1 and Fig. 7). These results thus indicate down-dip extensional stress.

Based on the above facts, it is possible to suggest the

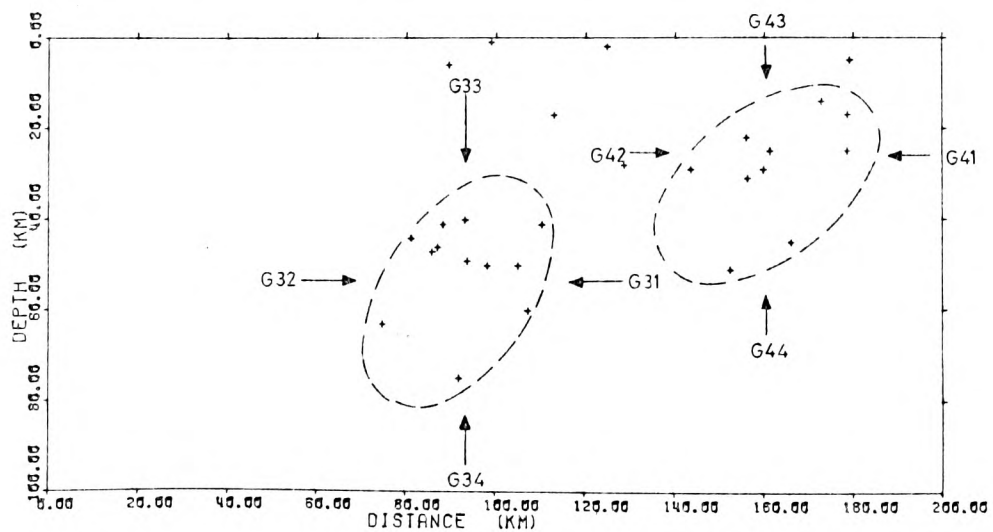
Fig. 7.8 : Grouping of events



RABUL DATA : SECTION FROM ETV (AZ=50)



RABUL DATA : SECTION FROM ETV (AZ=120)



RABUL DATA : SECTION FROM ETV (AZ=140)

following directions of trigger for the assumed dislocation
in the case of Group (3) (Fig. 7.8):

G31 : Along fault strike in a SE-NW direction
G32 : " " " " NW-SE "
G33 : " " dip " " DOWNWARD "
G34 : " " " " an UPWARD "

As regards Groups (2) and (4) we are unfortunately left to conjecture. A possible fault orientation may be one in which a sequence of trigger similar to Group (3) is assumed. This means that the faulting reflected by the concentration of the earthquake hypocenters of Groups (2) and (4) essentially trend and plunge in a similar fashion to the Baining fault system. This postulation, under the available information, seems to be the most plausible since it generally agrees with the tectonic pattern of the region.

The situation is even more difficult in the case of Group (1) where only a few events occur. Therefore any fault orientation is possible. However, from the schematic representation of inferred plate motions shown in Figure 7.4, there appears to be some sort of faulting in that area. The distribution of epicenters (again assuming their locations are accurate) perhaps indicate a NE-SW fracture although there is a large scatter in the depth section of this group. Based on the above assumptions we may suggest the following trigger directions:

G11 : Along fault strike in a NE-SW direction
G12 : " " " " SW-NE "

G13 : Along fault dip in a downward direction

G14 : " " " "an upward "

Although this grouping is rather crude, elementary and highly governed by the accuracy of epicentral locations, it nevertheless complies with the feature discussed under local magnitude estimation. By this we mean that not only does earthquake size increase with range but also with increased azimuths. In other words as we move in azimuth from 50° to 140° the average size of the shocks increases. The most obvious interpretation to this feature would be the fact that as distance increases and as we swing in azimuth we are effectively moving into the major part of the seismic activity which is attributed to the complicated triple plate junction southwest of New Ireland. This is evident on both the spectra of the respective groups and in the rupture propagation speeds used to sum the individual earthquakes in each group (see Section 6.0.0).

5.3.2 Rupture Velocity at the Near-Field:

We stated in Section 2.6.0 of Chapter 3 that at short distances the seismic spectrum becomes independent of the total area of the fault and depends only on the amount of dislocation. Another important factor is azimuth. According to Aki (1968a) the maximum seismic radiation in a given azimuth occurs when the component of the rupture velocity along the azimuth agrees with the wave velocity because the contributions from all the parts of the fault add constructively for all frequencies. Therefore, the near-field spectrum depends critically on the

Mach number (see Section 3.3.1, Chapter 6), rather than on its absolute value.

Unlike the situation for the Chile source in which we did not have relatively accurate S-wave velocities, here we have consistent velocity estimates for the first S-wave onset. Furthermore there is no ambiguity regarding the validity of using kinematic unidirectional propagation as a basis for modelling near-field faults since this has been considered by other investigators.

Based on the assumption of a 2-dimensional kinematic dislocation propagating at constant rupture velocities, which according to the work of Boore and Zoback (1974a, and b) rarely exceeds Mach numbers >1.0 in the near-field of a fault, we set up the following criteria for our summation procedure:

- 1 - The seismograms of each group were collated to match the S-wave onset to within 5 samples, i.e: ± 160 ms.
- 2 - Based on the S-wave velocities obtained in Section 5.2.0, we summed each group with the appropriate azimuth, and according to the trigger sequence outlined in the previous section, by inputting to "BEAM" a range of velocities between 1-5km/s.
- 3 - The summed outputs in each direction which gave the maximum construction, sharpest onset, and optimum coherency within the S-wave group was taken as the best simulated seismogram of a larger source constructed from that particular group.

As will be shown in the next section only the final results are reported with the input Mach numbers giving a definite trend.

6.0.0 RESULTS AND DISCUSSION:

6.1.0 Individual Group Sums:

In this section we present the results obtained from the summation of the 4 groups of shocks. Figures 7.9a and c through to 7.12 a and c show the complete input records and the resulting summed outputs of the 4 groups all plotted to the same x-y scale except Figures 7.12a and c where the seismograms are slightly compressed in length in order to display both P and S. For the purpose of observing the S-wave group only we include Figures 7.9b and d to 7.12b and d again plotted to the same scale.

For the 4 groups, Table 7.3 gives the range of input velocities selected for each group and that which satisfies the third criterion given in Section 5.3.2:

Table 7.3 Rupture Velocities

GROUP	VELOCITY OF FIRST S-ARRIVAL (km/s)	RANGE OF INPUT VELOCITIES (km/s)	VELOCITY OF MAX. CONSTRUCTION (km/s)	MACH NUMBER
1	3.11	1.10 - 1.25	1.16	0.37
2	3.36	1.60 - 1.80	1.66	0.49
3	3.35	2.30 - 2.60	2.40	0.72
4	3.20	2.40 - 2.80	2.55	0.80

RABAUL DATA: GROUP (1) (100/1000/1400/0.00004/0.001)

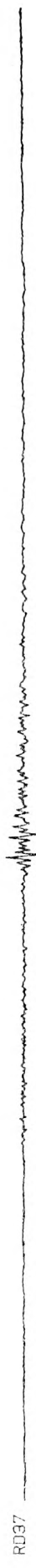


Fig. 7.9a GROUP (1)

RABAUUL DATA: GROUP (1) S-WAVES (30/1500/420/0.00006/0.001)



Fig. 7.9b GROUP (1) : S-waves

RABAU DATA: GROUP (1) SUMS IN FOUR DIRECTIONS (100/1000/1400/0.00004/0.001)

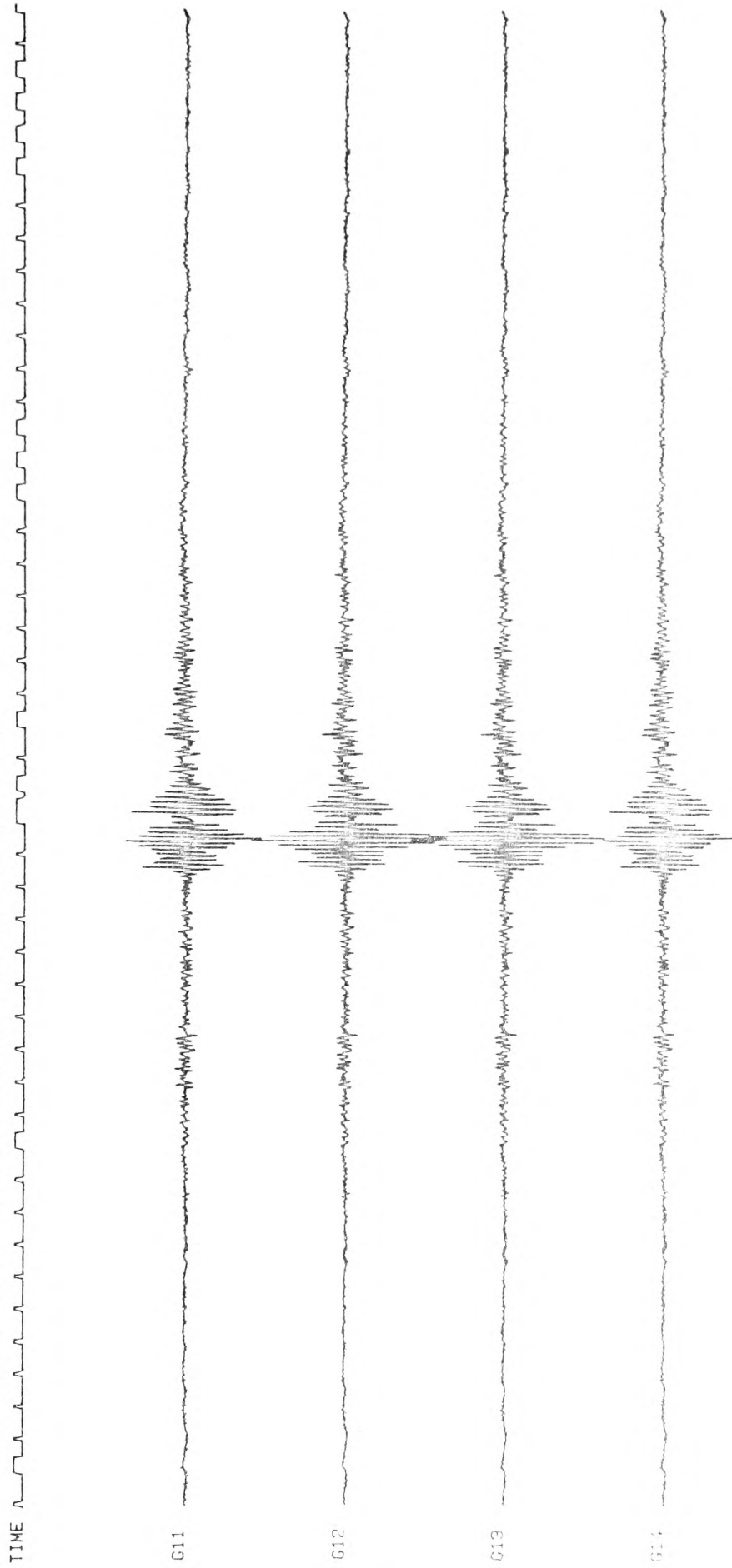


Fig. 7.9c SUM OF GROUP (1)

RABAU DATA: GROUP (1) SUMS: S-WAVES (30/1500/420/0.00006/0.001)

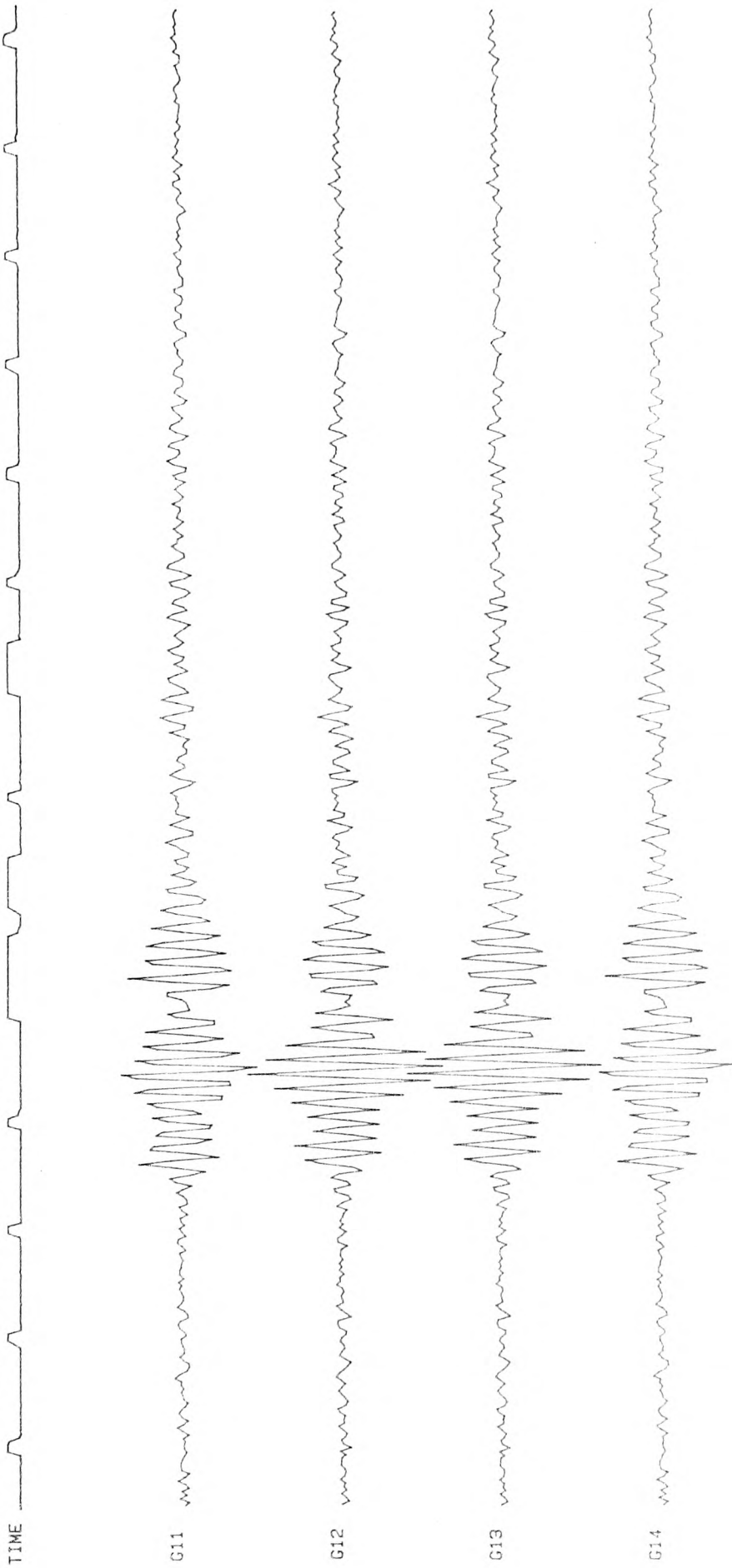


Fig. 7.9d SUM OF GROUP (1) : S-waves with $M = 0.37$

RABAU DATA: GROUP (2) (100/1000/1400/0.00004/0.001)

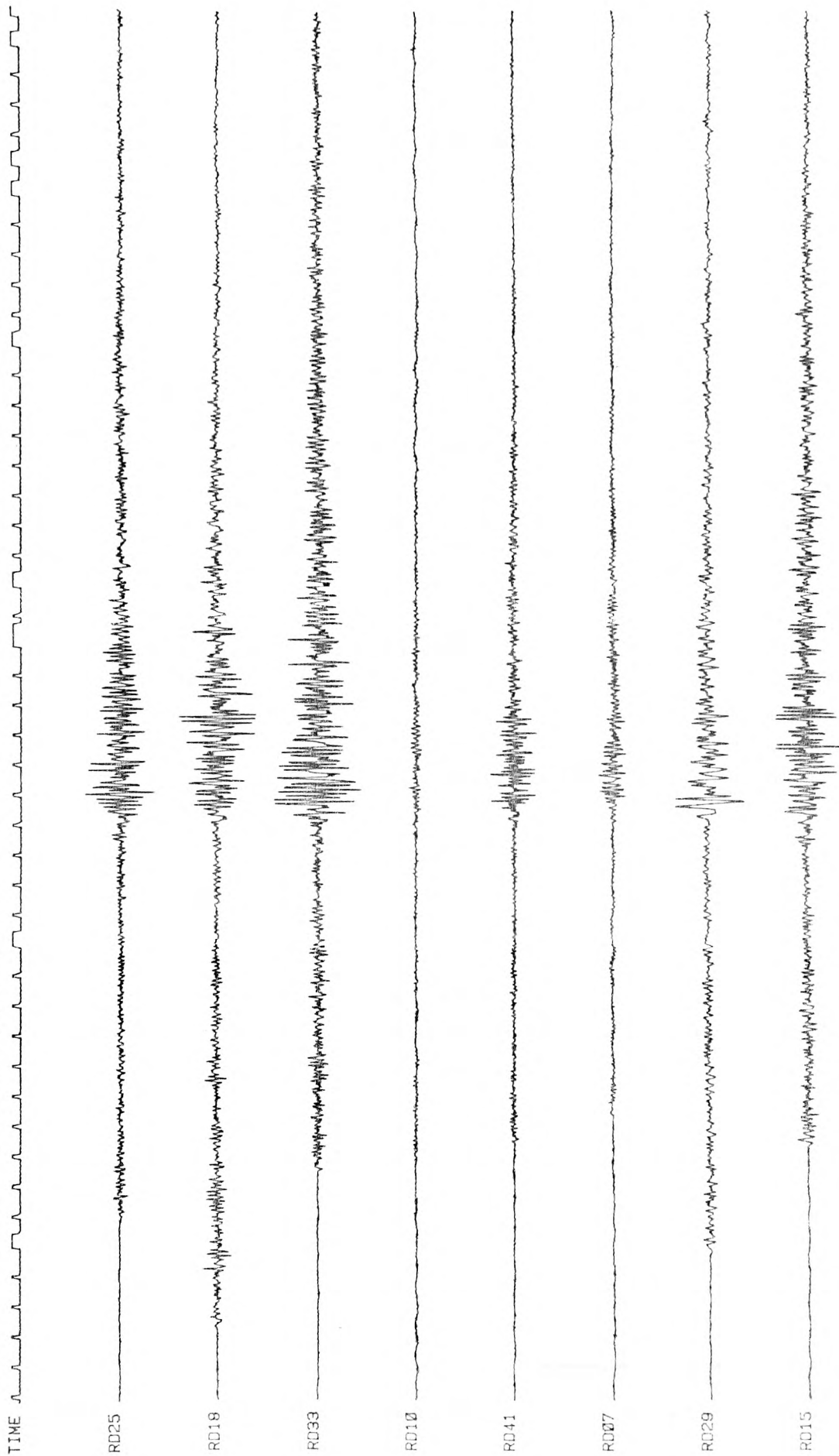


Fig. 7.10a GROUP (2)

RABAUŁ DATA GROUP (2) S-WAVES (30/1530/420/0.00006/0.001)

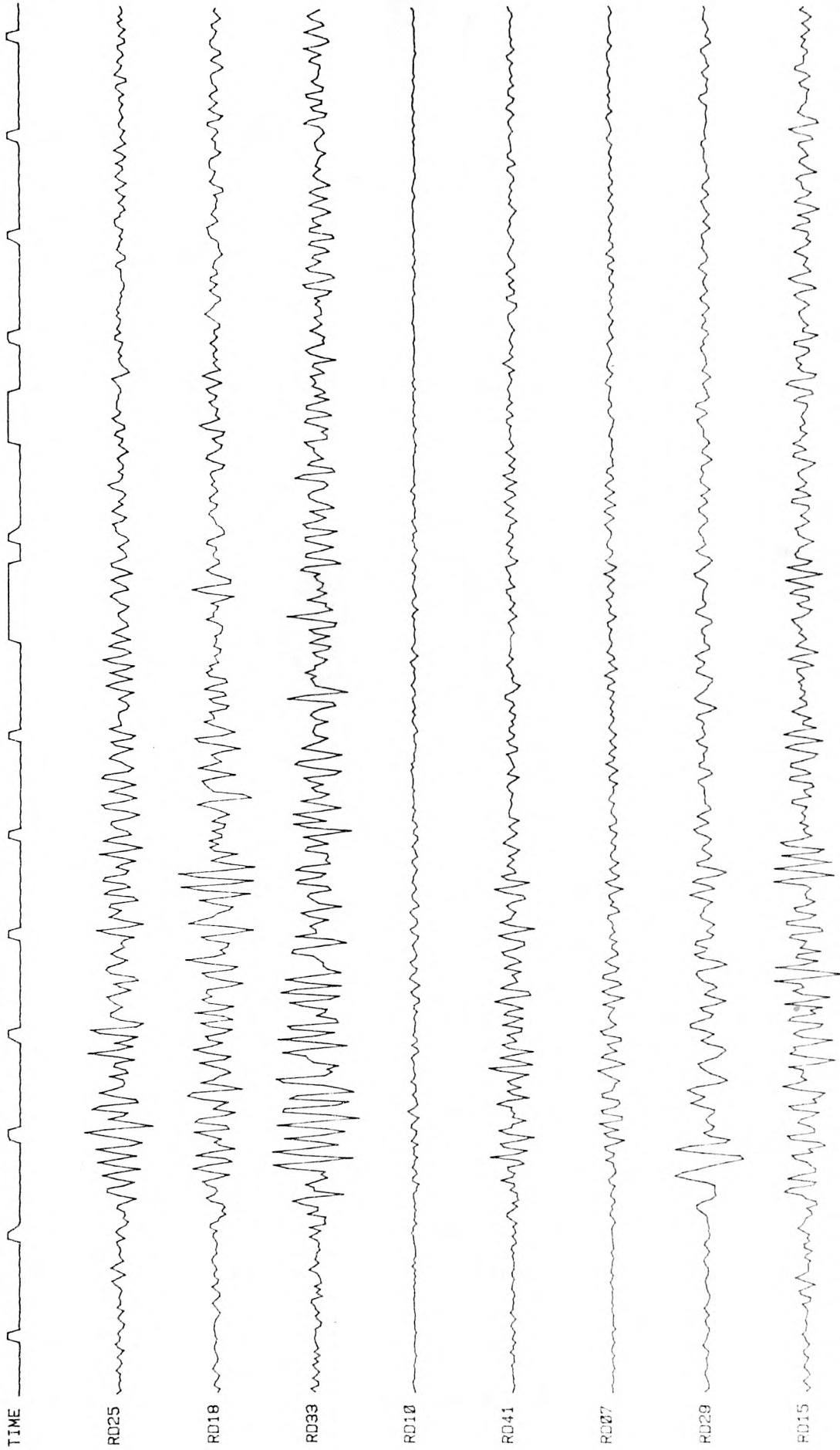


Fig. 7.10b GROUP (2) : S-waves

RABAU DATA, GROUP (2) SUMS IN FOUR DIRECTIONS (100/1000/1400/0.00004/0.001)

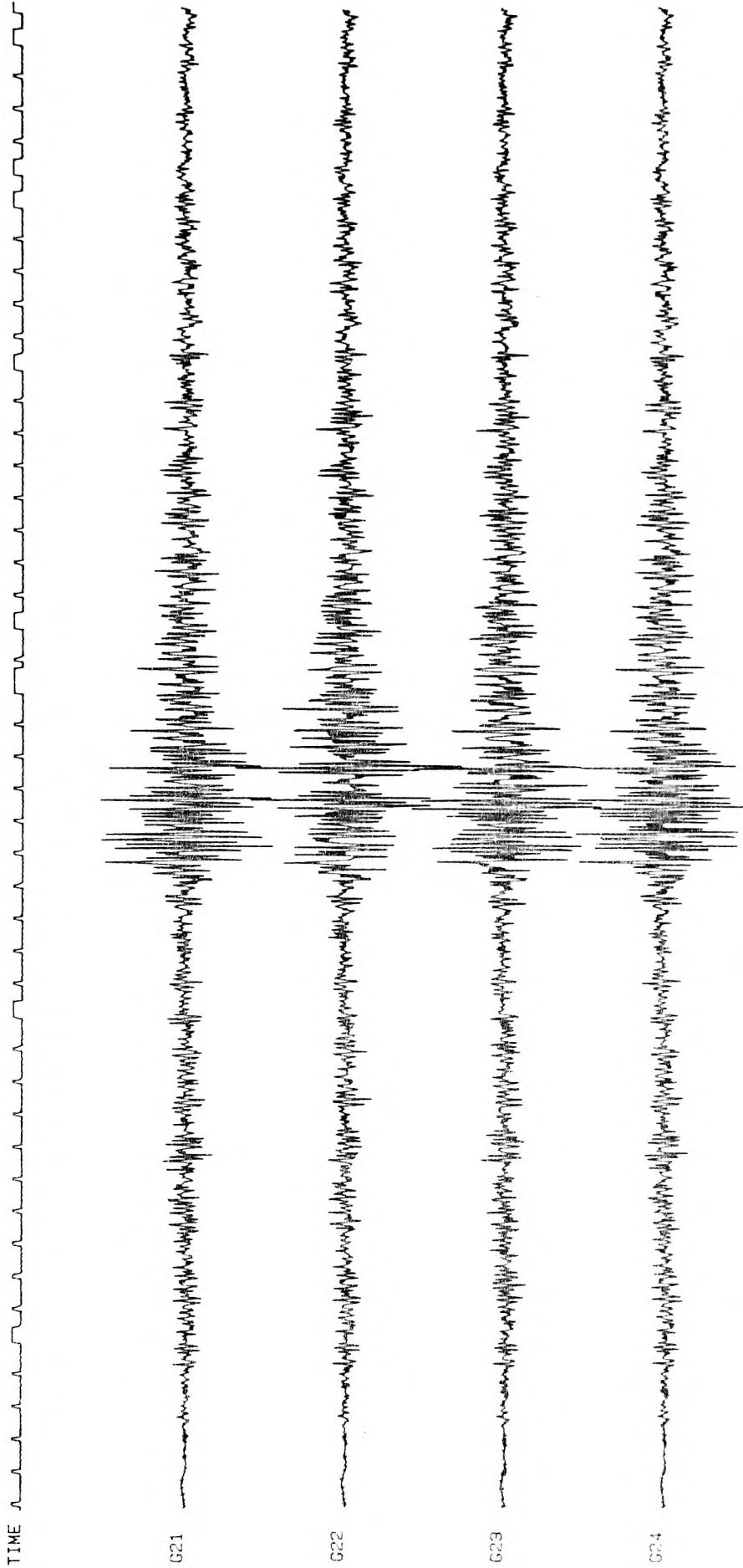


Fig. 7.10c SUM OF GROUP (2)

RABAU L DATA: GROUP (2) SUMS: S-WAVES (30/1530/420/0.00008/0.001)

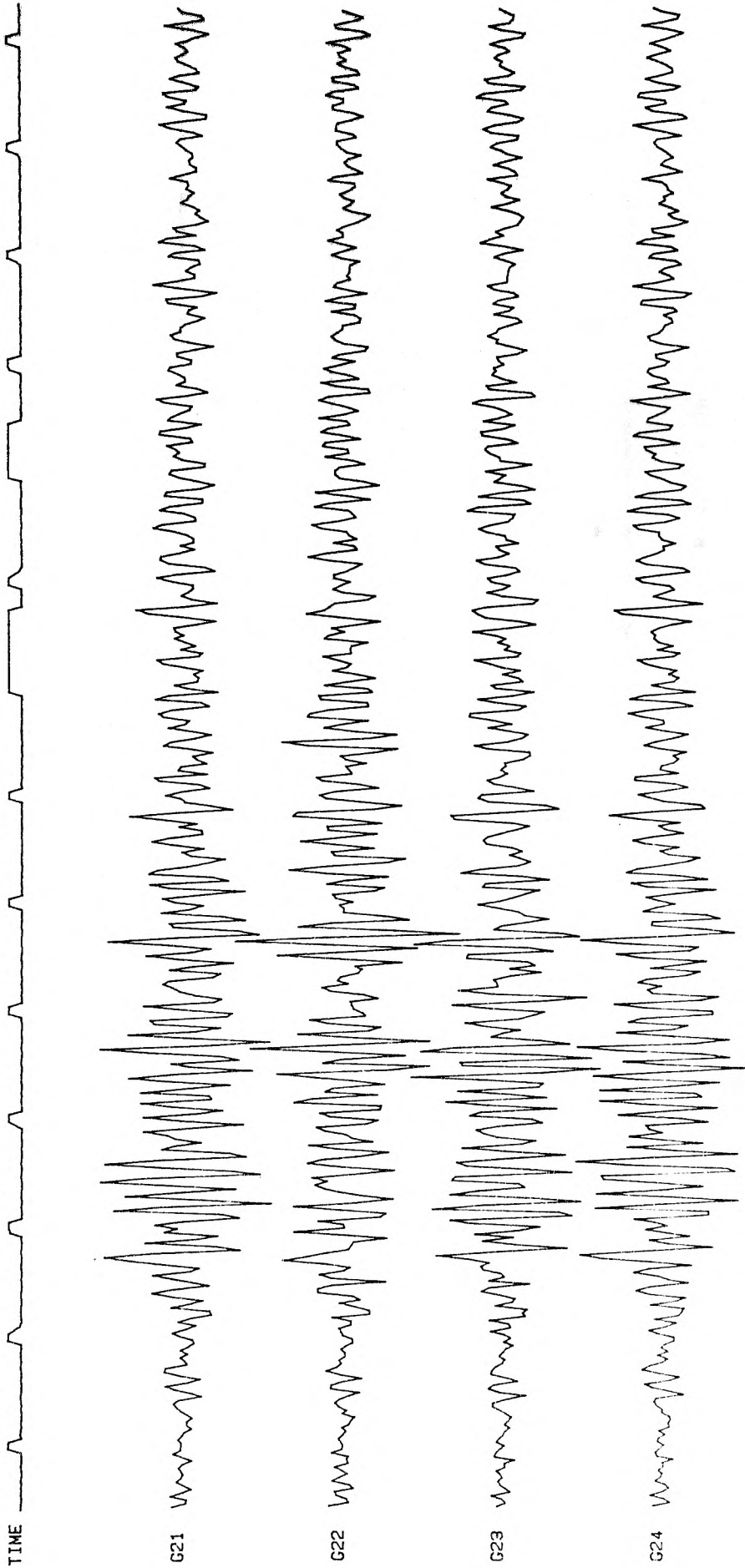


Fig. 7.10d SUM OF GROUP (2) : S-waves with $M = 0.47$

RABAU DATA: GROUP (3) (100/1000/1400/0.00004/0.001)

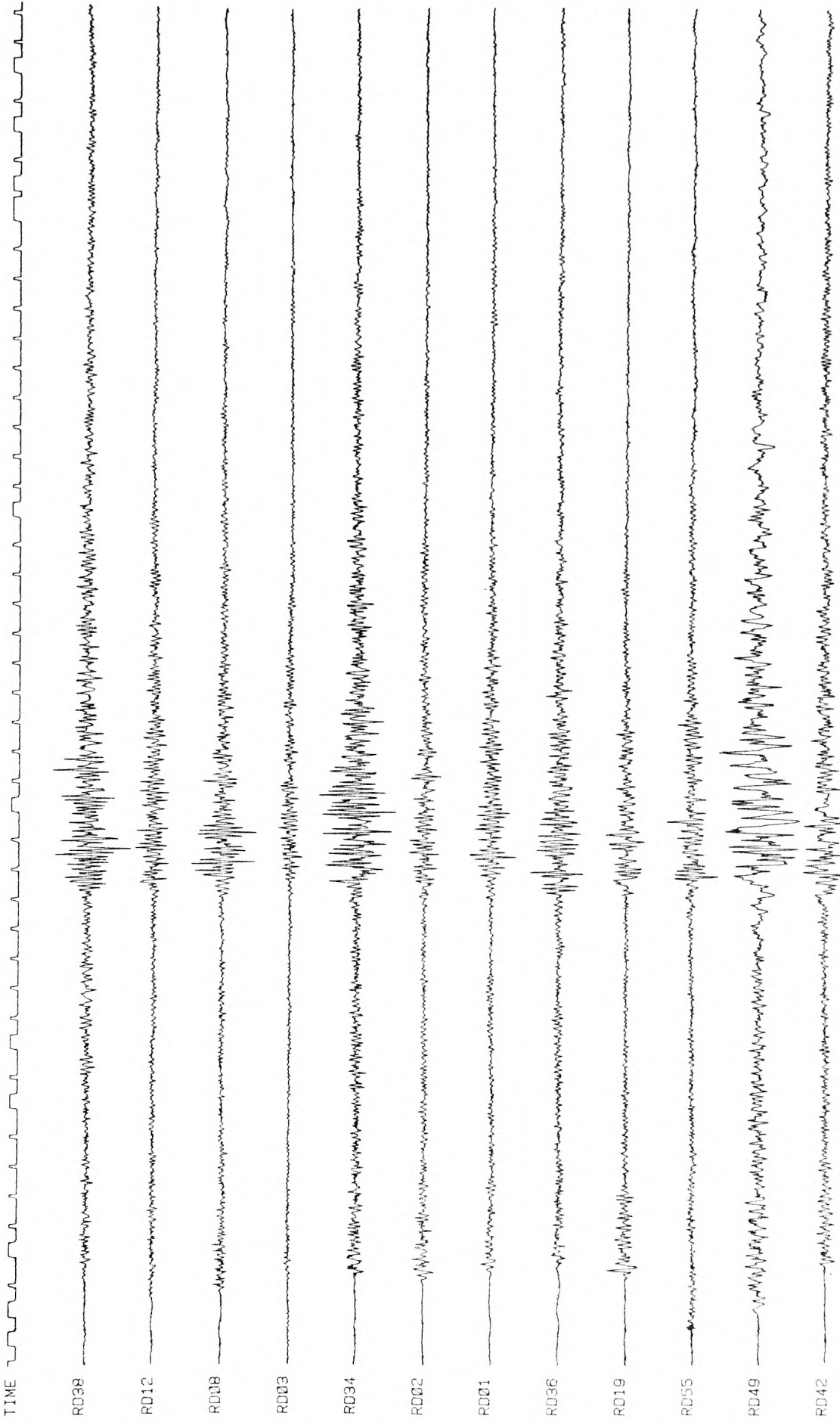


Fig. 7.11a GROUP (3)

RABUL DATA: GROUP (3) S-WAVES (30/1530/420/0.00006/0.001)

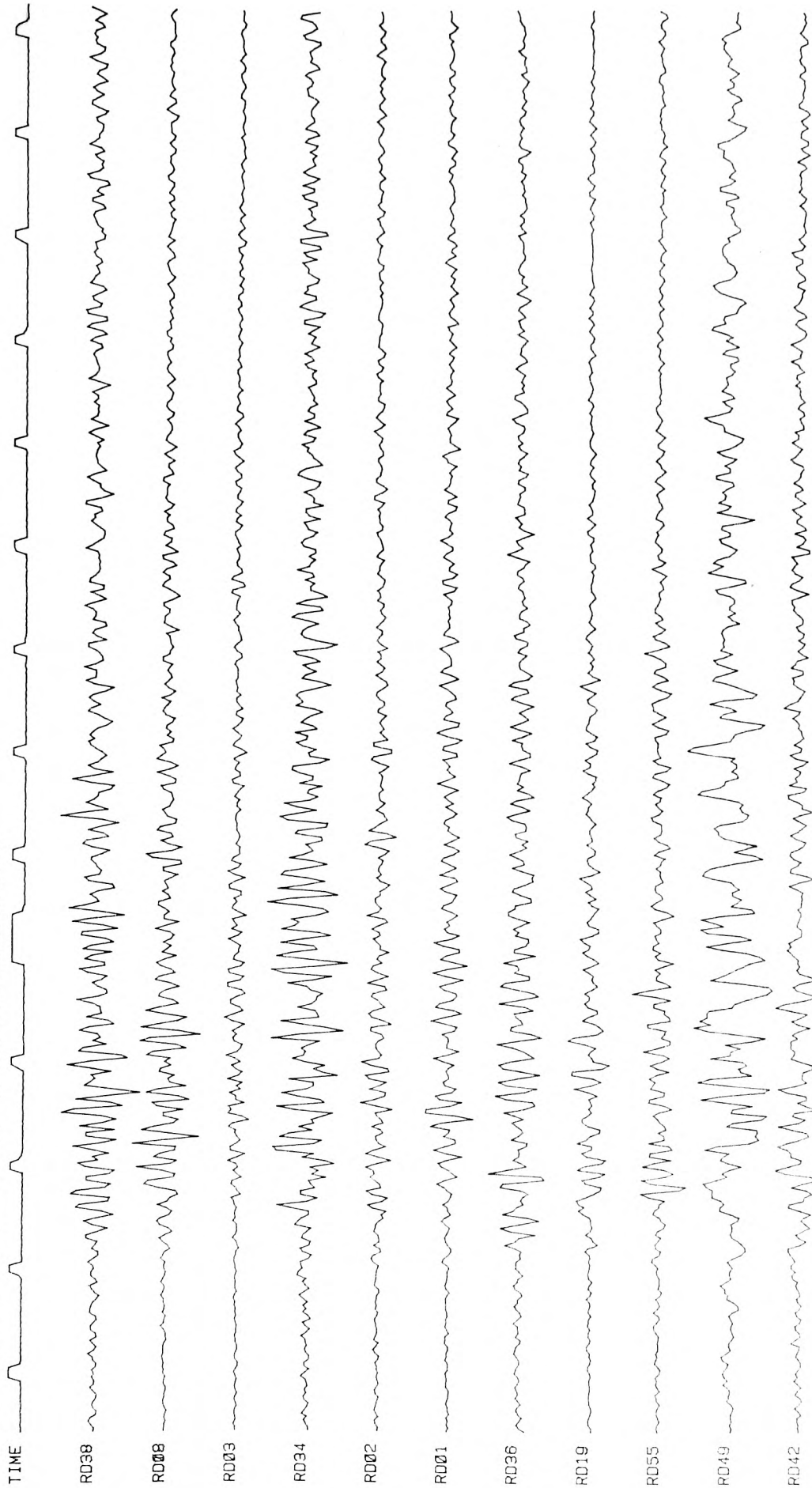


Fig. 7.11b GROUP (3) : S-waves

RABAU DATA: GROUP (3) SUMS IN FOUR DIRECTIONS (100/1000/1400/0.00004/0.001)

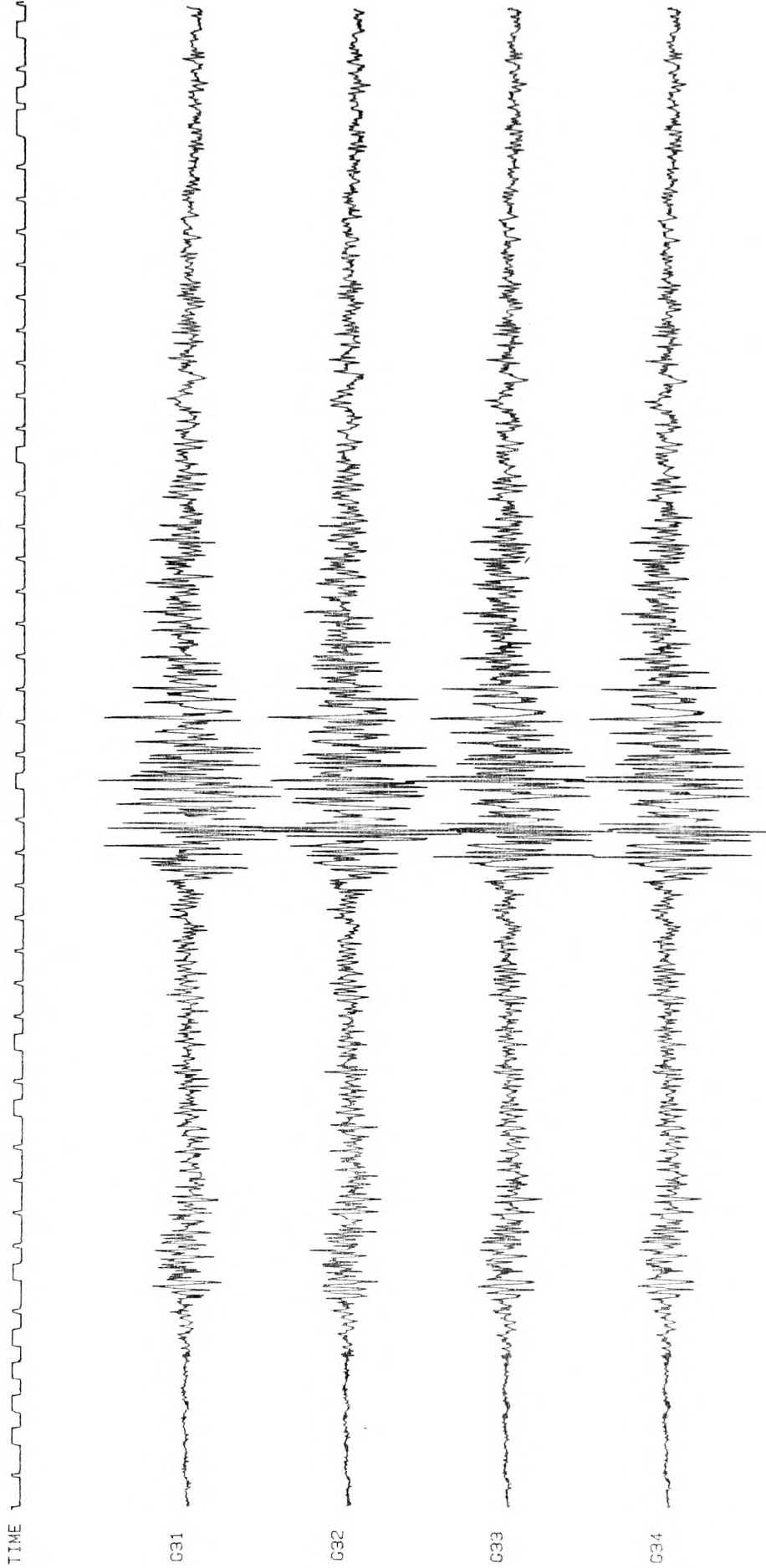


Fig. 7.11c SUM OF GROUP (3)

RABAU DATA: GROUP (3) SUMS: S-WAVES (30/1530/420/0.00006/0.001)

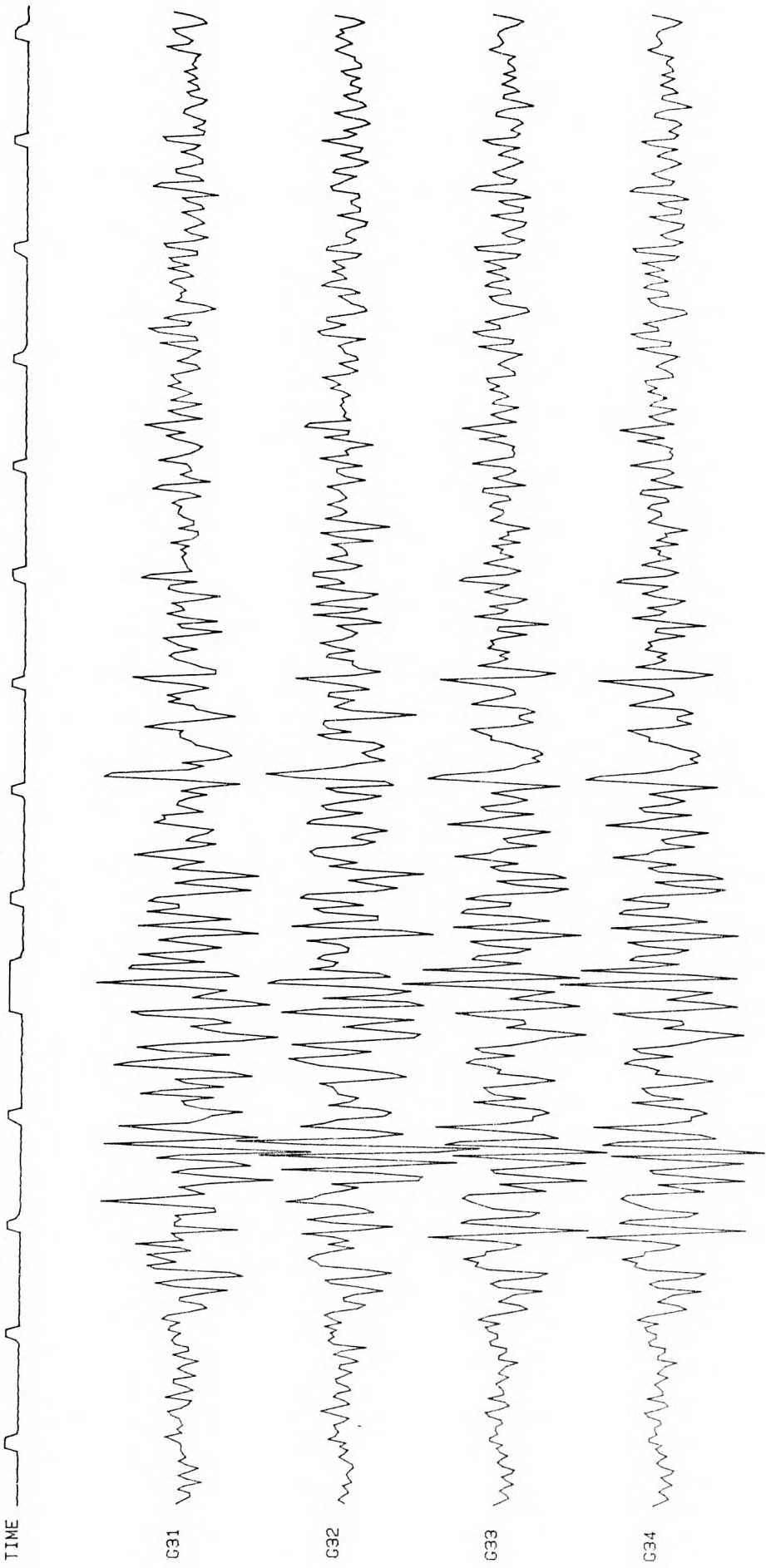


Fig. 7.11d SUM OF GROUP (3) : S-waves with M = 0.72

RABAU DATA: GROUP (4) (130/750/1820/0.00004/0.001)

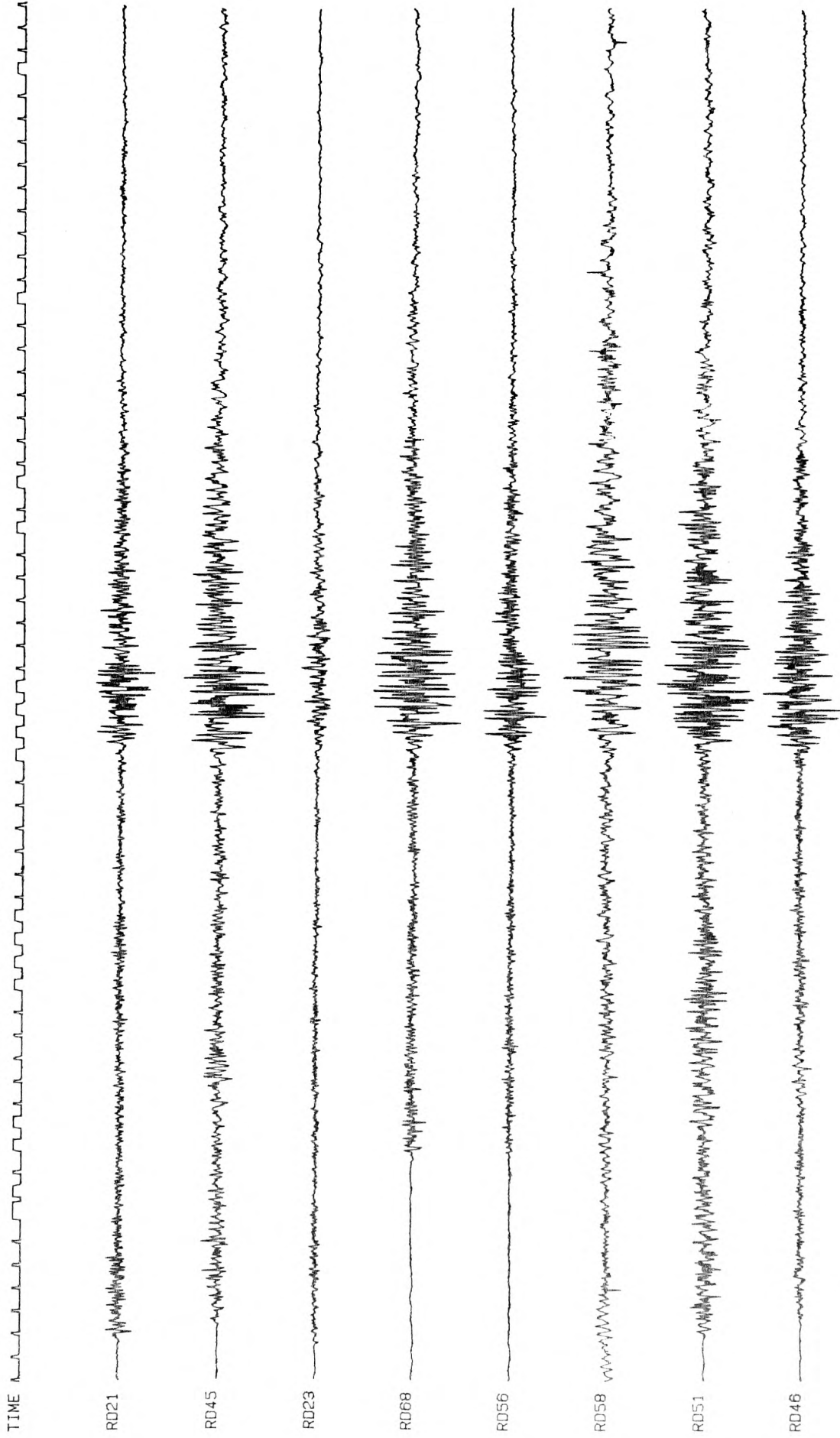


Fig. 7.12a GROUP (4)

RABAU DATA: GROUP (4) S-WAVES (30/1530/420/0.00006/0.001)

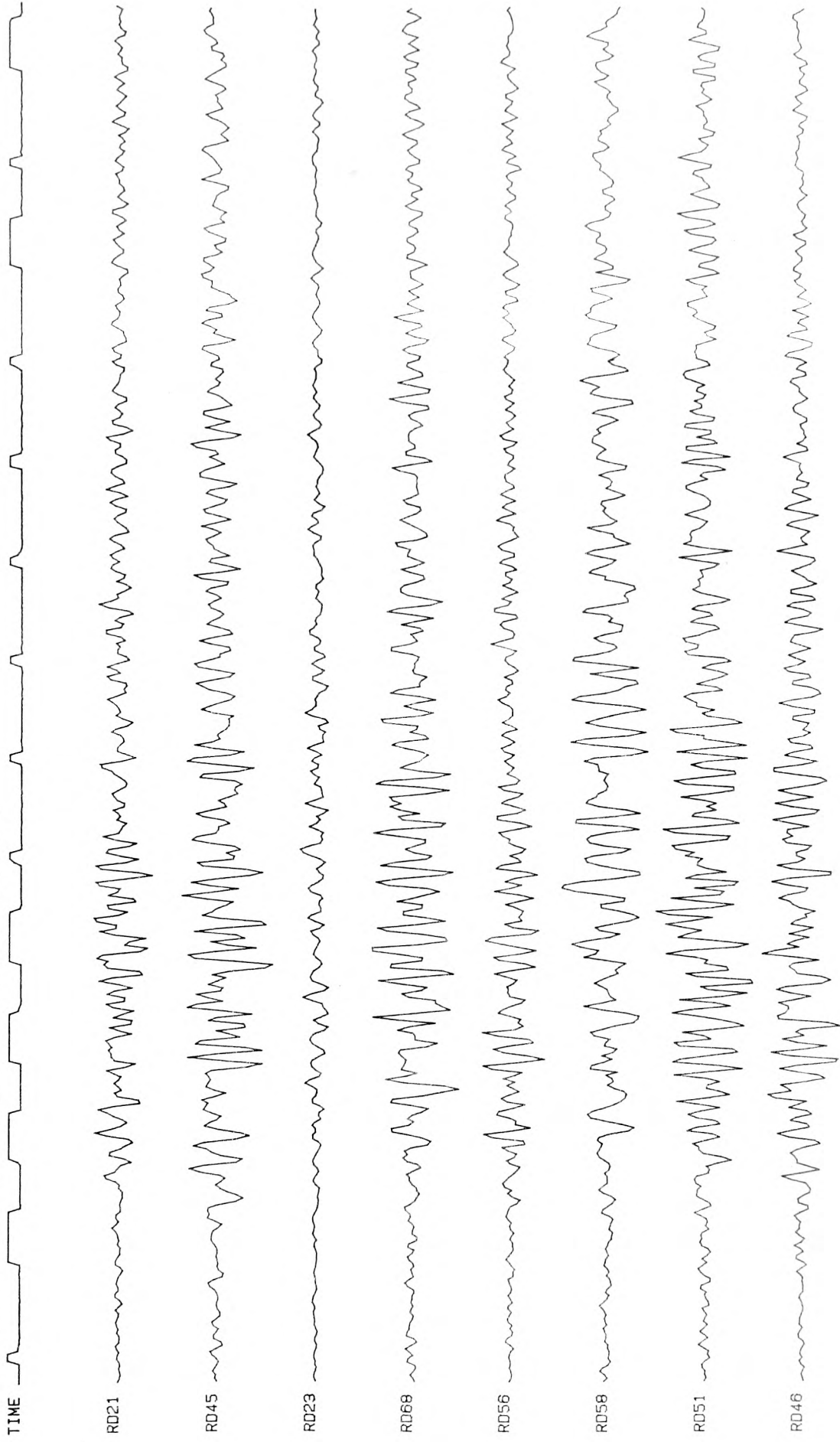


Fig. 7.12b GROUP (4) : S-waves

RABAU DATA: GROUP (4) SUMS IN FOUR DIRECTIONS (130/700/1820/3.03004/0.001)

TIME 

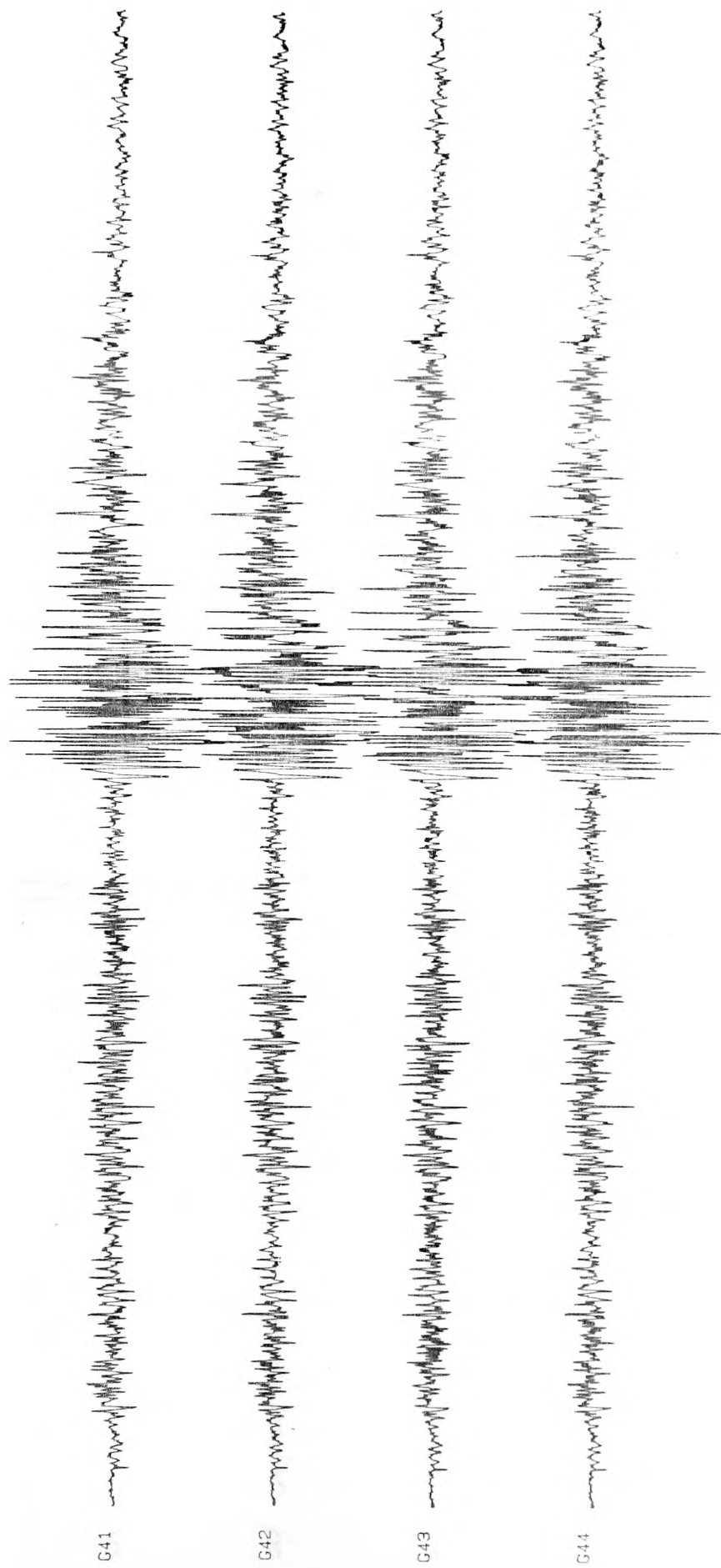


Fig. 7.12c SUM OF GROUP (4)

RABAU DATA: GROUP (4) SUMS: S-WAVES (30/1530/420/0.00006/0.001)

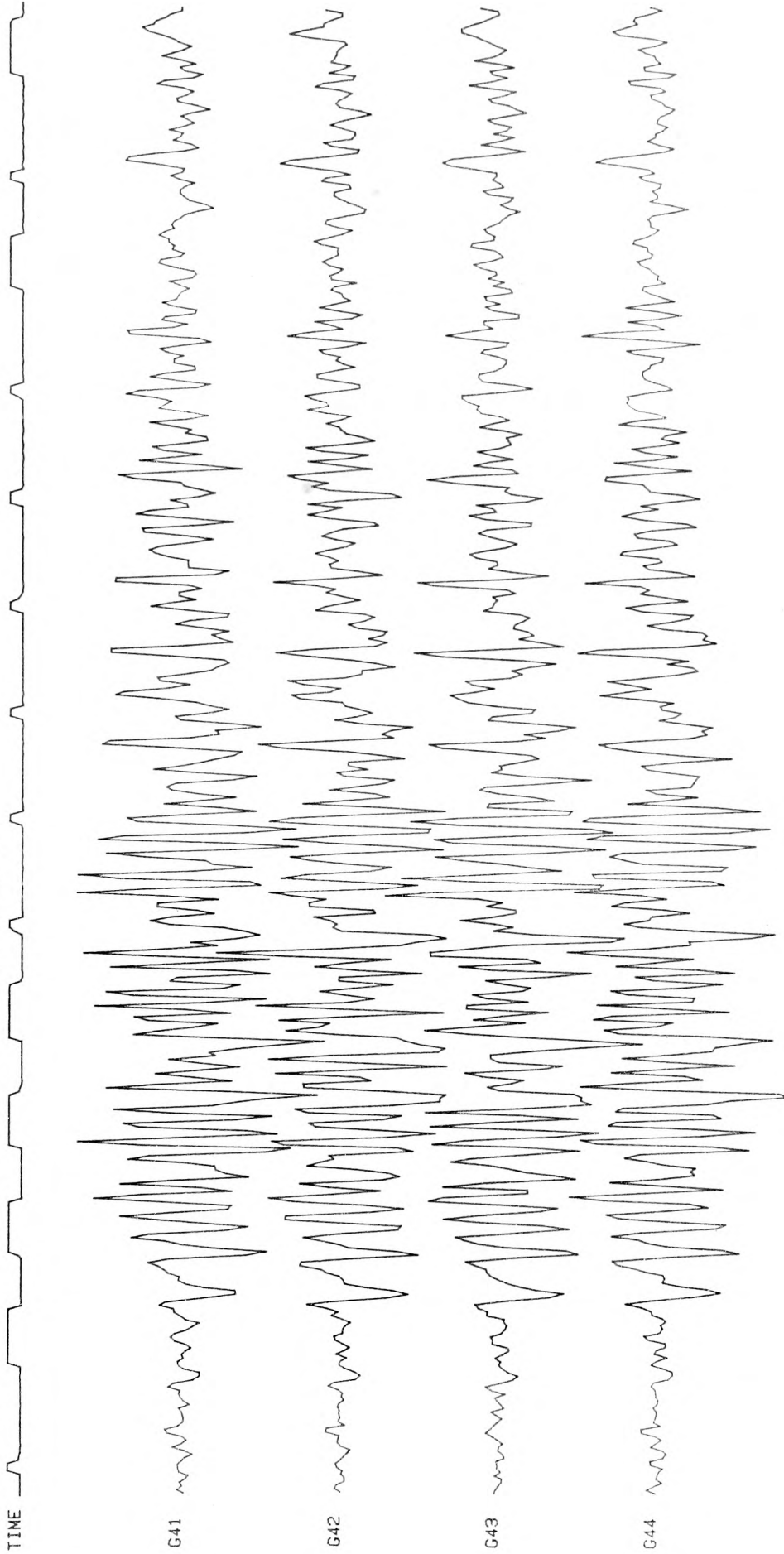


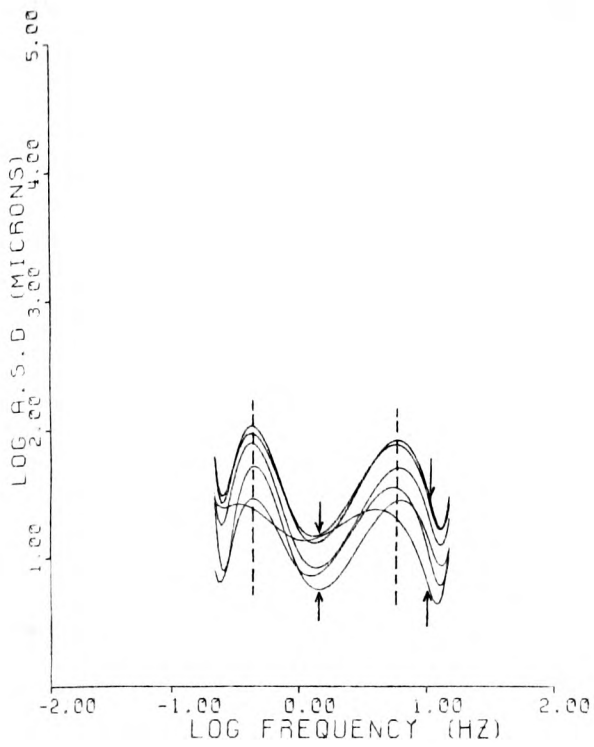
Fig. 7.12d SUM OF GROUP (4) : S-waves with $M = 0.80$

The most outstanding result from these plots and from Table 7.3 is the remarkable increase in fracture propagation as we swing in azimuth. This feature is discussed in more detail in later sections.

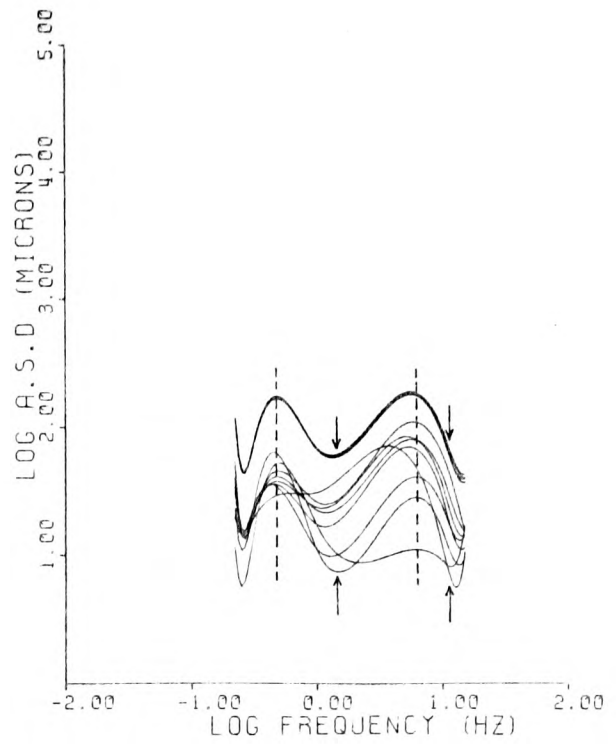
Before discussing the resulting spectra in depth and in order to clarify later sections, we proceed to outline a certain convention which we use and adhere to in our interpretations.

The first impression we get when studying the spectral curves of Figures 7.13 and 7.14 is that they are markedly different in shape compared to the far-field spectra of the Chile data where there is a definite long period level (static part), a single corner frequency and a high frequency roll-off (dynamic part). This is expected in the near-field of a fault where frequency content, short distance, and radiation pattern play a major role. Therefore we assume that within our bandwidth, frequencies around 10Hz represent the short period content of our earthquake spectra, while frequencies around 1Hz describe the threshold of the long period range. Accordingly we mark them with arrows. Furthermore in all the spectral plots we observe two "humps" round about 8Hz and 0.5-0.8Hz. These are marked with broken vertical lines as in Figure 7.13. Having established this we make the following observations regarding Figure 7.13:

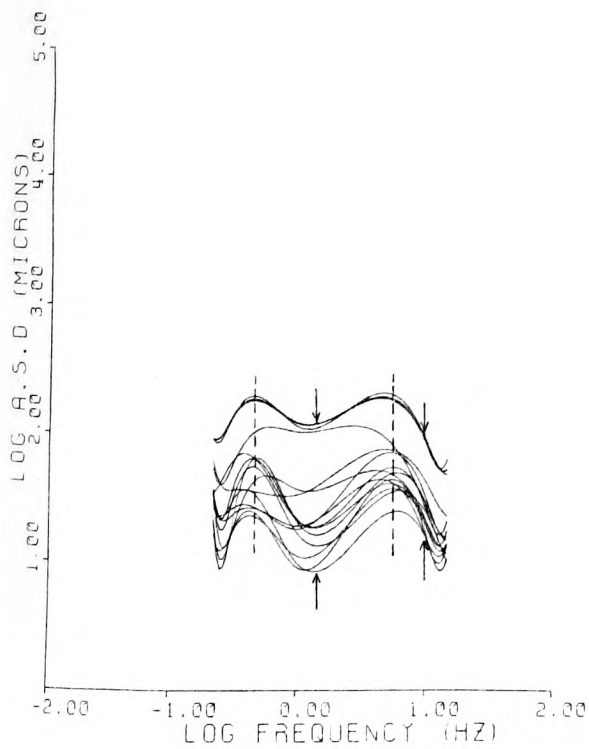
- (1) There is no significant difference between the spectra of the summed seismograms in each group in the 4 assumed trigger directions. Except for Group (1) where there are slight differences, one can hardly make out the total sums in the 4 directions (top group of curves in each plot)



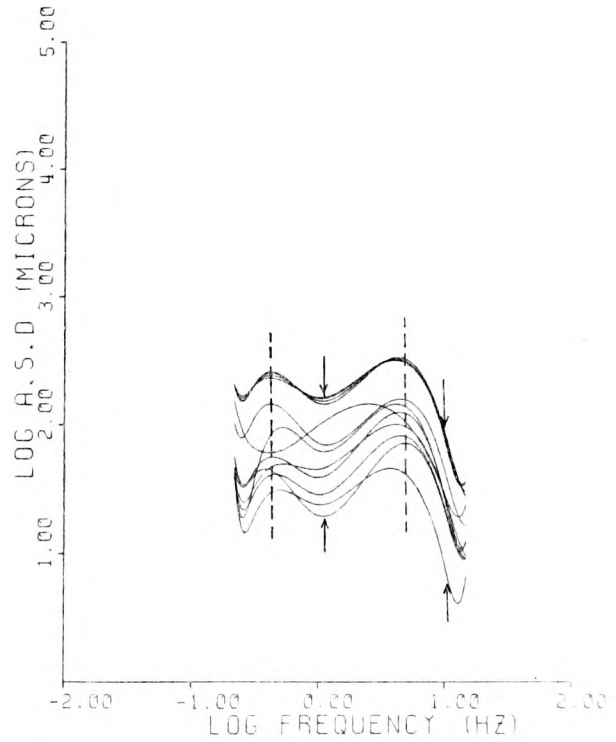
CUBIC SPLINE FIT TO SEISMIC SPECTRUM.
 RABAU DATA: SPECTRA OF EVENTS AND SUMS
 GROUP (1) & G11,12,13,14



CUBIC SPLINE FIT TO SEISMIC SPECTRUM.
 RABAU DATA: SPECTRA OF EVENTS AND SUMS
 GROUP (2) & G21,22,23,24

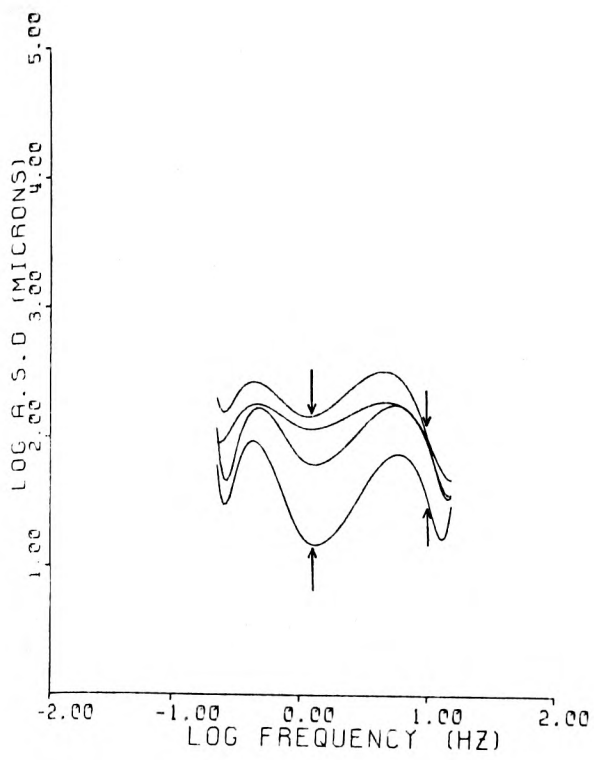


CUBIC SPLINE FIT TO SEISMIC SPECTRUM.
 RABAU DATA: SPECTRA OF EVENTS AND SUMS
 GROUP (3) & G31,32,33,34



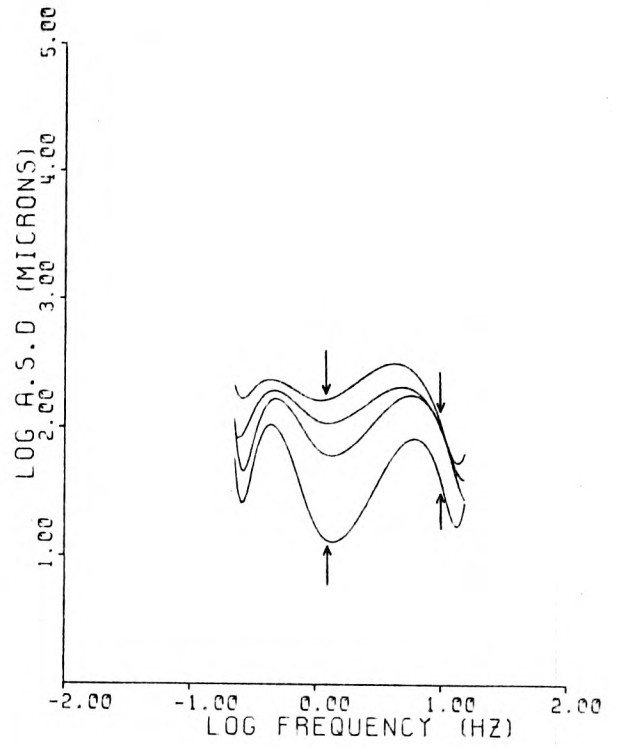
CUBIC SPLINE FIT TO SEISMIC SPECTRUM.
 RABAU DATA: SPECTRA OF EVENTS AND SUMS
 GROUP (4) & G41,42,43,44

Fig. 7.13 Spectra of each Group with their sums



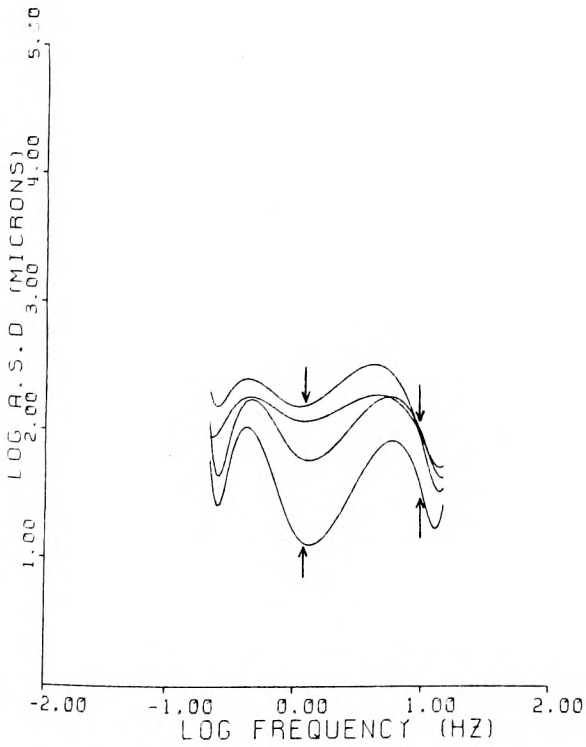
CUBIC SPLINE FIT TO SEISMIC SPECTRUM.

RABUL DATA: SPECTRA OF SUMS
IN FOUR DIRECTIONS: G11,21,31,41



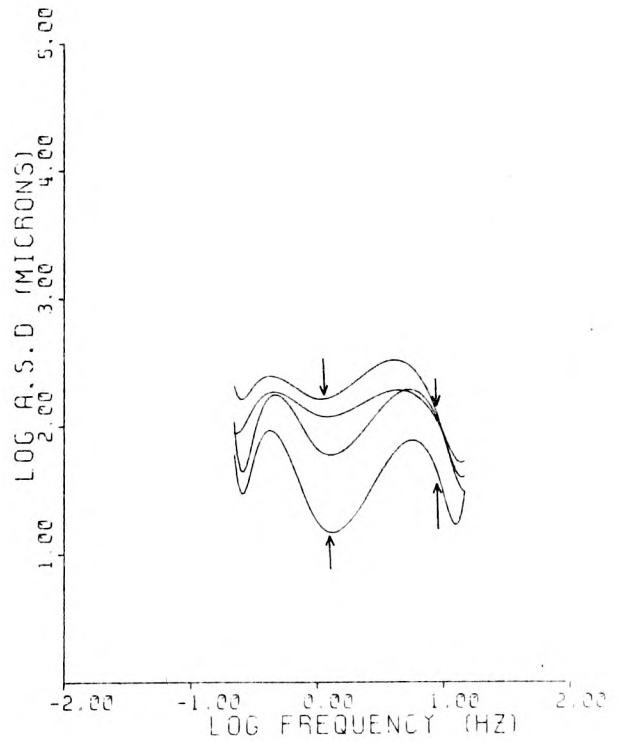
CUBIC SPLINE FIT TO SEISMIC SPECTRUM.

RABUL DATA: SPECTRA OF SUMS
IN FOUR DIRECTIONS: G12,22,32,42



CUBIC SPLINE FIT TO SEISMIC SPECTRUM.

RABUL DATA: SPECTRA OF SUMS
IN FOUR DIRECTIONS: G13,23,33,43



CUBIC SPLINE FIT TO SEISMIC SPECTRUM.

RABUL DATA: SPECTRA OF SUMS
IN FOUR DIRECTIONS: G14,24,34,44

Fig. 7.14 Spectra of each group in each direction

since they have almost identical shape.

- (2) The observation that earthquake size increases with range and with azimuth as we swing to face the major subduction zone is reflected in the spectra.

Groups (1) and (2) seem to show similar spectral shape with no definite long period level or high frequency slope. However as we move to the larger magnitude earthquakes of Groups (3) and (4), we notice, and particularly in Group (4), that the spectra begins to assume a more characteristic shape of a seismic spectrum, i.e: a better defined short period slope and a less pronounced drop in amplitude at the lower frequencies.

- (3) We tend to believe that the "humps" mentioned earlier may be significant in that they appear to indicate the regions where higher corner frequencies possibly related to ω^{-2} and ω^{-3} may exist (see Section 6.3.0).

- (4) As expected, the total summed output in each group shows more on the amplitude axis. That is, the number of input records has a direct bearing on the resulting spectra. This is evident in Group (3) where we summed 12 records as compared to Groups (2) and (4) in which we input 8 seismograms. In contrast the enhancement in the final sum of Group (1) is difficult to recognize since only 4 events were used.

- (5) Most interesting of all observations in Figure 7.13 is the fact that the long period range constructs remarkably better than the short period range. Here again the larger

magnitude spectra of Groups (3) and (4) illustrate this more clearly. This striking result is also evident when we compare the spectra of the total sums in the 4 directions of the 4 groups (Fig. 7.14).

6.2.0 Comparison of the Summed Spectra:

Figure 7.14 illustrates 4 plots, each containing the summed output spectrum of each group in each direction of trigger. From top to bottom the curves correspond to Groups (4), (3), (2) and (1) respectively.

Here perhaps there is a slight difference in construction due to the different sequences of summation although it still remains insignificant. Possibly the group of spectra indicating the left-right trigger directions (see Fig. 7.8), i.e: G12, G22, G32 and G42 (top right plot of Fig. 7.14) could be taken as the best representation since the spectra in both the long and short period ranges progress systematically, until in the sum of the larger magnitude events of Group (4) the long period ranges becomes more level. Note the amplitude difference between long and short period ranges for the 4 groups.

6.3.0 Comparison of the Spectra with RDD72 and RDM73:

According to our hypothesis, the ideal situation would be to sum enough small shocks then compare the spectrum of the constructed source with an already existing one such as the spectra of RDD72 and RDM73 whose parameters are given in Table 7.2. Figure 7.6 also shows their locations. As will be

discussed later this was not achieved. The only other alternative is to try and construct a source from the separate group sums averaged over a range of azimuths. By doing so we would include a bigger focal region representing a larger fault. The input records to this summation will be the already constructed records from the individual groups.

Looking back at the location map of Figure 7.6 and recalling our discussion in Section 5.3.1, it may be possible to assume that the shocks of Groups (2), (3), and (4) originate from a common source. In other words if the shaded areas representing these 3 groups were taken to be 3 focal regions then a source constructed from the shocks within all 3 regions would be an averaged earthquake occurring inside a larger focal region encompassing the 3 primary ones. This larger region therefore stretches over a range of distance and azimuth determined by the epicentral distances and azimuths of all the shocks in Groups (2), (3) and (4). Note that Group (1) is not included since the constituent shocks probably belong to a separate source of activity as shown by their azimuth.

Having established this we next consider the triggering sequence and rupture velocity. Regarding the trigger directions we take the total sum in each group in that direction and sum them together thus the following directions become apparent:

- (1) $G_{22} + G_{32} + G_{42}$: Along fault strike in a NW-SE direction
- (2) $G_{41} + G_{31} + G_{21}$: " " " " " SE-NW "
- (3) $G_{23} + G_{43} + G_{33}$: " " dip " " DOWNWARD "
- (4) $G_{34} + G_{44} + G_{24}$: " " " " an UPWARD "

As far as rupture velocity is concerned we based our input on

the parameters listed in Table 7.3. With an average S-wave velocity of 3.3km/s for Groups (2), (3) and (4) and bearing in mind the criteria given in Section 5.3.2, we input a range of phasing velocity between 1.5-3.0km/s. The best results were obtained with a velocity of 2.3km/s. This gives a subsonic propagation of 0.7M.

The results are illustrated in Figure 7.15a and b through to 7.18a and b plotted to the same scale. Figure 7.19a and b show the records of the final sums according to the trigger directions mentioned above. Figure 7.20 illustrates the equivalent spectral plots with those of RDD72 and RDM73 for comparison. Studying the seismograms and spectra we make the following observations:

- 1 - From Figure 7.19a it appears that the best coherency within the S-wave train is in the downward trigger direction. This however does not affect the spectral plots significantly as shown in Figure 7.20.
- 2 - The spectra of the sums (indicated by "ALL" on Figure 7.20) of Groups (2), (3) and (4) in the 4 directions generally indicate that we are achieving substantial construction in the long period range, but that we do not have enough samples to step-up the long period level to that of a large source such as RDD72 by filling-in the hatched area under the curve. On the other hand, at the short period range, we are well within the construction according to the square root of the high frequency wave amplitudes.
- 3 - From these presentations, it transpires that the short

RABAUL DATA, SUM OF GROUPS: 2, 3, 4 (NW-SE) (130/700/1820/0.00004/0.0005)

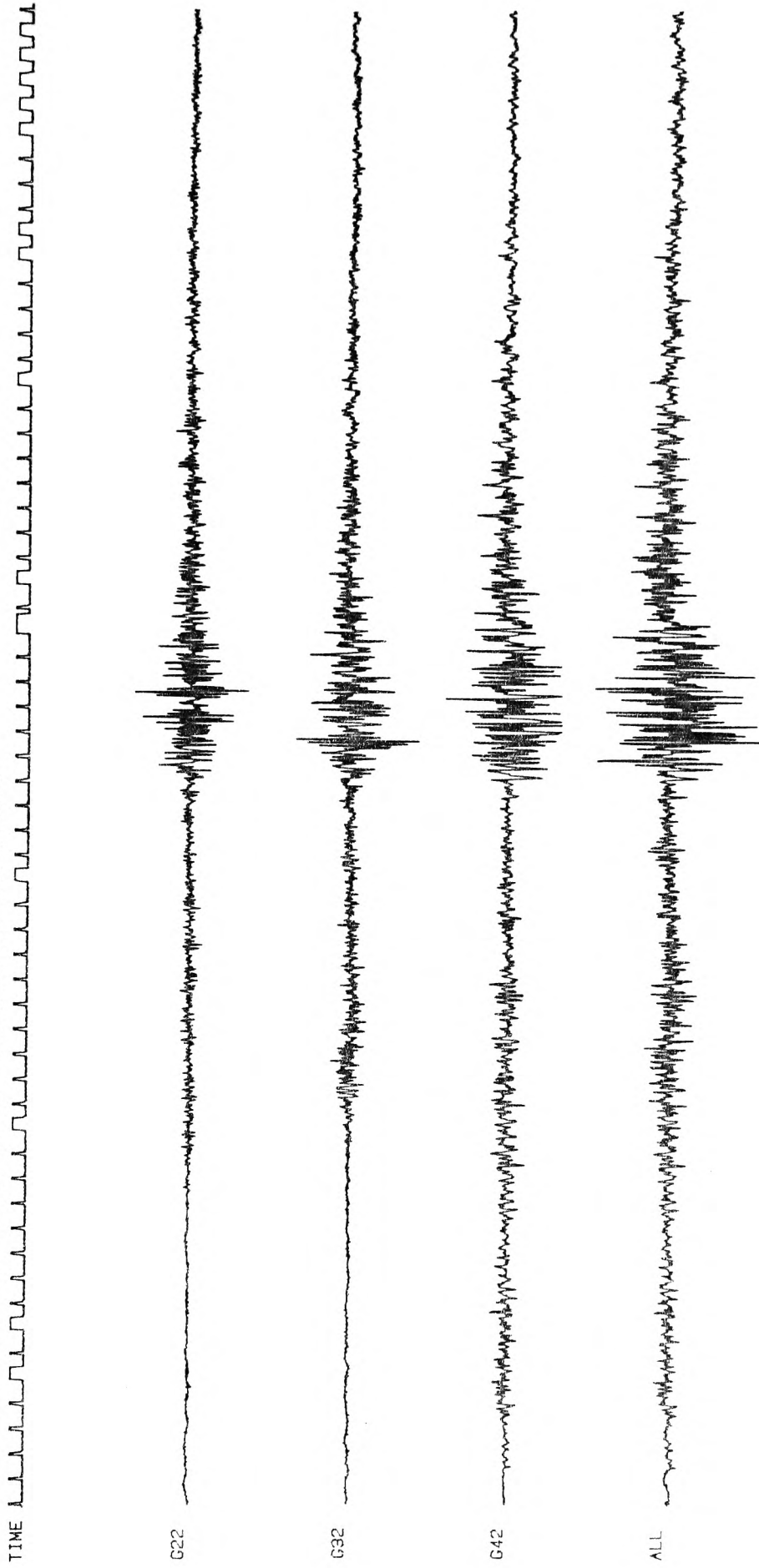


Fig. 7.15a GROUP SUMS : NW-SE

RABAU DATA: SUM OF GROUPS: 2, 3, 4 (NW-SE) S-WAVES

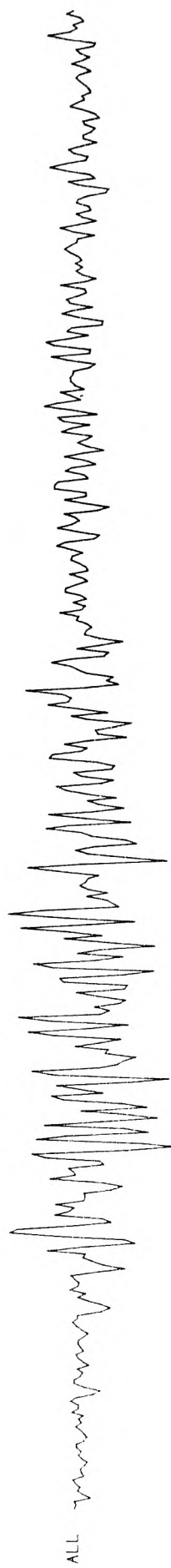
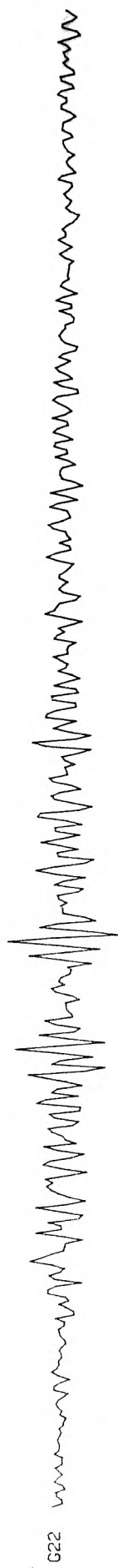


Fig. 7.15b Group Sums : NW-SE : S-waves with $M = 0.70$

RABAUUL DATA: SUM OF GROUPS: 4, 3, 2 (SE-NW) (130/700/1820/0.00004/0.0005)

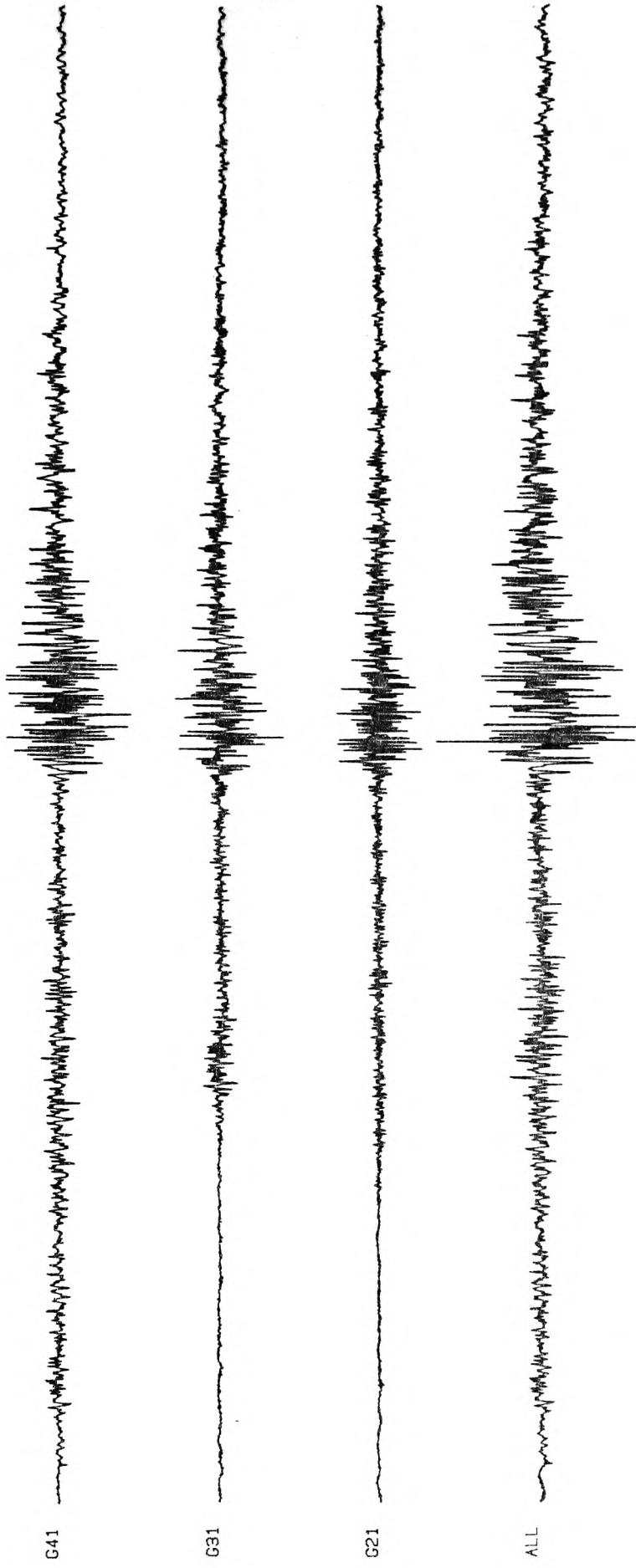
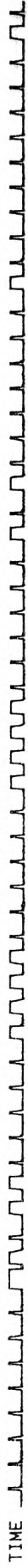


Fig. 7.16a Group Sums : SE-NW

RABAU DATA: SUM OF GROUPS: 4, 3, 2 (SE-NW) S-WAVES

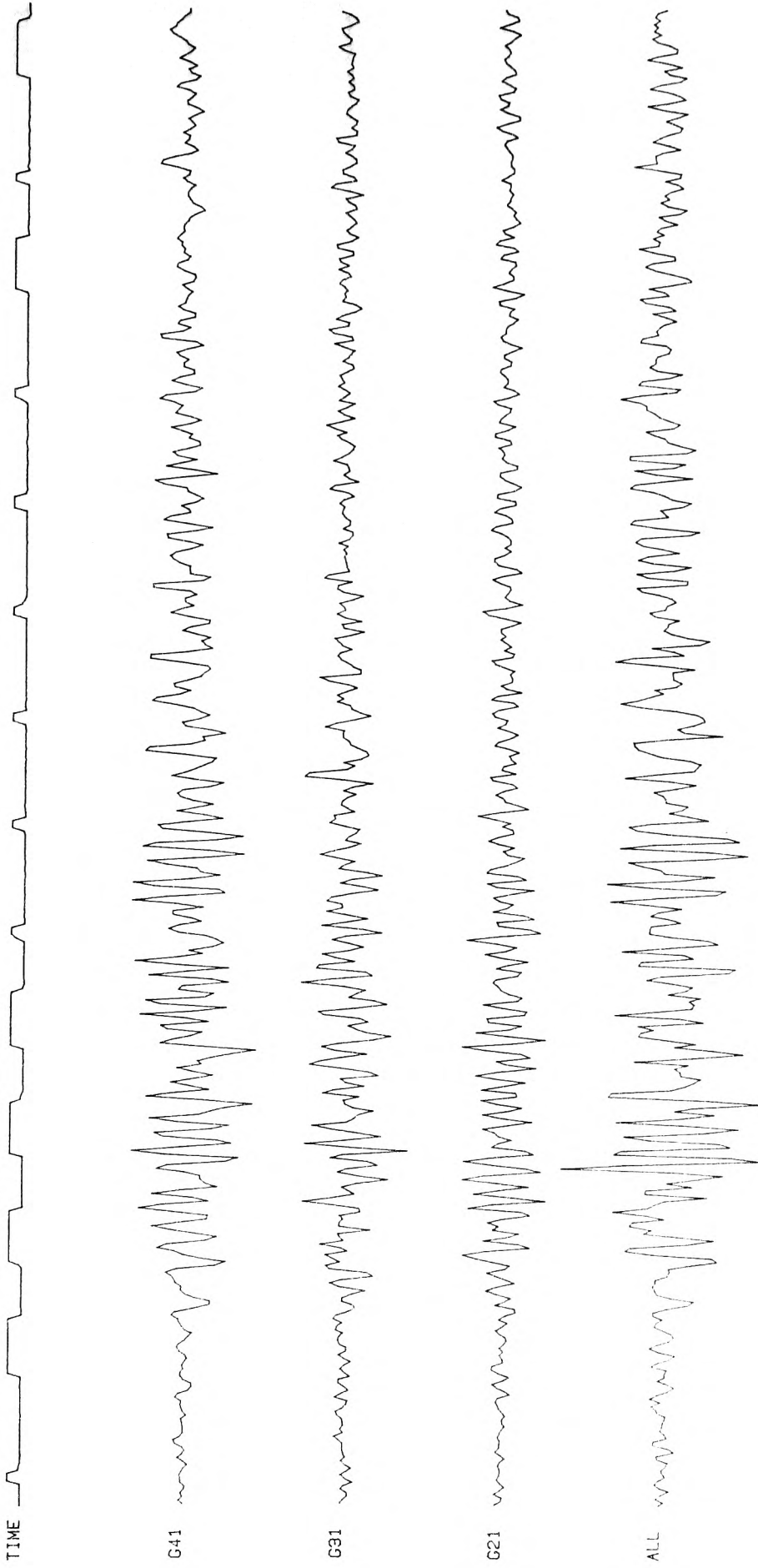


Fig. 7.16b Group Sums : SE-NW : S-waves with $M = 0.70$

RABUL DATA: SUM OF GROUPS: 2, 4, 3 (DOWNWARD) (130/700/1820/0.00004/0.0005)

TIME 



Fig. 7.17a Group Sums : DOWNWARD

RABAU DATA: SUM OF GROUPS 2, 4, 3 (DOWNWARD) S-WAVES

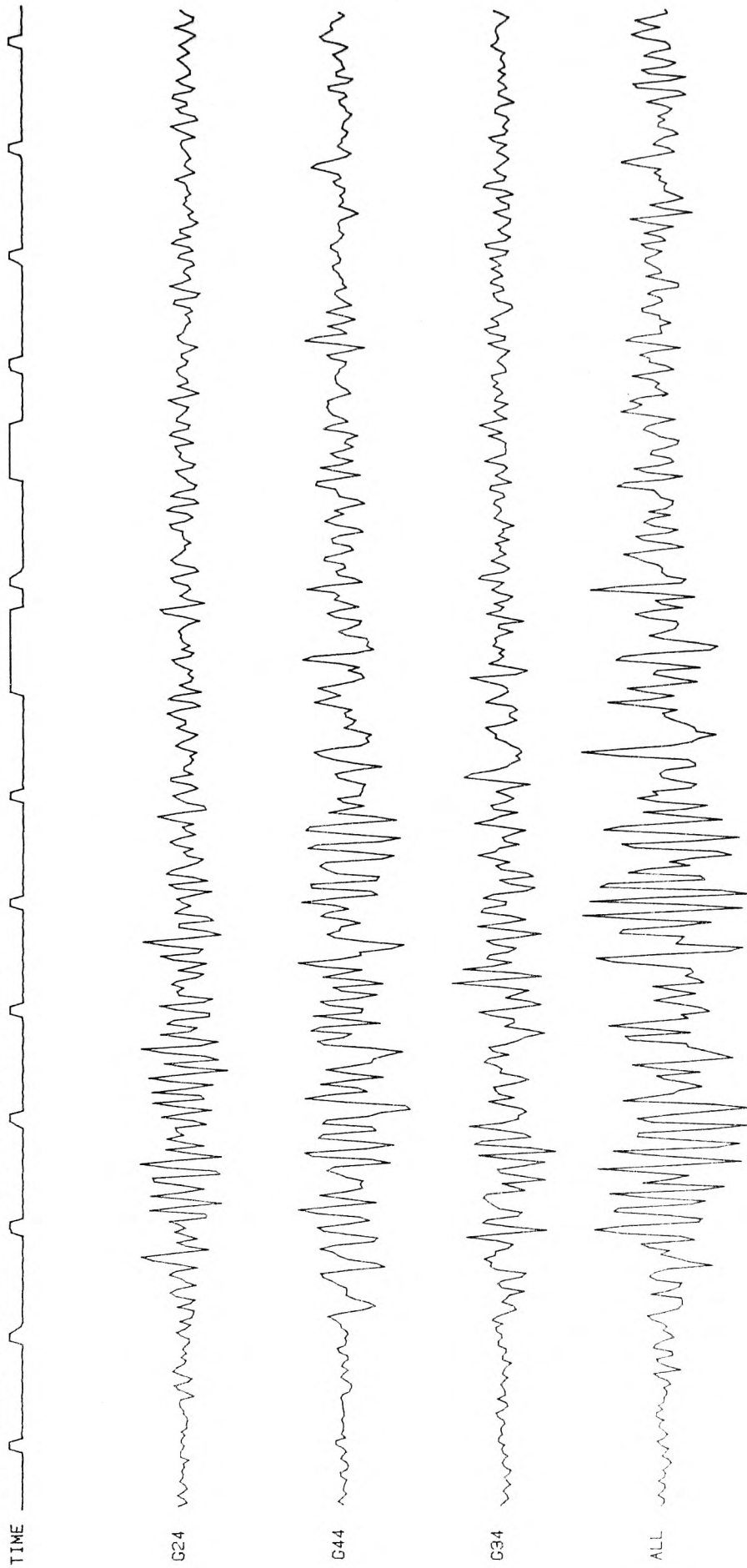


Fig. 7.17b Group Sums : DOWNWARD : S-waves with $M = 0.70$

RABUL DATA: SUM OF GROUPS: 3, 4, 2 (UPWARD) (130/700/1820/0.00004/0.0005)

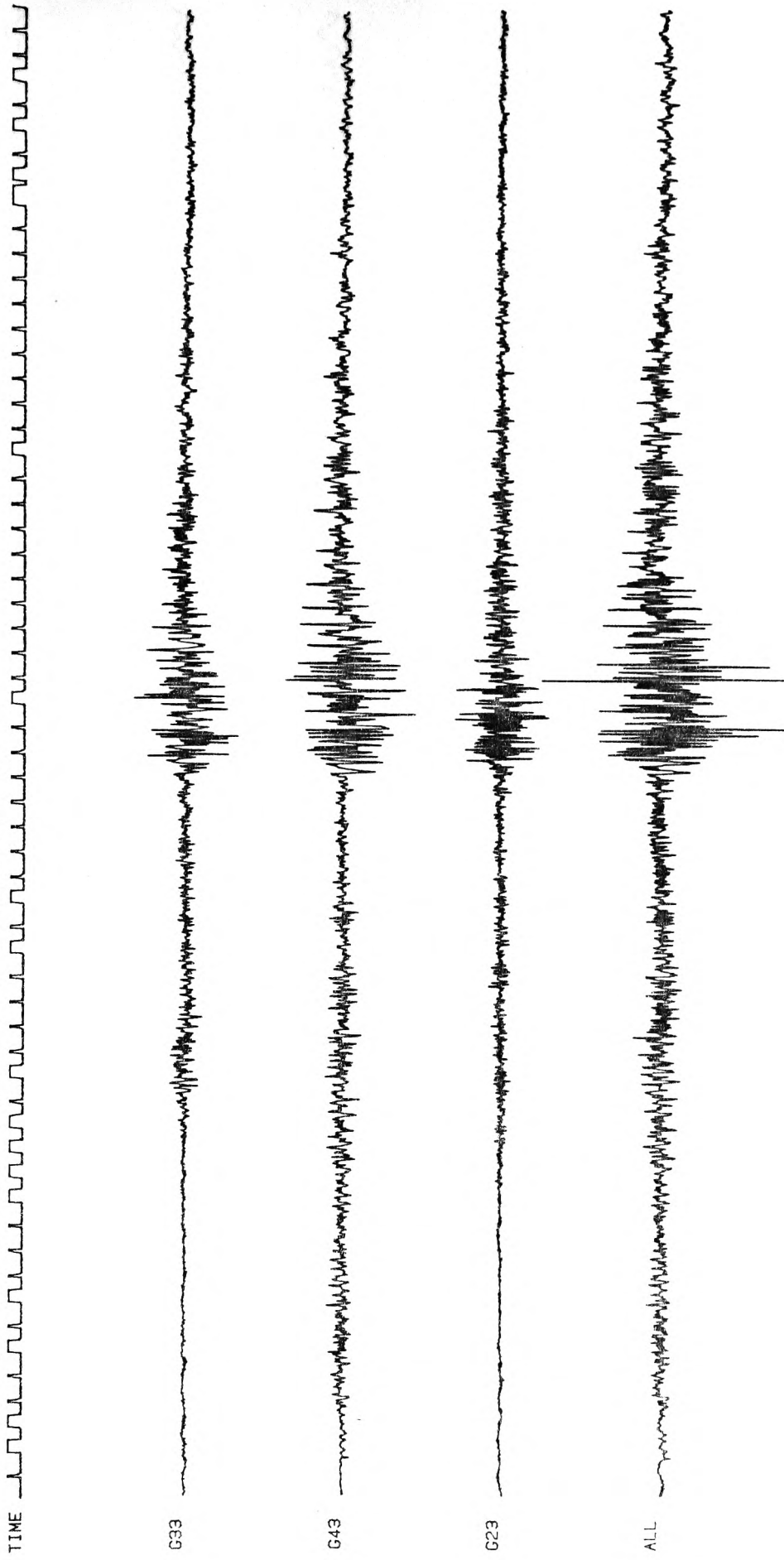


Fig. 7.18a Group Sums : UPWARD

RABAUL DATA: SUM OF GROUPS: 3, 4, 2 (UPWARD) S-WAVES

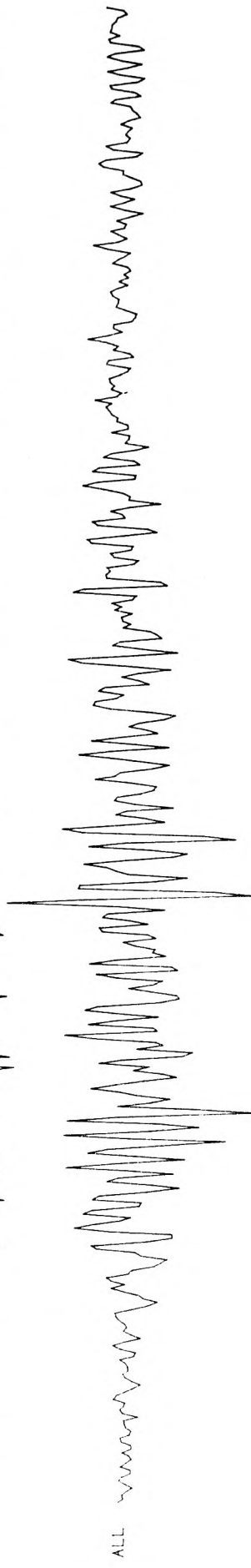
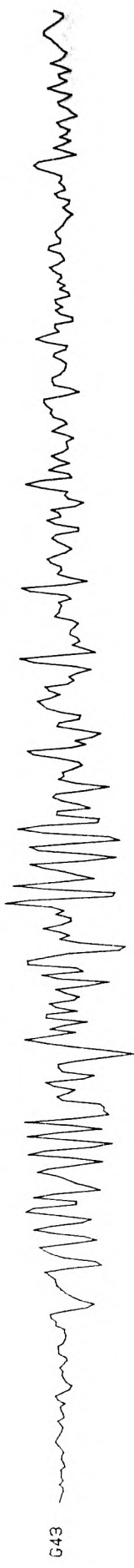


Fig. 7.18b Group Sums : UPWARD : S-waves with $M = 0.70$

RABAU DATA; SUMS OF GROUPS 2, 3, 4 IN FOUR DIRECTIONS

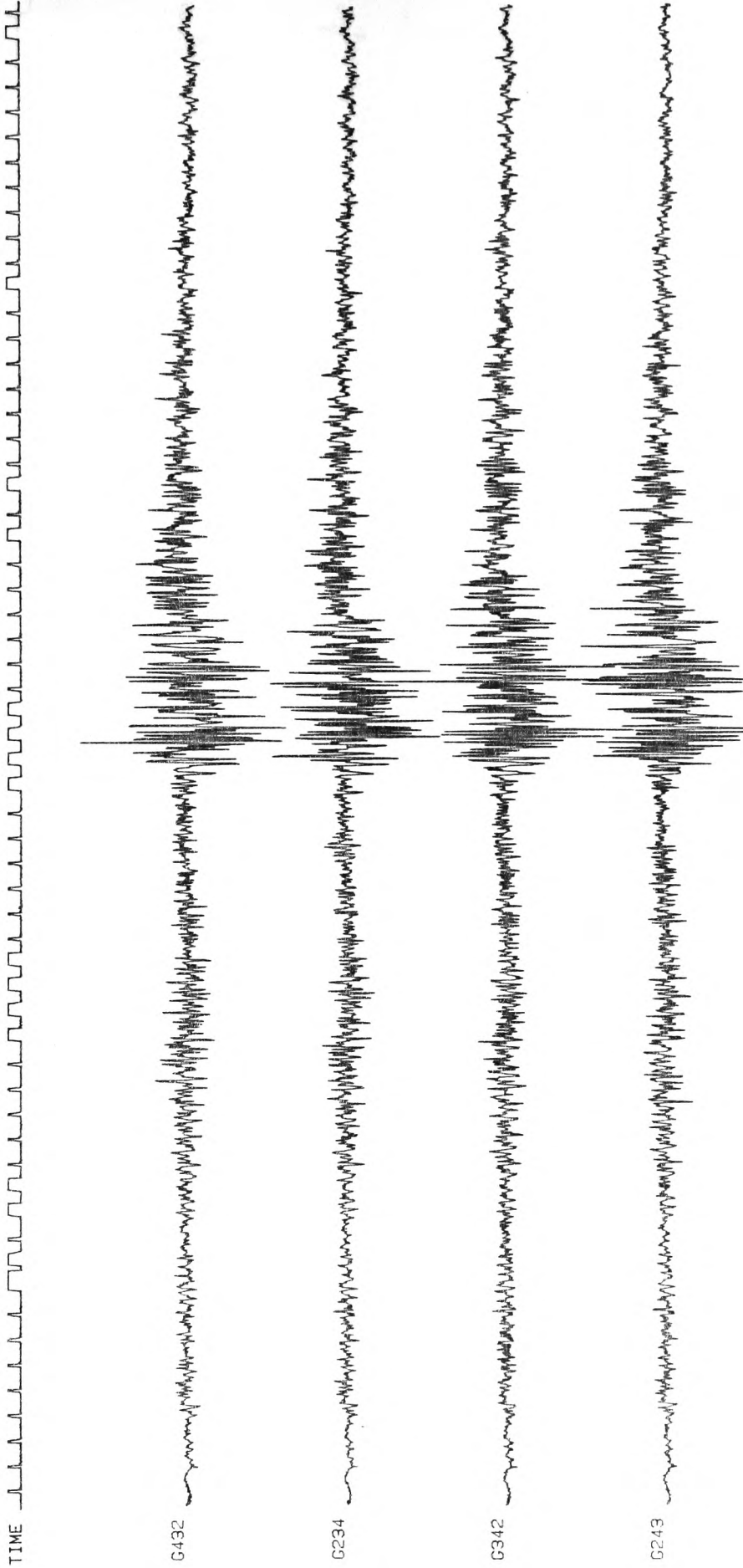


Fig. 7.19a Final Sums

RABAUL DATA: SUMS OF GROUPS: 2, 3, 4 IN FOUR DIRECTIONS S-WAVES

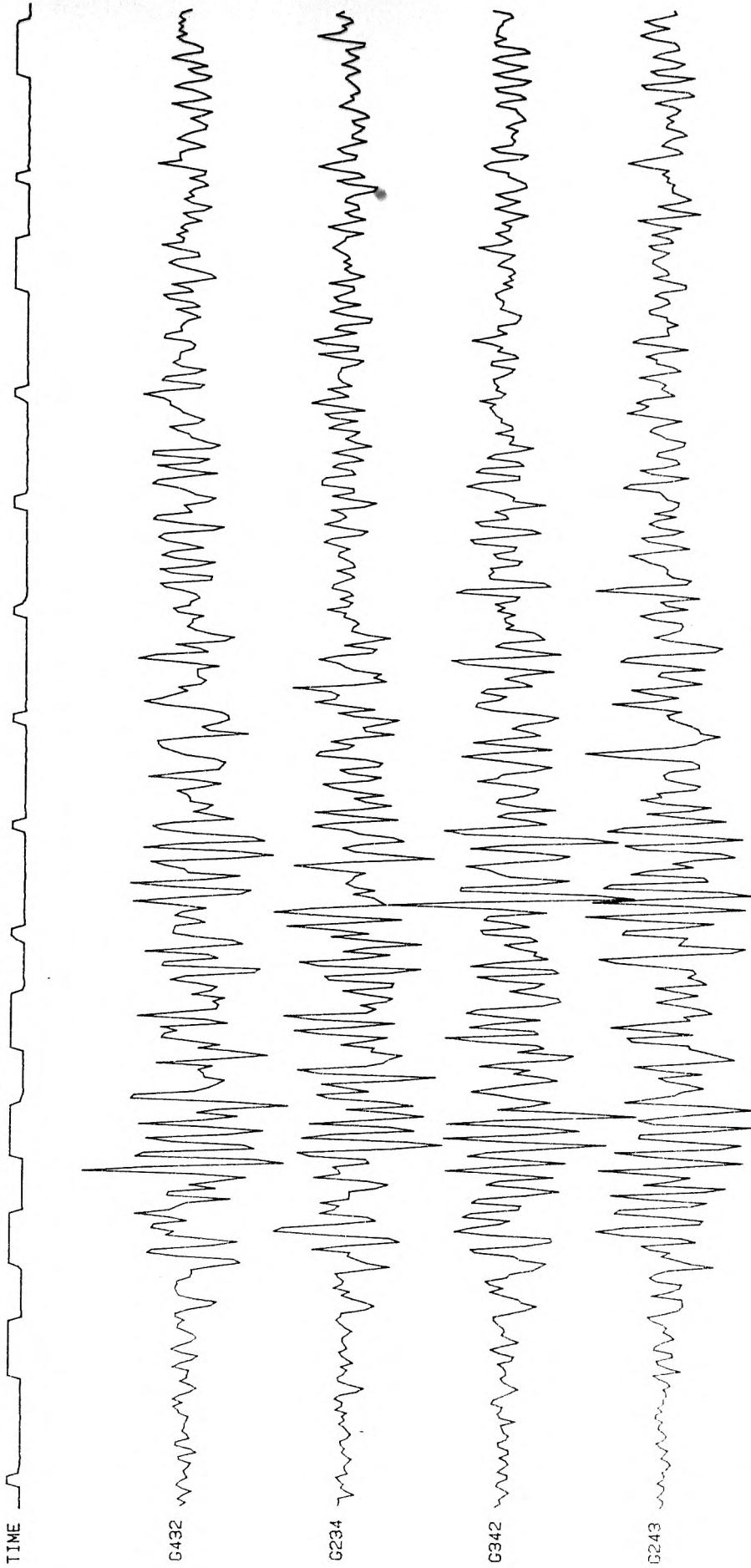
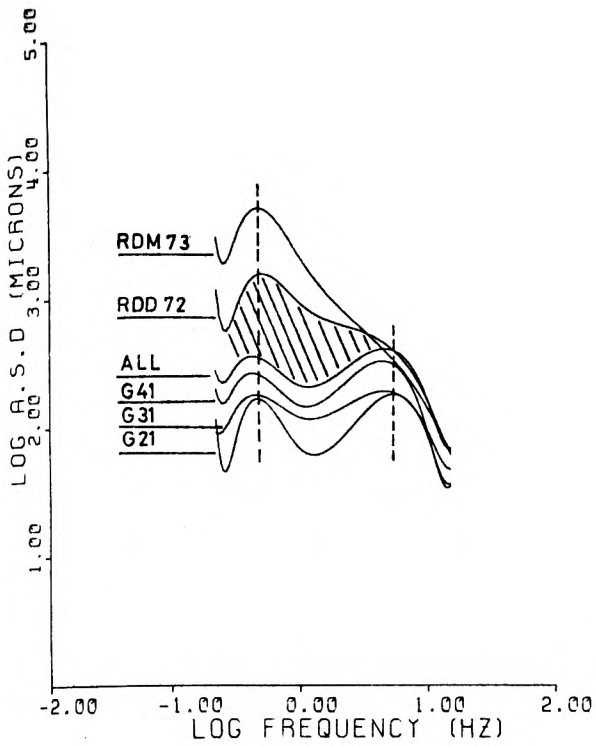
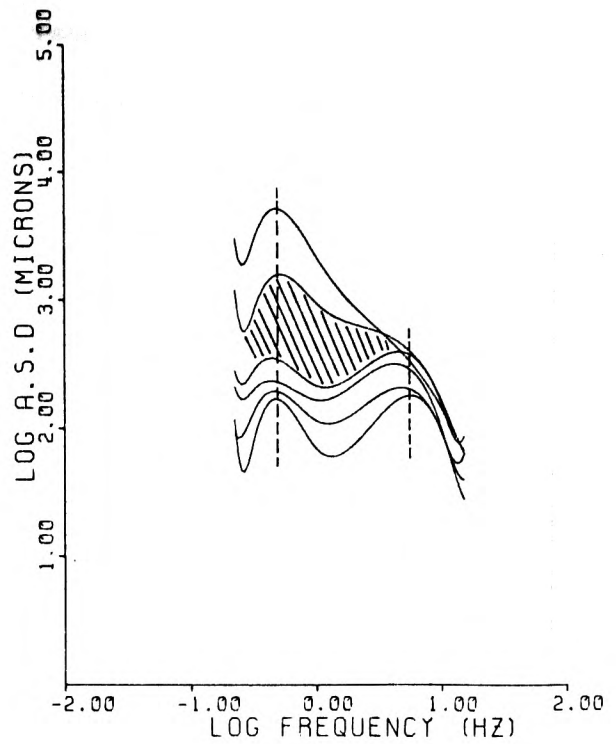


Fig. 7.19b Final Sums : S-waves with $M = 0.70$



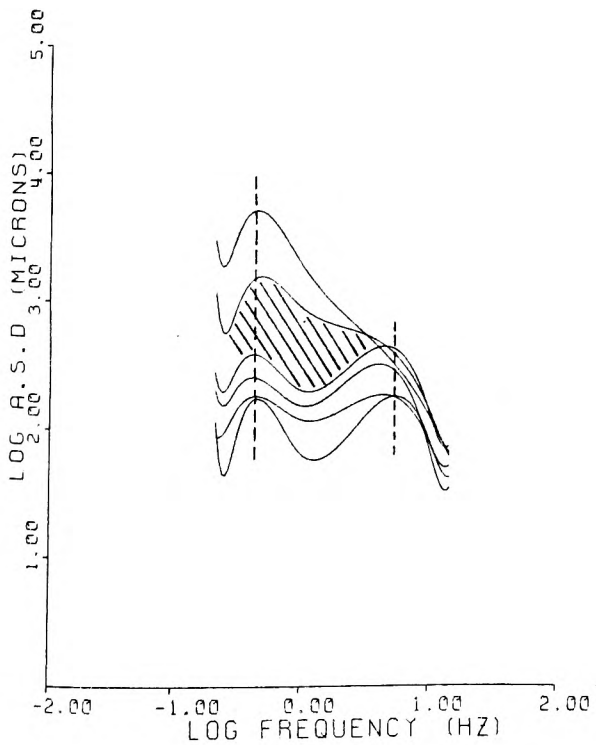
CUBIC SPLINE FIT TO SEISMIC SPECTRUM.

RABAUl DATA: SPECTRA OF EVENTS AND SUMS
RDM73, D72, G41, 31, 21, & ALL (SE-NW)



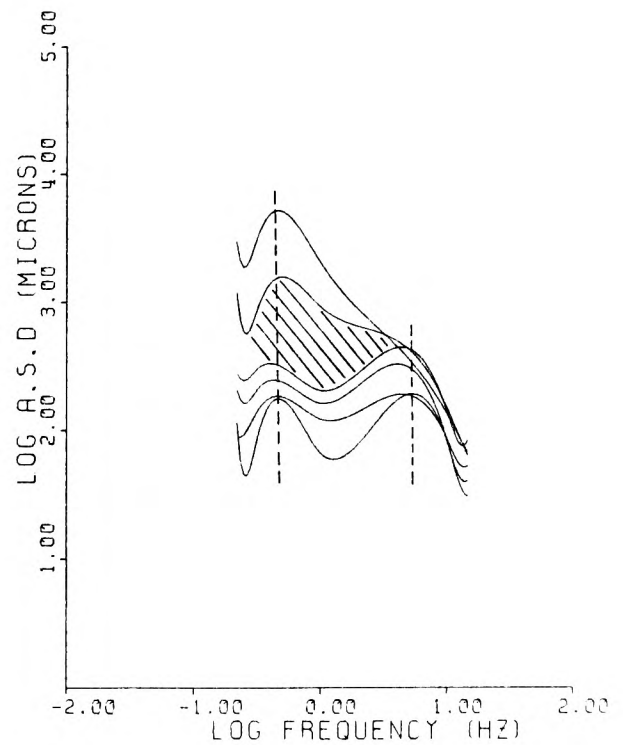
CUBIC SPLINE FIT TO SEISMIC SPECTRUM.

RABAUl DATA: SPECTRA OF EVENTS AND SUMS
RDM73, D72, G22, 32, 42, & ALL (NW-SE)



CUBIC SPLINE FIT TO SEISMIC SPECTRUM.

RABAUl DATA: SPECTRA OF EVENTS AND SUMS
RDM73, D72, G33, G43, G23, & ALL (UP)



CUBIC SPLINE FIT TO SEISMIC SPECTRUM.

RABAUl DATA: SPECTRA OF EVENTS AND SUMS
RDM73, D72, G24, 44, 34, & ALL (DOWN)

Fig. 7.20 Comparison of Summed Spectra

period "hump" which may correspond to an ω^{-3} corner diminishes as the size of the source becomes larger. This seems to occur simultaneously with the construction of the long period amplitudes to the extent where only one corner frequency, possibly pertaining to ω^{-2} , is observed as is the case with the largest earthquake spectrum, viz: ROM73.

7.0.0 GENERAL CONCLUSIONS:

From our investigation of near-field earthquakes we arrive at the following conclusions:

- 1 - Local magnitude estimations indicate that earthquake size increases with range. This also seems to correlate with azimuth as we turn to face the major subduction zone between New Britain and New Ireland.
- 2 - Using reduced time record sections based on the observed S-P interval we have estimated apparent velocities for the first S-wave onset.
- 3 - From the location map and based on the available information on local surface structure and tectonics we grouped the earthquakes according to azimuth, range, and depth. The trigger directions for the assumed dislocation in each group was then deduced from this limited information.
- 4 - Based on the discussion of rupture velocities in the near-field we deduced that for each earthquake group, the best simulated record is that which, upon summation, shows the sharpest onset, maximum construction and coherency within the S-waveform.

- 5 - The individual group sums indicate the remarkable increase in fracture propagation velocity which could be related to the first conclusion.
- 6 - The spectral plots show 2 "humps" around about 8Hz and 0.5-0.8Hz. These regions may be significant in that they could be correlated with corner frequencies such as ω^{-2} and ω^{-3} .
- 7 - Based on the conception that closely spaced groups of events may be related to a larger common source we summed Groups (2), (3) and (4). We found that the best construction is obtained when a subsonic rupture propagation of 0.7M is used.
- 8 - The observed short period "hump" seems to diminish as the size of the source becomes larger. This observation is substantiated when we compare the summed spectra with the spectra of actual larger earthquakes.
- 9 - The n/\sqrt{n} concept for the construction of the long/short period ranges is distinctly observed but has not been quantified.

8.0.0 DISCUSSION:

It appears from this study that the hypothesis is generally applicable to near-field observations. Although we have not simulated a real source we have obtained an averaged source from the available data which seems to be closer in spectral content to the actual larger earthquakes. Given the available data and information, we believe that this is a significant result.

Many factors may have had a direct bearing on this result, the most obvious of which are:

- a) Insufficiency of number of input seismograms.
- b) Differences in focal mechanisms between individual events and the larger shocks.
- c) More importantly is the proximity to the fault. This factor undoubtedly influenced our results since at this short distance range, and because most events appear to originate in the crustal layers, there is not enough path attenuation to filter the high frequencies. Furthermore our magnitudes indicate that the size of these earthquakes are too small to excite periods longer than the S-wave range of frequencies. If such long periods were excited and do exist, they are not significant enough to be enhanced by the bass-lift instrument.

As we have seen the most interesting of all is the phenomenon of increase in the size of earthquakes with distance. This feature seems to correlate with the rupture speeds used to sum the 4 groups. One possible interpretation would be that as distance increases and as we gradually face the triple plate junction the stress pattern has an orientation such that the component of rupture velocity along that azimuth gets closer to the shear wave velocity of the medium. The trend of larger Mach numbers as we approach the major subduction zone may indicate that the stress generating the shocks in the vicinity of subduction is of greater magnitude and has a more definite trend with respect to the strike of the subduction zone.

CHAPTER 8
CONCLUSIONS

1.0.0 GENERAL:

During our nearly 4 years in research we have come to learn and cherish many facts. Above all that progress cannot be achieved overnight neither can a reliable result be obtained at the flick of a switch. Instead, achievement can only come through hard sweat, relentless efforts, and perseverance.

From a general degree in Geology we have - through this project - evolved a basic understanding of one of the most challenging fields in Geophysical Research. We have experienced how an idea, an approach and a method can be tested and implemented irrespective of the ultimate result. As a consequence we have gained a fundamental knowledge of how to conduct scientific research.

Through this research project we have learnt numerous methods and techniques, directly or indirectly related to seismological theory and practice. Most important of all, however, is the fact that the seismogram is the master key to almost all the information released by a seismic disturbance.

With these main conclusions in mind we move towards outlining what we have achieved thus far.

2.0.0 SPECIFIC CONCLUSIONS:

From the first part of this thesis in which we discussed the topics of data processing, experimental procedure and analysis we conclude the following:

1 - An analogue instrument was introduced, tested, and used

on real data whereby the long period content is recovered from magnetic tape recordings of short period seismograms.

This bass-lift instrument and its use had a direct bearing on the results obtained in this research since it was possible to utilize the bass-lifted traces in experimentation with the objective of constructing a larger earthquake motion from smaller earthquake records (see Chapter 2).

- 2 - The method used to construct the long period content characteristic of large earthquake motions is a simple time domain summation in which the bass-lifted traces of a selected population of smaller earthquakes were used as input.

The phasing of the input records is controlled by two parameters: apparent velocity and azimuth. It is shown in this research that this method is effective provided the appropriate parameters are used (see Chapter 3).

- 3 - To assess the resulting simulated source in the frequency domain we have approximated our data by a geometrically simple kinematic source model. The spectral signature of the transformed seismograms especially in the far-field data set, are shown to be similar in character to a "Butterworth Low-Pass Response", with a single corner frequency marking the change in trend between the static Ω_0 level and the dynamic high frequency role-off (see Chapter 4).

4 - To smooth seismic spectra we employed in our analysis (Chapter 4) a numerically stable technique known as the Cubic Spline Approximation. This method enables us to compare spectral curves more accurately than by the use of manual methods.

The major advantage of cubic spline fits is its ability in revealing aliasing at high frequencies and exhibiting unwanted frequencies below the bass-lift cutoff. The technique shows some promise as an efficient means for determining the overall shape of seismic spectra.

From the second part of our thesis in which we presented the results obtained, employing the methods and techniques developed in the first part, we can conclude the following:

5 - The Far-Field Chile Source: This study has shown that the hypothesis is applicable in the far-field (see Section 5.0.0, Chapter 6). We have been able to reconstruct not only the wave motion of a given large source but the motions of even larger sources. In this latter case, however, we were confronted with the limitation of spectral bandwidth and therefore we need to widen the lower frequency threshold to periods substantially longer than 10s.

6 - The Near-Field Rabaul Source: Our investigations in the near-field have demonstrated that the hypothesis may be applied to simulations of local shocks (see Section 7.0.0, Chapter 7). We have not been able to approximate the motion nor the spectral signature of an already existing

large earthquake, but have obtained an averaged source closer to the real spectra.

- 7 - Our results might be convincing but they lack an important and integral part which is quantification. Had such quantitative techniques been available, we would have assessed our results more accurately.
- 8 - We maintain that our technique is elementary and requires a great deal of refinements especially on the theoretical level backed up by much numerical consideration and treatment. Nevertheless, we feel that our research and the contribution made in this thesis has given some foundation for future investigations of earthquake source theory and observation.
- 9 - In this research we have utilized data from an array and a network monitoring seismic activity from two different parts of the world. We therefore, believe that we have made some use of two important projects developed through many years by the collective efforts of UK seismologists.

3.0.0 THE CONTRIBUTION OF THIS RESEARCH IN RELATION TO THE ORIGINAL PROPOSAL:

Recalling our discussion under Section 3.1.0 of Chapter 1 we stated that this research had two main objectives:

- (1) To improve the general understanding of an earthquake process.
- (2) To improve the basis of seismic zoning.

In this research we have only been able to render some contribution towards the first goal. The second objective remains unconsidered.

Regarding the better understanding of an earthquake process our research, particularly in the far-field, has revealed the following:

- 1 - Within the same focal region, i.e: belonging to a common source, large and small earthquakes are essentially similar phenomena. The major difference in spectral character, therefore, is source size.

- 2 - Based on the reasoning in (1) above, we have been able to construct from real earthquake records a larger source similar in appearance to an already existing one. This supports the original conception that a major earthquake can be modelled by a succession of a number of smaller sources triggered in an appropriate temporal and spatial sequence.

As far as the foreseen difficulties - mentioned in Chapter 1 are concerned, we have not been able to contribute to the first 2 problems more than concluding that non-linearity at the observation point and at the focal region do not seem to constitute a critical disadvantage to our methods and techniques. Evidently, at the point of observation, there will be structural and near-surface responses due to the effects of large earthquake motions but this problem enters the realm of engineering seismology and is outside the scope of the present research. Regarding the second problem of

non-linearity at the source we have come to realize that this particular point is indeed not serious since it had very little effect on our results. It follows, therefore, that within the linear portion of propagation our technique is more effective.

The problem of expected differences in fracturing mechanism between the main shock, the "foreshocks" and aftershock sequence, was not encountered. On the contrary our solutions, especially for the foreshocks indicate that they are generally identical to that of the main source.

Out of all the expected problems explained in Section 3.2.0 of Chapter 1, the fourth remains outstanding. The suggested technique of "filling-in" the focal region by synthetic interpolation would have been useful in the application of our hypothesis to near-field data. As we stated in Chapter 4, however, pursuing such a suggestion was not possible mainly because of our involvement in the search for real earthquake data.

Having established one basic aim of this research especially in the far-field, the possibilities for further work mentioned in Section 3.3.0 of Chapter 1 become positive suggestions and are well worth investigating. The first suggestion could be tied in with the second unaccomplished aim in this research, i.e: to carry out a field study in a region where a micro-zoning survey is required with the objective of establishing scientifically sound criteria upon which microzoning studies and maps could be based.

The other two suggestions - namely: using explosive sources instead of earthquakes and path reversal studies in assessing the seismic hazards of a seismically quiet area in which a potential induced source was expected - are equally plausible and certainly merit separate research efforts.

REFERENCES

Unless otherwise stated the following abbreviations are used for some frequently referred to journals or reports:

- AAPG : American Association of Petroleum Geologists, USA.
- AG : Annali di Geofisičca, Italy.
- AGU : American Geophysical Union, USA.
- AWRE : Atomic Weapons Research Establishment, UK.
- BAAS : British Association for the advancement of science, UK.
- BERI : Bulletin of the Earthquake Research Institute, Japan.
- BGSA : Bulletin of the Geological Society of America, USA.
- BMRA : Bureau of Mineral Resources of Australia, Australia.
- BSSA : Bulletin of the Seismological Society of America, USA.
- CJES : Canadian Journal of Earth Sciences, Canada.
- CJP : Canadian Journal of Physics, Canada.
- GEO : Geophysics, Society of Exploration Geophysicists, USA.
- GJRAS : Geophysical Journal of the Royal Astronomical Society, UK.
- GP : Geophysical Prospecting, Holland.
- GSU-IR : Global Seismology Unit - Internal Report, UK.
- IEEE : Institute of Electrical and Electronic Engineers, USA.
- JGR : Journal of Geophysical Research, USA.
- JPE : Journal of Physics of the Earth, Japan.
- JGSA : Journal of the Geological Society of Australia, Australia.
- NATO-ASI : NATO - Advanced Study Institute, Norway.
- NPL-NAC : National Physical Laboratory - Numerical Analysis and Computations, UK.
- PAG : Pure and Applied Geophysics, Switzerland.
- PCPS : Proceedings of the Cambridge Philosophical Society, UK.
- PDOO : Publication of the Dominion Observatory, Ottawa, Canada.

PERI : Physics of the Earth and Planetary Interiors, USA.
PRS : Proceedings of the Royal Society, UK.
PTRS : Philosophical Transactions of the Royal Society, UK.
RG : Reviews in Geophysics, AGU, USA.
RGSP : Reviews in Geophysics and Space Physics, AGU, USA.
SB-IGS : Seismological Bulletin - Institute of Geological Sciences, UK.
WDC-A : World Data Center - A, USA.
ZG : Zeitschrift für Geophysik, Germany.

- ABE, K., 1975: Reliable estimation of the seismic moment of large earthquakes. JPE, 23, 381-390.
- AKI, K., 1967: Scaling law of seismic spectrum. JGR, 72, 1217-1231.
- AKI, K., 1968a: Seismic displacements near a fault. JGR, 73, 5359-5376.
- AKI, K., 1968b: Seismicity and Seismological method. Tectonophysics, 6, 41-58.
- AKI, K., 1969: Study of earthquake sources from the seismic spectrum. PD00, 37, 190-193.
- AKI, K., 1972: Scaling law of earthquake source time function. GJRAS, 31, 3-25.
- ARCHAMBEAU, C.B., 1968: General theory of elastodynamic source fields. RGSP, 6, 241-288.
- BALAKINA, L.M., SAVARENSKY, E.F. and A.V. VVEDENSKAYA, 1961: On determination of earthquake mechanisms. Phys. Chem. Earth, 4, 211-238.
- BARAZANGI, M. and ISACKS, B.L., 1976: Spatial distribution of earthquakes and subduction of the Nasca plate beneath South America. Geology, 4, 686-692.
- BÄTH, M., 1958: The energies of seismic body waves and surface waves. In: Contributions in Geophysics, BENIOFF, EWING, HOWELL, and PRESS (Ed). Pergamon Press, 1, 1-16.
- BÄTH, M. and DUDA, S.J., 1964: Earthquake volume, fault plane area, seismic energy, strain, deformation, and related quantities. AG, 17, 353-368.

- BÄTH, M., 1974: Spectral Analysis in Geophysics Developments in Solid Earth Geophysics, 7, Elsevier, Amsterdam, 563pp.
- BEAUCHAMP, K.G., 1973: Signal Processing. Allen and Unwin, London, 547pp.
- BEN-MENACHEM, A., 1961: Radiation of seismic surface waves from finite moving sources. BSSA, 5, 401-435.
- BERROCAL, J., 1974: South American Seismotectonics from SAAS Data. Ph.D. Thesis, University of Edinburgh, 240pp.
- BIRTILL, J.W., and WHITEWAY, F.E., 1965: The application of phased arrays to the analysis of seismic body waves. PTRS, Ser. A, 258, 421-493.
- BRACEWELL, R., 1965: The Fourier Transform and Its Applications. McGraw-Hill, 381pp.
- BRADY, B.T., 1976: Dynamics of fault growth - A physical basis for aftershock sequences. PAG, 114, 727-739.
- BRUNE, J.N., 1970: Tectonic stress and the spectra of seismic shear waves from earthquakes. JGR, 75, 4997-5009.
- BRUNE, J.N., 1973: Earthquake modelling by stick-slip along pre-cut surfaces in stressed foam rubber. BSSA, 63, 2105-2119.
- BRUNE, J.N., 1976: The physics of earthquake strong motion. In seismic risk and engineering decisions, Lomnitz and Rosenblueth (Ed). Developments in Geotechnical Engineering, 15, Elsevier, Amsterdam, 141-177.

- BURRIDGE, R., 1969: The numerical solution of certain integral equations with non-integrable kernels arising in the theory of crack propagation and elastic wave diffraction. PTRS, Ser. A, 265, 353-381.
- BURRIDGE, R., 1975: The effect of sonic rupture velocity on the ratio of S to P corner frequencies. BSSA, 65, 667-676.
- BURTON, P.W. and BLAMEY, C., 1972: A computer program to determine the spectrum and dispersion characteristics of a transient signal. AWRE Report No. 048/72, 74pp.
- BURTON, P.W., 1978: The IGS file of seismic activity and its use for hazard assessment. SB-IGS, 6, 1-13.
- CAPON, J., 1971: Analysis of long period microseismic noise at NORSAR. In: Seismic Discrimination Semiannual Technical Report, M.I.T., Lincoln Laboratory, p.17.
- CHILDERS, D.G. and DURLING, A.E., 1975: Digital Filtering and Signal Processing. West Publishing Co., California, 539pp.
- COX, M.G., 1972: The numerical evaluation of B-splines. J. Inst. Maths. Applics., 10, 134-149.
- COX, M.G. and HAYES, J.G., 1975: Curve fitting: A guide and suite of algorithms for the non-specialist user. NPL-NAC Report 26, 54pp.
- CURTIS, J.W., 1973: The spatial seismicity of Papua New Guinea and the Solomon Islands. JGSA, 20, 1-20.
- DAHLEN, F.A., 1974: On the ratio of P-wave to S-wave corner frequencies for shallow earthquake sources. BSSA, 64, 1159-1180.

- DAHLMAN, O. and ISRAELSON, H., 1977: Monitoring Underground Nuclear Explosions. Elsevier, Amsterdam, 440pp.
- DeBoor, C., 1972: On calculating with B-splines. J. Approx. Theory, 6, 50-62.
- DENHAM, D., 1969: Distribution of earthquakes in the New Guinea - Solomon islands region. JGR, 74, 4290-4299.
- DOUGLAS, A., 1966: A special purpose least squares program. AWRE Report 054/66.
- DOUGLAS, A., LILWALL, R.C. and J.B. YOUNG, 1974: Computer programs for epicentre determination. AWRE Report No. 028/74, 108pp.
- DZIEWONSKI, A., BLOCH, S. and LANDISMAN, M., 1969: A technique for the analysis of transient seismic signals. BSSA, 59, 427-444.
- ESHELBY, J.D., 1957: The determination of the elastic field of an ellipsoidal inclusion and related problems. PRS, Ser. A, 241, 376-396.
- EVERINGHAM, I.B., 1974: Large earthquakes in the New Guinea - Solomon islands area, 1873-1972. Tectonophysics, 23, 323-338.
- EWING, M., JARDETZKY, W.S., and F. PRESS, 1957: Elastic waves in Layered Media. McGraw-Hill, New York, 380pp.
- FINLAYSON, D.M., CULL, J.P., WIEBENGA, W.A., FURUMOTO, A.S. and WEBB, J.P., 1972: New Britain - New Ireland crustal seismic refraction investigations 1967 and 1969. GJRS, 29, 245-253.
- FLINN, E.A., 1965: Confidence regions and error determination for seismic event location. RG, 3, 157-185.

- FREEDMAN, H., 1966: A statistical discussion of P-residuals from explosions. BSSA, 56, 677-695.
- FUCHS, K., 1975: Synthetic seismograms of PS-reflections from transition zones computed with the reflectivity method. ZG, 41, 445-462.
- GELLER, R.J., 1976: Scaling relations for earthquake source parameters and magnitude. BSSA, 66, 1501-1523.
- GENTLEMAN, W.M., 1974: Basic procedures for large sparse or weighted linear least squares problems. Appl. Statist., 23, 448-454.
- GENTLEMAN, W.M., 1975: Least squares computations by Givens transformations without square roots. J. Inst. Maths. Applics., 12, 329-336.
- GONZALEZ-FERRAN, O., 1972: Distribution, migration and tectonic control of upper cenozoic volcanism in West Antarctica and South America, in Antarctic Geology and Geophysics. Internat. Union Geol. Sci., Ser. B, 1, 173-179.
- GREEN, P.E., FROSCHE, R.A. and ROMNEY, C.F., 1965: Principles of an experimental large aperture seismic array. Proc. IEEE, 53, 1821-1833.
- GUTENBERG, B., 1945a: Amplitude of surface waves and magnitudes of shallow earthquakes. BSSA, 35, 3-12.
- GUTENBERG, B., 1945b: Amplitudes of P, PP, and S and magnitude of shallow earthquakes. BSSA, 35, 57-69.
- GUTENBERG, B., 1945c: Magnitude determination for deep-focus earthquakes. BSSA, 35, 117-130.

- GUTENBERG, B. and RICHTER, C.F., 1956a: Magnitude and energy of earthquakes. AG, 9, 1-15.
- GUTENBERG, B. and RICHTER, C.F., 1956b: Earthquake magnitude, intensity, energy, and acceleration. BSSA, 46, 105, 145.
- HANKS, T.C. and WYSS, M., 1972: The use of body-wave spectra in the determination of seismic source parameters. BSSA, 62, 561-589.
- HANSON, M.E., SANFORD, A.R. and SHAFFER, R.J., 1971: A source function for a dynamic bilateral brittle shear fracture. JGR, 76, 3375-3383.
- HARTZELL, S.H., 1978: Earthquake aftershocks as Green's functions. Geoph. Res. Letters, 5, 1-4.
- HASKELL, N., 1964: Total energy and energy spectral density of elastic wave radiation from propagating faults - I. BSSA, 54, 1811-1842.
- HASKELL, N., 1966: Total energy and energy spectral density of elastic wave radiation from propagating faults - II. BSSA, 56, 125-140.
- HASKELL, N., 1969: Elastic displacements in the near-field of a propagating fault. BSSA, 59, 865-908.
- HAUBRICH, R.A., 1968: Array design. BSSA, 58, 977-991.
- HAYES, J.G., 1974: Numerical methods for curve and surface fitting. NPL-NAC Report 50, 34pp.
- HAYES, J.G., 1978: Data-fitting Algorithms available in preparation, and in prospect, for the NAG Library. NPL-DNACS Report 5/78, 20pp.

- HERRIN, E., TUCKER, W., TAGGART, J.N., GORDON, D.W., and J.L. LOBDELL,
1968: Estimation of surface-focus P-travel times. BSSA, 58,
1273-1291.
- HERRIN, E., 1968: 1968 Seismological Tables for P-Phases. BSSA, 58,
1196-1239.
- HODGSON, J.H., 1957: The null vector as a guide to regional tectonic
patterns. PD00, 30, 369-384.
- HONDA, H., 1957: The mechanism of earthquakes. PD00, 20, 295-340.
- HOULISTON, D.J., 1975: The seismic data-processing systems of the
Institute of Geological Sciences in Edinburgh. SB-IGS, 2,
1-13.
- HOULISTON, D.J., LAUGHLIN, J., and WAUGH, G., 1976: Developments of
the seismic data-processing systems of the Institute of
Geological Sciences in Edinburgh. GSU-IR, 74, 1-21.
- ISACKS, B., and MOLNAR, P., 1971: Distribution of stresses in the
descending lithosphere from a global survey of focal mechanism
solutions of mantle earthquakes. RGSP, 9, 103-174.
- JAMES, D., 1971: Plate tectonic model for the evolution of the central
Andes. BGSA, 82, 3325-3346.
- JEFFREYS, H., 1939: Unknown Title. Mon. Not. R.A.S. Geophys. Suppl.,
4, 498-?
- JEFFREYS, H. and BULLEN, K.E., 1967: Seismological Tables. BAAS, 50pp.
- JEFFREYS, H., 1976: The Earth : its origin, history and physical
constitution. Cambridge University Press, 574pp.

- JONES, R.B., 1976: A study of the low gain component in the Rabaul Network. GSU-IR, 63, 1-4.
- JOHNSON, L.R. and McEVILLY, T.V., 1974: Near-field observations and source parameters of central California earthquakes. BSSA, 64, 1855-1886.
- JOHNSON, T., and MOLNAR, P., 1972: Focal mechanisms and plate tectonics of the Southwest Pacific. JGR, 77, 5000-5032.
- JULIAN, B.R. and ANDERSON, D.L., 1968: Travel times, apparent velocities and amplitudes of body waves. BSSA, 58, 339-366.
- JUNGELS, P.H., and FRAZIER, G.A., 1973: Finite element analysis of the residual displacement for an earthquake rupture: source parameters for the San Fernando earthquake. JGR, 78, 5062-5083.
- KAMB, B., SILVER, L.T., ABRAMS, M., CARTER, B., JORDAN, T., and MINSTER, B., 1971: Pattern of faulting and the nature of fault movement in the San Fernando earthquake. U.S. Geol. Surv. Profess. Paper, 733, 41-54.
- KANAMORI, H. and ANDERSON, D.L., 1975: Theoretical basis of some empirical relations in seismology. BSSA, 65, 1073-1095.
- KANAMORI, H., 1977a: The energy release in great earthquakes. JGR, 82, 2981-2987.
- KANAMORI, H., 1977b: Seismic and aseismic slip along subduction zones and their tectonic implications. In Island Arcs, Deep Sea Trenches and Back-Arc Basins, Maurice Ewing Ser., Vol. 1, TALWANI and PITMAN (Ed), AGU, 162-174.

- KANAMORI, H., 1978: Quantification of earthquakes. *Nature*, 271, 411-414.
- KANASEWICH, E.R., 1975: *Time Sequence Analysis in Geophysics*.
University of Alberta Press, Canada, 2nd Edition, 364pp.
- KEILIS-BOROK, V.I., 1957: The determination of earthquake mechanism using both longitudinal and transverse waves. *AG*, 10, 105-128.
- KEILIS-BOROK, V.I., 1959: On estimation of the displacement in an earthquake source and of source dimension. *AG*, 12, 205-214.
- KEITH, C.M. and CRAMPIN, S., 1977: Seismic body waves in anisotropic media : synthetic seismograms. *GJRS*, 49, 209-223.
- KELLEHER, J., 1972: Rupture zones of large South American earthquakes and some predictions. *JGR*, 77, 2087-2103.
- KELLEHER, J., SYKES, L.R. and OLIVER, J., 1973: Possible criteria for predicting earthquake locations and their applications to major plate boundaries of the Pacific and Caribbean. *JGR*, 78, 2547-2585.
- KELLY, E.J., 1964: The representation of seismic waves in frequency-wave number space. M.I.T., Lincoln Lab. Group Report, 15.
- KELLY, K.R., WARD, R.W. and TREITEL, S., 1976: Synthetic seismograms: a finite-difference approach. *GEO.*, 41, 2-27.
- KENNETT, B.L.N., 1975: The use of theoretical seismograms in elucidating the earth's structure. In *Exploitation of Seismograph Networks : Proceedings of NATO-ASI, Norway, 1974*.

- KHATTRI, K. and GIR, R., 1976: A study of the seismic signatures of sedimentation models using synthetic seismograms. GP, 24, 454-477.
- KNOPOFF, L., 1958: Energy release in earthquakes. GJRS, 1, 44-52.
- KNOPOFF, L. and GILBERT, F., 1959: Radiation from a strike-slip fault. BSSA, 49, 163-178.
- KOSTROV, B.V., 1966: Unsteady propagation of longitudinal shear cracks. Appl. Math. Mech., 30, 163-178.
- LAHSEN, A., 1976: Geothermal exploration in northern Chile - summary. In Circum-Pacific Energy and Mineral Resources. HALBOUTY, MAHER, LIAN (Ed), AAPG, MEM., 25, 170-175.
- LATTER, J.H., 1969: Possibilities for the study of seismicity in the southwest Pacific by the use of tele-metered networks of seismographs. GSU-IR, 1E, 1-39.
- LATTER, J.H., 1970: The Interdependence of Seismic and Volcanic Phenomena. PhD Thesis, Edinburgh University, 359pp.
- LAUGHLIN, J. and WAUGH, G., 1979: An instrument for recovering long period seismic data from magnetic tape records of short period seismometers. GSU-IR, 104, 1-8.
- LEHMANN, I., 1934: Unknown Title. Geodaetisk Institute, Copenhagen, Rep. 5.
- LEHMANN, I., 1961: S and the structure of the upper mantle. GJRS, 4, 124-138.

- LEHMANN, I., 1962: The travel times of the longitudinal waves of the Logan and Blanca atomic explosions and their velocities in the upper mantle. BSSA, 52, 519-526.
- LEHMANN, I., 1964: On the travel times of P as determined from nuclear explosions. BSSA, 54, 123-139.
- LEHMANN, I., 1970: The 400-km discontinuity. GJRS, 21, 359-372.
- LILWALL, R.C., 1969: The Determination of Epicentres and Seismic Travel Times. PhD Thesis, Birmingham University, 110pp.
- LOMNITZ, C., 1974: Global Tectonics and Earthquake Risk. Developments in Geotectonics, 5, Elsevier, Amsterdam, 320pp.
- LOVE, A.E.H., 1927: The Mathematical Theory of Elasticity. Cambridge University Press, 1934.
- LUH, P.C., 1977: A scheme for expressing instrumental response parametrically. BSSA, 67, 957-969.
- MACNAB, R.P., 1970: The geology of the Gazelle Peninsula, New Britain. BMRA, Record 1970/63 (unpublished).
- MADARIAGA, R., 1978: The dynamic field of Haskell's rectangular dislocation fault model. BSSA, 68, 869-887.
- MADARIAGA, R., 1976: Dynamics of an expanding circular fault. BSSA, 65, 163-182.
- MAKROPOULOS, K.C., 1979: The Statistics of Large Earthquake Magnitude and an Evaluation of Greek Seismicity. PhD Thesis, Edinburgh University, 193pp.

- MARSHALL, P.D., 1970: Aspects of spectral difference between earthquakes and underground explosions. GJRS, 20, 397-416.
- McEVILLY, T.V. and CASADAY, K.B., 1967: The earthquake sequence of September 1965 near Antioch, California. BSSA, 57, 113-124.
- MOLNAR, P., TUCKER, B.E. and BRUNE, J.N., 1973: Corner frequencies of P and S waves and models of earthquake sources. BSSA, 63, 2091-2104.
- OTSUKA, M., 1966: Azimuth and slowness anomalies of seismic waves measured on the Central California Seismographic Array. Part II, Interpretation. BSSA, 56, 655-675.
- PAGE, R., 1968: Aftershocks and microaftershocks of the great Alaskan earthquake of 1964. BSSA, 58, 1131-1168.
- PEPPIN, W.A. and SIMILA, G.W., 1976: P- and S-wave corner frequencies over low-loss paths : A discriminant for earthquake source theories? JPE, 24, 177-188.
- PRESS, F. and EWING, M., 1952: Two slow surface waves across North America. BSSA, 42, 1952, 219-228.
- RANDALL, M.J., 1973: The spectral theory of seismic sources. BSSA, 63, 1133-1144.
- REID, H.F., 1910: Mechanics of the earthquake. In : The California Earthquake of April 18, 1906, 2. Carnegie Institute of Washington, D.C. (updated in 1969).
- RICHTER, C.F., 1935: An instrumental earthquake magnitude scale. BSSA, 25, 1-32.

- RICHTER, C.F., 1958: Elementary Seismology. Freeman, San Francisco, 768pp.
- RITSEMA, A.R., 1964: Some reliable fault plane solutions. PAG, 59, 58-74.
- ROBINSON, E.A., 1967: Statistical communication and Detection : with special reference to digital data processing of radar and seismic signals. Griffin, London, 362pp.
- RUIZ, C., 1965: Geologia y yacimientos metaliferos de Chile : Santiago, Chile, Inst. Invest. Geol., 305pp.
- RYBURN, R.J., 1971: Geology : in BROOKS, J.A. (Ed). Investigations of crustal structure in the New Britain - New Ireland region, 1969: Geophysical and Geological Data. BMRA, Record 1971/131 (unpublished).
- SACKS, S. and OKADA, H., 1974: A comparison of the anelasticity structure beneath South America and Japan. PEPI, 9, 211-219.
- SANTO, T., 1969: Characteristics of seismicity in South America. BERI, 47, 635-672.
- SATO, T. and HIRASAWA, T., 1973: Body wave spectra from propagating shear cracks. JPE, 21, 415-432.
- SAVAGE, J.C., 1972: Relation of corner frequency to fault dimensions. JGR, 77, 3788-3795.
- SAVAGE, J.C., 1974: Relation between P- and S-wave corner frequencies in the seismic spectrum. BSSA, 64, 1621-1627.

- SPRENKE, K.F. and KANASEWICH, E.R., 1977: Synthetic seismograms and the response of an anisotropic attenuating medium. CJES, 14, 1062-1076.
- STARR, A.T., 1928: Slip on a crystal and rupture in a solid due to shear. PCPS, 24, 489-500.
- STAUDER, W., 1962: The focal mechanism of earthquakes. Adv. Geophys., 9, 1-76.
- STAUDER, W. and BOLLINGER, G.G., 1966: The focal mechanism of the Alaska earthquake of March 28, 1964 and of its aftershocks. JGR, 71, 5283-5296.
- STAUDER, W., 1973: Mechanism and spacial distribution of Chilean earthquakes with relation to subduction of the oceanic plate. JGR, 78, 5033-5061.
- STEKETEE, J.A., 1958: Some geophysical applications of the elasticity theory of dislocations. CJP, 36, 1168-1198.
- STONELY, R., 1937: The Mongolian earthquake of 1931, August 10. Brit. Ass. Seism. Comm., 42nd Rep., 5-6.
- SWIFT, S. and CARR, M., 1974: The segmented nature of the Chilean seismic zone. PEPI, 9, 183-191.
- THOMPSON, J.E. and FISHER, N.H., 1965: Mineral deposits of New Guinea and Papua and their tectonic setting. BMRA, Record 1965/10 (unpublished).
- TRIFUNAC, M. and BRUNE, J.N., 1970: Complexity of energy release during the Imperial Valley, California, earthquake of 1940. BSSA, 69, 137-160.

- TSUBOI, C., 1956: Earthquake energy, earthquake volume, aftershock area, and strength of the earth's crust. JPE, 4, 63-66.
- USAMI, T., 1956: Seismometrical study of Boso-oki earthquake of November, 26, 1953. Quart. J. Seismology of the Japan Meteor. Agency, 21, 3.
- UYEDA, S. and KANAMORI, H., 1979: Back-arc opening and the model of subduction. JGR, 84, 1049-1061.
- VERED, M. and BEN-MENACHEM, A., 1974: Application of synthetic seismograms to the study of low-magnitude earthquakes and crustal structure in the northern Red Sea region. BSSA, 64, 1221-1237.
- VVEDENSKAYA, A.V., 1956: The determination of displacement fields by means of dislocation theory. Izv. Akad. Nauk. S.S.S.R., Ser. Geofiz., 3, 227-284.
- WIGGINS, R.A. and HELMBERGER, D.V., 1974: Synthetic seismogram computation by expansion in generalized rays. GJRAS, 37, 73-90.
- WILLMORE, P.L., 1960: Detection of earth movements. In S.K. Runcorn (Ed), Methods and Techniques in Geophysics, 1, 230-276.
- WILLMORE, P.L. and BURTON, P.W., 1975: The U.K. approach to hazard assessment. Royal Netherlands Meteorol. Inst. Public., 153, 35-38.
- WYSS, M., and BRUNE, J.N., 1967: The Alaskan earthquake of 28 March 1964 : A complex multiple rupture. BSSA, 57, 1017-1023.

YEGULALP, T.M. and KUD, J.T., 1974: Statistical prediction of the occurrence of maximum magnitude earthquakes. BSSA, 64, 393-414.

ADDITIONAL REFERENCES

- AGGER, H.E. and CARPENTER, E.W., 1964: A crustal study in the vicinity of the Eskdalemuir Seismological Array Station. GJRS, 9, 69-83.
- ALGERMISSEN, S.T. and PERKINS, D.M., 1972: A technique for seismic zoning: general considerations and parameters. Proc. Intern. Conf. on Microzonation for Safer Construction, Research and Application, Seattle, Washington, Vol. II, 865-878.
- ALGERMISSEN, S.T., RINEHART, W.A. and STEPP, J.C., 1972: A technique for seismic zoning: economic considerations. Proc. Intern. Conf. on Microzonation for Safer Construction, Research and Application, Seattle, Washington, Vol. II, 943-957.
- BOORE, D.M., AKI, K. and TODD, T., 1971: A two-dimensional moving dislocation model for a strike-slip fault. BSSA, 61, 177-194.
- BOORE, D.M. and ZOBACK, M.D., 1974a: Near-field motions from kinematic models of propagating faults. BSSA, 64, 321-342.
- BOORE, D.M. and ZOBACK, M.D., 1974b: Two-dimensional kinematic fault modelling of the Pacoima Dam strong-motion recordings of the February 9, 1971, San Fernando earthquake. BSSA, 64, 555-570.
- BURRIDGE, R. and KNOPOFF, L., 1964: Body force equivalents for seismic dislocations. BSSA, 54, 1874-1888.
- BURTON, P.W., 1979: Seismic risk in Southern Europe through to India examined using Gumbel's third distribution of extreme values. GJRS, 59, 249-286.
- CLEARY, J.R., WRIGHT, C. and MUJIRHEAD, K.J., 1968: The effects of local structure upon measurements of the travel time gradient at the Waramunga Seismic Array. GJRS, 16, 21-29.

- CORBISHLEY, D.J., 1970: Structure under seismic arrays. GJRS, 21, 415-425.
- CORNELL, C.A., 1968: Engineering seismic risk analysis. BSSA, 68, 1583-1606.
- CRAMPIN, S., 1973: FAMG: A computer program for the location of local earthquakes recorded by large-aperture low-density seismic networks. GSU-IR, 33, 1-41.
- ESTEVA, L., and VILLAVERDE, R., 1974: Seismic risk design spectra and structural reliability. Proc. 5th World Conf. Earthq. Engng. Rome, Vol. II, 2586-2596.
- GRANT-TAYLOR, T.L., ADAMS, R.D., HATHERTON, T., MILNE, J.D.G., NORTHEY, R.D. and STEPHENSON, W.R., 1974: Microzoning for earthquake effects in Wellington, N.Z. New Zealand Dept. Scient. Indust. Res. Bull. 213, 61pp.
- JACOB, A.W.B. and NEILSON, G., 1977: Magnitude determination on LOWNET GSU-IR, 86, 1-9.
- KALLBERG, K.T., 1969: Seismic risk in Southern California. M.I.T. Report 69-31, 70pp.
- KARNIK, V. and ALGERMISSEN, S.T., 1978: Seismic zoning. In: The Assessment and Mitigation of Earthquake Risk, Paris, 1976. UNESCO Publ., 11-47.
- LILWALL, R.C., 1976: Seismicity and seismic hazards in Britain. SB-IGS, 4, 1-9.
- MARUYAMA, T., 1963: On the force equivalent dynamic elastic dislocations with reference to the earthquake mechanism. BERI, 41, 467-487.

- MERZ, M.A. and CORNELL, C.A., 1974: Aftershocks in engineering risk and analysis. Proc. 5th World Conf. Earthq. Engng., Rome, Vol. II, 2568-2571.
- MILNE, W.G. and DAVENPORT, A.G., 1965: Statistical parameters applied to seismic regionalization. Proc. 3rd World Conf. Earthq. Engng. New Zealand, Vol. III, 181-194.
- MILNE, W.G. and DAVENPORT, A.G., 1969: Distribution of earthquake risk in Canada. BSSA, 59, 729-754.
- NIAZI, M., 1966: Corrections to apparent azimuths and travel time gradients for a dipping Moho discontinuity. BSSA, 56, 491-509.
- OHSAKI, Y., 1972: Japanese microzonation methods. Proc. Intern. Conf. on Microzonation for Safer Construction, Research and Application, Seattle, Washington, Vol. I, 161-182.
- PETROVSKI, J.T., 1978: Seismic microzoning and related problems. In: The Assessment and Mitigation of Earthquake Risk, Paris, 1976, UNESCO Publ., 48-65.
- SIMON, R.B., 1969: Earthquake Interpretation. Colorado School of Mines Pub., 99p.
- VERE-JONES, D., 1973: The statistical estimation of earthquake risk. Bull. New Zealand Soc. Earthq. Engng., Sept. 1973, 122-127.
- WILLMORE, P.L. and KARNIK, V., 1970: Manual of Seismological Observatory Practice. International Seismological Center Publication, Edinburgh.

WRIGHT, C., CLEARY, J.R. and MUIRHEAD, K.J., 1974: The effect of local structure and the adjacent upper mantle on short-period P wave arrivals recorded at the Waramunga Seismic Array. GJRS, 36, 295-319.

APPENDIX (A)
LISTING OF "BEAM"

BEAM

THIS IS A BEAMFORMING PROGRAM. IT USES THE COLLATED SEISMOGRAMS PLUS A STATION OR EVENT COORDINATE FILE AS INPUT. THE APPARENT VELOCITY AND AZIMUTH RANGES AND THEIR INCREMENTS ARE INPUT INTERACTIVELY.

WRITTEN ORIGINALLY BY: C.J.FYFE (1974)

NOTE THAT "BEAM" IS SMALL ENOUGH TO BE RUN ON THE IGS PDP11/50 COMPUTER.

INTEGER DT(225),BEAM(8192),BUFEND,BUFFPOS,POS,FRAME(8),TCDEL
LOGICAL*1 FILEN(14),FILET(14),FILEX(14)

DIMENSION STLAT(15),STLONG(15),STCODE(15),DUM(15)

DOUBLE PRECISION STLAT,STLONG

DATA BEAM/8192*0/

A1=1.0/60.0

A2=A1*A1

WRITE(5,91)

91 FORMAT(' SAMPLING RATE ? ',#)

READ(5,92) ISPS

92 FORMAT(I2)

WRITE(6,705) ISPS

705 FORMAT(' SAMPLING RATE = ',I2,' SPS',/)

SPS=FLOAT(ISPS)

WRITE(5,93)

93 FORMAT(' ASSIGN STATION COORDINATE FILE ',#)

READ(5,704) (FILEX(I),I=1,14)

704 FORMAT(14A1)

CALL ASSIGN(8,FILEX,14)

WRITE(6,710) (FILEX(I),I=1,14)

710 FORMAT(' STATION COORDINATE FILE IS : ',14A1,/)

WRITE(5,90)

90 FORMAT(' ASSIGN INPUT FILE NAME ',#)

READ(5,704) (FILEN(I),I=1,14)

CALL ASSIGN(1,FILEN,14)

WRITE(6,715) (FILEN(I),I=1,14)

715 FORMAT(' FILE TO BE BEAMED IS : ',14A1,/)

WRITE(5,94)

94 FORMAT(' ASSIGN OUTPUT FILE NAME ',#)

READ(5,704) (FILET(I),I=1,14)

CALL ASSIGN(2,FILET,14)

WRITE(6,720) (FILET(I),I=1,14)

720 FORMAT(' BEAMED FILE IS : ',14A1,/)

READ(8,2) NOS

2 FORMAT(I2)

WRITE(6,102) NOS

102 FORMAT(' NO. OF ARRAY STATIONS TO BE BEAMED =',I2,/)

WRITE(6,725)

725 FORMAT(//)

WRITE(6,730)

730 FORMAT(' STATION COORDINATES',/)

WRITE(6,735)

735 FORMAT(' *****',/)

DO 3 I=1,NOS

READ(8,4) STCODE(I),I1,I2,R3,I4,I5,R6

4 FORMAT(A2,2I3,F5.1,2X,2I3,F5.1)

WRITE(6,44) STCODE(I),I1,I2,R3,I4,I5,R6

```

C
44  FORMAT(1X,A2,2I3,F5.1,2X,2I3,F5.1)
    A=FLOAT(IABS(I1))+FLOAT(I2)*A1+R3*A2
    B=FLOAT(IABS(I4))+FLOAT(I5)*A1+R6*A2
    IF(I1.LT.0) A=-A
    IF(I4.LT.0) B=-B
    STLAT(I)=A
3    STLONG(I)=B
105  WRITE(6,104)
104  FORMAT(//)
    WRITE(5,10)
10   FORMAT(10X,' SUPPLY AZIMUTH & APPARENT VELOCITY PARAMETERS',/)
    WRITE(6,103)
103  FORMAT(10X,' *****',/)
    WRITE(6,740)
740  FORMAT(10X,' AZIMUTH & APPARENT VELOCITY PARAMETERS',/)
    WRITE(6,745)
745  FORMAT(10X,' *****',/)
    WRITE(5,11)
11   FORMAT(' STARTING AZIMUTH (DEG)(F6.2) ? ',)
    READ(5,12) STAZ
12   FORMAT(F6.2)
    WRITE(6,750) STAZ
750  FORMAT(' STARTING AZIMUTH = ',F6.2,' DEG',/)
17   WRITE(5,13)
13   FORMAT(' NUMBER OF AZIMUTHS (<16) ? ',)
    READ(5,14) NAZ
14   FORMAT(I2)
    WRITE(6,755) NAZ
755  FORMAT(' NUMBER OF AZIMUTHS USED = ',I2,/)
    IF(NAZ.LT.16) GO TO 15
    WRITE(5,16)
    GO TO 17
15   IF(NAZ.EQ.1) GO TO 20
    WRITE(5,18)
18   FORMAT(' AZIMUTHAL INCREMENT (DEG)(F6.2) ? ',)
    READ(5,12) IAZ
    WRITE(6,760) IAZ
760  FORMAT(' AZIMUTHAL INCREMENT = ',F6.2,/)
20   WRITE(5,19)
19   FORMAT(' STARTING VELOCITY (KM/S)(F6.2) ? ',)
    READ(5,12) STVEL
    WRITE(6,765) STVEL
765  FORMAT(' STARTING VELOCITY = ',F6.2,' KM/S',/)
22   WRITE(5,21)
21   FORMAT(' NUMBER OF VELOCITIES (<16) ? ',)
    READ(5,14) NVEL
    WRITE(6,770) NVEL
770  FORMAT(' NUMBER OF VELOCITIES USED = ',I2,/)
    IF(NVEL.LT.16) GO TO 23
    WRITE(5,16)
16   FORMAT(' TOO MANY AZIMUTHS !!!',/)
    GO TO 22
23   NOPASS=NAZ*NVEL
    IF(NOPASS.LT.16) GO TO 100
    WRITE(5,101)
101  FORMAT(' NUMBER OF AZIM*VEL MUST BE < 16 !! ')
    GO TO 105
100  IF(NVEL.EQ.1) GO TO 25
    WRITE(5,24)
24   FORMAT(' VELOCITY INCREMENT (KM/S)(F6.2) ? ',)
    READ(5,12) DVEL
    WRITE(6,775) DVEL
775  FORMAT(' VELOCITY INCREMENT = ',F6.2,/)
C

```

```

C
25      PI=3.14159265/180.0
        STAZ=STAZ*PI
        DAZ=DAZ*PI
        WRITE(6,197)
197     FORMAT(10X,' CALCULATIONS & RESULTS',/)
        WRITE(6,198)
198     FORMAT(10X,' *****',/)
        WRITE(6,200) STCODE(1)
200     FORMAT(' DISTANCE AND AZIMUTH FROM STATION ',A2,' IS: ')
        WRITE(6,199)
199     FORMAT(' *****',/)
        DO 32 I=2,NOS
        N=0
        CALL DANDA(STLAT(I),STLONG(I),STLAT(1),STLONG(1),D,A)
        AZ=A/PI
        WRITE(6,201) STCODE(I),D,AZ
201     FORMAT(1X,' STATION : ',A2,5X,F6.2,' KM',5X,F6.2,' DEG',/)
        DO 32 J=1,NAZ
        DO 32 K=1,NVEL
        N=N+1
        DT((I-1)*NOPASS+N)=IFIX(D*COS(STAZ+DAZ*FLOAT(J-1)-A)*
1SPS/(STVEL+DVEL*FLOAT(K-1)))
32      CONTINUE
        DO 33 I=1,NOPASS
33      DT(I)=0
        WRITE(6,202)
202     FORMAT(' TABLE OF DELAYS')
        WRITE(6,203)
203     FORMAT(' *****',/)
C      FIND MINIMUM DELAY
        MIN=0
        DO 34 I=1,NOS
        WRITE(6,301) (DT((I-1)*NOPASS+J),J=1,NOPASS)
301     FORMAT(20I5)
        DO 34 J=1,NOPASS
34      IF(DT((I-1)*NOPASS+J).LT.MIN) MIN=DT((I-1)*NOPASS+J)
C      MAKE DELAY TABLE POSITIVE
        WRITE(6,500) MIN
500     FORMAT(' MINIMUM VALUE = ',I4)
        WRITE(6,501)
501     FORMAT(' *****',/)
        DO 36 I=1,NOS
        DO 35 J=1,NOPASS
35      DT((I-1)*NOPASS+J)=DT((I-1)*NOPASS+J)-MIN
36      WRITE(6,301) (DT((I-1)*NOPASS+J),J=1,NOPASS)
        CALL CLOSE(6)
C      BEAMFORMING - PRODUCE BEAM AND WRITE IN OUTPUT FILE
        NOCH=NOS+1
        NOTR=NOPASS+1
        BUFEND=(8192/NOTR)*NOTR
        BUFPOS=1
        TCDEL=DT(1)*NOTR
50      READ(1,51,END=60) (FRAME(I),I=1,NOCH)
51      FORMAT(1X,20I6)
        POS=BUFPOS+TCDEL
        IF(POS.GT.BUFEND) POS=POS-BUFEND
        BEAM(POS)=FRAME(1)
        DO 52 I=1,NOS
        DO 52 J=1,NOPASS
        POS=BUFPOS+J+NOTR*DT((I-1)*NOPASS+J)
        IF(POS.GT.BUFEND) POS=POS-BUFEND
52      BEAM(POS)=BEAM(POS)+FRAME(I+1)
C
C

```

```

53 WRITE(2,53) (BEAM(BUFFOS+I),I=0,NOPASS)
   FORMAT(1X,20I6)
54 DO 54 I=0,NOPASS
   BEAM(BUFFOS+I)=0
   BUFFOS=BUFFOS+NOTR
   IF(BUFFOS.GT.BUFEND) BUFFOS=1
   GO TO 50
60 ENDFILE 2
   WRITE(5,59)
59   FORMAT(//)
   WRITE(5,61)
61   FORMAT(' BEAMFORMING COMPLETED !!!!!',/)
   WRITE(5,62)
62   FORMAT(' *****',///)
   STOP
   END

C
SUBROUTINE DANDA(LAT1,LONG1,LAT2,LONG2,DIST,AZ)
DOUBLE PRECISION LAT1,LONG1,LAT2,LONG2,LA1,L01,LA2
ONE=1.0
PI=3.14159265/180.0
LA1=LAT1*PI
LA2=LAT2*PI
L01=(LONG1-LONG2)*PI
LA1=ARCTAN(ONE,TAN(LA1))*0.993277)
LA2=ARCTAN(ONE,TAN(LA2))*0.993277)
W=DSIN(LA2)*DSIN(LA1)+DCOS(LA1)*DCOS(LA2)*DCOS(L01)
X=0.0
IF(ABS(W).LT.1.0) X=DSQRT(1-W*W)
DIST=ARCTAN(W,X)*6371.0
Y=(DSIN(LA1)-DSIN(LA2)*W)/(DCOS(LA2)*X)
Z=DCOS(LA1)*DSIN(L01)/X
AZ=ARCTAN(Y,Z)
IF(AZ.LT.0.0) AZ=AZ+2*3.14159265
RETURN
1  AZ=0.0
   RETURN
   END

C
FUNCTION ARCTAN(X,Y)
Z=Y/X
A=ABS(DATAN(Z))
IF(Z.LT.0.0) A=ABS(-DATAN(-Z))
IF(X.LE.0.0) GO TO 2
IF(Y.LE.0.0) GO TO 5
6  ARCTAN=A
   RETURN
5  ARCTAN=-A
   RETURN
2  IF(Y.GT.0.0) GO TO 4
3  ARCTAN=-3.14159265+A
   RETURN
4  ARCTAN=3.14159265-A
   RETURN
   END

C
FUNCTION TAN(X)
TAN=DSIN(X)/DCOS(X)
RETURN
END

```

APPENDIX (B)
LISTING OF "CUFIT"

The following description of routine E02BAF and E02BBF is taken from the INAG LIBRARY DOCUMENTATIONS : NAGFLIB : 1345/041356/0 : MK5 : 1976, Chapter E02 - Curve and Surface Fitting :

B.1 : SUBROUTINE - E02BAF:

This subroutine determines a least-squares cubic-spline approximation $S(X)$ to the set of data points $(X(R), Y(R))$ with weights $W(R)$ where $R = 1, 2, \dots, M$. The value of $NCAP7 = NCAP + 7$, where $NCAP$ is the number of intervals ($1 > K(I)$), and the values of the knots $K(5), K(6), \dots, K(NCAP+3)$, interior to the data interval, are prescribed by the user.

$S(X)$ has the property that it minimizes SS , the sum of the squares of the weighted residuals $EPS(R)$ ($R = 1, 2, \dots, M$), where:

$$EPS(R) = W(R) \times (S(X(R)) - Y(R))$$

The routine produces the minimizing value of SS and the coefficients $C(1), C(2), \dots, C(NCAP+3)$, in its B-spline representation.

B.2 : SUBROUTINE E02BBF:

This subroutine evaluates the cubic spline $S(X)$ at a prescribed argument X from its augmented knot set $K(I)$ and from the coefficients $C(I)$ obtained in routine E02BAF. The representation is known as the B-spline where:

$$S(X) = C(1)XN1(X) + C(2)XN2(X) + \dots + C(2)XN2(X)$$

here $2 = NCAP+3$ and $NI(X)$ denotes the normalized B-spline of degree 3 defined upon $K(I), K(I+1), K(I+2), K(I+3)$ and $K(I+4)$.

The prescribed argument X must satisfy:

$$K(4) < X < K(\text{NCAP}+4)$$

The method of evaluation is based on a scheme which involves taking repeated convex combinations of the B-spline coefficients. This scheme is unconditionally stable. (Cox, 1972; DeBoor, 1972).

B.3 : KNOTS:

Multiple knots are permitted provided their multiplying does not exceed 4, i.e. the set of knots must satisfy:

$$K(I) < K(I+4) \quad (I = 1, 2, \dots, \text{NCAP}+3)$$

At $K(I) = 1$, $S(X)$, $S'(X)$ and $S''(X)$ are continuous; At $K(I) = 2$, $S(X)$ and $S'(X)$ are continuous; At $K(I) = 3$, $S(X)$ is continuous only and at $K(I) = 4$, $S(X)$ is generally discontinuous.

In order to define the full set of B-splines required, 8 additional knots: $K(1)$, $K(2)$, $K(3)$, $K(4)$, $K(\text{NCAP}+4)$, $K(\text{NCAP}+5)$, $K(\text{NCAP}+6)$, and $K(\text{NCAP}+7)$ are inserted automatically by routine E02BAF. The first 4 are set equal to the smallest $X(R)$ and the last 4 to the largest $X(R)$.

B.4 : CUFIT: ... (Listing next page).

CUFIT

THIS IS A CURVE FITTING PROGRAM. IT USES
TWO NAG LIBRARY SUBROUTINES: E02BAF & E02BBF
E02BAF COMPUTES A WEIGHTED LEAST SQUARES APPROX.
TO AN ARBITRARY SET OF DATA POINTS BY A CUBIC
SPLINE WITH KNOTS PRESCRIBED BY THE USER.
E02BBF EVALUATES A CUBIC SPLINE FROM ITS B-SPLINE
REPRESENTATION.
THE INPUT IS AN OUTPUT FILE OF SPECTRAL
COORDINATES FROM 'TSAP'.

REF: NAGFLIB:1354/0;MK5:MARCH 1976
CHAPTER E02 'CURVE AND SURFACE FITTING'

NOTE THAT ERCLIB.NAGFLIB MUST BE APPENDED
TO GAIN ACCESS TO THESE SUBROUTINES. BECAUSE OF THIS
AND THE SIZE OF ARRAYS 'CUFIT' MUST BE RUN ON THE
LARGE CORE ERCC ICL 4-75 COMPUTERS.

```
COMMON/GRFF/TITLE(20),XMAX,XMIN,YMAX,YMIN,INDX,INDY,IND,
1          IDOT,ANSTR1,IF,XLIMIT,YLIMIT,SCALX,SCALY
INTEGER I,M,NCAP,IWGHT,NCAP2,NCAP3,NCAP7,J,
1IFAIL,J2,M2,R,R2
REAL*8 X(2048),Y(2048),W(2048),K(20),W1(2048),
1W2(4,20),C(20),SS,XARG,FIT(2048),RES
REAL*8 TITLE,BTITLE(20),BLANK,DATE,MIDFIT(2048)
REAL*4 FREQ(2048),AMP(2048),ATITLE(10)
LOGICAL MIDPT
DATA BTITLE/'          FREQUENCY (HZ)  A.S.D (MICRONS)      CUBIC SPL
1LINE FIT TO SEISMIC SPECTRUM.
2'/
```

```
CALL PLOTS('K.J.FAHMI-MURCHSEIS',20,70)
CALL FACTOR(0.703)
```

```
READ(5,99) ATITLE
WRITE(6,98) ATITLE
99 FORMAT(10A4)
98 FORMAT(///10X,10A4)
20 READ(5,97) M
97 FORMAT(2I4)
IF(M.LE.0.OR.M.GT.2048) CALL EXIT
READ(5,97) NCAP,IWGHT
NCAP2=NCAP+2
NCAP3=NCAP+3
NCAP7=NCAP+7
IF(NCAP.EQ.1) GO TO 40
READ(5,96) (K(J),J=5,NCAP3)
96 FORMAT(F6.3)
40 DO 10 R=1,M
IF(IWGHT.NE.1) GO TO 60
READ(5,95) X(R),Y(R)
95 FORMAT(3E15.7)
W(R)=1.0
GO TO 10
60 READ(5,95) X(R),Y(R),W(R)
```



```

10 CONTINUE
   WRITE(6,93) M
93  FORMAT(//10X,'CUBIC SPLINE FIT TO SEISMIC SPECTRUM'/
1 // ' NO. OF DATA POINTS USED IN CALCULATION= ',I4)
   WRITE(6,92) NCAF
92  FORMAT(' NO. OF INTERVALS (1+NO. OF KNOTS) = ',I4)
   IF(IWGHT.NE.1) GO TO 100
   WRITE(6,91)
91  FORMAT(' UNIT WEIGHTING FACTORS')
   GO TO 120
100 WRITE(6,90)
90  FORMAT(' USER SUPPLIED WEIGHTING FACTORS')
120 IF(NCAF.EQ.1) GO TO 140
   WRITE(6,89)
89  FORMAT(//4X,'J',10X,'KNOT K(J)')
   WRITE(6,88) (J,K(J),J=5,NCAF/3)
88  FORMAT(1X,I4,E20.5)
140 IF(IWGHT.NE.1) GO TO 160
   WRITE(6,87)
87  FORMAT(//4X,'R',12X,'X(R)',16X,'Y(R)')
   GO TO 180
160 WRITE(6,86)
86  FORMAT(//4X,'R',12X,'X(R)',16X,'Y(R)',
1      8X,'WEIGHT W(R)')
180 DO 220 R=1,M
   IF(IWGHT.NE.1) GO TO 200
   WRITE(6,85) R,X(R),Y(R)
   GO TO 220
200 WRITE(6,85) R,X(R),Y(R),W(R)
85  FORMAT(1X,I4,3E20.5)
220 CONTINUE
   IFAIL=1
   CALL E02BAF(M,NCAF/7,X,Y,W,K,W1,W2,C,SS,IFAIL)
   IF(IFAIL.NE.0) GO TO 360
   WRITE(6,84)
84  FORMAT(//8X,'RESULTS',///,3X,'J',10X,'KNOTS K(J+2)',
14X,' B-SPLINE COEFF C(J)')
   J=1
   WRITE(6,83) J,C(1)
83  FORMAT(1X,I4,20X,E20.5)
   DO 240 J=2,NCAF/2
   J2=J+2
   WRITE(6,85) J,K(J2),C(J)
240 CONTINUE
   WRITE(6,83) NCAF/3,C(NCAF/3)
   WRITE(6,82) SS
82  FORMAT(//8X,'RESIDUAL SUM OF SQUARES= ',E15.7,///'CUBIC
1 SPLINE APPROXIMATION AND RESIDUALS',//3X,'R',11X,
2'ABSCISSA',9X,'APPROXIMATION',9X,'RESIDUAL')
   MIDPT= .FALSE.
   M2=2*M-1
   R=0
   DO 340 R2=1,M2
   IF(.NOT.MIDPT) GO TO 280
   XARG=0.5*(X(R)+X(R+1))
   IFAIL=1
   CALL E02BBF(NCAF/7,K,C,XARG,MIDFIT(R),IFAIL)
   IF(IFAIL.NE.0) GO TO 260
   WRITE(6,81) XARG,MIDFIT(R)
81  FORMAT(5X,2E20.5)
   GO TO 320
260 WRITE(6,80) XARG
80  FORMAT(5X,E20.5,'ARGUMENT OUTSIDE RANGE')

```

```

      GO TO 999
280  R=R+1
      IFAIL=1
      CALL E02BBF(NCAP7,K,C,X(R),FIT(R),IFAIL)
      IF(IFAIL.NE.0) GO TO 300
      RES=FIT(R)-Y(R)
      WRITE(6,85) R,X(R),FIT(R),RES
C
      GO TO 320
300  WRITE(6,79) R,XARG
      GO TO 999
320  MIDPT=.NOT.MIDPT
340  CONTINUE
      YMIN=0.0
      YMAX=4.0
      XMIN=-2.0
      XMAX=2.0
      INDX=1
      INDY=1
      IND=1
      ANSTRI=1.0
      IDOT=-1
      ANSTR1=2.0
      IF=1
      DO 1 I=1,20
        TITLE(I)=BTITLE(I)
1     CONTINUE
      DO 2 R=1,M
        FREQ(R)=X(R)
        AMP(R)=FIT(R)
        WRITE(7,3) FREQ(R),AMP(R)
3     FORMAT(2E15,7)
2     CONTINUE
      CALL FACTOR(1.0)
      CALL CUGRF(FREQ,AMP,M)
      CALL SYMBOL(2,3,0.5,0.10,ATITLE,0.0,40)
      GO TO 990
360  GO TO (380,400,420,440,460),IFAIL
380  WRITE(6,78)
      GO TO 999
400  WRITE(6,77)
      GO TO 999
420  WRITE(6,76)
      GO TO 999
440  WRITE(6,75)
      GO TO 999
460  WRITE(6,74)
      GO TO 999
79  FORMAT(1X,I3,E20.5,'ARGUMENT OUTSIDE RANGE')
78  FORMAT(/8X,'KNOTS DISORDERED OR NOT INTERIOR TO DATA INTERVAL')
77  FORMAT(/8X,'NON-POSITIVE WEIGHT')
76  FORMAT(/8X,'DISORDERED VALUES OF THE INDEPENDANT VARIABLE')
75  FORMAT(/8X,'TOO MANY KNOTS FOR NO. OF DISTINCT VALUES
1 OF THE INDEPENDENT VARIABLE')
74  FORMAT(/8X,'NO UNIQUE SOLUTION SINCE SCHOENBERG-WHITNEY
1 CONDITIONS NOT SATISFIED')
990  WRITE(6,73)
73  FORMAT(///10X,'SUCCESSFUL CUBIC SPLINE EVALUATION')
      CALL PLOT(0.0,0.0,999)
999  END

```

C
C
C
C
C

SUBROUTINE CUGRF(X,Y,N)

SAME AS CARGRF OF TSAP

SINGLE PRECISION VERSION
FROM THE CALL CARGRF(X,Y,N) THIS PACKAGE PLOTS N POINTS
THE CARTESIAN CO-ORDINATES OF THE ITH POINT BEING SPECIFIED AS
X(I),Y(I)

THE OPTIONS ARE SET BY USING THE COMMON -

COMMON /GRFF/ TITLE(20), XMAX, XMIN, YMAX, YMIN, INDX, INDY, IND,
IDOT, ANSTR1, IF, XLIMIT, YLIMIT, SCALX, SCALY

THE TITLE ARRAY CARRIES INFORMATION FOR ANNOTATING THE OUTPUT
GRAPH. THIS ARRAY MUST BE SET UP AS FOLLOWS -

TITLE(1) -)
)CONTAINS 24 HOLLERITH CHARACTERS GIVING THE UNITS
TITLE(3) -)OF THE ABSCISSAE

TITLE(4))CONTAINS 16 HOLLERITH CHARACTERS GIVING THE UNITS
TITLE(5))OF THE ORDINATE

TITLE(6) -)
)CONTAINS 80 HOLLERITH CHARACTERS GIVING A TITLE TO
)THE GRAPH
TITLE(15) -)

TITLE(16) -CONTAINS 8 HOLLERITH CHARACTERS GIVING DATE OF
 PROCESSING

TITLE(17) -CONTAINS 8 HOLLERITH CHARACTERS GIVING TIME OF
 PROCESSING

TITLE(18) -)
)UNUSED

TITLE(20) -)

XMAX)SET BOTH EQUAL IF PROGRAM TO CHOOSE THE ABSCISSAE
XMIN)SCALE. OTHERWISE SET TO CHOSEN LIMITS OF ABSCISSAE SCALE
YMAX)SET BOTH EQUAL IF PROGRAM TO CHOOSE THE ORDINATE SCALE
YMIN)OTHERWISE SET TO CHOSEN VALUES OF ORDINATE SCALE

INDX IS AN INDICATOR FOR PLOTTING THE ABSCISSAE ON A LOG SCALE
INDX=1 ABSCISSAE ON LINEAR SCALE
INDX=2 ABSCISSAE ON LOG SCALE

INDY IS A SIMILAR INDICATOR FOR THE ORDINATE SCALE

N.B. CONTENTS OF ARRAYS ARE MODIFIED USING LOG SCALE

IND IS AN INDICATOR FOR CONTROLLING FRAME CALLS -
IND=1 CARGRF CALLS ADVFLM AND PLOTS ON A NEW FRAME
 =2 CARGRF PLOTS ON THE CURRENT FRAME

IDOT IS THE CODE FOR THE PLOTTING SYMBOL

ANSTR1 INDICATES WHETHER THE PLOTTED POINTS HAVE TO BE JOINED UP
ANSTR1=1. POINTS NOT JOINED
 =2. POINTS JOINED

```
COMMON/GRFF/ TITLE(20),XMAX,XMIN,YMAX,YMIN,INDX,INDY,IND,  
IIDOT,ANSTR1,IF
```

C

```
DIMENSION X(N), Y(N)  
DIMENSION ARRAY(4)  
DIMENSION IORD(5),IABSC(7)  
DIMENSION IORD(4),IABSC(6),ISUBT(20)  
REAL*8 TITLE  
REAL*4 INSTR1,JOIN/4HJOIN/,BLANK/4H /  
DATA ILOG/4HLOG /,IBLANK/4H /  
DATA YFRAME/2.0/  
DATA FRAME/0.0/
```

C

C

C

C

C

C

C

C

```
THE ABOVE TWO STATEMENTS CAUSE THE AMPLITUDE SPECTRUM PLOT  
TO BE PLOTTED IMMEDIATELY BELOW THE SEISMOGRAM. TO RETURN  
TO THE ORIGINAL DISTRIBUTION OF PLOTS REMOVE THE "C"  
FROM THE NEXT TWO STATEMENTS.
```

```
DATA YFRAME/-8.0/  
DATA FRAME/-10.0/  
EQUIVALENCE(TITLE(1),IABSC(1))  
EQUIVALENCE(TITLE(4),IORD(1))  
EQUIVALENCE(TITLE(6),ISUBT(1))
```

C

C

```
IF(IND.NE.2)IND=1  
IF(INDX.NE.2)INDX=1  
IF(INDY.NE.2)INDY=1  
INSTR1=JOIN  
IF(ANSTR1.EQ.1.)INSTR1=BLANK
```

C

C

C

```
LOGARITHMIC X(I) AND Y(I) UP TO N.
```

```
GO TO (30,10),INDX  
10 POSXT=PPMIN(X,N)*0.8  
DO 20 I=1,N  
IF(X(I).LT.POSXT)X(I)=POSXT  
X(I)=ALOG10(X(I))  
20 CONTINUE  
30 GO TO (60,40),INDY  
40 POSYT=PPMIN(Y,N)*0.8  
DO 50 I=1,N  
IF(Y(I).LT.POSYT)Y(I)=POSYT  
Y(I)=ALOG10(Y(I))  
50 CONTINUE
```

C

C

C

C

C

```
60 GO TO (100,200),IND
```

```
LINEAR X(I) AND Y(I).
```

```
100 IF(XMAX-XMIN)110,120,110  
110 XMX=XMAX  
XMN=XMIN  
GO TO 130  
120 CALL AAMAXX(X,N,XMX)  
CALL AAMIN(X,N,XMN)  
130 IF(YMAX-YMIN)140,150,140  
140 YMX=YMAX  
YMN=YMIN  
GO TO 160  
150 CALL AAMAXX(Y,N,YMX)  
CALL AAMIN(Y,N,YMN)
```

C

C

C

```

        IF (YFRAME.GT.14.0)YFRAME=2.0
        IF(YFRAME.LT.7.0)FRAME=FRAME+10.0
C SCALE X AXIS
C
200 ARRAY(1)=XMX
    ARRAY(2)=XMN
    CALL SCALE(ARRAY,4.0,2,1)
    XSTART=ARRAY(3)
    SCALX=1.0/ARRAY(4)
C SCALE Y AXIS
C
    ARRAY(1)=YMX
    ARRAY(2)=YMN
    CALL SCALE(ARRAY,4.0,2,1)
    YSTART=ARRAY(3)
    SCALY=1.0/ARRAY(4)
C*
C
C PLOT THE POINTS
C
    XLIM=FRAME+2.0-XSTART*SCALX
    YLIM=YFRAME-YSTART*SCALY
    XPLOT=XLIM+X(2)*SCALX
    YPLOT=YLIM+Y(2)*SCALY
    IF(IDOT.EQ.-1)GO TO 210
    CALL SYMBOL(XPLOT,YPLOT,0.1,IDOT,0.0,-1)
    NCHAR=-1
    GO TO 211
210 CALL PLOT(XPLOT,YPLOT,3)
    NCHAR=3
211 IF(INSTR1.EQ.JOIN)NCHAR=2
    DO 230 I=3,N
    XPLOT=XLIM+X(I)*SCALX
    YPLOT=YLIM+Y(I)*SCALY
    IF(IDOT.EQ.-1)GO TO 212
    NCHAR=-NCHAR
    CALL SYMBOL(XPLOT,YPLOT,0.1,IDOT,0.0,NCHAR)
    GO TO 230
212 CALL PLOT(XPLOT,YPLOT,NCHAR)
230 CONTINUE
C
C PLOT THE AXES
C
    GO TO (300,400),IND
300 CONTINUE
    IIORD(1)=IBLANK
C IF(INDY.EQ.2)IIORD(1)=ILOG
    IF(INDY.EQ.1) IIORD(1)=ILOG
    DO 70 I=2,5
    IIORD(I)=IORD(I-1)
70 CONTINUE
    IIABSC(1)=IBLANK
    IIABSC(2)=IBLANK
C IF(INDX.EQ.2)IIABSC(1)=ILOG
    IF(INDX.EQ.1)IIABSC(3)=ILOG
    DO 80 I=4,7
    IIABSC(I)=IABSC(I-1)
80 CONTINUE
    YAX=YFRAME
    XAX=FRAME+2.0
    CALL PLOT(XAX,YAX,3)
    YAX=YFRAME+1.0
    CALL PLOT(XAX,YAX,2)
C
C

```

C

```
START=YSTART+STEP
CALL AXIS(XAX,YAX,IIORD,20,4.0,90.0,START,STEP)
YAX=YFRAME
START=XSTART
STEP=1.0/SCALX
CALL AXIS(XAX,YAX,IIABSC,-28,4.0,0.0,START,STEP)
C PLOT THE SUBTITLE
YAX=YFRAME-1.0
XAX=FRAME+2.0
CALL SYMBOL(XAX,YAX,0.1,ISUBT,0.0,80)
400 RETURN
END
```

C

```
FUNCTION PPMIN (X,N)
```

C

```
C FINDS MINIMUM POSITIVE VALUE OF ARRAY X
DIMENSION X(N)
```

```
DO 1 KQ=1,N
IF(X(KQ).LE.0.0)GO TO 1
GO TO 5
1 CONTINUE
PPMIN=1.25
GO TO 6
5 KP=KQ
2 IF(KQ-N)3,4,4
3 KQ=KQ+1
IF(X(KQ).LE.0.0)GO TO 2
IF(X(KP)-X(KQ))2,5,5
4 PPMIN=X(KP)
6 RETURN
END
SUBROUTINE AAMAXX (X,N,XMAX)
```

C

```
C FINDS MAXIMUM VALUE OF ARRAY X
DIMENSION X(N)
```

```
KQ = 1
2 KP = KQ
5 IF(KQ -N)3,4,4
3 KQ = KQ + 1
IF(X(KP) - X(KQ))2,5,5
4 XMAX = X(KP)
RETURN
END
SUBROUTINE AAMIN (X,N,XMIN)
```

C

```
C FINDS MINIMUM VALUE OF ARRAY X
DIMENSION X(N)
```

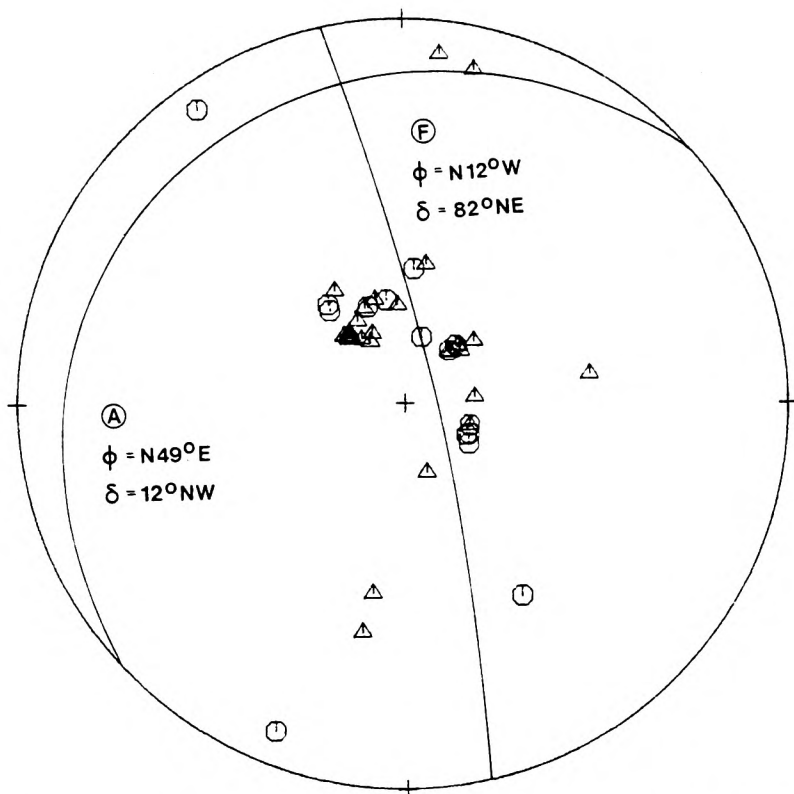
```
KQ = 1
5 KP = KQ
2 IF(KQ-N)3,4,4
3 KQ = KQ + 1
IF(X(KP) - X(KQ))2,5,5
4 XMIN = X(KP)
RETURN
END
```

APPENDIX (C)

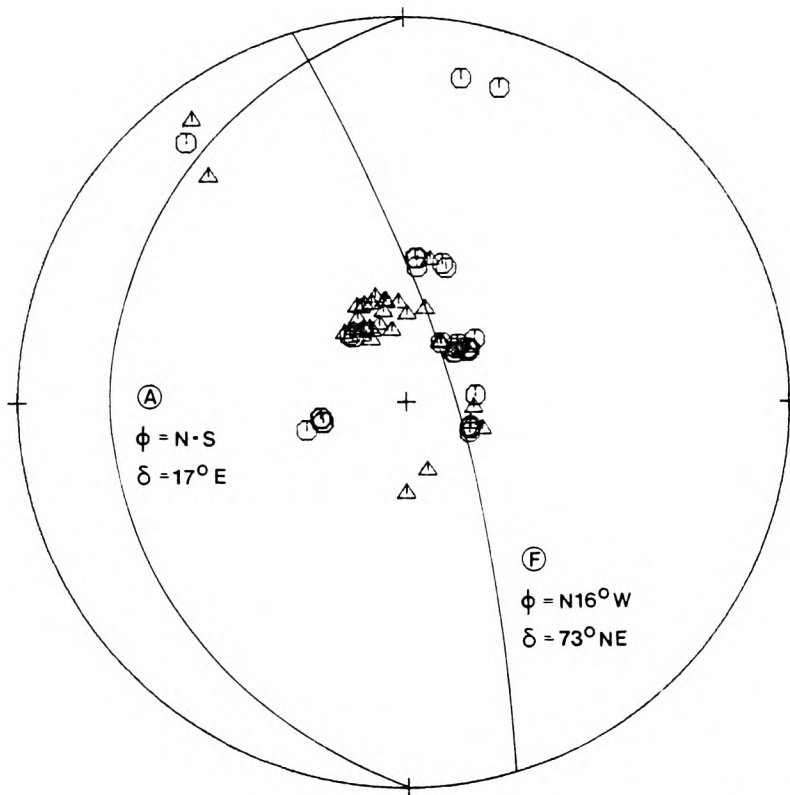
FOCAL MECHANISMS

OF

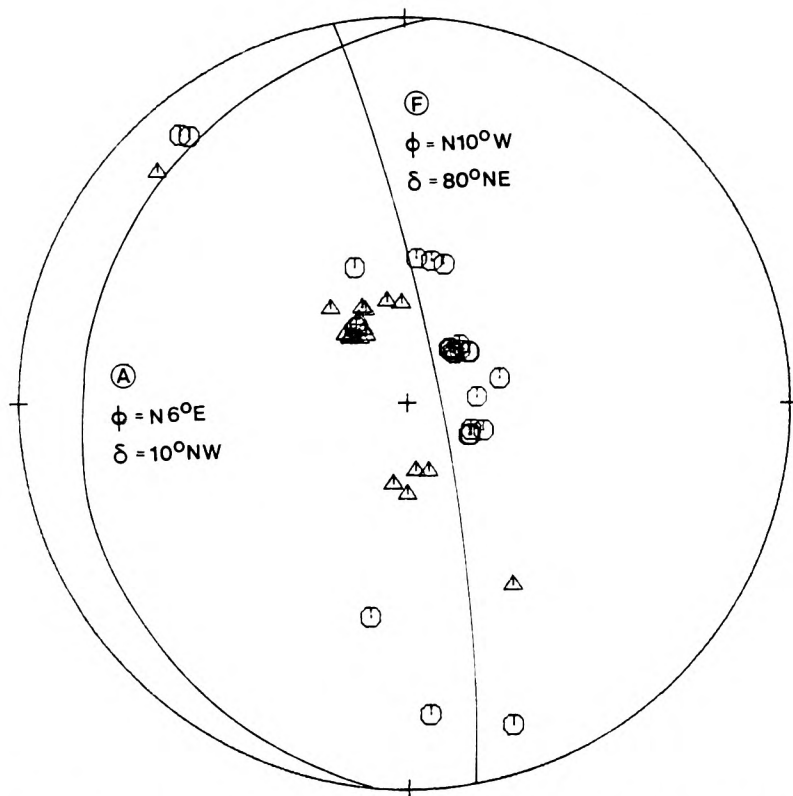
THE CHILE EARTHQUAKES



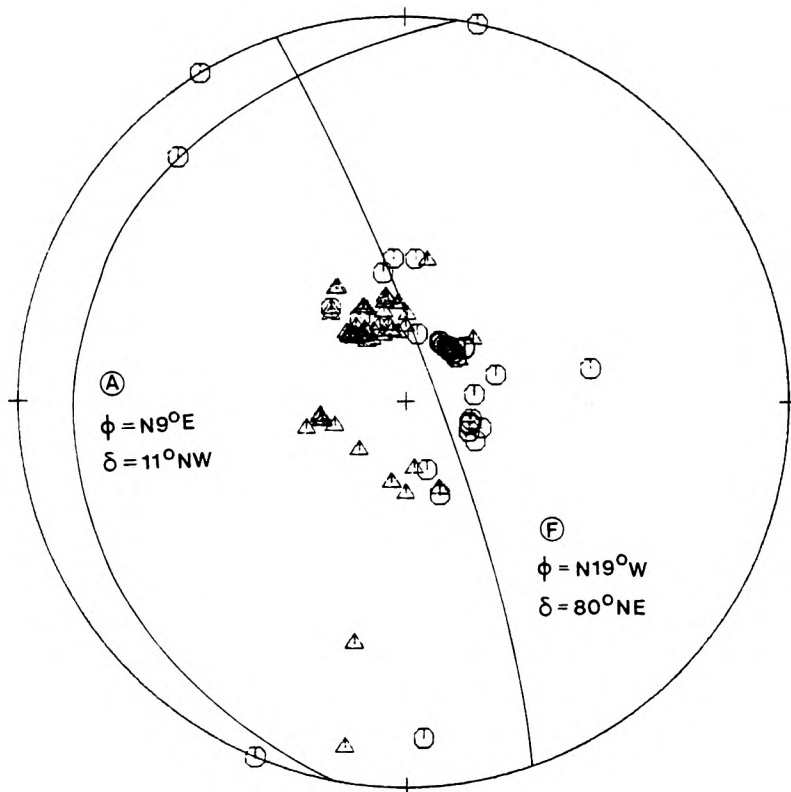
CB00A 10/10/72 20.12S 68.88W MB5.5 H103
 P-FIRST MOTION (47 OBS/ZSP LOWER HEMI)
 COMPRESSION (UP) = ⊙
 DILATATION (DOWN) = △



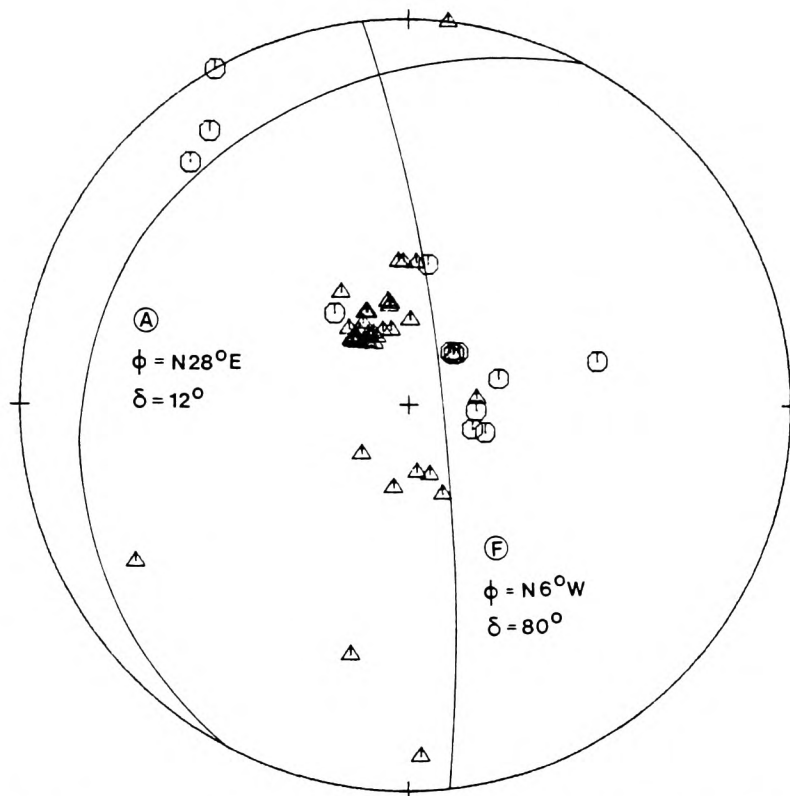
CB00B 12/05/74 19.57S 69.05W MB5.6 H107
 P-FIRST MOTION (70 OBS/SPZ LOWER HEMI)
 COMPRESSION (UP) = \odot
 DILATATION (DOWN) = \triangle



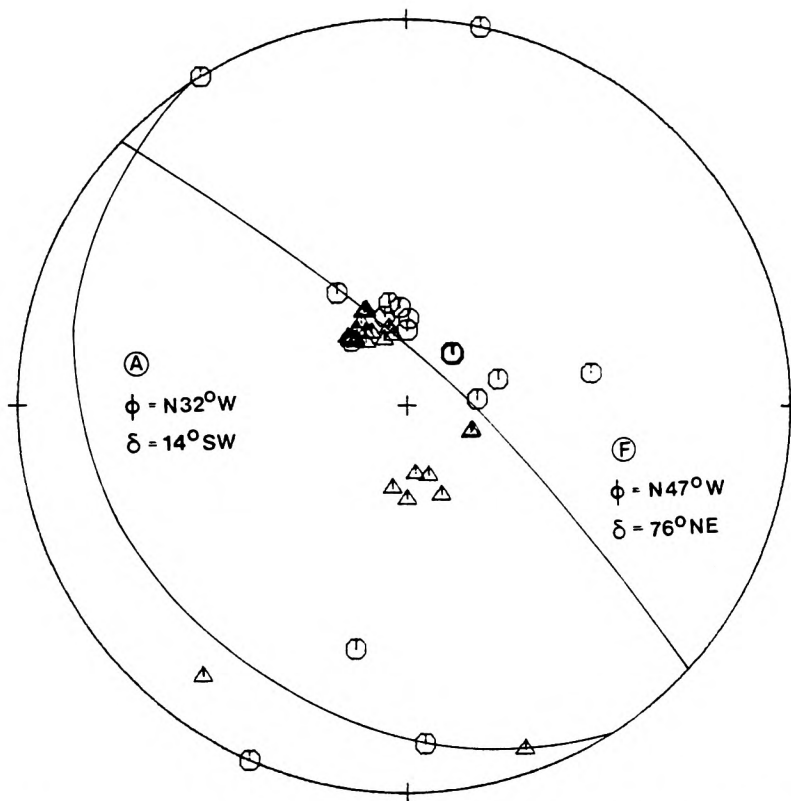
CB00C 25/08/75 19.26S 69.15W MB5.7 H101
 P-FIRST MOTION (48 OBS/SPZ LOWER HEMI)
 COMPRESSION (UP) = \odot
 DILATATION (DOWN) = \triangle



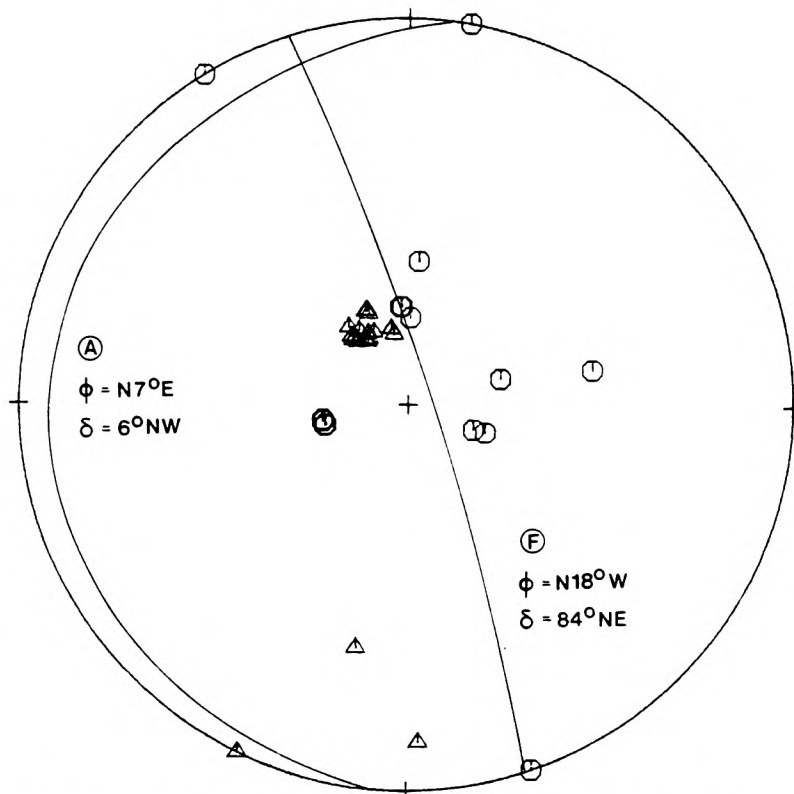
CB001 30/11/76 20.52S 68.93W MB6.5 H70
 P-FIRST MOTION (116 OBS/SPZ LOWER HEMI)
 COMPRESSION (UP) = \odot
 DILATATION (DOWN) = \triangle



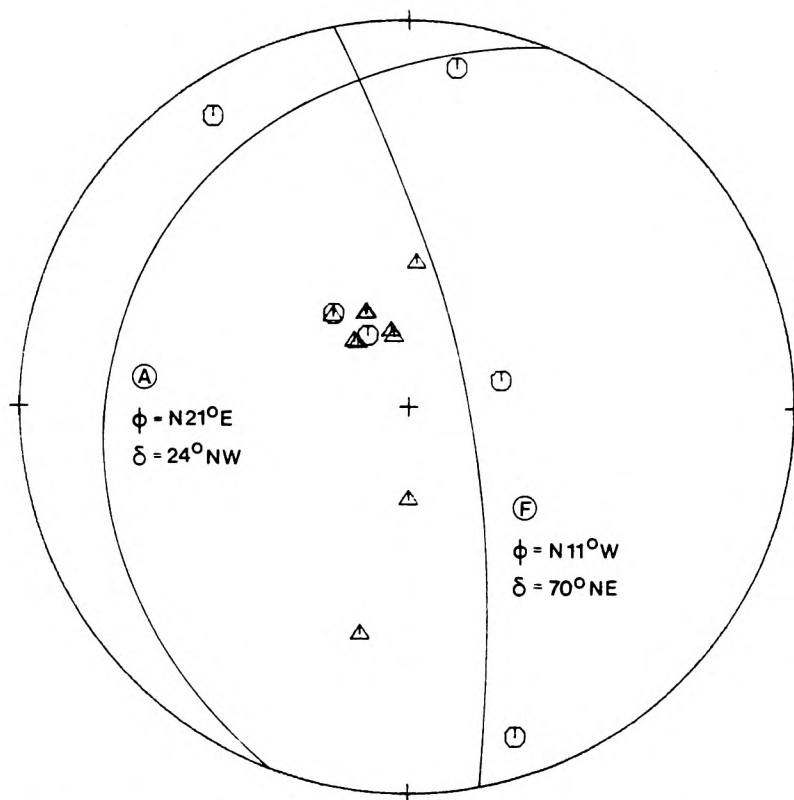
CB022 28/12/76 21.27S 68.64W MB5.7 H85
 P-FIRST MOTION (58 OBS/SPZ LOWER HEMI)
 COMPRESSION (UP) = ○
 DILATATION (DOWN) = △



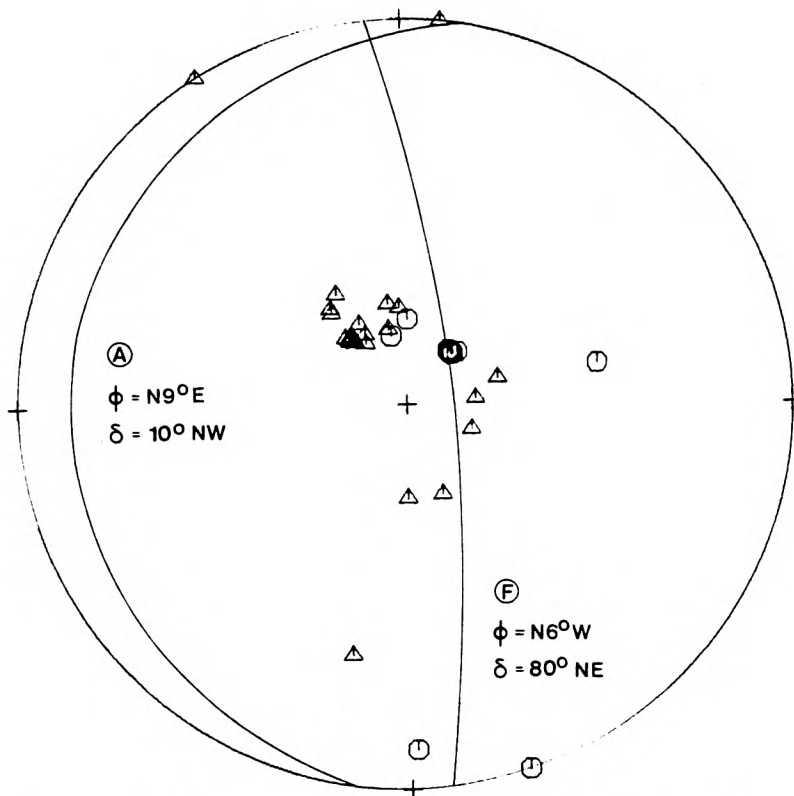
CB014 04/12/76 20.485 68.89W MB5.5 H87
 P-FIRST MOTION (51 OBS/SPZ LOWER HEMI)
 COMPRESSION (UP) = ○
 DILATATION (DOWN) = △



CB011 03/12/76 20.64S 68.77W MB5.3 H88
 P-FIRST MOTION (39 OBS/SPZ LOWER HEMI)
 COMPRESSION (UP) = ○
 DILATATION (DOWN) = △



CB013 04/12/76 20.51S 68.65W MB5.1 H95
 P-FIRST MOTION (16 OBS/SPZ LOWER HEMI)
 COMPRESSION (UP) = \oplus
 DILATATION (DOWN) = \triangle



CB018 17/12/76 20.98S 68.55W MB5.4 H76
 P-FIRST MOTION (44 OBS/SPZ LOWER HEMI)
 COMPRESSION (UP) = \ominus
 DILATATION (DOWN) = \triangle

ERRATUM

<u>PAGE</u>	<u>PLACE</u>	<u>ERROR</u>	<u>CORRECTION</u>
22	under (ii) line 2	by the ink	by the ink:pump
25	lines 5 and 6	12.5S.Giving	12.5S,giving
25	-	page No. 25	page No. 26
26	-	page No. 26	page No. 25
124	under 3.1.2 line 7	CB002	CB022
144	under 6.0.0 line 4	or a large	of a large
152	line 12	attitudes	altitudes

177 JAN 2011